JYU DISSERTATIONS 222

Tiia Haverinen

Development of Nuclear Energy Density Functionals from Optimization to Uncertainty Analysis

UNIVERSITY OF JYVÄSKYLÄ
FACULTY OF MATHEMATICS
AND SCIENCE

JYU DISSERTATIONS 222

Tiia Haverinen

Development of Nuclear Energy Density Functionals from Optimization to Uncertainty Analysis

Esitetään Jyväskylän yliopiston matemaattis-luonnontieteellisen tiedekunnan suostumuksella
julkisesti tarkastettavaksi toukokuun 29. päivänä 2020 kello 12.

Academic dissertation to be publicly discussed, by permission of
the Faculty of Mathematics and Science of the University of Jyväskylä,
on May 29, 2020 at 12 o'clock noon.

JYVÄSKYLÄN YLIOPISTO
UNIVERSITY OF JYVÄSKYLÄ

JYVÄSKYLÄ 2020

Editors
Timo Sajavaara
Department of Physics, University of Jyväskylä
Ville Korkiakangas
Open Science Centre, University of Jyväskylä

Permanent link to this publication: http://urn.fi/URN:ISBN:978-951-39-8170-9

ISBN 978-951-39-8170-9 (PDF)
URN:ISBN:978-951-39-8170-9
ISSN 2489-9003

Physicists have a talent for
producing equations that
they are quite unable to solve.
— Fabio Finocchi[1]

[1] On the notes *Density Functional Theory for Beginners*, 2011.

Preface

I see this doctoral thesis not only as the finish line of my four-year doctoral studies but as the outcome of all the eight years I spent at the Department of Physics in Jyväskylä. During these years I could concretize my passion for science and I met countless wonderful and talented colleagues around the world. This thesis would not have been actualized without the support of many, many, people.

I want to thank Dr. Markus Kortelainen for providing me an opportunity for doctoral studies and for opportunities to work abroad. Thanks are also due to my peer colleague Dr. Gianluca Salvioni for all the advice and for always being willing to help. I am grateful for the occasion to be a member of the multinational research collaboration led by Prof. Jacek Dobaczewski, thank you.

I want to thank IPN Lyon for the ineffable hospitality in the autumn 2017 and 2018 for providing me such an inspirational environment to do research. Particularly, I want to express my deepest gratitude to Dr. Karim Bennaceur for all the various discussions and for organizing my two stays in Lyon. Without him this thesis would never have been written. *Merci pour tout!*

Thanks Dr. Juha Merikoski, Dr. Jussi Maunuksela and Dr. Sami Räsänen for checking that my studies are progressing on time and Prof. Jouni Suhonen for introducing the field of nuclear physics to me many years ago in the form of a Bachelor Thesis. Thank you Dr. Kai Loo, M.Sc. Maciej Slupecki and M.Sc. Lama Al Ayoubi for the great peer support in the office.

I thank Dr. Andrea Idini and Prof. Tamara Nikšić for reviewing the manuscript carefully and providing constructive comments and Prof. Gianluca Colò for being my opponent on the day of my dissertation.

In addition, I have been privileged to have so many supporting people around me also outside of the office. I want to thank all my friends and family for the support and for believing in me, especially my brother Tomi. Last but not least, I want to thank my beloved Miha for all the support and care.

Jyväskylä, May 2020
Tiia Haverinen

Acknowledgements

This thesis was supported by North Karelia Regional Fund of Finnish Cultural Foundation, Helsinki Institute of Physics and University of Jyväskylä. CSC IT Center for Science Ltd. is acknowledged for the allocation of significant computational resources.

Abstract

This doctoral thesis covers the different aspects of the development of nuclear energy density functionals (EDFs). The nuclear EDFs are still the only microscopic models that can be applied along the whole nuclear chart. Despite their versatile applicability to predict various properties of experimentally unknown nuclei, the shortcomings of present state-of-the-art EDFs have become apparent. The deficiencies of these models must be studied, and this gained knowledge must be used to create better novel approaches.

In this thesis an uncertainty analysis of the UNEDF models is carried out. Since nuclear EDFs contain a set of parameters that must be fitted to experimental data, they carry statistical uncertainty that propagates into theoretical predictions. Even though error estimates are important by themselves, the uncertainty analysis may also bring additional information as to where the deficiencies of the studied model lie. Thereby the uncertainty propagation of the UNEDF models is studied in detail in the thesis with emphasis regarding the contributions to the errors given by different model parameters.

The optimization processes of nuclear EDFs are discussed by explaining different optimization strategies but also by demonstrating the difficulties of the task. Since the fitting data often includes properties of both single nuclei and infinite nuclear matter (INM), analytical formulas of INM properties are derived from a novel interaction, namely from the regularized finite-range pseudopotential.

Tiivistelmä

Tämä väitöskirja käsittelee ytimen energiatiheysfunktionaalien kehittämistä eri näkökulmista. Ytimen energiatiheysfunktionaalit ovat yhä ainoita mikroskooppisia malleja, joita voidaan soveltaa läpi koko ydinkartan. Vaikka nämä mallit soveltuvat monipuolisesti eri kokeellisesti tuntemattomien ytimien ominaisuuksien ennustamiseen, myös viimeisimpien mallien puutteet ovat tulleet ilmi. Käytössä olevien mallien puutteita täytyy tutkia, ja kertynyttä ymmärrystä tulee käyttää uusien parempien menetelmien luomiseksi.

Tässä väitöskirjassa on toteutettu UNEDF-mallien epävarmuusanalyysi. Koska ytimen energiatiheysfunktionaalit sisältävät joukon parametreja, jotka täytyy sovittaa kokeelliseen dataan, nämä mallit kantavat tilastollista virhettä, joka puolestaan kantautuu annettuihin ennusteisiin. Vaikka virhearviot ovat tärkeitä jo niiden itsensä takia, voi epävarmuusanalyysi tuottaa lisätietoa siitä, missä mallin heikkoudet piilevät. Siksi tässä työssä UNEDF-mallien virheiden etenemistä tutkitaan yksityiskohtaisesti huomioiden virheen kertyminen eri mallien parametreista.

Energiatiheysfunktionaalien optimointiprosesseja käsitellään esittelemällä eri optimointistrategioita, mutta myös havainnollistamalla tehtävän haastavuutta. Koska parametrien sovittamiseen käytetty data sisältää usein niin yksittäisten ytimien kuin äärettömän ydinmaterian (INM) ominaisuuksia, tässä väitöskirjassa on johdettu myös muutamia INM-ominaisuuksia uutta äärellisen kantaman vuorovaikutusta käyttäen.

Author Tiia Haverinen
Department of Physics
University of Jyväskylä
Finland

Supervisor Dr. Markus Kortelainen
Department of Physics
University of Jyväskylä
Finland

Reviewers Dr. Andrea Idini
Department of Physics
Lund University
Sweden

Prof. Tamara Nikšić
Department of Physics
University of Zagreb
Croatia

Opponent Prof. Gianluca Colò
Department of Physics
University of Milan
Italy

List of Publications

I **Uncertainty propagation within the UNEDF models**
T. Haverinen and M. Kortelainen
J. Phys. G: Nucl. Part. Phys. 44, 044008 (2017)

II **Towards a novel energy density functional for beyond-mean-field calculations with pairing and deformation**
T. Haverinen, M. Kortelainen, J. Dobaczewski and K. Bennaceur
Acta Physica Polonica B, 50 (3), 269-274 (2019)

III **Regularized pseudopotential for mean-field calculations**
K. Bennaceur, J. Dobaczewski, T. Haverinen and M. Kortelainen
arxiv:1909.12879
Accepted for publication in Journal of Physics: Conference Series – Proceedings of the 27th International Nuclear Physics Conference (INPC) 2019, Glasgow, UK.

IV **Properties of spherical and deformed nuclei using regularized pseudopotentials in nuclear DFT**
K. Bennaceur, J. Dobaczewski, T. Haverinen and M. Kortelainen
arXiv:2003.10990

The author has written the original drafts of the manuscripts and performed all the numerical calculations in Articles I and II. The author derived the analytical form of the (S, T) decomposition of binding energy per nucleon in infinite nuclear and neutron matter for Article III and Article IV.

Contents

Chapter 1

Introduction

There is no standard model in nuclear physics. The large variety of nuclear phenomena, the disparity of nuclear systems and the limits of computational resources have resulted in the absence of such a model [1]. Understanding the atomic nucleus is still a fundamental research problem, despite the research continued more than half a century.

Before the discovery of the nucleus itself, there were many epoch-making discoveries that changed the understanding of the atom, the nucleus and the related mechanisms. Henri Becquerel's discovery of radioactivity in the end of 19th century [2], soon followed by Joseph John Thomson's discovery of the electron [3], shed light on the existence of the internal structure of the atom. In the forthcoming years, alpha [4], beta [4] and gamma [5] radiation were discovered. *The plum pudding model* supported by Thomson had to give way to Rutherford's model [6], after the famous measurements of alpha particles and their scattering out of the foil [7, 8, 9, 10]. By analyzing the data of scattered alpha particles, Rutherford found out that there must be a tiny, very dense nucleus inside the atom, instead of negatively-charged *plums* in a positive-charged *pudding*.

The passionate studies of nuclei carried on. Already at that time, in 1911, Rutherford's model was correct in many ways but it was still lacking some revolutionary concepts. Nuclear processes were linked to the evolution of stars for the first time in 1920, when Arthur Stanley Eddington speculated that the fusion of hydrogen into helium could be the source of the stellar energy [11]. It was known that matter can convert into energy according to the mass-energy equivalence proposed by Albert Einstein [12], but fusion reactions and matter composition of stars had not yet been discovered – thus Eddington's reasoning was quite exceptional. Around ten years later, in 1932, James Chadwick discovered the neutron [13] while identifying the unknown particle of radiation studies [14, 15]. During the same year Dmitri Iwanenko updated Rutherford's model and suggested that there are no electrons in nuclei, but protons and Chadwick's neutrons instead [16].

The modern simple view of the atom and its nucleus was almost ready in the early 30s. There was only one big open question, namely what makes the nucleus a bound system. The first major step in solving the puzzle was taken by Hideki Yukawa in 1935, when he proposed a theory for describing the strong force [17]. He explained that there must be an attractive force between all nucleons, and this force is mediated by a virtual particle (later named as a meson). The existence of the strong force explained how the nucleons can cohere despite the repulsive Coulomb force.

Not only the structure of the nucleus was studied but the related phenomena as well. Some properties of nuclei could be approximated surprisingly well via classical reasoning, for example nuclear binding energy could be described roughly in terms of the liquid drop model [18]. Even though classical approximations worked in some specific occasions, nuclei were understood to be quantum mechanical objects. Nucleons were not wandering around the nucleus randomly, but the structure of the nucleus could be described through different energy levels, shell structures and magic numbers, as it was proposed first by E. Gapon and D. Iwanenko [19], and later by M. Goeppert Mayer and J. H. D. Jensen *et al.* [20, 21] The different forms of nuclear decay were studied further [22, 23, 24, 25], and the possibilities of fusion and fission processes were brought to bear.

The number of theories and models kept increasing. Various models and theories were created to understand and predict all the versatile phenomena. Separate classes of models were built on different principles and points of view. In the field of nuclear structure, the shell model was created to describe nuclei via energy levels filled by nucleons, starting from the lowest level [26]. *Ab initio* methods aimed to provide a more fundamental approach by starting from nucleons and inter-nucleon forces and solving the corresponding Schrödinger equation without empirical parameters [27, 28]. The other extreme of nuclear models were microscopic-macroscopic (mic-mac) methods which are vastly phenomenological but equipped with great predictive power [29]. The nuclear density functional theory (DFT) lied somewhere between mic-mac and ab initio methods, together with the shell model. In DFT, nuclei were studied through nucleonic densities and self-consistently determined mean-fields, while the effective interactions were phenomenological and had fitted parameters [30].

Thus a great number of theories and methods came into being, not to mention plentiful specific models or parametrizations. *There is no nuclear standard model*, even the description of nuclear structure is challenging. The reasons are manifold:

1. There are not enough nucleons in nuclei that they could be treated by using statistical methods. However, there are far too many nuclei so that the Schrödinger equation of the system could be solved directly.

2. Ab initio treatment of all nuclei and their excited states is presently infeasible.

Figure 1.1: The main steps in the development of a model.

Even though the used interaction is usually acquired from an effective theory, retaining the low-energy symmetries of the quantum chromodynamics, the nuclear many-body problem is too challenging to solve in ab initio framework in general due to the computational costs.

3. There is evidence that three nucleon interaction is significant in nuclei. This naturally increases the complexity of the problem.

4. The variety of all the nuclear phenomena and properties is vast.

Evidently, there is a compulsive need to use models and approximations in nuclear physics. In DFT, the unknown component is the effective interaction describing the force between nucleons. There are three main types of effective interactions: finite-range, zero-range and relativistic interactions. All the different types include even dozens of models that differ in the constituting terms. What is more, some models do have different parametrizations – those differ only in the fitted model parameters. Different models have been designed for particular applications, or they were aimed to be improvements of previously formulated ones.

The development of a model is a multi-step process illustrated in Figure 1.1. All the work starts from the mathematical, analytical formulation of the model. In this "*pen & paper*" step not only the effective interaction is formulated but all the necessary interaction-dependent equations are derived as well. An example of a necessary equation is binding energy per nucleon in infinite nuclear matter, which is often used in optimization.

The second step in the model development is the optimization of the model parameters. As long as the model parameters cannot be derived from the underlying theory or any other piece of knowledge, they are most often optimized on a selected data set. This holds for effective interactions and energy density functionals, even for machine learning models in general. Depending on the chosen data set, the formulated optimization problem and the complexity of the model, the optimization process can be performed in a blink of an eye, or it may turn out to be a task far from trivial.

When the model parameters have been successfully optimized, the model must be tested by applying the obtained model. Naturally, the model should be tested on data that was not used in the optimization process. The model is used to give predictions, which are compared to the experimental values. Various statistical estimates can be computed, such as mean squared error (MSE) and coefficient of determination (R^2). These measures give a rough estimate of the goodness-of-fit. For instance, if MSE is far too great or the value of R^2 implies that the model is not able to reproduce experimental results, the analytical formulation of the model and the implementation of the optimization process must be re-examined.

All models are wrong [31]. However, a model can still be useful. To estimate the usefulness, the uncertainties of the predictions are estimated in the final step of the model development. Every model having fitted parameters will carry the uncertainty of the model parameters into the obtained predictions. There are tools for tracking this uncertainty, and they are more deeply discussed in Chapter 5. As we will notice later, the uncertainty estimation can give us valuable information as to where the model uncertainties originate and what are the shortcomings of the model. It may help us to find missing imporant features and to reformulate the model – and this way we end up from the last step to the first one.

The steps seen in Figure 1.1 are not high-tech. However, many of them are relatively new concepts in the field of nuclear structure. During many decades, the model parameters were tuned by hand, instead of determining the coefficient via a well defined optimization process. A hand-tuned parameterization may produce reasonable results, but the information on the prediction power is more or less lost. This is one of the reasons why there are error bars missing from scientific papers: Many of the most used models were hand-tuned. It was not feasible to reproduce the models by optimizing them and as a consequence, statistical errors will be beyond one's reach. The other reasons for the lack of uncertainty analysis were the limited computational resources and faint requirements of the scientific journals. Most often uncertainty estimates are computationally demanding and the increased availability of supecomputers has enabled the work. In addition, as weird as it may sound, the requirements for error bars have not been strict in scientific journals among this field. The editors of Physical Review A wrote an article to discuss the importance of uncertainty estimates as recently as in 2011 [32]. Soon several workshops were organized (e.q. *Information and Statistics in Nuclear Experiment and Theory*, ISNET), guides were written and the general interest grew up rapidly [33, 34].

This thesis is a cross-section of the steps in Figure 1.1. The main theoretical tools, namely the Hartree-Fock-Bogoluybov theory and density functional theory are described in Chapters 2 and 3 respectively, not forgetting the introduction of the most used effective interactions. The optimization methods and some obtained re-

sults are outlined in Chapter 4. The main steps in uncertainty analysis are wrapped up in Chapter 5 with the uncertainty estimates of the UNEDF models. The conclusions and the outlook of this work are provided in Chapter 6.

Chapter 2

The Hartree-Fock-Bogolyubov Method

In this chapter the some of the key concepts of Hartree-Fock-Bogolyubov (HFB) method are introduced: A more detailed introduction can be found e.g. in Ref. [35]. The HFB method is a mean-field method starting from the definition of quasi-particles and ending up in the set of iteratively solvable equations. Generally in mean-field theories one facilitates the original complex problem by one or several approximations. The interacting nucleons are seen as independent particles in an external potential, namely in a mean-field. In contrast to the simpler Hartree-Fock (HF) method, the HFB method takes into account pairing correlations that are crucial for most of nuclei and for many nuclear phenomena. The importance of pairing effects can be seen in the bulk properties such as in binding energies, particularly in pairing gaps – in those binding energy differences of even-even and odd-A nuclei.

2.1 Bogolyubov transformation

As it was mentioned earlier, the Bogolyubov transformation is introduced in order to include pairing correlations into the theory. In the Bogolyubov transformation, the complex system of interacting nucleons is seen as a simple collection of independent quasiparticles moving in an external field. Thus, instead of trying to describe the complex motion of a nucleon while the motion is disturbed by all the possible interactions, it is approximated that the nucleon is more or less like a nucleon with a different mass and moves without any disturbation in free space. The "different mass" is called *an effective mass*, resulting from the underlying nucleon-nucleon interaction.

Naturally, the Bogolyubov transformation is the connection between the single-particle and quasiparticle states. Bogolyubov quasi-particle operators $(\beta_\mu, \beta_\mu^\dagger)$ are

linked to particle operators $c_\mu, c_\mu^\dagger$ through the unitary transformation [35]

$$\beta_\mu = \sum_i U_{i\mu}^* c_i + V_{i\mu}^* c_i^\dagger \tag{2.1}$$

$$\beta_\mu^\dagger = \sum_i V_{i\mu} c_i + U_{i\mu} c_i^\dagger. \tag{2.2}$$

In matrix form the equations are written as

$$\begin{pmatrix} \beta \\ \beta^\dagger \end{pmatrix} = \begin{pmatrix} U^\dagger & V^\dagger \\ V^T & U^T \end{pmatrix} \begin{pmatrix} c \\ c^\dagger \end{pmatrix}. \tag{2.3}$$

The matrices U and V and their matrix elementes are not known in the beginning, they must be solved. Since the quasiparticles must obey the same anticommutation rules as the original particles, the transformation must be unitary and it fulfills the relationships

$$U^\dagger U + V^\dagger V = 1, \quad UU^\dagger + V^* V^T = 1, \tag{2.4}$$

$$U^T V + V^T U = 0 \quad \text{and} \quad UV^\dagger + V^* U^T = 0. \tag{2.5}$$

The ground state $|\phi\rangle$ is the state having the lowest energy. In the HFB theory, the ground state of the many-body system is also defined as the quasiparticle vacuum, that is

$$\beta_k |\phi\rangle = 0 \quad \text{for all} \quad k = 1, ..., M, \tag{2.6}$$

where M denotes the size of the configuration space. The quasiparticle state can be expressed in a compact way by nucleonic densities. The normal and pairing one-body densities are defined in configuration space as

$$\rho_{nn'} = \langle\phi| c_{n'}^\dagger c_n |\phi\rangle = (V^* V^T)_{nn'}, \tag{2.7}$$

$$\kappa_{nn'} = \langle\phi| c_{n'} c_n |\phi\rangle = (V^* U^T)_{nn'}, \tag{2.8}$$

and they can be expressed in coordinate space so that

$$\rho(\mathbf{x}, \mathbf{x}') = \langle\phi| c_{\mathbf{x}'}^\dagger c_{\mathbf{x}} |\phi\rangle = \sum_n \phi_n^V(\mathbf{x}) \phi_n^{(V)*}(\mathbf{x}'), \tag{2.9}$$

$$\kappa(\mathbf{x}, \mathbf{x}') = \langle\phi| c_{\mathbf{x}'} c_{\mathbf{x}} |\phi\rangle = \sum_n \phi_n^U(\mathbf{x}) \phi_n^{(V)*}(\mathbf{x}'). \tag{2.10}$$

However, the definition of the ground state as a vacuum does not provide a tool for finding it. In the HFB method, the ground state is obtained by minimizing the total energy

$$E = \langle\psi| \hat{H} |\psi\rangle = E[\rho, \kappa, \kappa^*], \tag{2.11}$$

and as Equation (2.11) implies, the total energy can be expressed as a pure function of one-body densities. This holds for any expectation value of an operator related to a HFB state. While minimizing the energy, constraints on proton and neutron number must be used, since a particle number is not a good quantum number in the HFB theory. That is why – in practice – one minimizes the Routhian, which is defined as

$$E^{\lambda} = E - \sum_{q=n,p} \lambda_q \langle \psi | \hat{N}_q | \psi \rangle, \tag{2.12}$$

where $\hat{N}_q$ is the particle number operator and λ_q are the corresponding Lagrange multipliers so that

$$\lambda = \frac{\mathrm{d}E}{\mathrm{d}N_q}. \tag{2.13}$$

The minimization of the Routhian practically means that the energy E^{λ} is minimized while keeping the neutron and proton number fixed, that is applying the constraints $N_p = Z$ and $N_n = N$. However, the particle number is no longer a good quantum number of HFB states – this can be avoided by projecting on the particle number. The minimization leads us to the HFB equations,

$$\mathcal{H} \begin{pmatrix} U_n \\ V_n \end{pmatrix} = e_n \begin{pmatrix} U_n \\ V_n \end{pmatrix} \quad \text{where} \quad \mathcal{H} = \begin{pmatrix} h - \lambda & \Delta \\ -\Delta^* & -h^* + \lambda \end{pmatrix}. \tag{2.14}$$

The mean field and pairing field matrix elements are the variations of energy with respect to the one-body densities, formulated as

$$h_{ij} = \frac{\delta E}{\delta \rho_{ji}} = h^*_{ji} \quad \text{and} \quad \Delta_{ij} = \frac{\delta E}{\delta \kappa^*_{ij}} = -\Delta_{ji}. \tag{2.15}$$

If the used Hamiltonian is a general two-body Hamiltonian of a fermionic system,

$$\hat{H} = \hat{T} + \hat{V} \tag{2.16}$$

$$= \sum_{n_1 n_2} T_{n_1 n_2} c^{\dagger}_{n_1} c_{n_2} + \frac{1}{4} \sum_{n_1 n_2 n_3 n_4} V_{n_1 n_2 n_3 n_4} c^{\dagger}_{n_1} c^{\dagger}_{n_2} c_{n_4} c_{n_3}, \tag{2.17}$$

where c and $c^{\dagger}$ are annihilation and creation operators so that $c^{\dagger}_{\alpha}$ creates a particle in state $|\alpha\rangle$ and c_{α} deletes a particle from state $|\alpha\rangle$, and the antisymmetrized two-body interaction matrix elements are

$$V_{n_1 n_2 n_3 n_4} = \langle n_1 n_2 | \hat{V} | n_3 n_4 - n_4 n_3 \rangle = \hat{V}_{n_1 n_2 n_3 n_4} - \hat{V}_{n_1 n_2 n_4 n_3}, \tag{2.18}$$

then the matrices h and Δ of Equation (2.15) become

$$h_{ij} = T_{ij} + \sum_{kl} V_{ijkl} \rho_{lk} \quad \text{and} \quad \Delta_{ij} = \frac{1}{2} \sum_{kl} V_{ijkl} \kappa_{kl}. \tag{2.19}$$

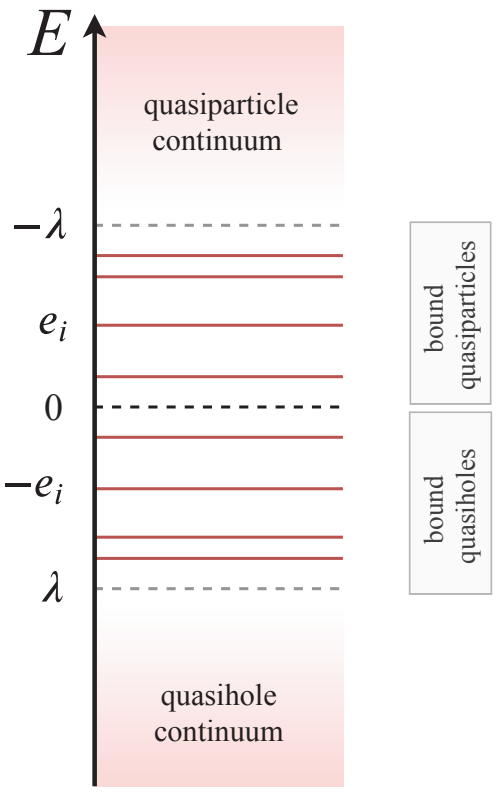

Figure 2.1: The quasiparticle spectrum of the HFB method. Every quasiparticle state with the energy e_i there is a state with the energy $-e_i$. Bound HFB states have the energy $\lambda \leq E \leq -\lambda$, where the chemical potential λ is negative.

2.2 HFB solutions and constraints

The full quasiparticle HFB spectrum $\{e_n\}$ is unbound in both directions, above and below, as it is illustrated in Figure 2.1. If time-reversal symmetry is assumed, there is always an opposite eigenvalue $-e_i$ for an eigenvalue e_i, and only one of these is needed for getting all the information related to these states. Since only a half of the states is relevant, one is free to choose which half of the states is used. A common choice is to pick the states having the positive eigenvalues.

The energies range of bound states is limited by the Lagrangian multiplier λ, referred to as the chemical potential. The chemical potential λ is negative for a particle system, and thus the bound HFB states have the energy $e_i \leq -\lambda$.

If the HFB calculation is only constrained by proton and neutron particle numbers, the obtained solution corresponds to a local or global minimum depending on the starting point. If there are no other constraints than the particle number, the

calculation is most often called an *unconstrained* HFB calculation. It is not usually guaranteed by a HFB solver that the obtained unconstrained calculation finds the global minimum. This is because the basic minimization algorithms determine the minimum by exploring the vicinity of the minimum candidate, they do not compare multiple solutions. It would be possible to implement a HFB solver that gives the global minimum as an outcome with a good probability, but the global minimum is often discovered in the following way.

In order to determine the global minimum, namely the theoretical ground state, several *constrained* calculations are performed. In the constrained calculation a constraint is put on the deformation parameter that describes the shape of the nucleus, and this constraint is handled with the help of a Lagrangian multiplier in similar manner as it was done for the particle number constraint. If axial quadrupole deformation is assumed, the nucleus can be spherical, oblate or prolate, and which correspond to zero, negative and positive values of the deformation parameter β, respectively. When compared to the spherical deformation, a prolate nucleus is elongated at the poles (an American football), and the oblate one is flattened at the poles (a pancake). After performing multiple constrained calculations, it can be seen how the energy varies as a function of nuclear deformation in general and the stablest deformation between an oblate and prolate deformation can be spotted (Figure 2.2). This plot visualizing binding energy as a function of deformation is often called *the deformation energy surface*. It provides additional support for the choice of starting point of the HFB calculation, and next the unconstrained calculation can be confidently performed to determine the exact theoretical ground state.

Figure 2.2 demonstrates two different deformation energy surfaces as well. The binding energy of ^{148}Dy has only one minimum and it corresponds to the spherical shape. In this case the initial deformation β_i of the unconstrained HFB calculation can be anything in the interval $[-0.5, 0.5]$, and the ground state will be determined. The better the initial guess is, the faster the final solution is found. However, the deformation energy surface of ^{172}Dy requires quite a good starting point for the unconstrained HFB calculation, since there are two local minima.

2.3 Solving the HFB equations in practice

In practice, the HFB method is an iterative method. Like any iterative method, the HFB equations require an initial guess and termination criteria. The initial guess is needed to generate a sequence of improving approximate solutions, and the termination criteria dictate when the iterative process stops: On one hand, they define when the solution is eligible, and on the other hand, they fix the maximum number of iterations that will be used in the quest for the solution. If the solution

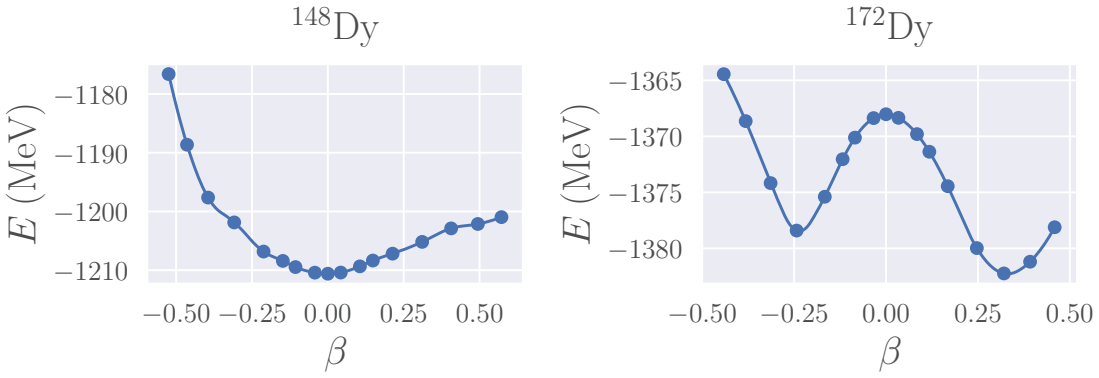

Figure 2.2: Binding energies of ^{148}Dy and ^{172}Dy nuclei as a function of a deformation parameter β. There can be one or multiple local minima in the binding energy corresponding to different deformations. Calculations performed using UNEDF0.

satisfies the convergence criteria, the HFB calculation is *converged*.

The iterative process of the HFB method is illustrated in Figure 2.3. The process gets started by an initial guess for the mean-field h and the pairing field Δ. In the following, the matrices U and V defining the Bogolyubov transformation are solved (Equation (2.14)), and when U and V are known, the normal density ρ and the pairing density κ can determined via Equations (2.7) and (2.8). Finally the energy of the system is solved, since it can be expressed as a function of densities.

Before running the HFB method, one has defined the convergence criteria. In addition to the maximum number of the HFB iterations, various different criteria are used to determine if the solution candidate is satisfactory. One of the simplest options is to check if the difference in energy is small enough between two latest iterations. Alternatively, one may require that the solution is converged if the matrix elements of h and Δ change less than a given constant when continuing from one iteration to the following. In principle, these two convergence criteria are equivalent when approaching the variational minimum. In practice, however, monitoring convergence of all matrix elements leads to a more stringent condition when some finite convergence criteria is used. Despite the implementation of the criteria, one checks if the convergence criteria were fulfilled, and if they were, one obtained a nonconverged or converged solution. Otherwise the next HFB iteration is started and one may solve the fields h and Δ by applying the one-body densities ρ and κ of the previous iteration.

There are various HFB solvers available, and they differ in the assumptions on the solutions and the practical implementation of the method. There are two main classes of implementations: Implementations on a basis of orthogonal functions and implementations in a coordinate space mesh. If the basis functions are used, the

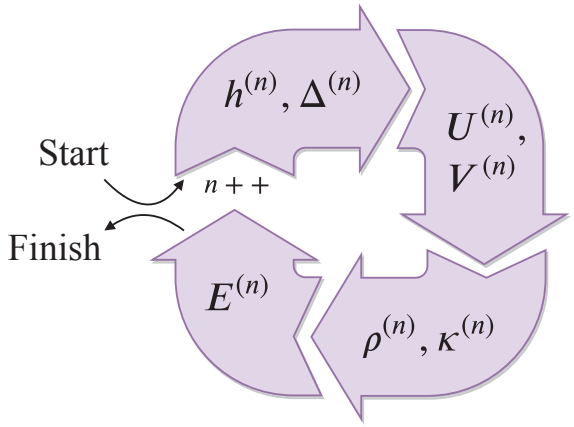

Figure 2.3: The iterative process of the HFB method. The iterations start from the initial guesses for the fields h and Δ, and the equations are solved iteratively till the maximum number of iterations is reached or the solution meets the convergence criteria.

typical choice is the harmonic oscillator basis. Even though this approach is efficient, the harmonic oscillator wave functions may hide the correct fine aspects of the system, such as some asymptotic behaviors. The implementations in a mesh are free from those challenges, but they involve a set of integro-differential equations that are computationally heavy to solve. As a consequence, coordinate space implementations are mainly applied for the simple zero-range forces, since the integro-differential equations become a set of simpler differential equations. The zero-range and finite-range interactions are discussed more in detail in Chapter 3.

All the used HFB solvers have not been published, and that makes it challenging to wrap up what kind of implementations already exist. The program HFBRAD solves the HFB equations in the coordinate space representation and assumes the nucleus to obey spherical symmetry [36]. The latest version of HFBTHO allows to use finite-range interaction in addition to the zero-range force in deformed harmonic oscillator basis [37]. Similarly, the code HFODD uses the Cartesian deformed harmonic oscillator basis [38] and in the latest version both a zero-range and a finite-range interaction have been implemented in the code. Nowadays there is an interface between HFBTHO and HFODD, which allows to constrain HFODD calculations on multiple moments, for instance. The template code HFBTEMP aims to be a modular HFB program allowing the usage of various interactions and bases (axial, cartesian, 3D) [39].

Chapter 3

Density Functional Theory

Density Functional Theory (DFT) is a computational modelling method, that allows us to predict properties of a many-nucleon or many-electron system by using *functionals*. A functional is a function of one or several other functions – in nuclear DFT, those other functions are nucleonic densities.

DFT was originally created for studying many-electron systems. In 1964 Walter Kohn and Pierre Hohenberg published two theorems that were restricted to non-degenerate ground states without an interacting magnetic field. The theorems, later named as Hohenberg-Kohn (H-K) theorems, state that [40]

I The ground state properties of a many-electron system are uniquely determined by an electron density

II There exists an energy functional for the system and the ground state electron density gives the minimum energy.

Despite the limitations of the original H-K theorems (a nearly constant and slowly varying electron density was assumed, and an external potential was needed), the work of Hohenberg and Kohn gave a start for the long-lasting development of DFT. H-K theorems implied that there is a way to transform the original, highly complex, problem of N electrons with $3N$ spatial coordinates to a simper problem of one function and three spatial coordinates. The paper proved that the total energy of the system can be written as a functional and, indeed, that the functional exists, but despite the great importance of the paper, it did not give any tools to build the functional.

The H-K theorems were studied further by Walter Kohn himself together with Lu Jeu Sham [41]. They created a framework (later denominated Kohn-Sham DFT, KS-DFT) in which the interacting electrons in a static external potential were transformed into noninteracting particles in an effective potential. The effective potential was a concept piecing together the original external potential and the

effects of mutual interaction, namely the effects of the Coulomb interaction. As an outcome, the problem was computationally less demanding, since the wavefunctions of noninteracting fermions could be written as single Slater determinants. Already in the mid-60s, Kohn and Sham noticed that the approximations lead to equations analogous to the Hartree-Fock equations [41].

The DFT formalism was created to study many electron systems, but it was found to be a relevant tool to describe nuclear structure analogously. However, the many-nucleon and the many-electron systems have some significant differences. First of all, electrons of an atom move in an external potential created by a nucleus. The nuclei in an atomic nucleus do not sense external potential but form a self-bound system, instead. Additionally, a two-body interaction is complicated enough to describe the many-electron systems, but three-body interactions are relevant for nuclei and even the four-body interactions may be noticeable [42].

3.1 Densities

One-body densities ρ and κ defined in Equations (2.7) and (2.8) are the building blocks of the nuclear DFT. In addition to these two fundamental variables, some of their derivatives are needed as well.

Normal densities are scalars and spin densities are vectors, in addition they can be isoscalar or isovector. The scalar-isoscalar density ρ_0, the scalar-isovector density ρ_1, the vector-isoscalar density s_0 and the vector-isovector density s_1 are expressed as

$$\rho_0 = \rho_{n\uparrow} + \rho_{n\downarrow} + \rho_{p\uparrow} + \rho_{p\downarrow} = \rho_n + \rho_p \tag{3.1}$$
$$\rho_1 = \rho_{n\uparrow} + \rho_{n\downarrow} - \rho_{p\uparrow} - \rho_{p\downarrow} = \rho_n - \rho_p \tag{3.2}$$
$$s_0 = \rho_{n\uparrow} - \rho_{n\downarrow} + \rho_{p\uparrow} - \rho_{p\downarrow} = s_n + s_p \tag{3.3}$$
$$s_1 = \rho_{n\uparrow} - \rho_{n\downarrow} - \rho_{p\uparrow} + \rho_{p\downarrow} = s_n - s_p \tag{3.4}$$

Since the three Pauli matrices and the unit matrix form a complete basis, we can expand the density matrix $\rho(\vec{x}, \vec{x}')$,

$$\rho(\vec{r}\sigma\tau, \vec{r}'\sigma'\tau') = \frac{1}{4}\left[\rho_0(\vec{r}, \vec{r}')\delta_{\sigma\sigma'}\delta_{\tau\tau'} + s_0(\vec{r}, \vec{r}')\vec{\sigma}\delta_{\tau\tau'} + \rho_1\delta_{\sigma\sigma'}\vec{\tau} + s_1(\vec{r}, \vec{r}')\vec{\sigma}\vec{\tau}\right] \tag{3.5}$$

where we assume pure proton and neutron states. We can express these four densities and some of their derivatives as a function of the full density matrix. The local

forms can be written as

$$\rho_0(\vec{r}) = \rho_0(\vec{r},\vec{r}) = \sum_{\sigma\tau} \rho(\vec{r}\sigma\tau,\vec{r}\sigma\tau), \tag{3.6}$$

$$\rho_1(\vec{r}) = \rho_1(\vec{r},\vec{r}) = \sum_{\sigma\tau} \rho(\vec{r}\sigma\tau,\vec{r}\sigma\tau)\tau, \tag{3.7}$$

$$\vec{s}_0(\vec{r}) = \vec{s}_0(\vec{r},\vec{r}) = \sum_{\sigma\sigma'\tau} \rho(\vec{r}\sigma\tau,\vec{r}\sigma'\tau)\vec{\sigma}_{\sigma'\sigma}, \tag{3.8}$$

$$\vec{s}_1(\vec{r}) = \vec{s}_1(\vec{r},\vec{r}) = \sum_{\sigma\sigma'\tau} \rho(\vec{r}\sigma\tau,\vec{r}\sigma'\tau)\vec{\sigma}_{\sigma'\sigma}\tau, \tag{3.9}$$

$$\vec{j}_T(\vec{r}) = \frac{i}{2}(\nabla' - \nabla)\rho_T(\vec{r},\vec{r}')\Big|_{\vec{r}-\vec{r}'}, \tag{3.10}$$

$$\mathbb{J}(\vec{r}) = \frac{i}{2}(\nabla - \nabla') \otimes \vec{s}_T(\vec{r},\vec{r}')\Big|_{\vec{r}=\vec{r}'} \tag{3.11}$$

$$\tau_T(\vec{r}) = \nabla\cdot\nabla'\rho_T(\vec{r},\vec{r}')|_{\vec{r}=\vec{r}'} \tag{3.12}$$

$$\mathbf{T}_T(\vec{r}) = \nabla\cdot\nabla'\vec{s}_T(\vec{r},\vec{r}')|_{\vec{r}=\vec{r}'} \tag{3.13}$$

that are called the density, spin density, spin-current tensor, kinetic density and kinetic spin density in the literature [30].

3.2 Gogny interaction

One of the first attemps to find a finite-range phenomenological two-body nucleon-nucleon interaction was made by D. M. Brink and E. Boecker in 1967 [43]. They implemented an interaction that was a sum of two Gaussian potentials and used the novel interaction in Hartree-Fock calculations, but the obtained theoretical binding energies were not compatible with the experimental results. The work was continued by J. Dechargé and D. Gogny, who proposed two additional terms to the interaction, one describing spin-orbit interaction and one having a density dependence [44], and the interaction got the form

$$\begin{aligned} V_{\text{Gogny}}(\vec{r}_1,\vec{r}_2) =& \sum_{j=1}^{2} e^{\frac{|\vec{r}_1-\vec{r}_2|^2}{\mu_j^2}} (W_j + B_j\hat{P}^\sigma - H_j\hat{P}^\tau - M_j\hat{P}^\sigma\hat{P}^\tau) \\ &+ t_3(1+x_0\hat{P}^\sigma)\delta(\vec{r}_1-\vec{r}_2)\rho^\alpha\left(\frac{\vec{r}_1+\vec{r}_2}{2}\right) \\ &+ iW_{so}(\vec{\sigma}_1+\vec{\sigma}_2)\cdot\vec{k}^\dagger\times\delta(\vec{r}_1-\vec{r}_2)\vec{k}, \end{aligned} \tag{3.14}$$

where $\hat{P}^\sigma = \frac{1}{2}(1+\vec{\sigma}_1\cdot\vec{\sigma}_2)$ is the spin-exchange operator and $\hat{P}^\tau = \frac{1}{2}(1+\vec{\tau}_1\cdot\vec{\tau}_2)$ is the corresponding isospin-exchange operator. The relative momentum operator

is defined as $\vec{k} = -\frac{i}{2}\left(\vec{\nabla}_1 - \vec{\nabla}_2\right)$, and it is acting on the right, while the adjoint operator $\vec{k}^\dagger$ is acting on the left.

The interaction of Equation (3.14) is known as the Gogny force. The first term having the Gaussians and the exchange operators is more or less the original force proposed by Brink and Boecker. Two Gaussian functions create the finite-range effect with the ranges μ_j. The exchange terms $\hat{P}^\sigma, \hat{P}^\tau$ and $\hat{P}^\sigma\hat{P}^\tau$ are needed to ensure *nuclear saturation*, the measured fact that the binding energies of nuclei are proportional to the number of nucleons A, apart from the few lightest nuclei, and consequently the average binding energy per nucleon is pretty much constant in nuclei. If the exchange operators do not exist in the interaction, the repulsion originating from the simpler interaction is not strong enough to compete against the attraction. When the exchange terms $\hat{P}^\sigma, \hat{P}^\tau$ and $\hat{P}^\sigma\hat{P}^\tau$ are included, they increase repulsion and the saturation is possible. [1]

The second term is density dependent, and the density dependence has been proven to be an essential ingredient to reproduce a reasonable value for the effective mass [45]. However, the density dependent term has its own shortcomings: It is conceptually dangerous, since it is not derived from an underlying Hamiltonian, and in addition, it introduces problems in particle number restoration and in restoration of broken symmetries in general, which will be discussed later [46, 47, 48].

The last term of the Gogny interaction is the spin-orbit term. The spin-orbit interaction splits the states having the same orbital angular momentum quantum number l into two separate states with total angular momenta $j = l \pm 1/2$. The nuclear spin-orbit interaction is different from the well-understood electromagnetic spin-orbit interaction seen at the atomic level, and phenomenological models must be used. The spin-orbit interaction is relatively weaker in the atomic fine structure: In this case the impact of the spin-orbit interaction is of the order of meV's whereas the energy differences in level structures are eV's. The nuclear spin-orbit splitting is more significant, since it is of the same energy scale as the differences of single-particle energies [26]. The spin-orbit term is a zero-range term for the sake of computational simplicity.

Altogether the general Gogny interaction has 14 parameters to be fixed, namely $\mu_j, W_j, B_j, H_j, M_j, t_3, x_0, \alpha$ and W_{so} with the indeces $j = \{1, 2\}$. The original parametrization D1 by J. Dechargé and D. Gogny is shown in Table 3.2. [44]

3.3 Skyrme interaction

One of two main classes of non-relativistic interactions used in nuclear DFT is the Skyrme interaction. The Skyrme interaction is a zero-range force but mimics finite-range effects by applying relative momentum operators, which makes the calculations faster than the actual finite-range calculations. T. H. R. Skyrme pro-

j	μ_j [fm]	W_j [MeV]	B_j [MeV]	H_j [MeV]	M_j [MeV]
1	0.7	-402.4	-100.0	-496.2	-23.56
2	1.2	-21.30	-11.77	37.27	-68.81

α	x_0	t_3 [MeV fm^4]	W_{so} [MeV fm^5]
1/3	1	1350	115

Table 3.1: An example of the parameters of Gogny interaction, namely the D1 parametrization by J. Dechargé and D. Gogny [44].

posed an effective zero-range force in the 50s in which he combined a two-body and a three-body force [49]. The interaction was formulated as

$$\hat{V} = \sum_{i<j} \hat{V}(i,j) + \sum_{i<j<k} \hat{V}(i,j,k), \tag{3.15}$$

where the two-body force was an expansion in the momentum space,

$$\begin{aligned}\hat{V}(1,2) = & t_0(1 + x_0\hat{P}^\sigma)\delta(\vec{r}_1 - \vec{r}_2) \\ & + \frac{1}{2}t_1\left(\vec{k}^{\dagger 2}\delta(\vec{r}_1 - \vec{r}_2) + \delta(\vec{r}_1 - \vec{r}_2)\vec{k}^2\right) \\ & + t_2\vec{k}^\dagger \cdot \delta(\vec{r}_1 - \vec{r}_2)\vec{k} \\ & + iW_{so}(\vec{\sigma}_1 + \vec{\sigma}_2) \cdot \vec{k}^\dagger \times \delta(\vec{r}_1 - \vec{r}_2)\vec{k},\end{aligned} \tag{3.16}$$

where the relative momentum is defined as $\vec{k} = \frac{1}{2i}(\nabla_1 - \nabla_2)$. The three-body interaction was assumed to be the simplest possible, namely a zero-range interaction formulated as

$$\hat{V}(1,2,3) = t_3\delta(\vec{r}_1 - \vec{r}_2)\delta(\vec{r}_2 - \vec{r}_3). \tag{3.17}$$

The first term, t_0-term, is a pure zero-range force together with a spin-exchange. The finite-range effects are simulated by the t_1- and t_2-terms, and the W_{so}-term is the spin-orbit interaction.

The original Skyrme force included six parameters to be adjusted, namely t_0, t_1, t_2, t_3, x_0 and W_{so}. Different parametrizations are obtained when the parameters are fitted to different data. One example of those parametrizations is SIII whose parameters are gathered in Table 3.3 [50].

After the 70s the two-body Skyrme interaction has been tuned. The spin-exchange operator has been incorporated in each term, which increases the flexibility of the model but the number of the free parameters as well. Most of the

t_0 [MeV fm^3]	t_1 [MeV fm^5]	t_2 [MeV fm^5]	t_3 [MeV fm^6]	x_0	W_{so} [MeV fm^5]
-1128.75	395.0	-95.0	14000.0	0.45	120

Table 3.2: Parameters of the Skyrme force SIII by M. Beiner *et al.* [50]

Skyrme models can be more or less formulated as [1]

$$\begin{aligned} V_{\text{Skyrme}}(\vec{r}_1,\vec{r}_2) = & t_0(1+x_0\hat{P}^\sigma)\delta(\vec{r}_1-\vec{r}_2) \\ & +\frac{1}{2}t_1(1+x_1\hat{P}^\sigma)\left(\vec{k}^{\dagger 2}\delta(\vec{r}_1-\vec{r}_2)+\delta(\vec{r}_1-\vec{r}_2)\vec{k}^2\right) \\ & +t_2(1+x_2\hat{P}^\sigma)\vec{k}^\dagger\cdot\delta(\vec{r}_1-\vec{r}_2)\vec{k} \\ & +\frac{1}{6}t_3(1+x_3\hat{P}^\sigma)\delta(\vec{r}_1-\vec{r}_2)\rho^\alpha\left(\frac{\vec{r}_1+\vec{r}_2}{2}\right) \\ & +iW_{so}(\vec{\sigma}_1+\vec{\sigma}_2)\cdot\vec{k}^\dagger\times\delta(\vec{r}_1-\vec{r}_2)\vec{k}, \end{aligned} \tag{3.18}$$

where the new parameters x_1, x_2 and x_3 correspond to the spin-exchange terms.

The t_3-term is the additional density dependent term, which has a connection to the three-body force. When $\alpha = 1$, the density-dependent term is equivalent to the zero-range three-body force of Equation (3.17) in a time-even functional [1]. The zero-range three-body interaction was used in SI, SII [51] and SIII [50], but the next generation of Skyrme forces have generalized the exponent α, since the exponent $\alpha = 1$ results in too large an incompressibility of the infinite nuclear matter (K_∞) [52]. The density-dependent term with a fractional power was found to be essential to produce effective masses and properties of infinite nuclear matter [52]. Various other generalizations have been implemented and tested (See Ref. [30], but this simple generalization of α has been the most efficient.

Despite the vast usefulness of the density-dependent term, it has its own shortcomings as well. As it was mentioned earlier, the term is conceptually dangerous, since it does not correspond to any underlying Hamiltonian when a fractional α is used. The density-dependent term has been discovered to lead to unconvergent calculations and anomalies illustrated in Figure 3.1 [53]. M. Bender *et al.* demonstrated in Ref. [53] that when a density-dependent functional is used (e.g. SLy4) in particle-number-restored multi-reference calculations, localized divergences are spotted in the deformation energy surface of ^{18}O when a single-particle level crosses the Fermi energy. When the calculation is performed with a more moderate commonly used precision, the anomalies are not visible. They can be spotted when the precision is increased well beyond the one used in practical calculations.

The Skyrme interaction is often used as a generator for energy density functional (EDF). Originally the Skyrme EDF was derived as an expectation value from the

[1] Time-even functional is a functional made of time-even densities.

effective Hamiltonian, but many of the recent models do not consider the Hamiltonian as the starting point any longer. The work is begun by defining a suitable EDF that models the system. Density dependencies are applied, different effective interactions are used to describe the particle-hole and pairing parts, and some computationally expensive (exchange) terms are omitted, approximated or modified. The arguments in favor of these actions are diverse ranging from phenomenological reasons to savings in computational costs. However, the price for the sloppiness will be paid in the end: In addition to the aforementioned anomalies, the EDFs result in non-physical phenomena such as self-interaction and self-pairing. Clearly these phenomena are non-physical, since the nucleons should not gain energy by interacting with themselves. Self-interaction and self-pairing are not present if the energy is calculated directly as an expectation value of the Hamiltonian [30, 53, 54].

One series of Skyrme functionals that was created starting from the functional, not from the Hamiltonian, was the UNEDF models [55, 56, 57] which are discussed in detail later in Chapter 5. The total energy of the UNEDF models is a sum of kinetic energy and the energy of two-body Skyrme interaction and the Coulomb force, namely

$$\begin{aligned} E(\vec{r}) &= \int \mathrm{d}^3\vec{r}\,\mathcal{H}(\vec{r}) \\ &= \int \mathrm{d}^3\vec{r}\,\left[\mathcal{E}^{\mathrm{Kin}}(\vec{r}) + \mathcal{E}^{\mathrm{Skyrme}}(\vec{r}) + \mathcal{E}^{\mathrm{Coul}}(\vec{r})\right]. \end{aligned} \tag{3.19}$$

The total energy is a function of one-body densities, $E(\vec{r}) = E[\rho, \tilde{\rho}]$, since the energy densities $\mathcal{E}^i$ are functions of the normal and pairing densities. The Skyrme energy density is divided into particle-hole $(\chi_0(\vec{r}), \chi_1(\vec{r}))$ and pairing $(\tilde{\chi}(\vec{r}))$ densities so that

$$\mathcal{E}^{\mathrm{Skyrme}}(\vec{r}) = \chi_0(\vec{r}) + \chi_1(\vec{r}) + \tilde{\chi}(\vec{r}), \tag{3.20}$$

where the densities are modelled as

$$\chi_t(\vec{r}) = C_t^{\rho\rho}\rho_t^2 + C_t^{\rho\tau}\rho_t\tau_t + C_t^{JJ}\sum_{\mu\nu} J_{\mu\nu,t}J_{\mu\nu,t} + C_t^{\rho\Delta\rho}\rho_t\Delta\rho_t + C_t^{\rho\nabla J}\rho_t\vec{\nabla}\cdot\vec{J}_t \tag{3.21}$$

$$\tilde{\chi}(\vec{r}) = \sum_{q=n,p}\frac{V_0^q}{2}\left[1 - \frac{1}{2}\frac{\rho_0(\vec{r})}{\rho_c}\right]\tilde{\rho}^2(\vec{r}). \tag{3.22}$$

with the index $t = \{0, 1\}$ denoting isoscalar and isovector densities, respectively. The zero-range pairing term results in a pairing channel which needs to be regularized in a way or another, and most often this is done by applying a pairing window . The quasiparticle states up to a certain cut-off energy E_{cut} are taken into account, that is, a quasiparticle states within the energy range $0 < e_i < E_{cut}$ are considered. The saturation density ρ_c is fixed to the generally accepted value $0.16\,\mathrm{fm}^{-3}$. The

Coulomb term $\mathcal{E}^{\mathrm{Coul}}$ is divided into two pieces, of which the direct term is computed exactly but the exchange term is approximated due to the computational costs:

$$\mathcal{E}^{\mathrm{Coul}} = \mathcal{E}^{\mathrm{Coul}}_{\mathrm{Dir}} + \mathcal{E}^{\mathrm{Coul}}_{\mathrm{Exc}}, \quad \text{where} \tag{3.23}$$

$$\mathcal{E}^{\mathrm{Coul}}_{\mathrm{Exc}} \approx -\frac{3}{4}e^2 \left(\frac{3}{\pi}\right)^{1/3} \rho_p^{4/3}, \tag{3.24}$$

and the energy coming from the direct Coulomb term is

$$E^{\mathrm{Coul}}_{\mathrm{Dir}} = \frac{e^2}{2} \int \mathrm{d}^3\vec{r}\, \mathrm{d}^3\vec{r}\,' \, \frac{\rho_p(\vec{r})\rho_p(\vec{r}\,')}{\vec{r} - \vec{r}\,'}. \tag{3.25}$$

The parameters C_t^i are real numbers, the only exception being

$$C_t^{\rho\rho} = C_{t0}^{\rho\rho} + C_{tD}^{\rho\rho}\rho_0^{\gamma} \tag{3.26}$$

that is density-dependent. Thus Skyrme energy density contains 13 parameters from the particle-hole part and two from pairing, namely

$$C_{t0}^{\rho\rho},\ C_{tD}^{\rho\rho},\ C_t^{\rho\Delta\rho},\ C_t^{\rho\tau},\ C_t^{J^2},\ C_t^{\rho\nabla J},\ \gamma,\ V_0^p \quad \text{and} \quad V_0^n \tag{3.27}$$

with $t = \{0, 1\}$. When a Skyrme ED is derived directly from the Skyrme interaction, the parameters C_t^i can be related to the original Skyrme parameters t_i and x_i [58]. However, neither the (t, x)- nor the C-representation is directly connected to physical observables. In order to estimate the range of the parameter values, some of them can be related to the properties of infinite nuclear matter which have known or approximated range of value [55].

3.4 Finite-range pseudopotential

As we have seen, the most used non-relativistic EDFs cannot avoid the usage of the "dangerous" density-dependent term. Since this term causes problems in beyond mean field calculations (Section 3.5), the classic Skyrme and Gogny EDFs had to be abandoned and novel models were created [2]. The formalism for contact and finite-range pseudopotentials was developed, and the first parametrizations were published in the last few years [59, 60, 61, 62, 63].

The finite-range pseudopotential involves concepts that are already familiar, and it can be seen as a generalization of Skyrme and Gogny interactions. The pseudopotential has all the different spin and isospin exchange terms and the Gaussian finite-range regulator, analogously to the Gogny force. On the other hand,

[2] The SV_T interaction has been applied surprisingly well in multireference calculations. It is a Skyrme force with the tensor EDF terms [48].

the pseudopotential is built on different orders of relative momenta $\vec{k}$. The total pseudopotential is expressed as

$$\mathcal{V}\left(\vec{r}_1,\vec{r}_2;\vec{r}_3,\vec{r}_4\right)=\sum_{n,j}\mathcal{V}_j^{(n)}\left(\vec{r}_1,\vec{r}_2;\vec{r}_3,\vec{r}_4\right), \tag{3.28}$$

where the different orders n of the pseudopotential are written as

$$\begin{aligned}\mathcal{V}_j^{(n)}\left(\vec{r}_1,\vec{r}_2;\vec{r}_3,\vec{r}_4\right)=&\left(W_j^{(n)}\hat{1}_\sigma\hat{1}_\tau+B_j^{(n)}\hat{1}_\tau\hat{P}^\sigma-H_j^{(n)}\hat{1}_\sigma\hat{P}^\tau-M_j^{(n)}\hat{P}^\sigma\hat{P}^\tau\right)\\&\times\hat{O}_j^{(n)}\left(\vec{k}_{12},\vec{k}_{34}\right)\delta(\vec{r}_{13})\delta(\vec{r}_{24})g_a(\vec{r}_{12}).\end{aligned}$$

The exchange operators $\hat{P}^\sigma$, $\hat{P}^\tau$ and the relative momentum operator $\vec{k}$ are the ones defined earlier. The relative position is written as $\vec{r}_{ij}=\vec{r}_i-\vec{r}_j$ and $W_j^{(n)}$, $B_j^{(n)}$, $H_j^{(n)}$ and $M_j^{(n)}$ are constants. The finite-range regulator $g_a(\vec{r})$ has a Gaussian form,

$$g_a(\vec{r})=\frac{1}{(a\sqrt{\pi})^3}\mathrm{e}^{-\frac{\vec{r}^2}{a^2}} \tag{3.29}$$

with a fixed range $a=1.15$ fm in Article III. The orders p denoting the pseudopotential order N^{p}LO are connected to the orders of differential operators of the corresponding terms. The operators $\hat{O}_j^{(n)}\left(\vec{k}_{12},\vec{k}_{34}\right)$ are scalars that are built out of relative momenta at the order $n=2p$. The index j tallies different scalars of the order n. At the leading order (LO), when $n=2p=0$, there is only one operator

$$\hat{O}_1^0(\vec{k}_{12},\vec{k}_{34})=\hat{1}, \tag{3.30}$$

which gives the local (momentum independent) pseudopotential

$$\begin{aligned}\mathcal{V}_1^{(0)}\left(\vec{r}_1,\vec{r}_2;\vec{r}_3,\vec{r}_4\right)=&\left(W_1^{(0)}\hat{1}_\sigma\hat{1}_\tau+B_1^{(0)}\hat{1}_\tau\hat{P}^\sigma-H_1^{(0)}\hat{1}_\sigma\hat{P}^\tau-M_1^{(0)}\hat{P}^\sigma\hat{P}^\tau\right)\\&\times\delta(\vec{r}_{13})\delta(\vec{r}_{24})g_a(\vec{r}_{12}).\end{aligned} \tag{3.31}$$

When going higher in the orders of the pseudopotential, there are two operators at the next-to-leading order (NLO), namely

$$\hat{O}_1^1(\vec{k}_{12},\vec{k}_{34})=\frac{1}{2}(\vec{k}_{12}^{*2}+\vec{k}_{34}^2)\quad\text{and} \tag{3.32}$$

$$\hat{O}_2^1(\vec{k}_{12},\vec{k}_{34})=\vec{k}_{12}^*\cdot\vec{k}_{34}, \tag{3.33}$$

which define the corresponding non-local (momentum dependent) pseudopotential terms $\mathcal{V}_1^{(1)}\left(\vec{r}_1,\vec{r}_2;\vec{r}_3,\vec{r}_4\right)$ and $\mathcal{V}_2^{(1)}\left(\vec{r}_1,\vec{r}_2;\vec{r}_3,\vec{r}_4\right)$. The complete derivation of the non-local functional up to N^{3}LO can be found in Ref. [62]. Apart from the lowest order, the pseudopotential is local only when the operators fulfill the condition

$$\hat{O}_j^{(n)}(\vec{k}_{34}+\vec{k}_{12})=\hat{O}_j^{(n)}(\vec{k}_{34}-\vec{k}_{12}^*), \tag{3.34}$$

which results in the following relationships between the coefficients of NLO pseudopotential:

$$W_2^{(1)} = -W_1^{(1)}, \quad B_2^{(1)} = -B_1^{(1)}, \quad H_2^{(1)} = -H_1^{(1)}, \quad \text{and} \quad M_2^{(1)} = -M_1^{(1)}. \quad (3.35)$$

In order to describe the nucleus, the spin-orbit and the Coulomb terms must be included as well. However, at the present implementations, that deal only with a local version of NLO interaction (e.g. Ref. [63], Article III), included the zero-range term also found in the Skyrme interaction

$$\mathcal{V}_\delta(\vec{r}_1, \vec{r}_2; \vec{r}_3, \vec{r}_4) = t_0 \left(1 + x_0 \hat{P}^\sigma\right) \delta(\vec{r}_{13})\delta(\vec{r}_{24})\delta(\vec{r}_{12}) \quad (3.36)$$

as well, with $x_0 = 1$ and $t_0 = 1000$ MeV fm^3. It was discovered in the preliminary studies that without any additional terms, the pairing is too strong at the nuclear surface and leads to too large pairing energies and average pairing gaps of neutron rich nuclei. The zero-range term of Equation (3.36) is not density-dependent but may still be problematic in beyond-mean-field calculations discussed in Section 3.5. To avoid the troubles, the term may be replaced by a similar term but with a short finite-range, but no studies have been published so far.

In the present implementations, due to the choice of x_0, the term of Equation (3.36) is active only in the particle-hole channel and counteracts the strong attraction from the finite-range term, so that the pairing interaction is strong enough in the bulk. In the end, there were nine free parameters at local NLO because of the relationships in Equation (3.35) and the spin-orbit interaction. The more general non-local pseudopotential has four additional parameters resulting in 13 free parameters.

Order n	W_1^n	B_1^n	H_1^n	M_1^n	W_{so}
0	41.68	-1405.79	202.88	-2460.68	177.07
2	-79.75	73.11	-681.30	-48.16	

Table 3.3: Parameters of the local NLO pseudopotential by K. Bennaceur *et al.* rounded to two decimals [63]. The general pseudopotential up to NLO has 13 free parameters, but the requirement of locality decreases the amount. See Ref. [63] for the more precise values and the statistical uncertainties.

3.5 Beyond Mean Field

The traditional DFT with a static mean-field allows us to study the bulk properties of ground states through the whole nuclear chart by handling only one time-independent mean-field state. The bulk properties are properties such as binding

energies and proton rms radii. On the contrary, the beyond mean field methods refer to the methods including more than one mean-field state and symmetry restoration such as exact particle number restoration and time evolution of states – thus these methods go "beyond" the traditional mean field methods. For example, for the calculation of excitation spectra and transition rates between states, one should use proper symmetry restored states. Since these states are now a linear combination of multiple mean-field states, the role of correlations becomes important.

There are justified tools for handling the correlations in DFT, despite the conceptual puzzle: The EDFs are built by assuming that the multi-nucleonic effects are included in quasiparticles and the corresponding wave functions. Thus it is conceptually dangerous to build correlations on top of these particles and wave functions, since the correlations could be taken into account twice. Fortunately, the procedure works for the zero and low energy states that are influenced vastly by the nuclear shell effects. Since the shell effects are sharp in a sense, the EDFs are too smooth to grasp the effects and the double counting is not a real concern in low energy part of nuclear spectra, but at high energies it is an issue [30].

There are several concepts beyond the original static mean-field methods: configuration mixing (e.g. generator coordinate method, GCM), symmetry restoration and time dependent mean-field approaches (e.g. Time-Dependent Hartree-Fock theory, TDHF) [30]. The GCM was one of the first methods trying to combine both the single-particle and the collective aspects of nuclear physics. In GCM multiple configurations are mixed, which means that the superposition of multiple mean-field states is handled resulting in theoretical excitation spectra and transition matrix elements. TDHF and TDHFB are generalizations of HF and HFB, so that the one-body density matrix $\hat{\rho}(t)$ is assumed to be time-dependent, and the time-evolution is described through the time-dependent Schrödinger equation. The TDHF and TDHFB methods have a lot of applications, they are used for example to describe fission and fusion processes. However, the GCM and TDHFB schemes are beyond the work described in this thesis, but more information can be found e.g. in Ref. [35].

Symmetry restoration is a real puzzle in theoretical nuclear physics. We desire to describe the nuclear system by simple wave functions for example by approximating the strongly interacting nucleons as independently moving quasiparticles whose wave functions could be written as product states. We would also desire to take into account both the symmetries and the correlations between the nucleons. However, we are not capable of fulfilling all the requirements: The nucleon-nucleon interaction should be translationally invariant, but the only translationally invariant product wave functions are products of plane waves. Unfortunately, it is obvious that plane waves cannot describe the strong correlations that cause the nucleons to cluster and to constitute a self-bound nucleus [35]. Thus, in the usual mean-field ap-

proach, translational symmetry becomes violated and, in principle, should be later restored. The (deformed) HFB states are not eigenstates of the particle-number operator or the total angular momentum, so different kinds of projection methods must be used, such as a variation after projection (VAP), a projection after variation (PAV) or approximate methods such as the Lipkin-Nogami method [64, 65, 35].

3.6 Bulk properties of nuclei

The choices of fitting observables affect the model parameters, and thus the model itself. The future applications of the model dictate which properties are more crucial to be included in the fitting data than the others. When the theoretical formulation of the model is fixed, one may emphasize some properties by addressing a greater weight on the related data or adding data points related to the property of interest.

The nuclear EDFs are mostly used for exploring the general properties of atomic nuclei around the whole nuclear chart. That is why the commonly selected fitting observables are mainly nuclear bulk properties such as binding energies and proton rms radii of nuclei from light to heavy ones. The nuclear binding energy E_{nucl} (simply E later in the text) is extracted from the atomic binding energy E_{atom} by removing the binding energy of electrons E_{elec},

$$E_{\mathrm{nucl}}(Z,N) = E_{\mathrm{atom}}(Z,N) - E_{\mathrm{elec}}(Z), \tag{3.37}$$

where the electronic binding energy can be approximated as [55]

$$E_{\mathrm{elec}}(Z) \approx -1.433 \times 10^{-5} Z^{2.39}\ (\mathrm{MeV}). \tag{3.38}$$

In addition to the binding energy, one of the bulk properties of nuclei that can be experimentally measured is the nuclear charge radius. Nuclear charge radii can be measured for example via laser spectroscopy. The theoretically accessible proton rms point radius $\langle R_p^2 \rangle$ is connected to the charge radii via the equation

$$\langle R_{ch}^2 \rangle = \langle R_p^2 \rangle + \langle r_p^2 \rangle + \frac{N}{Z} \langle r_n^2 \rangle, \tag{3.39}$$

with the proton charge radius $\langle r_p^2 \rangle = 0.7691\ \mathrm{fm}^2$ and the neutron charge radius $\langle r_n^2 \rangle = -0.1161\ \mathrm{fm}^2$ [66].

Pairing correlations of EDFs are typically constrained by odd-even staggering (OES) of binding energy. OES measures how much the binding energy of a nucleus having odd number of nucleons is lower than that of the two neighboring nuclei. OES is measured via the empirical pairing gap that is mathematically defined as

(three point formula)

$$\Delta^{(3)}(N) \equiv \frac{\pi_N}{2}[E(N-1) + E(N+1) - 2E(N)], \quad \text{with} \tag{3.40}$$

$$\pi_N = (-1)^N. \tag{3.41}$$

In Equation (3.40) the negative binding energy E is a function of the particle number N.

Even though OES has been understood to originate from nucleonic pairing correlations for a long time, there are several mechanisms that contribute to OES. It was shown 20 years ago, that OES is also strongly attributed to the deformed mean field in light nuclei [67]. A similar observation was also made in DFT calculations on clusters of alkali-metal atoms at that time [68].

3.7 Concept of infinite nuclear matter (INM)

One concept that is often used for estimating the goodness and functionality of nuclear models is the concept of infinite nuclear matter (INM). INM is a boundless homogeneous nuclear medium where only nuclear forces exist. The impact of Coulomb interaction is usually neglected, and pairing correlations are also usually excluded.

Infinite nuclear matter can be used as an approximation for the interior of heavy nuclei, and it has been studied through different nuclear theories. In 2013, the first up-to-date coupled-cluster (CC) calculations were performed to study infinite nuclear matter [69], even though INM has been studied via several approximate *ab initio* methods already many decades ago [70, 71]. INM has been studied also via self-consistent Green's function method [72].

Translationally invariant INM is described with the plane wave wavefunction,

$$\phi_{\vec{k}}(\vec{r}\sigma q) = (2\pi)^{-\frac{3}{2}} \exp(i\vec{k}\cdot\vec{r})\chi_\sigma\chi_q, \tag{3.42}$$

where the particle type $q = \{n, p\}$ and the spin and isospin parts of the wave function are represented as χ_σ and χ_q. The Fermi momentum is connected to the scalar-isoscalar density ρ_0 as

$$\rho_0 = \sum_{\sigma q} \int_{|\vec{k}|\leq k_F} \mathrm{d}^3\vec{p}\,\phi^*_{\vec{k}}(\vec{r}\sigma q)\phi_{\vec{k}}(\vec{r}\sigma q) \equiv \frac{2k_F^3}{3\pi^2}, \tag{3.43}$$

The kinetic density is also derived from the wavefunction as

$$\tau_{q\sigma} = \int_{|\vec{k}|\leq k_{F,q\sigma}} \mathrm{d}^3\vec{k} \left[\vec{\nabla}\phi^*_{\vec{k}}(\vec{r}\sigma q)\right] \cdot \left[\vec{\nabla}\phi_{\vec{k}}(\vec{r}\sigma q)\right] \tag{3.44}$$

$$= \left(\frac{1}{2\pi}\right)^3 \int_0^{k_F} \int_0^{\pi} \int_0^{2\pi} k^4 \sin(\theta)\, \mathrm{d}\theta\, \mathrm{d}\phi\, \mathrm{d}k \tag{3.45}$$

$$= \frac{3}{20}\frac{2}{3\pi^2} k^5_{F,q\sigma} \tag{3.46}$$

and it can be expressed with ρ_0 as

$$\tau_0 \;=\; \frac{3}{5}\frac{2k_F^5}{3\pi^2} \;=\; \frac{3}{5}\left(\frac{3\pi^2}{2}\right)^{2/3} \rho_0^{5/3}. \tag{3.47}$$

In infinite homogeneous nuclear matter all gradient terms vanish. If the studied system is assumed to be unpolarized, time-odd spin densities and currents also vanish. One of the most studied observables of infinite nuclear matter is its *equation of state (EOS)*. EOS is a quantity that describes the binding energy per nucleon in infinite nuclear matter. Let us denote EOS as a function W, so that

$$\frac{E}{A} = W(\rho_n, \rho_p), \tag{3.48}$$

let us expand it around the saturation density ρ_c and the zero relative neutron excess I,

$$W(\rho_n, \rho_p) = W(\rho_0, I) = W(\rho_0) + S_2(\rho_0) I^2 + \mathcal{O}(I^4), \tag{3.49}$$

where the relative neutron excess is defined as

$$I = \frac{\rho_1}{\rho_0}. \tag{3.50}$$

The leading term of the expansion is written as

$$W(\rho_0) = \frac{E^{\mathrm{NM}}}{A} + \frac{P^{\mathrm{NM}}}{\rho_c^2}(\rho_0 - \rho_c) + \frac{K^{\mathrm{NM}}}{18\rho_c^2}(\rho_0 - \rho_c)^2, \tag{3.51}$$

whereas the next-to-leading term is

$$S_2(\rho_0) = a^{\mathrm{NM}}_{\mathrm{sym}} + \frac{1}{3\rho_c} L^{\mathrm{NM}}_{\mathrm{sym}}(\rho_0 - \rho_c) + \frac{1}{18\rho_c^2}\Delta K^{\mathrm{NM}}(\rho_0 - \rho_c)^2. \tag{3.52}$$

The different coefficients in Equations (3.51) and (3.52) represent the total energy per nucleon at equilibrium (E^{NM}/A), the nucleonic pressure (P^{NM}), the nuclear matter incompressibility (K^{NM}), the symmetry energy coefficient ($a^{\mathrm{NM}}_{\mathrm{sym}}$), the density

dependence of the symmetry energy ($L_{\rm sym}^{\rm NM}$) and the incompressibility correction term ($\Delta K^{\rm NM}$), which are mathematically defined as

$$\frac{E^{\rm NM}}{A} = W(\rho_c) \tag{3.53}$$

$$P^{\rm NM} = \rho^2 \frac{{\rm d}W(\rho_0)}{{\rm d}\rho_0}\bigg|_{\rho_0=\rho_c} \tag{3.54}$$

$$K^{\rm NM} = \frac{18P^{\rm NM}}{\rho_0} + 9\rho_0^2 \frac{{\rm d}^2W(\rho_0)}{{\rm d}\rho_0^2} \tag{3.55}$$

$$a_{\rm sym}^{\rm NM} = S_2(\rho_c) = \frac{1}{2}\frac{{\rm d}^2W(\rho_0, I)}{{\rm d}I^2}\bigg|_{\substack{\rho_0=\rho_c \\ I=0}} \tag{3.56}$$

$$L_{\rm sym}^{\rm NM} = 3\rho_c \frac{{\rm d}S_2(\rho_0)}{{\rm d}\rho_0}\bigg|_{\rho_0=\rho_c} \tag{3.57}$$

$$\Delta K^{\rm NM} = 9\rho_c^2 \frac{{\rm d}^2S_2(\rho_0)}{{\rm d}^2\rho_0}\bigg|_{\rho_0=\rho_c}, \tag{3.58}$$

and the saturation density ρ_c is defined as the point where the nucleonic pressure equals to zero, namely $P^{\rm NM}(\rho_c) = 0$.

Infinite nuclear matter can be divided into several subcategories. *Symmetric infinite nuclear matter (SNM)* is infinite nuclear matter with an equal number of neutrons and protons, and it is also non-polarized with an equal amount of spin up and spin down particles. Thus, for SNM,

$$\rho_1 = 0, \quad \rho_n = \rho_p = \frac{1}{2}\rho_0, \quad \tau_n = \tau_p = \frac{1}{2}\tau_0 \quad \text{and} \quad I = 0. \tag{3.59}$$

The assumption of symmetric nuclear matter leads to the following values for the INM properties, namely [55]

$$\rho_c \approx 0.16\,{\rm fm}^{-3}, \quad P^{\rm NM} = 0, \quad \frac{E^{\rm NM}}{A} \approx -16\,{\rm MeV} \quad \text{and} \quad K^{\rm NM} \approx 220\,{\rm MeV}, \tag{3.60}$$

which were used in the optimization of the UNEDF models.

Asymmetric nuclear matter (ANM) is a form of nuclear matter for which the neutron and proton densities are assumed to be different, thus $I \neq 0$, and the corresponding EOS depends on the neutron excess. The properties $S_2(\rho_c)$, $L_{\rm sym}^{\rm NM}$ and $\Delta K^{\rm NM}$ are theoretically accessible via ANM, but the experimental values are significantly sloppier. Experimentally the values of $S_2(\rho_c)$ and $L_{\rm sym}^{\rm NM}$ are around [55]

$$S_2(\rho_c) \approx 30\,{\rm MeV} \quad \text{and} \quad L_{\rm sym}^{\rm NM} \approx 80\,{\rm MeV}. \tag{3.61}$$

The last but not least form of infinite nuclear matter is *pure neutron matter (PNM)*. It is infinite nuclear matter made only from neutrons.

In practice, EOS is derived from the functional by

$$\frac{E}{A} \equiv \frac{\mathcal{E}}{\rho_0}. \tag{3.62}$$

EOS from different spin and isospin channels can derived and used in optimization, see Appendices A-E.

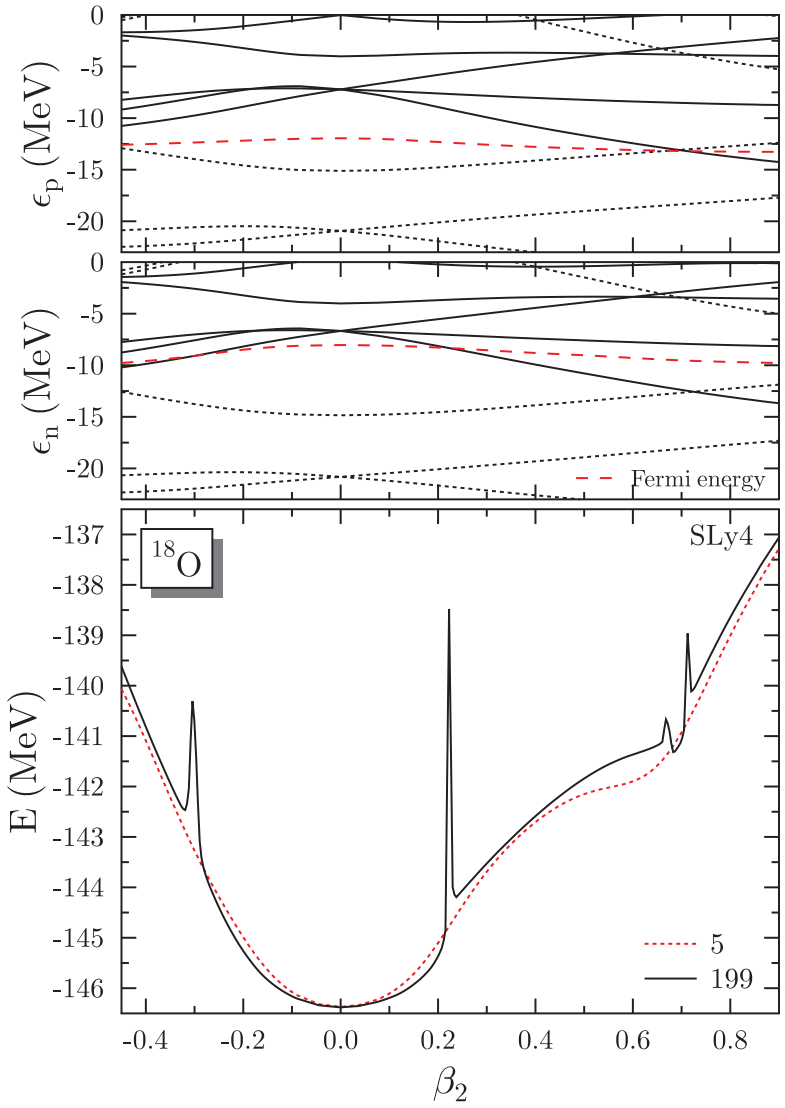

Figure 3.1: Deformation energy surface for ^{18}O calculated with the zero-range Skyrme force SLy4. When the calculation is performed by using more gauge points in the integration (black curve), anomalies become clearly visible. Figure adapted from the work by M. Bender *et al.* [53]

Chapter 4

Optimization

For the present, the parameters of nuclear energy density functionals cannot be derived from the underlying theories. There has been general interest to create a connection between *ab initio* and DFT methods, and the parameters of EDFs have been tried to link to *ab initio* calculations [73, 74], but without proper success.

As long as there is no analytical way to derive the parameters, one has to obtain the parameters by other means. The model parameters can be tuned by hand or optimized on experimental data of atomic nuclei. Optimization of the parameter set with respect to a selected set of experimental data is handy, since at the end of the optimization procedure one has ended up in the minimum of χ^2, and may use the information about the curvature of χ^2 to estimate the propagated model uncertainties. This is explained in more detail in Chapter 5. In the following, the different aspects of an optimization process are discussed and few example studies are explained.

4.1 Multi-objective approach

The optimization of an EDF can be seen as a multi-objective optimization problem. A desired final functional should be able to describe some predefined nuclear properties and thus the parameters must be fitted to carefully selected data. Most often the selected data set includes several nuclear bulk properties such as binding energies, proton rms radii and pairing gaps, which makes the optimization problem to be a multiobjective optimization problem in which every separate observable type represents a separate objective. Mathematically the problem is formulated as

$$\begin{aligned} &\min(f_1(x), f_2(x), ..., f_k(x)) \\ &\text{s.t. } x \in X \end{aligned} \tag{4.1}$$

where x represents the parameters to be optimized, f_i denotes an objective function i, and X is the feasible set of solutions. The feasible set is typically defined by intervals, inequalities and constraining functions if needed. Here, the objective functions $f_i(x)$ correspond to the minimization of the difference between theoretical and experimental values, i.e.

$$f_i(x) = \sum_{j=1}^{N_i} \left(\mathcal{O}_j^{i,th}(x) - \mathcal{O}_j^{i,exp} \right)^2 \tag{4.2}$$

where i represents an index for the various datatypes, and index j labels different datapoints of type j. N_i is the number of data points of type i: E.g. there may be different number of binding energies than proton rms radii in the data set.

In general, there is no feasible solution that minimizes all the objective functions simultaneously. Instead, the best solutions form a set and and the set is called *Pareto optimal* solutions. A Pareto optimal solution is a solution that cannot be improved with respect to any of the objective functions without degrading another objective. That is to say, if x_P is a Pareto optimal solution, there is no solution x^* so that

$$\begin{aligned} &f_i(x^*) \leq f_i(x_P) \quad \text{for all objectives } f_i \text{ and} \\ &f_j(x^*) < f_j(x_P) \quad \text{for any objective } f_j. \end{aligned} \tag{4.3}$$

Pareto optimal solutions are illustrated in Figure 4.1. F_1 and F_2 represent two separate objective functions of a bi-objective optimization problem in arbitrary units (a.u.). The set of feasible solutions is marked in blue. When minimizing F_1 and F_2 simultaneously, there are infinite number of Pareto optimal solutions, including solutions p_1 and p_2. Solutions p_3, p_4 and p_5 are not Pareto optimal: Solution p_1 is better in both of the objectives F_1 and F_2 when comparing to solution p_3. The same holds for solution p_2 when comparing it to solution p_4. Solution p_2 is better than solution p_5 in F_1, therefore p_5 not being Pareto optimal.

Finding a representative set of Pareto optimal solutions is not as straightforward as solving a single-objective optimization problem. It may be computationally demanding or even infeasible. If that is the case, one may be forced to transform the multiobjective problem into a single-objective problem such that the obtained solution is one of the Pareto optimal solutions of the original problem. One of the simplest methods to perform the transformation is *scalarization*. In *linear scalarization* the objective function is defined as a weighted sum of original objective functions, so that the transformed optimization problem is written as

$$\begin{aligned} &\min \sum_{i=1}^{k} w_i f_i(x) \\ &\text{s.t.} \quad x \in X, \end{aligned} \tag{4.4}$$

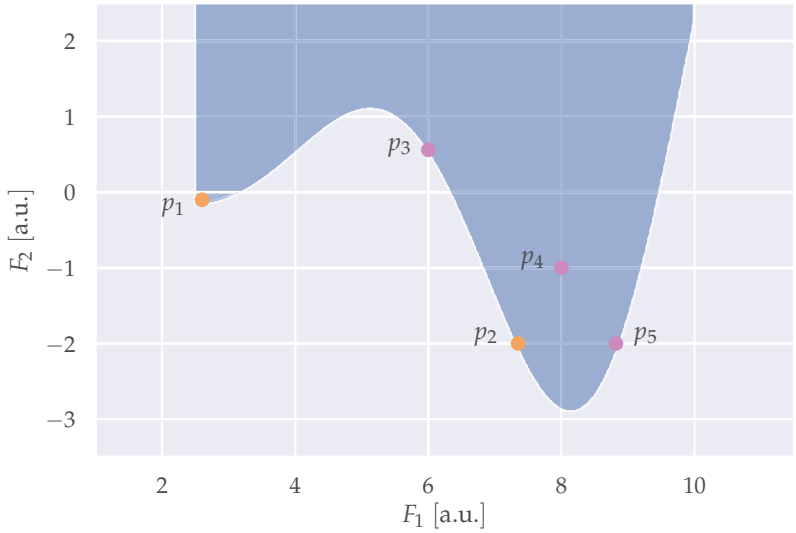

Figure 4.1: Illustration of Pareto optimal solutions in two-objective optimization problem. The set of feasible solutions is marked in blue, F_1 and F_2 represent two objectives to be minimized in arbitrary units. Solutions p_1 and p_2 are Pareto optimal, whereas solutions p_3, p_4 and p_5 are not.

where $w_i > 0$ represents a weight of the objective i. If one aims to treate all the objective functions equally, a weight of an objective function should be approximately an inverse of the scale of the corresponding objective function. The inverse value of the scale, in the units of data type i, makes the product $w_i f_i(x)$ dimensionless and different data types can be summed. Thus, the optimization problem of model parameters (Equation (4.2)) may be scalarized as

$$\begin{aligned} &\min \sum_{i=1}^{k} \sum_{j=1}^{N_i} w_i \left(\mathcal{O}_j^{i,th}(x) - \mathcal{O}_j^{i,exp} \right)^2 \\ &\text{s.t.} \quad x \in X, \end{aligned} \tag{4.5}$$

or if one treats every squared residual $\left(\mathcal{O}_j^{i,th}(x) - \mathcal{O}_j^{i,exp} \right)^2$ as a separate objective, one may address a separate weight $w_{i,j}$ for every data point of every data type and then solve the minimization problem

$$\begin{aligned} &\min \sum_{i=1}^{k} \sum_{j=1}^{N_i} w_{i,j} \left(\mathcal{O}_j^{i,th}(x) - \mathcal{O}_j^{i,exp} \right)^2 \\ &\text{s.t.} \quad x \in X. \end{aligned} \tag{4.6}$$

Sometimes it is justified to assign a different weight for a single data point of a given type, even though all the other weights of the specific data type are the same.

For instance, it may be known that a specific data point would be very helpful in the optimization of model parameters, but the data point is not precisely fixed, the data point is pseudo-data (e.g. the data is not measured but comes from an underlying theory) or the experimentally measured data point has an expectionally large error bar. In this case the data point is used, but with a smaller weight.

4.2 Penalty function approach

One may look at the optimization problem the other way around. The optimization problem of model parameters can be seen as a penalty function minimization problem, so that the starting point is to choose the χ^2 function describing the goodness-of-fit. It is defined as [34, 75]

$$\chi^2(x) = \sum_{k=1}^{N_d} \frac{\left(\mathcal{O}_k^{\text{th}}(x) - \mathcal{O}_k^{\text{exp}}\right)^2}{\Delta\mathcal{O}_k^2}, \tag{4.7}$$

where x represents the model parameters to be optimized, $\mathcal{O}_k^{\text{th}}$ and $\mathcal{O}_k^{\text{exp}}$ correspond to theoretical and experimental values of observables, N_d is the number of all data points and $\Delta\mathcal{O}_k$ is the adopted errors of data point k. The adopted total errors accumulate from theoretical, numerical and experimental errors:

$$\Delta\mathcal{O}_k^2 = \left(\Delta\mathcal{O}_k^{\text{th}}\right)^2 + \left(\Delta\mathcal{O}_k^{\text{num}}\right)^2 + \left(\Delta\mathcal{O}_k^{\text{exp}}\right)^2. \tag{4.8}$$

The total penalty function reflects the distribution of residuals $|\mathcal{O}_k^{\text{th}} - \mathcal{O}_k^{\text{exp}}|$. Statistically, the average penalty function per degree of freedom should equal to one at the minimum x_0, that is

$$\frac{\chi^2(x_0)}{N_d - N_p} \leftrightarrow 1, \tag{4.9}$$

where N_p is the number of optimized parameters. The justification for Equation (4.9) comes from the distribution. Since the χ^2 is a random variable, it has a normalized probability distribution. It can be shown, that for this kind of a statistic, the expectation value (mean value) corresponds to the degrees of freedom $\nu = N_d - N_p$, with the standard deviation $\sigma_{\chi^2} = \sqrt{2\nu}$. Since the expectation value equals to the degrees of freedom, the different degrees of freedom should bring a contribution of 1 on average.

Most often in the field of nuclear density functional theory, the main error contribution comes from the theoretical error $\Delta\mathcal{O}_k^{\text{th}}$ that covers deficiency rooted in the theoretical formulation of the model. The two latter contributions, namely the numerical error $\Delta\mathcal{O}_k^{\text{num}}$ and the experimental error $\Delta\mathcal{O}_k^{\text{exp}}$, are usually only marginal

when compared to the theoretical error, leading to the approximation

$$\Delta\mathcal{O}_k^2 \approx \left(\Delta\mathcal{O}_k^{\text{th}}\right)^2. \tag{4.10}$$

The estimated errors $\Delta\mathcal{O}_k^2$ have a substantial effect on the outcome of the optimization process. Even though it is crucial to give reasonable estimates for the theoretical errors $\Delta\mathcal{O}_k^{\text{th}}$, there is always some haphazardness in the choices which cannot be completely avoided. Theoretical errors can be evaluated after the model optimization, but good error estimates should already be given beforehand. In principle, it could be possible to give some reasonable estimates for $\Delta\mathcal{O}_k^{\text{th}}$, optimize the model, evaluate the statistical errors by using the optimized model and then use the calculated errors for another optimization run (and repeat the steps until the error estimates do not change significantly), but the optimization process is most often computationally demanding and cannot be repeated multiple times. That is why EDFs are mainly optimized by applying "educated guesses" for $\Delta\mathcal{O}_k^{\text{th}}$.

If the educated guesses do not produce $\chi^2 = 1$, or if different variations of a fit are studied without changing the error estimates, the normalization condition of Equation (4.9) is not fulfilled. However, if we assume $\Delta\mathcal{O}_k^2 \approx \left(\Delta\mathcal{O}_k^{\text{th}}\right)^2$, we can renormalize the penalty function so that the normalization condition is actualized,

$$\chi^2_{\text{norm}}(x_0) = \frac{\chi^2(x_0)}{s} = N_d - N_p, \tag{4.11}$$

and the scale factor s does not affect the minimum x_0. The scale factor

$$s = \frac{\chi^2(x_0)}{N_d - N_p}, \tag{4.12}$$

that leads to the optimization of the penalty function

$$\chi^2_{\text{norm}}(x) = \frac{1}{N_d - N_p} \sum_{k=1}^{N_d} \frac{\left(\mathcal{O}_k^{\text{th}}(x) - \mathcal{O}_k^{\text{exp}}\right)^2}{\Delta\mathcal{O}_k^2}, \tag{4.13}$$

has an impact on the calculation of the Jacobian and covariance matrices that will be discussed in Chapter 5.

4.3 Optimization of the UNEDF models

There are various different optimization methods that can be applied to optimize the parameters of nuclear EDFs. Since the derivatives of functions are not computationally feasible, the derivative-free optimization methods are used, even basic

ones such as the Nelder-Mead method. Genetic algorithms may be used as well, but they often require a lot of calculations which is problematic in HFB calculations.

The optimization of the UNEDF models was done in co-operation together with mathematicians and computer scientists. The used optimization algorithm is called POUNDerS (*Practical Optimization Using No Derivatives for Squares*), see Reference [76] for details. The algorithm was used to minimize the normalized penalty function of Equation (4.13) and optimize the parameters (3.27), with the exception that C_0^{JJ} and C_1^{JJ} terms were non-zero only in UNEDF2 [57]. Since some of the optimized parameters were INM properties, it was possible to put a few bounds on them.

The first data set, namely the data set for the optimization of UNEDF0 [55], included properties of spherical and deformed nuclei that can be seen in Figure 4.2. Binding energies, proton rms radii and average odd-even mass staggering of 72 nuclei around the nuclear chart were used. The free parameters of the UNEDF1 [56] model were the same, but a few binding energies and 4 fission isomer energies were added and the center of mass correction was neglected, since the aim of UNEDF1 was to create an EDF suitable for fission studies. The aim of the UNEDF2 optimization was to produce an EDF that would be an improvement with respect to single particle spectra, so nine single-particle splittings were included in the data set, five additional data points for odd-even staggering were added and also the C_0^{JJ} and C_1^{JJ} terms were optimized.

4.4 Optimization of the finite-range pseudopotential

The optimization of the local finite-range pseudopotential up to NLO was carried out in Ref. [63] for spherical nuclei and some INM properties. One goal of this doctoral thesis was to implement an optimization procedure that allowed nuclear deformation and thereby the finite-range pseudopotential could be optimized on data of deformed nuclei.

The optimization program was implemented by using POUNDerS that was already found out to be successful in the UNEDF project. The first test to check whether the implementation was working as expected was done on the same data set as the original optimization [63]. Since the HF(B) solvers were different between these two projects – Bennaceur *et al.* used the spherical radial code FINRES$_4$ whereas the program HFBTEMP with an axial HO basis was used in this project – the optimized parameters would not be the same but comparable [77, 39].

The parameters of the pseudopotential were successfully optimized on spherical nuclei by using HFBTEMP and POUNDerS, and the obtained parameters were

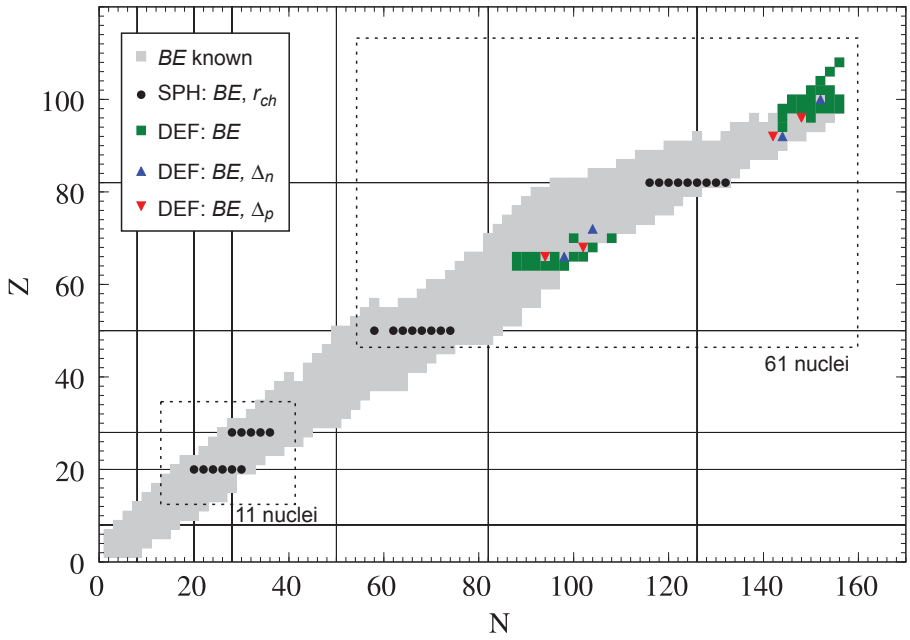

Figure 4.2: Data set of the optimization of the UNEDF0 model. Binding energies, charge radii and odd-even staggering were used to optimize the model parameters. Figure adapted from Ref. [55].

comparable to the results of Ref. [63]. Different sizes of the model space were tested, and the optimization was carried out in a basis consisting of 10, 12 and 14 harmonic oscillator (HO) shells. As it can be seen in Figure 4.3, the size of the model space does not significantly affect the number of needed iterations in the optimization process, but the final value of the (unnormalized) χ^2 penalty function is different. The choice of the size of the model space has an impact not only on the theoretical predictions but the computational costs such as computational time and required memory as well. Even though the number of optimization iterations is the same, each HFB calculation on 14 HO shells requires more computation time.

The first test on the data of the selected spherical nuclei was performed successfully. Since the implementation already allowed deformation, everything was more or less ready for the optimization on deformed nuclei. All that was needed was to decide which nuclei would be added to the data set and then do the optimization on the updated data. A simple task, one may think – just add the data points and let a supercomputer calculate.

Unfortunately, the optimization on deformed nuclei revealed to be a task far from trivial. Various attempts were performed with different data sets but without success. The nuclei of two trial data sets are illustrated in Figure 4.4. The data set of Subplot 4.4a was more or less the data set used in the optimization of UNEDF0,

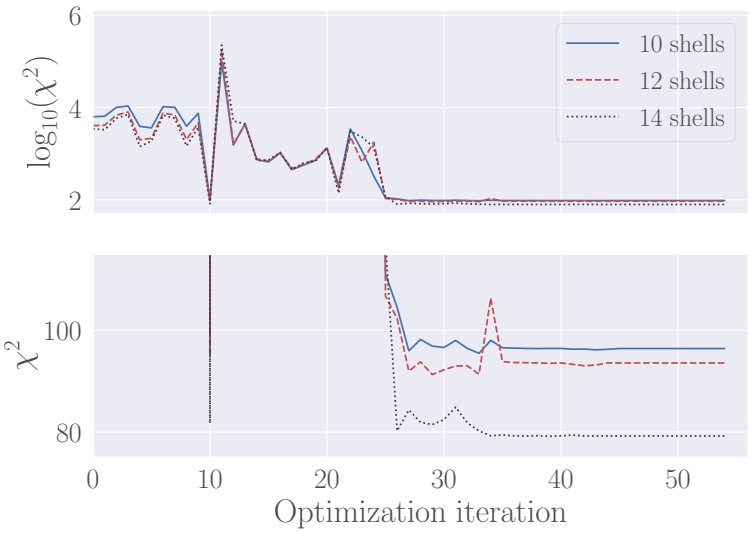

Figure 4.3: Convergence of the χ^2 penalty function when computed with a computation space of 10, 12 and 14 harmonic oscillator shells. The upper panel is in logarithmic scale whereas the scale of lower panel is natural. The data was originally published in Article II.

but the heaviest nuclei were left out. The data set of nuclei in Subplot 4.4b included isotonic and isotopic middle-shell nuclei that had a clear deformation ($|\beta| > 0.25$). Their binding energies, radii, average pairing gaps and intrinsic quadrupole moments were used: The quadrupole moments were believed to constrain deformation properties better.

It is often difficult to explain why something did not work, also in this case. It seems that the data sets including deformed nuclei do not constrain the parameters sufficiently. Most often the optimization failed after one hundred optimization iterations because of one nucleus for which the HFB calculations did not converge in the end. If the problematic nucleus was removed from the data set and the optimization was performed again, another nucleus became problematic and the corresponding HFB calculation did not converge. This may indicate that the optimized parameters tended to wander into regions of parameter space that cause finite-size instabilities. The connection between the unconverged HFB calculations and the appearance of finite-size instabilities of symmetric nuclear matter has been studied and demonstrated during the last two decades [78, 79, 80, 81].

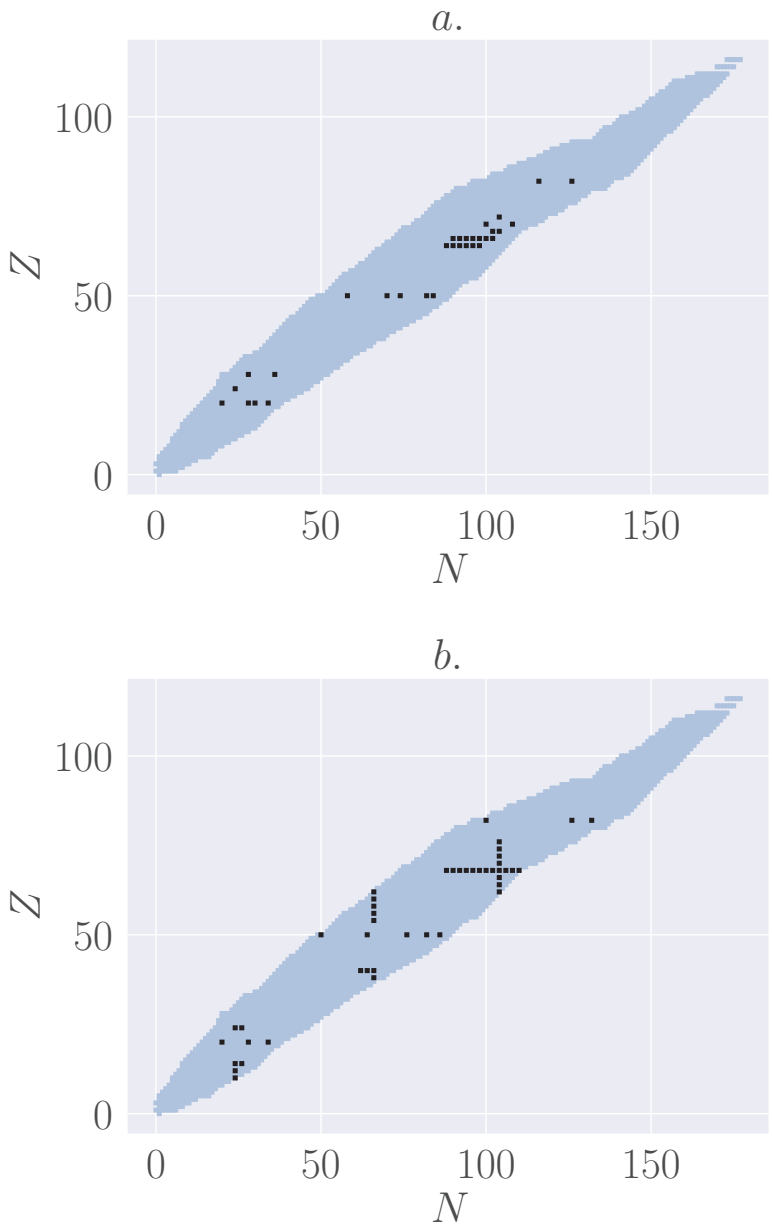

Figure 4.4: Nuclei of two trial data sets. The aim was to optimize the local NLO pseudopotential on deformed nuclei and their properties. Subplot a illustrates a data set motivated by the UNEDF0 optimization, only the very heaviest nuclei and the corresponding data points were left out of the set. Subplot b shows how the isotopic and isotonic chains of nuclei were selected around the nuclear chart. Their binding energies, proton rms radii, pairing gaps and quadrupole moments formed the fitting data.

Chapter 5

Uncertainty Analysis

Still today the nuclear interaction is not perfectly understood. As a concequence, the relationships between operators and observables are not completely apprehended. Effective theories, that are adjusted on experimental data, are commonly used in the field of nuclear physics. Since the structure of the models is justified by general arguments and the rest is fitted, one may understandably question the predictive power of the models. The uncertainty analysis is needed, undoubtably, and a set of tools have already been presented [34].

Uncertainty analysis is not important only for the uncertainty estimation itself. By studying how the uncertainties propagate from the model parameters to the predicted observables we may gain important insights as to where the shortcomings of the model lie. Since the nuclear EDFs are optimized through the least squares fitting method, statistical analysis and the resultant error estimates are available.

The model error (theoretical error) estimates can be subcategorized. *The statistical model error* is most often possible to estimate, since the prediction power

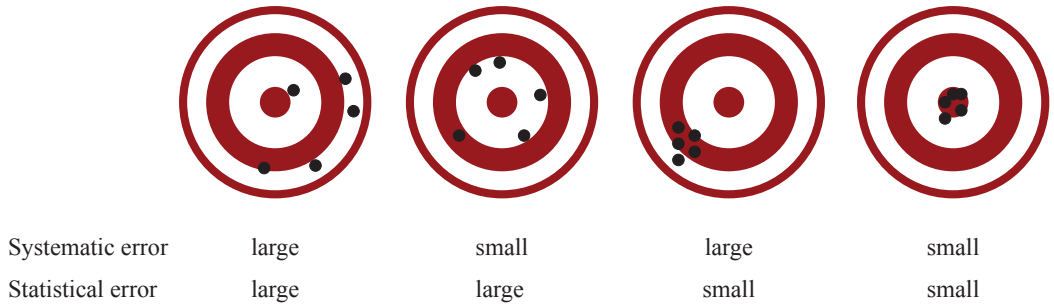

Figure 5.1: Two main classes of model error illustrated. Adapted from Ref. [82]

of the model is related to the quality of the optimized fit. It describes the random errors of theoretical predictions. *The systematic model error* is grounded on the theoretical structure of the model. If there are false assumptions included or some relevant components missing in the model, they will show up in the systematic model error. Unfortunately, the systematic model error is difficult to assess since there is no exact reference model. The systematic and statistical error are illustrated in Figure 5.1. A model can be *precise* (a small statistical error), *accurate* (a small systematic error), both precise and accurate, or neither of them. Third error source, namely *the numerical error* emanating from the computational precision, exists but is most often negligible in DFT calculations.

The expressions uncertainty and error are not completely fixed in literature, but in this thesis we connect the term *uncertainty* to the imperfection of models, and *error* is used to describe the imperfection of single predictions. Next we focus to study uncertainty of theoretical models by using standard deviation as a measure of statistical errors of theoretical predictions.

5.1 Standard deviation

One of the most fundamental but a straightforward method to estimate the predictive power of a model is to study the uncertainties of optimized model parameters and determine how this uncertainty propagates into given predictions. The statistical error can be expressed as the statistical standard deviation of theoretical values, for instance.

The standard deviation σ of the observable y can be computed from the relationship

$$\sigma^2(y) = \sum_{i,j=1}^{n} \mathrm{Cov}\,(x_i, x_j) \left[\frac{\partial y}{\partial x_i}\right] \left[\frac{\partial y}{\partial x_j}\right], \tag{5.1}$$

where x_i and x_j are model parameters and $\mathrm{Cov}\,(x_i, x_j)$ is the covariance matrix between parameters x_i and x_j. For the standard deviation one needs to compute a set of partial derivatives that are demanding or impossible to calculate for these numerical models explicitly. That is why approximations are used. Following the definition of a partial derivate, a derivative of function $y(x)$ at the point a can be estimated by a finite difference, such that

$$y'(a) \approx \frac{y(a+h) - y(a-h)}{2h}, \tag{5.2}$$

where h represents the finite step. Equation (5.2) can be improved e.g. by applying Richardson extrapolation [83], or one may use other higher-order methods for the approximation.

	χ^2	Normalized χ^2
Penalty function	$\sum_i \frac{\left(\mathcal{O}_i - \mathcal{O}_i^{\exp}\right)^2}{\Delta\mathcal{O}_i^2}$	$\frac{1}{N_d - N_p} \sum_i \frac{\left(\mathcal{O}_i - \mathcal{O}_i^{\exp}\right)^2}{\Delta\mathcal{O}_i^2}$
Covariance matrix	$s\left(\hat{J}^T\hat{J}\right)^{-1}$	$\chi^2(\mathbf{p}_0)\left(\hat{J}^T\hat{J}\right)^{-1}$

Table 5.1: Different χ^2 functions and the corresponding covariance matrices. The scale factor is defined as $s = \frac{\chi^2(\mathbf{p}_0)}{N_d - N_p}$ [34]. The Jacobian matrix is the same for both of the χ^2 functions (see Equation (5.4)).

One of the most fundamental quantities that is needed for the calculation of standard deviations is a Jacobian matrix of observables, J. The matrix elements of J are partial derivatives of the observables $\mathcal{O}$ used in the optimization with respect to the model parameters p. The observables are approximated as linear functions of p in the vicinity of the minimal χ^2, and the parameters are estimated to be normally distributed. The matrix elements of J are mathematically defined as

$$J_{i\alpha} = \frac{1}{\Delta\mathcal{O}_i}\frac{\partial\mathcal{O}_i}{\partial p_\alpha}, \tag{5.3}$$

where $\Delta\mathcal{O}_i$ represents the weight of the corresponding data type. Depending on the normalization of χ^2, the covariance matrix can be approximated as [34]

$$\text{Cov} = s\left(\hat{J}^T\hat{J}\right)^{-1} \quad \text{or} \quad \text{Cov} = \chi^2(\mathbf{p}_0)\left(\hat{J}^T\hat{J}\right)^{-1}. \tag{5.4}$$

The scale factor s is defined as

$$s = \frac{\chi^2(\mathbf{p}_0)}{N_d - N_p}, \tag{5.5}$$

and it depends on the number of data points in the optimization N_d and the number of optimized parameters N_p. The penalty functions and corresponding covariance matrices are represented in Table 5.1.

A simple "recipe" for computing a standard deviation is the following:

1. Compute the Jacobian matrix J. Choose the Jacobian matrix that corresponds to the penalty function χ^2 used in the optimization process.

2. Compute the covariance matrix $\mathrm{Cov}(x_i, x_j)$ that is proportional to $(J^T J)^{-1}$.

3. Compute an observable y and its statistical error (standard deviation):

   (a) Compute the prediction $y(\vec{p}_0)$ with the optimized parameters $\vec{p}_0$.

   (b) Compute the partial derivatives $\frac{\partial y}{\partial x_i}$ for instance with a finite step method of Equation (5.2).

   (c) Calculate the standard deviation of Equation (5.1).

   (d) Get the result: $y_{\mathrm{Th}} = y(\vec{p}_0) \pm \sigma_y$

5.2 Broad prospects of uncertainty estimation

Naturally, the biggest motivation to estimate uncertainties and errors stems from the need to trust the prediction power of the model in question. However, the uncertainty analysis may provide much more information than mere error bars for some single predictions. In the following, different ways to represent the uncertainties and errors are shown, and the possible benefits of uncertainty analysis are discussed.

Statistical errors give insight on how reliable the theoretical predictions are. In Figure 5.2 the theoretical predictions and experimentally measured values of binding energies of even-even Gd isotopes are compared. Three different theoretical models, UNEDF0, UNEDF1 and UNEDF2, are used. The shaded bands represent the corresponding theoretical statistical errors, namely the standard deviations, of separate predictions. The standard deviations are plotted separately in Figure 5.2d as a function of mass number A. Experimental errors are not included since they are insignificant when compared to the scale of theoretical errors. The range of nuclei is greater in Subplot d, since the number of performed theoretical calculations is greater than the number of experimental measurements. If the models were perfect, all the binding energy residuals $E_{\mathrm{Th}} - E_{\mathrm{Exp}}$ in Subplots a–c would be zero within the error bars. However, this is not the case for most of the calculations.

Systematic studies of errors reveal how the errors change as a function of certain variables. We can read from Figure 5.2d that the uncertainties of the UNEDF

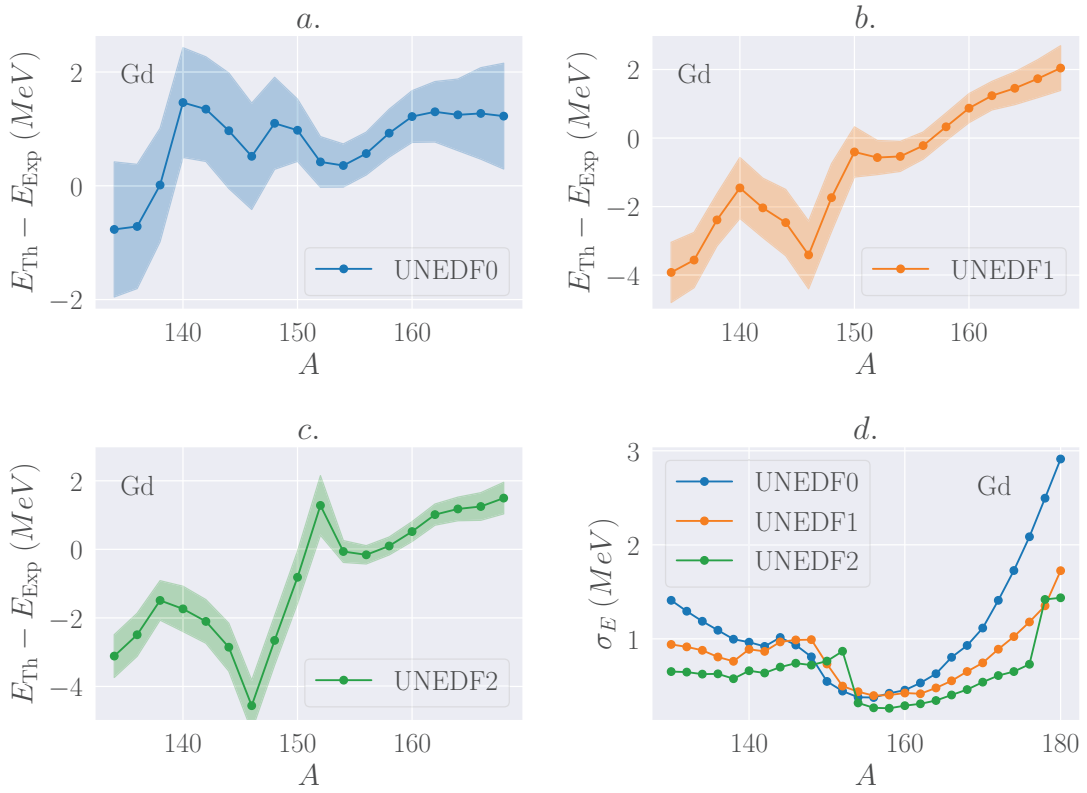

Figure 5.2: Binding energy residuals $E_{\mathrm{Th}} - E_{\mathrm{Exp}}$ of Gd isotopes as a function of mass number A. The calculations are perfomed by using three different Skyrme EDFs, namely UNEDF0 (a), UNEDF1 (b) and UNEDF2 (c). Shaded bands represent the theoretical uncertainties. Subplot d illustrates how theoretical errors change as a function of mass number A, among some experimentally unknown Gd isotopes as well. Experimental values are from AME2012 [84]. The theoretical data was originally published in Article I.

models increase when going towards neutron rich nuclei. This is not a surprise, since when the neutron number N increases, we move towards the experimentally unknown nuclei and simultaneosly outside of the set of nuclei that were used in the fitting process of these models. The predictive power of a model tends to weaken outside of the region where the model parameters were adjusted.

In contrast to measurement errors in general, theoretical errors of two observables may depend on each other. This is illustrated in Figure 5.3, which is otherwise the same as Figure 5.2 but the observable of interest is two neutron separation energy $S^{2\mathrm{n}}$. It is defined as a difference of two consecutive binding energies,

$$S^{2\mathrm{n}}(Z,N) = E(Z,N) - E(Z,N-2). \tag{5.6}$$

When comparing Figures 5.2 and 5.3, it is noticed that the theoretical results of S^{2n} differ less from the experimental measurements than the binding energies that were used for the calculations of S^{2n}. The same holds for the standard deviations $\sigma_{S,2n}$: They are smaller than the corresponding standard deviations of binding energies.

However, the standard deviations $\sigma_{S,2n}$ do not behave smoothly as a function of mass number A. The prominent peak in $\sigma_{S,2n}$ at the mass number $A = 178$ stands out in Figure 5.3d among the UNEDF2 calculations. The peak can be explained by studying the theoretical predictions for nuclear deformations that are seen in Figure 5.4.

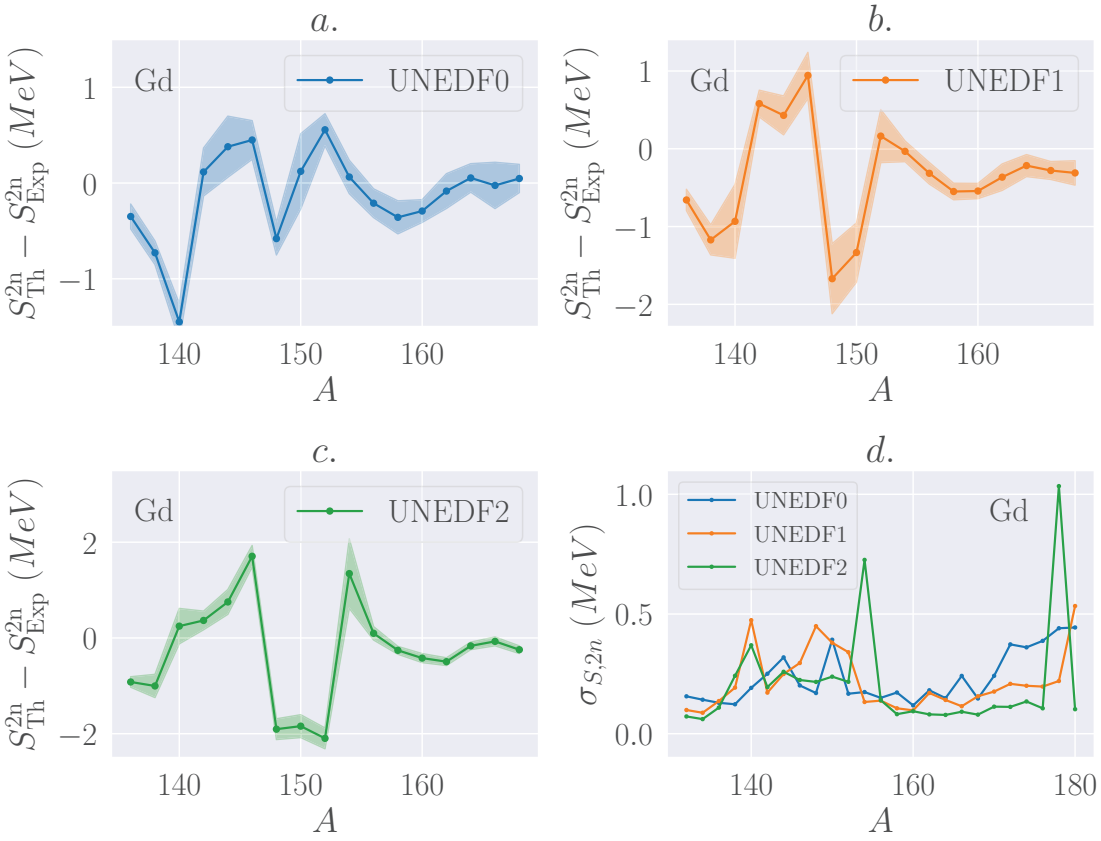

Figure 5.3: Same as Figure 5.2, but for the residuals of two neutron separation energies $S^{2n}_{Th} - S^{2n}_{Exp}$. The theoretical statistical errors of binding energy depend on each other and result in smaller errors of two neutron separation energies than of the original ones.

Figure 5.4a shows us the ground state deformations of Gd isotopes predicted by the UNEDF2 model. The ground state deformation is expressed by the deformation parameter β. Most of Gd isotopes within the range $A = [130, 180]$ are theoretically

prolate ($\beta \in [0.2, 0.4]$), some of them are spherical ($\beta \approx 0$) and the rest few are oblate ($\beta \approx -0.2$). When the differences of the ground state deformations of two consecutive isotopes are plotted and compared to the statistical error of the two neutron separation energy $\sigma_{S,2n}$ (Figure 5.4b), the clear relationship can be spotted. The statistical error $\sigma_{S,2n}$ increases when the deformation changes from prolate to oblate or the other way around.

Uncertainty analysis may help us to understand where the shortcomings of the studied theoretical model come from. Binding energy residuals of the isotonic chain of nuclei with the neutron number $N = 76$ are plotted in Figure 5.5. The theoretical calculations were perfomed by using the UNEDF2 model and the experimental values were taken from Ref. [84]. While the mass number A increases, the theoretical binding energies tend to deviate more and more from the experimental results (Figure 5.5a). However, the standard deviations σ_E do not change, and the wrong trend cannot be explained by the theoretical errors. Since the statistical error emerges from the fact how well the model parameters were constrained, the wrong trend seems to be related to the formulation and structure of the model. The model is lacking in some important physical aspects, and the model cannot be significantly improved by improving the optimization process.

In addition to the usage of standard deviation as an error bar for single predictions, the parameterwise contributions to the standard deviation can be studied as well. This gives information about which parameters create most of the theoretical error and if the error is caused equally by all the model parameters or mainly by a couple of them. Figure 5.6 demonstrates how the standard deviations of theoretical binding energies of two gadolinium isotopes, ^{154}Gd and ^{180}Gd, are composed in the UNEDF0, UNEDF1 and UNEDF2 calculations.

In each color matrix, one matrix element corresponds to one addend of the double sum in Equation (5.1), thus the total standard deviation for one binding energy is the sum of all the elements in the corresponding color matrix. The contributions are expressed in the unit of MeV^2 in Figure 5.6. Naturally, the total standard deviation σ_E is a positive number, but the separate contributions may be negative since covariance matrix elements and partial derivatives may be negative.

As we saw earlier in Figure 5.2, the standard deviation σ_E of the UNEDF0 parametrization increases rapidly when going towards neutron rich nuclei, and the theoretical binding energies at the mass number $A \approx 180$ have a statistical error of the order of 3 MeV. The increase in the statistical error shows up indirectly in Figure 5.6 as well: The scale of individual contributions is significantly different in ^{180}Gd than in ^{154}Gd. The other major remark is that the error composition of the heavy Gd isotopes is mainly due to a_{sym}^{NM} and L_{sym}^{NM} within the UNEDF0 calculations. The parameters related to the symmetry energy become more important in neutron rich nuclei.

When comparing the results given by the UNEDF0 and UNEDF2 models, the statistical errors of UNEDF2 originate more uniformly from the model parameters than the errors of UNEDF0. In addition, one can notice that the scale of parameter-wise contributions of UNEDF2 do not significantly increase in neutron rich nuclei. These are interesting remarks when remembering that the theoretical formulations of these models are relatively similar.

Even though the representation of Figure 5.6 is accurate and illustrates well the contributions, it is inconvinient when the error composition of series of nuclei is studied. Since the error composition is mainly focused on certain rows (or columns) of matrices in Figure 5.6, one can study row- or columnwise contributions by summing once over the model parameters.

In Figure 5.7 the addends of Equation (5.1) are represented after applying one of the two sums. From that point of view the labels of Figure 5.7 are slightly misleading, since the one sum over the parameters has already been applied. Anyhow, they still give a realistic impression as to which of the model parameters contribute to the errors the most. As we can notice, the standard deviations of binding energies of neutron rich Dy isotopes are mainly affected by the parameters a_{sym}^{NM} and L_{sym}^{NM} when applying the UNEDF0 model. This is not a surprise after the error study of Gd isotopes, since Gd and Dy nuclei are relatively similar, having the proton numbers $Z = 64$ and $Z = 66$, respectively. We can also notice that the error composition of the binding energies given by the UNEDF2 model is splitted among the model parameters, and the magnitude of contributions is smaller than the ones given by UNEDF0.

5.3 Eigenmode formalism

Until now, the statistical errors have been represented as components of standard deviation and their sums. Lastly we introduce the eigenmode formalism representing standard deviation after a transformation. If we denote the covariance matrix as C, the vector of partial derivatives of the observable y as $D_i = \frac{\partial y}{\partial x_i}$ and the transformation diagonalizing the covariance matrix as P so that $C_{diag} = P^{-1}CP$, then

$$\sigma_y^2 = D^T C D \tag{5.7}$$
$$= D^T P (P^{-1} C P) P^{-1} D \tag{5.8}$$
$$= D^T P (C_{diag}) P^{-1} D. \tag{5.9}$$

Since the covariance matrix C is symmetric, $P^T = P^{-1}$, and the columns of P are the eigenvectors of C, in such a way that an eigenvector v^i corresponds to the eigenvalue λ_i. The standard deviation of an observable y is then computed via the

equation

$$\sigma_y^2 = \sum_i \left(\sum_j \frac{\partial y}{\partial x_j} v_j^i \right)^2 \lambda_i. \tag{5.10}$$

The eigenmode formalism helps to see how many directions in the parameter space are causing the statistical error. For example, we can see in Figure 5.8 that the standard deviation of binding energies of neutron rich Gd isotopes are mainly caused by five eigenvectors (UNEDF0, UNEDF2) or 2-3 eigenvectors (UNEDF1). Of course, these eigenvectors are different from one model to another, since the covariance matrices are different. The eigenvectors are not shown here, they are just linear combinations of the model parameters.

The contributions of statistical errors are easy to show in eigenmode formalism, but it is difficult to exploit the gained knowledge in practice in future optimization work. Even though we would know that the eigenvector

$$v_1 = (0.3, 0.006, 0.02, 0.05, 0.0001, 0.01, 0.5, 0.11, 0.08, 0.004)$$

in some parameter space, it does not really help us to make a better model at the moment. The parameters of EDFs are difficult to optimize, not to mention linear combinations of them. Anyhow, the eigenmode formalism may give us some hints about the error composition and if the error is composed by a couple of directions or equally by the all eigenvectors.

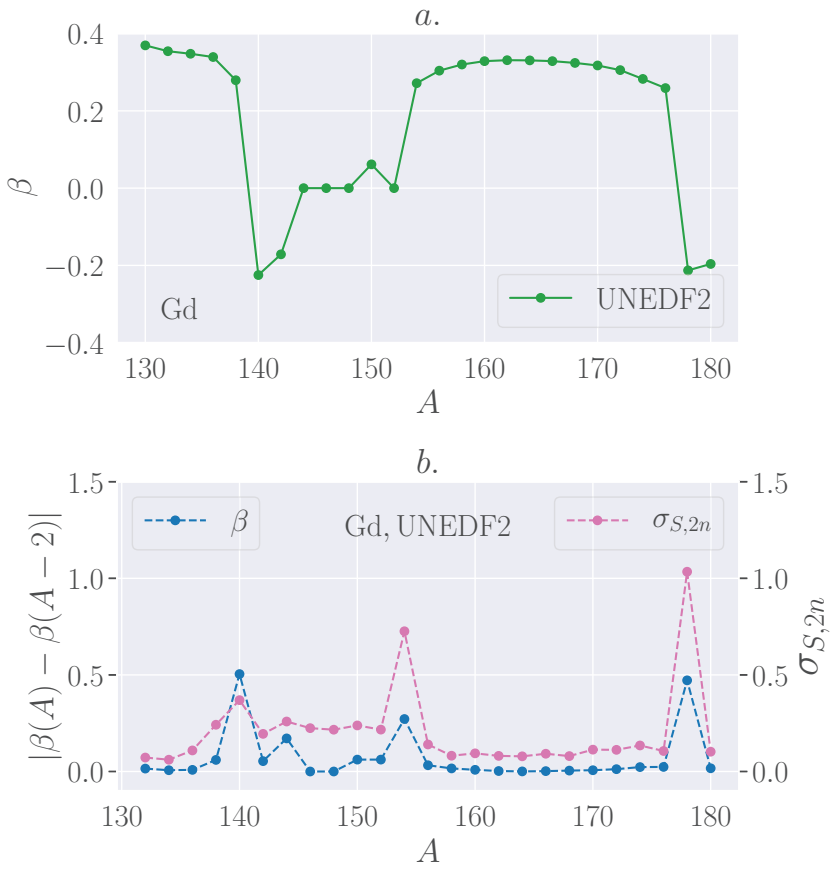

Figure 5.4: (*a.*) Ground state deformation of Gd isotopes as a function of mass number A. (*b.*) Illustration on the relationship between the rapid change of ground state deformation and the statistical errors of two neutron separation energies. The difference between ground state deformation parameter β of two consecutive isotopes is marked in blue, and the statistical errors of two neutron separation energies are marked in magenta.

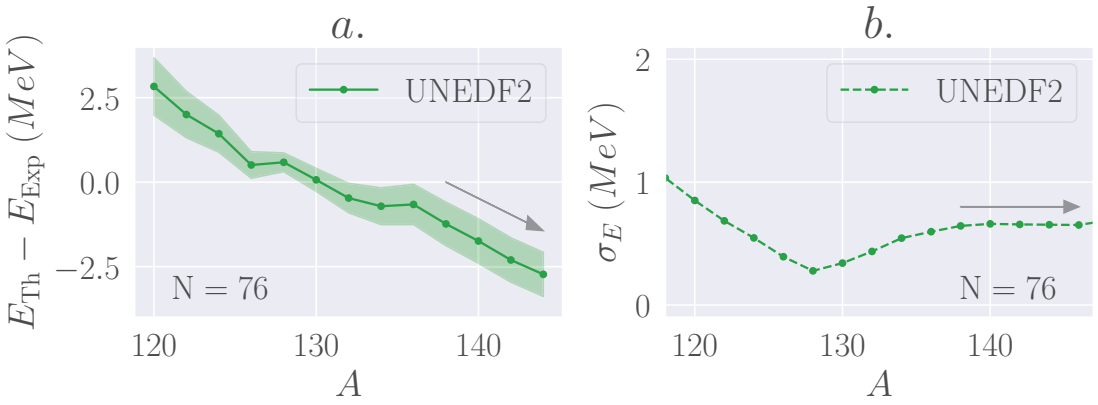

Figure 5.5: Binding energy residuals $E_{\mathrm{Th}} - E_{\mathrm{Exp}}$ of the isotonic chain of nuclei with the neutron number $N = 76$ computed by using UNEDF2. In Subplot a, the theoretical statistical errors are marked in green shaded bands. The same errors are plotted as a function of mass number A in Subplot b. The theoretical values tend to differ more and more from the experimental values when mass number A increases (a), but this trend cannot be explained by the statistical errors (b). The theoretical data was originally published in Article I. The experimental values are from AME2012 [84].

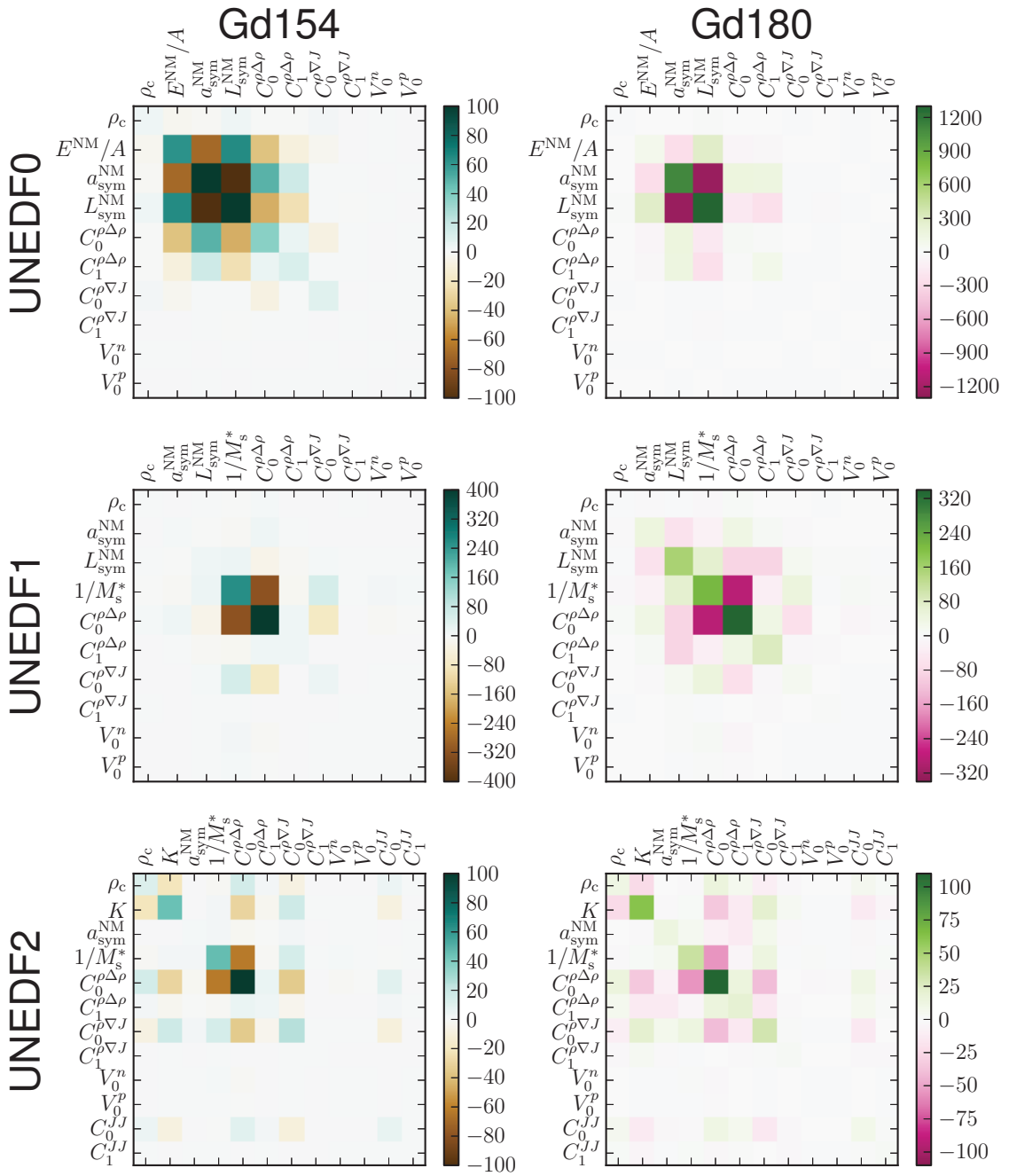

Figure 5.6: The contributions of the model parameters to the statistical errors of binding energy. Two different nuclei, ^{154}Gd and ^{180}Gd, are considered, and the results from all the three UNEDF models are compared. The values are expressed in MeV^2. The sum of matrix elements are the corresponding theoretical statistical error squared, σ_E^2. Originally published in Article I.

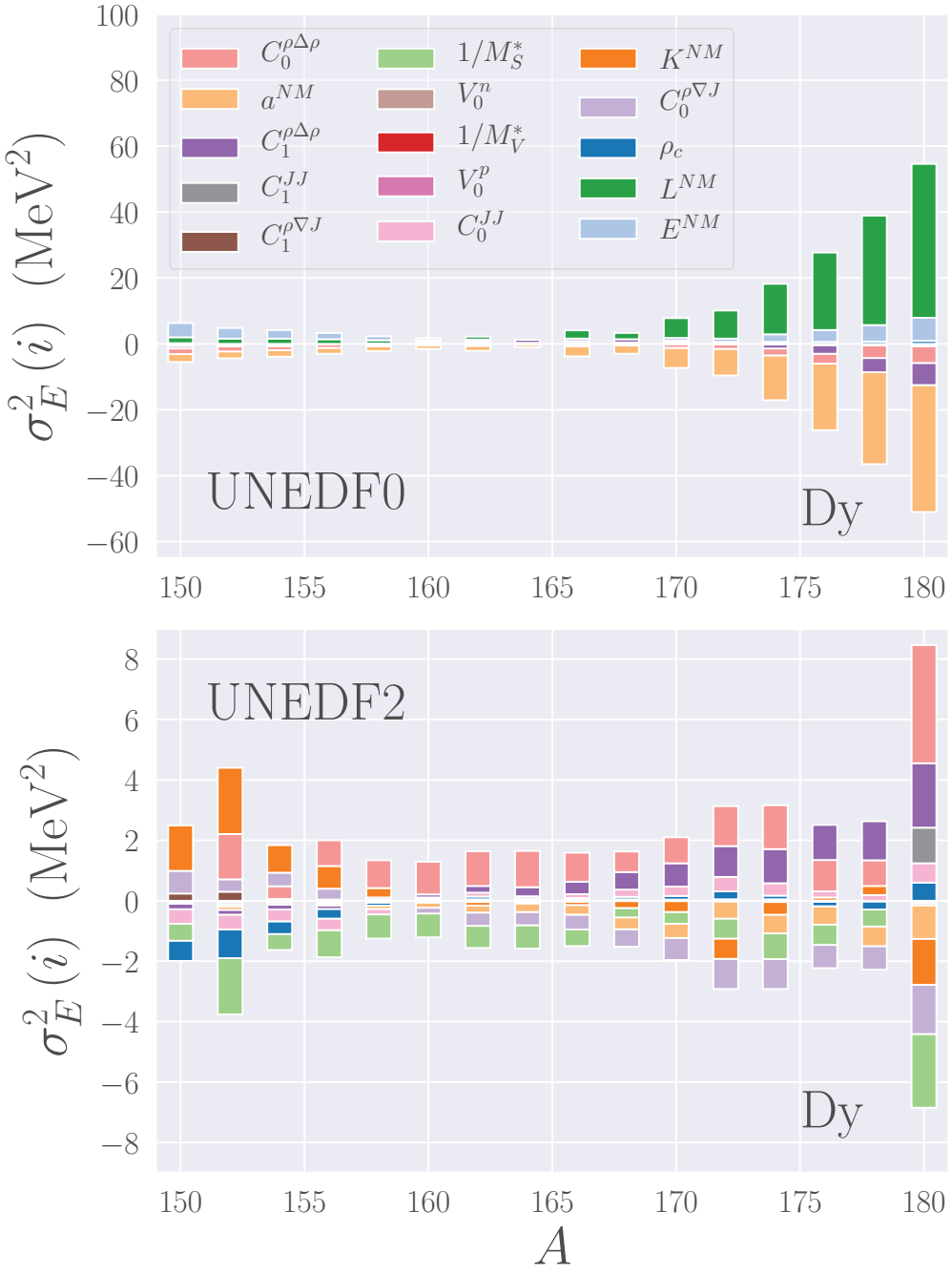

Figure 5.7: Contributions to the statistical errors of theoretical binding energies of Dy isotopes, illustrated so that the contributions are summed once over the parameters. The relationship of this figure and corresponding matrix representation of Figure 5.6 is such that the values here are sums of values in one row/column in the representation of Figure 5.6. Note that here we consider Dy isotopes, in contrast to the two Gd isotopes of Figure 5.6. The data was originally published in Article I.

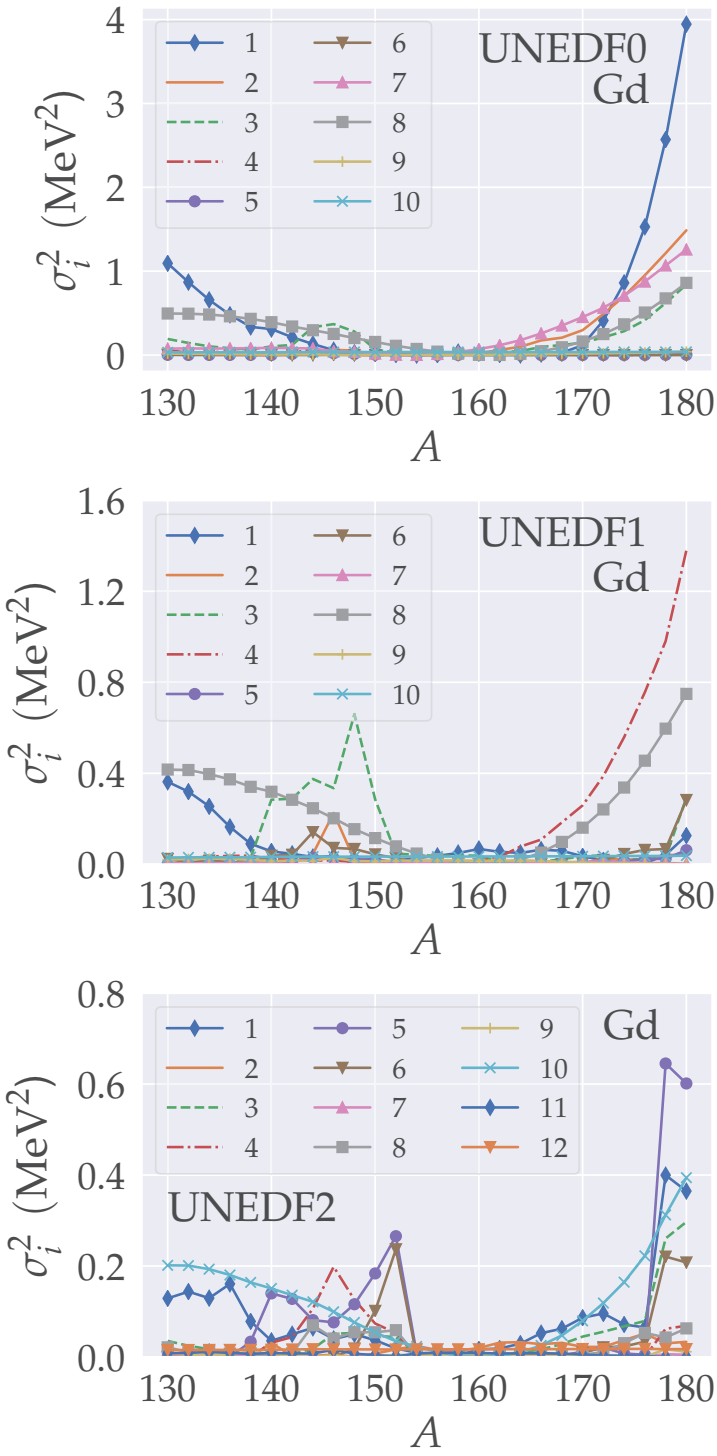

Figure 5.8: Composition of standard deviation of Gd isotopes $A \in [130, 180]$ in the eigenmode formalism. The data points represent the contribution of each eigenvector to the standard deviation. Despite the labels and symbols being the same, the eigenvectors are different between the models. The eigenvectors are not shown here. The data was originally published in Article I.

Chapter 6

Conclusions and outlook

In this thesis, different aspects of the development process of nuclear DFT models were discussed. Formation of a theoretical model starts from the mathematical formulation and derivation of the observables that are required in the development of the model. In the following steps, the model parameters are optimized to predetermined experimental data. After optimization of the model, it is tested and uncertainty analysis is performed. All the steps were discussed, with particular emphasis on uncertainty analysis and optimization.

Model development was described step-by-step, corresponding to an actual model development process. However, that order does not correspond to the chronological order of the performed separate projects: The doctoral studies started from the uncertainty analysis of the UNEDF models. The UNEDF models were created together with mathematicians and computer scientists to create "state-of-the-art" nuclear models that could be applied throughout the nuclear chart and whose uncertainty can be evaluated. The statistical errors of UNEDF0, UNEDF1 and UNEDF2 were computed for some bulk properties, and particularly the statistical errors of binding energies were studied in this thesis. It was found out, that the stastistical errors increase rapidly when going towards experimentally unknown neutron rich nuclei. Uncertainty analysis provided more information on which parameters are the main source of uncertainty.

The second project was related to the mathematical formulation and derivation of observables. The Equation of State (EOS) in infinite nuclear matter was derived for a four-body zero-range interaction and for the novel finite-range pseudopotential introduced a few years ago [63]. Various INM properties are needed in the fitting process of functionals to better constrain the model parameters. The derivations and resulting formulas can be found in Appendix, in the end of this thesis.

The third project of author's doctoral studies dealt with the optimization of the novel finite-range pseudopotential. The pseudopotential was already optimized to data of spherical nuclei in Ref. [63] up to NLO and N2LO, and the aim of our project

was to extend the optimization procedure and allow nuclear deformation. The interface between the optimization algorithm POUNDerS [76] and the HFB solver HFBTEMP [39] was implemented, and the implementation was tested successfully by reperforming the optimization of Ref. [63] and comparing the results. However, the optimization to deformed nuclei turned out to be a task far from trivial – despite various optimization runs on different data sets, the finite-range pseudopotential has not yet been optimized while allowing the nuclear deformation.

Fortunately, there are still some means to succeed in the optimization. Like in the case of the UNEDF models, one could use the derivations of INM properties, and instead of optimizing the pure model parameters, the INM properties derived from the pseudopotential could be used as fitting parameters among some of the original model parameters. By studing more directly the INM properties themselves, one could set boundaries on the selected INM parameters, potentially helping in the optimization procedure. Additionally, the possible problems related to the finite-size instabilities could be studied further in order to find out what kind of parameter sets tend to lead unconverged HFB calculations and finite-size instabilities.

Appendix A

S,T decomposition of EOS in INM in general

The purpose of this Appendix is to show how the spin-isospin decomposition of Equation of State can be calculated for different interactions in infinite nuclear matter. The calculation of (S,T) decomposition of EOS is straightforward. In order to get a potential energy in each (S,T) channel, one calculates the sum of expectation values

$$E_{pot}^{ST} = \frac{1}{2}\sum_{kl}\langle kl|\hat{V}\hat{P}^S\hat{P}^T|\overline{kl}\rangle \tag{A.1}$$

where $|\overline{kl}\rangle$ represents a non-normalized antisymmetrized two-body state. The spin and isospin projection operators are defined as

$$\hat{P}^{S=0} = \frac{1}{2}\left(\hat{1} - \hat{P}^\sigma\right), \quad \hat{P}^{S=1} = \frac{1}{2}\left(\hat{1} + \hat{P}^\sigma\right), \tag{A.2}$$

$$\hat{P}^{T=0} = \frac{1}{2}\left(\hat{1} - \hat{P}^\tau\right), \quad \hat{P}^{T=1} = \frac{1}{2}\left(\hat{1} + \hat{P}^\tau\right), \tag{A.3}$$

where $\hat{P}^\sigma$ and $\hat{P}^\tau$ are the spin and isospin exchange operators, mathematically defined as

$$\hat{P}_{12}^\sigma = \frac{1}{2}\left(1 + \hat{\boldsymbol{\sigma}}_1 \cdot \hat{\boldsymbol{\sigma}}_2\right) \quad \text{and} \quad \hat{P}_{12}^\tau = \frac{1}{2}\left(1 + \hat{\boldsymbol{\tau}}_1 \cdot \hat{\boldsymbol{\tau}}_2\right). \tag{A.4}$$

The spin and isospin operators, $\hat{P}_{12}^\sigma$ and $\hat{P}_{12}^\tau$, exchange the spins and isospins of particle 1 and 2. Since exchanging two spins or isospins twice does not make effectively any changes, the relationships

$$\hat{P}_{12}^\sigma\hat{P}_{12}^\sigma = \hat{1} \quad \text{and} \quad \hat{P}_{12}^\tau\hat{P}_{12}^\tau = \hat{1} \tag{A.5}$$

hold.

A.1 Products of densities in INM

The density can be expressed as an expansion in spin-isospin space. We can write

$$\begin{aligned}\rho(\mathbf{r}_1\sigma_1 q_1, \mathbf{r}_2\sigma_2 q_2) = \frac{1}{4}\,[&\rho_0(\mathbf{r}_1,\mathbf{r}_2)\delta_{\sigma_1\sigma_2}\delta_{q_1,q_2} + \rho_1(\mathbf{r}_1,\mathbf{r}_2)\delta_{\sigma_1\sigma_2}\langle q_1|\boldsymbol{\tau}_z|q_2\rangle \\ &+s_0(\mathbf{r}_1,\mathbf{r}_2)\langle s_1|\boldsymbol{\sigma}|s_2\rangle\delta_{q_1q_2} + s_1(\mathbf{r}_1,\mathbf{r}_2)\langle s_1|\boldsymbol{\sigma}|s_2\rangle\langle q_1|\boldsymbol{\tau}_z|q_2\rangle] \\ \overset{\text{INM}}{=}\frac{1}{4}&\rho_0(\mathbf{r}_1,\mathbf{r}_2)\delta_{\sigma_1\sigma_2}\delta_{q_1,q_2},\end{aligned} \tag{A.6}$$

where the last equality holds for homogeneous symmetric infinite nuclear matter. When the normal density is summed over spins and isospins, it becomes

$$\sum_{sq}\rho(\mathbf{r}_1 sq, \mathbf{r}_2 sq) = \rho_0(\mathbf{r}_1,\mathbf{r}_2), \tag{A.7}$$

and the products of two normal densities are

$$\begin{aligned}\sum_{ss'qq'}\rho(\mathbf{r}_1 sq, \mathbf{r}_2 sq')\rho(\mathbf{r}_3 s'q', \mathbf{r}_4 s'q) =&\frac{1}{2}\,[\rho_0(\mathbf{r_1},\mathbf{r_2})\rho_0(\mathbf{r_3},\mathbf{r_4}) + \rho_1(\mathbf{r_1},\mathbf{r_2})\rho_1(\mathbf{r_3},\mathbf{r_4})] \\ \overset{\text{INM}}{=}&\frac{1}{2}\rho_0(\mathbf{r_1},\mathbf{r_2})\rho_0(\mathbf{r_3},\mathbf{r_4})\end{aligned} \tag{A.8}$$

$$\begin{aligned}\sum_{ss'qq'}\rho(\mathbf{r}_1 sq, \mathbf{r}_2 s'q)\rho(\mathbf{r}_3 s'q', \mathbf{r}_4 sq') =&\frac{1}{2}\,[\rho_0(\mathbf{r_1},\mathbf{r_2})\rho_0(\mathbf{r_3},\mathbf{r_4}) + \mathbf{s}_0(\mathbf{r_1},\mathbf{r_2})\cdot\mathbf{s}_0(\mathbf{r_3},\mathbf{r_4})] \\ \overset{\text{INM}}{=}&\frac{1}{2}\rho_0(\mathbf{r_1},\mathbf{r_2})\rho_0(\mathbf{r_3},\mathbf{r_4})\end{aligned} \tag{A.9}$$

$$\begin{aligned}\sum_{ss'qq'}\rho(\mathbf{r}_1 sq, \mathbf{r}_2 s'q')\rho(\mathbf{r}_3 s'q', \mathbf{r}_4 sq) =&\frac{1}{4}\,[\rho_0(\mathbf{r_1},\mathbf{r_2})\rho_0(\mathbf{r_3},\mathbf{r_4}) + \rho_1(\mathbf{r_1},\mathbf{r_2})\rho_1(\mathbf{r_3},\mathbf{r_4}) \\ &+ \mathbf{s}_0(\mathbf{r_1},\mathbf{r_2})\cdot\mathbf{s}_0(\mathbf{r_3},\mathbf{r_4}) + \mathbf{s}_1(\mathbf{r_1},\mathbf{r_2})\cdot\mathbf{s}_1(\mathbf{r_3},\mathbf{r_4})] \\ \overset{\text{INM}}{=}&\frac{1}{4}\rho_0(\mathbf{r_1},\mathbf{r_2})\rho_0(\mathbf{r_3},\mathbf{r_4})\end{aligned} \tag{A.10}$$

In homogeneous symmetric infinite nuclear matter, the sums of products of three normal densities can be expressed as a products of three isoscalar densities. When all three densities depend on two separate (iso)spin indeces, the product is

$$\begin{aligned}\sum_{\substack{\sigma_1\sigma_2\sigma_3\\ q_1q_2q_3}}&\rho(\mathbf{r}_1\sigma_1 q_1, \mathbf{r}_2\sigma_2 q_2)\rho(\mathbf{r}_2\sigma_2 q_2, \mathbf{r}_3\sigma_3 q_3)\rho(\mathbf{r}_3\sigma_3 q_3, \mathbf{r}_1\sigma_1 q_1) \\ &\overset{\text{INM}}{=}\frac{1}{16}\rho_0(\mathbf{r}_1,\mathbf{r}_2)\rho_0(\mathbf{r}_2,\mathbf{r}_3)\rho_0(\mathbf{r}_3,\mathbf{r}_1).\end{aligned} \tag{A.11}$$

If one density depends on two same spin or isospin indeces (underlined),

$$\sum_{\substack{\sigma_1\sigma_2\sigma_3\\ q_1q_2q_3}} \rho(\mathbf{r}_4\underline{\sigma_1}q_2,\mathbf{r}_1\underline{\sigma_1}q_1)\rho(\mathbf{r}_6\sigma_3q_3,\mathbf{r}_2\sigma_2q_2)\rho(\mathbf{r}_5\sigma_2q_1,\mathbf{r}_3\sigma_3q_3) \overset{\text{INM}}{=} \frac{1}{8}\rho_0(\mathbf{r}_4,\mathbf{r}_1)\rho_0(\mathbf{r}_6,\mathbf{r}_2)\rho_0(\mathbf{r}_5,\mathbf{r}_3) \tag{A.12}$$

$$\sum_{\substack{\sigma_1\sigma_2\sigma_3\\ q_1q_2q_3}} \rho(\mathbf{r}_4\sigma_2\underline{q_1},\mathbf{r}_1\sigma_1\underline{q_1})\rho(\mathbf{r}_6\sigma_3q_3,\mathbf{r}_2\sigma_2q_2)\rho(\mathbf{r}_5\sigma_1q_2,\mathbf{r}_3\sigma_3q_3) \overset{\text{INM}}{=} \frac{1}{8}\rho_0(\mathbf{r}_4,\mathbf{r}_1)\rho_0(\mathbf{r}_6,\mathbf{r}_2)\rho_0(\mathbf{r}_5,\mathbf{r}_3), \tag{A.13}$$

and when one density depends on one isospin and another density depends on one spin,

$$\sum_{\substack{\sigma_1\sigma_2\sigma_3\\ q_1q_2q_3}} \rho(\mathbf{r}_4\sigma_2\underline{q_1},\mathbf{r}_1\sigma_1\underline{q_1})\rho(\mathbf{r}_6\sigma_1q_3,\mathbf{r}_2\sigma_2q_2)\rho(\mathbf{r}_5\underline{\sigma_3}q_2,\mathbf{r}_3\underline{\sigma_3}q_3) \overset{\text{INM}}{=} \frac{1}{4}\rho_0(\mathbf{r}_4,\mathbf{r}_1)\rho_0(\mathbf{r}_6,\mathbf{r}_2)\rho_0(\mathbf{r}_5,\mathbf{r}_3). \tag{A.14}$$

Appendix B

S,T decomposition for the Skyrme interaction

Expression for the stardard Skyrme effective force reads as

$$\begin{aligned} V(\mathbf{R},\mathbf{r}) =& \sum_{i=0}^{2} t_{0i}\left(1+x_{0i}\hat{P}_\sigma\right)\delta(\mathbf{r})\left[\rho_0(\mathbf{R})\right]^{i/3} \\ &+\frac{1}{2}t_1\left(1+x_1\hat{P}_\sigma\right)\left[\delta(\mathbf{r})\mathbf{k}^2+\mathbf{k}'^2\delta(\mathbf{r})\right] \\ &+t_2\left(1+x_2\hat{P}_\sigma\right)\mathbf{k}'\cdot\delta(\mathbf{r})\mathbf{k} \\ &+iW_0\left[\sigma_1+\sigma_2\right]\mathbf{k}'\times\delta(\mathbf{r})\mathbf{k}, \end{aligned} \tag{B.1}$$

and since we are dealing with the fermions, we have the property

$$\hat{P}_\sigma\hat{P}_\tau\hat{P}_x=-1. \tag{B.2}$$

for the exchange operators. For a zero-range interaction, $\hat{P}_x$ produces only a sign ±1 when it is applied — for the t_0 and t_1 terms of the Skyrme interactions it does nothing, and for the t_2 term it gives an additional -1. Thus we have a relation

$$\hat{P}_\sigma=-\hat{P}_\tau \quad \text{for the } t_0,t_1 \text{ terms} \tag{B.3}$$

$$\hat{P}_\sigma=\hat{P}_\tau \quad \text{for the } t_2 \text{ term.} \tag{B.4}$$

When we apply gradients to densities, we may have a gradient that acts only on one set of coordinates $\mathbf{r}_i$ of the density. Later, when taking limits (that is, when applying delta operators), we must know which $\mathbf{r}_i$ the gradient acted on. Thus we use the following notation of left (and similarly right) gradients:

$$\int \mathrm{d}^3\mathbf{r}_1\mathrm{d}^3\mathbf{r}_2\;\delta(\mathbf{r}_1-\mathbf{r}_2)\nabla_1\rho_0(\mathbf{r}_1,\mathbf{r}_2)=\int \mathrm{d}^3\mathbf{r}\;\nabla_l\rho_0(\mathbf{r}) \tag{B.5}$$

where we use the common notation $\rho_0(\mathbf{r},\mathbf{r}) = \rho_0(\mathbf{r})$. In fact, one can also write $\rho_0(\mathbf{r}) = \rho_0$. In addition, we recall the relationships between full gradients and laplacians:

$$\nabla\rho = \nabla_l\rho + \nabla_r\rho \tag{B.6}$$
$$2i\mathbf{j} = \nabla_r\rho - \nabla_l\rho \tag{B.7}$$

and

$$\nabla_l\rho = \frac{1}{2}\nabla\rho - i\mathbf{j} \tag{B.8}$$
$$\nabla_r\rho = \frac{1}{2}\nabla\rho + i\mathbf{j} \tag{B.9}$$

And for the laplacian, we have

$$\Delta\rho = \nabla_l^2\rho + 2\nabla_l\cdot\nabla_r\rho + \nabla_r^2\rho. \tag{B.10}$$

B.1 The t_0 term of the Skyrme interaction

For t_0 term $\hat{P}_\tau = -\hat{P}_\sigma$, so in the channel $S = 0$ and $T = 0$ we get

$$\begin{aligned}\hat{P}_{S=0}\hat{P}_{T=0} &= \frac{1}{4}\left(1 - \hat{P}_\sigma - \hat{P}_\tau + \hat{P}_\sigma\hat{P}_\tau\right)\\ &= \frac{1}{4}(1 - \hat{P}_\sigma + \hat{P}_\sigma - \hat{P}_\sigma\hat{P}_\sigma)\\ &= 0,\end{aligned} \tag{B.11}$$

when we recall that $\hat{P}_\sigma\hat{P}_\sigma = 1$. Thus, the contribution of t_0 term in (S,T) = (0,0) channel is 0 (see Equation (A.1)). In the very same manner we derive the contributions of the other S,T channels. For $S = 0, T = 1$,

$$\begin{aligned}\hat{P}_{S=0}\hat{P}_{T=1} &= \frac{1}{4}\left(1 - \hat{P}_\sigma\right)\left(1 + \hat{P}_\tau\right)\\ &= \frac{1}{4}\left(1 - \hat{P}_\sigma\right)\left(1 - \hat{P}_\sigma\right)\\ &= \frac{1}{2}\left(1 - \hat{P}_\sigma\right)\end{aligned} \tag{B.12}$$

and thus

$$\begin{aligned}&\left(1 + x_{0i}\hat{P}_\sigma\right)\frac{1}{2}\left(1 - \hat{P}_\sigma\right)\\ &\quad= \frac{1}{2}\left(1 - \hat{P} + x_{0i}\hat{P}_\sigma - x_{0i}\hat{P}_\sigma\hat{P}_\sigma\right)\\ &\quad= \frac{1}{2}(1 - x_{0i})\left(1 - \hat{P}_\sigma\right)\\ &\quad\to \frac{1}{2}(1 - x_{0i})\left(\delta_{\sigma_1\sigma_3}\delta_{\sigma_2\sigma_4}\delta_{q_1q_3}\delta_{q_2q_4} - \delta_{\sigma_1\sigma_4}\delta_{\sigma_2\sigma_3}\delta_{q_1q_3}\delta_{q_2q_4}\right),\end{aligned} \tag{B.13}$$

where the experission after the arrow shows the contribution of the term after inserted into the expectation value of Equation (A.1). The contribution to the EOS is then

$$\begin{aligned}
E_{t_0}^{01} = & \frac{1}{2}\sum_{q\sigma}\int \mathrm{d}^3r_1\mathrm{d}^3r_2\mathrm{d}^3r_3\mathrm{d}^3r_4\delta(r_1-r_3)\delta(r_2-r_4)\times \\
& \sum_i t_{0i}\delta(r_1-r_2)\left[\rho_0\left(\frac{1}{2}(r_1+r_2)\right)\right]^{i/3}\frac{1}{2}(1-x_{0i})\times \\
& (\delta_{\sigma_1\sigma_3}\delta_{\sigma_2\sigma_4}\delta_{q_1q_3}\delta_{q_2q_4}-\delta_{\sigma_1\sigma_4}\delta_{\sigma_2\sigma_3}\delta_{q_1q_3}\delta_{q_2q_4})\times \\
& [\rho(r_3\sigma_3q_3r_1\sigma_1q_1)\rho(r_4\sigma_4q_4r_2\sigma_2q_2)-\rho(r_4\sigma_4q_4r_1\sigma_1q_1)\rho(r_3\sigma_3q_3r_2\sigma_2q_2)] \qquad \text{(B.14)} \\
= & \frac{1}{4}\sum_{q\sigma}\int \mathrm{d}^3r_1\mathrm{d}^3r_2\sum_i t_{0i}\delta(r_1-r_2)\left[\rho_0\left(\frac{1}{2}(r_1+r_2)\right)\right]^{i/3}(1-x_{0i})\times \\
& [\rho(r_1\sigma_1q_1r_1\sigma_1q_1)\rho(r_2\sigma_2q_2r_2\sigma_2q_2)-\rho(r_2\sigma_2q_2r_1\sigma_1q_1)\rho(r_1\sigma_1q_1r_2\sigma_2q_2) \\
& -\rho(r_1\sigma_2q_1r_1\sigma_1q_1)\rho(r_2\sigma_1q_2r_2\sigma_2q_2)+\rho(r_2\sigma_1q_2r_1\sigma_1q_1)\rho(r_1\sigma_2q_1r_2\sigma_2q_2)] \\
= & \frac{1}{4}\int \mathrm{d}^3r\sum_i t_{0i}\left[\rho_0(r)\right]^{i/3}(1-x_{0i})\times \\
& \Big\{\rho_0(r)\rho_0(r)-\frac{1}{4}\left[\rho_0(r)\rho_0(r)+\rho_1(r)\rho_1(r)+s_0(r)s_0(r)+s_1(r)s_1(r)\right] \\
& -\frac{1}{2}\left[\rho_0(r)\rho_0(r)+s_0(r)s_0(r)\right]+\frac{1}{2}\left[\rho_0(r)\rho_0(r)+\rho_1(r)\rho_1(r)\right]\Big\} \qquad \text{(B.15)} \\
= & \frac{1}{4}\int \mathrm{d}^3r\sum_i t_{0i}\left[\rho_0(r)\right]^{i/3}(1-x_{0i})\times\frac{3}{4}\rho_0(r)\rho_0(r) \qquad \text{(B.16)} \\
= & \frac{3}{16}\int \mathrm{d}^3r\sum_i t_{0i}\left[\rho_0(r)\right]^{2+i/3}(1-x_{0i}), \qquad \text{(B.17)}
\end{aligned}$$

where we use the fact that $s_0 = s_1 = \rho_1 = 0$ in the symmetric non-polarized nuclear matter. We recall that for

$$E_{pot} = \int \mathrm{d}r\,\mathcal{E}(r), \qquad \text{(B.18)}$$

the Equation of State is

$$\frac{E}{A}^{(0,1)} = \frac{\mathcal{E}}{\rho_0} = \frac{3}{16}\sum_i t_{0i}\left[\rho_0(r)\right]^{1+i/3}(1-x_{0i}). \qquad \text{(B.19)}$$

For the channel $S = 1, T = 0$, we get

$$\frac{E}{A}^{(1,0)} = \frac{\mathcal{E}}{\rho_0} = \frac{3}{16}\sum_i t_{0i}\left[\rho_0(r)\right]^{1+i/3}(1+x_{0i}) \qquad \text{(B.20)}$$

and in the same manner as in the case of (S,T) = (0,0) we see that the contribution from t_0 term in (S,T) = (1,1) channel is zero, since:

$$\begin{aligned}\hat{P}_{S=1}\hat{P}_{T=1} &= \frac{1}{4}\left(1+\hat{P}_\sigma\right)\left(1+\hat{P}_\tau\right)\\ &= \frac{1}{4}\left(1+\hat{P}_\sigma\right)\left(1-\hat{P}_\sigma\right)\\ &= \frac{1}{4}\left(1-\hat{P}_\sigma\hat{P}_\sigma\right)\\ &= 0.\end{aligned} \tag{B.21}$$

B.2 The t_1 term of the Skyrme interaction

Again, the contribution of the channel $S = 0, T = 0$ is zero,

$$\frac{E}{A}^{(0,0)} = 0. \tag{B.22}$$

And the channel $S = 0, T = 1$ gives

$$\left(1+x_1\hat{P}_\sigma\right)\hat{P}_{S=0}\hat{P}_{T=1} = \frac{1}{2}\left(1-x_1\right)\left(1-\hat{P}_\sigma\right), \tag{B.23}$$

thus

$$\begin{aligned}E_{t_1}^{01} =& \frac{t_1}{8}\sum_{q\sigma}\int \mathrm{d}^3r_1\mathrm{d}^3r_2\mathrm{d}^3r_3\mathrm{d}^3r_4\delta(r_1-r_3)\delta(r_2-r_4)\\ &\left[\delta(r_1-r_2)\mathbf{k}_{34}^2+\mathbf{k}_{12}^{*2}\delta(r_1-r_2)\right]\times\left(1-x_1\right)\left(1-\hat{P}_\sigma\right)\\ &[\rho(r_3\sigma_3q_3r_1\sigma_1q_1)\rho(r_4\sigma_4q_4r_2\sigma_2q_2)-\rho(r_4\sigma_4q_4r_1\sigma_1q_1)\rho(r_3\sigma_3q_3r_2\sigma_2q_2)]\end{aligned} \tag{B.24}$$

$$\begin{aligned}=& \frac{t_1}{8}\sum_{q\sigma}\int \mathrm{d}^3r_1\mathrm{d}^3r_2\mathrm{d}^3r_3\mathrm{d}^3r_4\delta(r_1-r_3)\delta(r_2-r_4)\left[\delta(r_1-r_2)\mathbf{k}_{34}^2+\mathbf{k}_{12}^{*2}\delta(r_1-r_2)\right]\times\\ &\left(1-x_1\right)[\rho(r_3\sigma_1q_1r_1\sigma_1q_1)\rho(r_4\sigma_2q_2r_2\sigma_2q_2)-\rho(r_4\sigma_2q_2r_1\sigma_1q_1)\rho(r_3\sigma_1q_1r_2\sigma_2q_2)\\ &-\rho(r_3\sigma_2q_1r_1\sigma_1q_1)\rho(r_4\sigma_1q_2r_2\sigma_2q_2)+\rho(r_4\sigma_1q_2r_1\sigma_1q_1)\rho(r_3\sigma_2q_1r_2\sigma_2q_2)]\end{aligned} \tag{B.25}$$

$$\begin{aligned}=& \frac{t_1}{8}\int \mathrm{d}^3r_1\mathrm{d}^3r_2\mathrm{d}^3r_3\mathrm{d}^3r_4\delta(r_1-r_3)\delta(r_2-r_4)\left[\delta(r_1-r_2)\mathbf{k}_{34}^2+\mathbf{k}_{12}^{*2}\delta(r_1-r_2)\right]\\ &\left(1-x_1\right)\left[\sum_{q_1\sigma_1}\rho(r_3\sigma_1q_1r_1\sigma_1q_1)\sum_{q_2\sigma_2}\rho(r_4\sigma_2q_2r_2\sigma_2q_2)\right.\\ &-\sum_{q_1q_2\sigma_1\sigma_2}\rho(r_4\sigma_2q_2r_1\sigma_1q_1)\rho(r_3\sigma_1q_1r_2\sigma_2q_2)\\ &\left.-\sum_{\sigma_1\sigma_2}\left(\sum_{q_1}\rho(r_3\sigma_2q_1r_1\sigma_1q_1)\sum_{q_2}\rho(r_4\sigma_1q_2r_2\sigma_2q_2)\right)\right.\end{aligned}$$

$$+\sum_{q_1q_2}\left(\sum_{\sigma_1}\rho(r_4\sigma_1q_2r_1\sigma_1q_1)\sum_{\sigma_2}\rho(r_3\sigma_2q_1r_2\sigma_2q_2)\right)\Bigg] \tag{B.26}$$

$$\begin{aligned}
=&\frac{t_1}{8}\int \mathrm{d}^3r_1\mathrm{d}^3r_2\mathrm{d}^3r_3\mathrm{d}^3r_4\delta(r_1-r_3)\delta(r_2-r_4)\\
&\left[\delta(r_1-r_2)\mathbf{k}_{34}^2+\mathbf{k}_{12}^{*2}\delta(r_1-r_2)\right](1-x_1)\\
&\{\rho_0(r_3,r_1)\rho_0(r_4,r_2)\\
&-\frac{1}{4}\left[\rho_0(r_4,r_1)\rho_0(r_3,r_2)+\rho_1(r_4,r_1)\rho_1(r_3,r_2)\right.\\
&\left.+s_0(r_4,r_1)s_0(r_3,r_2)+s_1(r_4,r_1)s_1(r_3,r_2)\right]\\
&-\frac{1}{2}\left[\rho_0(r_3,r_1)\rho_0(r_4,r_2)+s_0(r_3,r_1)s_0(r_4,r_2)\right]\\
&+\frac{1}{2}\left[\rho_0(r_4,r_1)\rho_0(r_3,r_2)+\rho_1(r_4,r_1)\rho_1(r_4,r_1)\right]\}
\end{aligned}$$

$$\begin{aligned}
=&\frac{t_1}{8}\int \mathrm{d}^3r_1\mathrm{d}^3r_2\mathrm{d}^3r_3\mathrm{d}^3r_4\delta(r_1-r_3)\delta(r_2-r_4)\left[\delta(r_1-r_2)\mathbf{k}_{34}^2+\mathbf{k}_{12}^{*2}\delta(r_1-r_2)\right]\\
&(1-x_1)\left[\frac{1}{2}\rho_0(r_3,r_1)\rho_0(r_4,r_2)+\frac{1}{4}\rho_0(r_4,r_1)\rho_0(r_3,r_2)\right]
\end{aligned} \tag{B.27}$$

Next we apply the relative momentum operators $\mathbf{k}_{12}^*=-\frac{1}{2i}(\nabla_1-\nabla_2)$ and $\mathbf{k}_{34}=\frac{1}{2i}(\nabla_3-\nabla_4)$. We see that

$$\begin{aligned}
&\left[(\nabla_1-\nabla_2)^2+(\nabla_3-\nabla_4)^2\right]\rho_0(r_3,r_1)\rho_0(r_4,r_2)\\
=&\left[\nabla_1\nabla_1\rho_0(r_3,r_1)\right]\rho_0(r_4,r_2)-2\left[\nabla_1\rho_0(r_3,r_1)\right]\left[\nabla_2\rho_0(r_4,r_2)\right]\\
&+\rho_0(r_3,r_1)\left[\nabla_2\nabla_2\rho_0(r_4,r_2)\right]+\left[\nabla_3\nabla_3\rho_0(r_3,r_1)\right]\\
&\rho_0(r_4,r_2)-2\left[\nabla_3\rho_0(r_3,r_1)\right]\left[\nabla_4\rho_0(r_4,r_2)\right]+\rho_0(r_3,r_1)\left[\nabla_4\nabla_4\rho_0(r_4,r_2)\right]
\end{aligned} \tag{B.28}$$

After applying $\delta(r_1-r_2),\delta(r_1-r_3)$ and $\delta(r_2-r_4)$ and the corresponding three integrals, this takes the form of

$$\begin{aligned}
=&\left[\nabla_r\nabla_r\rho_0(r)\right]\rho_0(r)-2\left[\nabla_r\rho_0(r)\right]\left[\nabla_r\rho_0(r)\right]+\rho_0(r)\left[\nabla_r\nabla_r\rho_0(r)\right]\\
&+\left[\nabla_l\nabla_l\rho_0(r)\right]\rho_0(r)-2\left[\nabla_l\rho_0(r)\right]\left[\nabla_l\rho_0(r)\right]+\rho_0(r)\left[\nabla_l\nabla_l\rho_0(r)\right]\\
=&2\left[\nabla_r\nabla_r\rho_0(r)\right]\rho_0(r)-2\left[\nabla_r\rho_0(r)\right]\left[\nabla_r\rho_0(r)\right]\\
&+2\left[\nabla_l\nabla_l\rho_0(r)\right]\rho_0(r)-2\left[\nabla_l\rho_0(r)\right]\left[\nabla_l\rho_0(r)\right]\\
=&2\left[(\nabla_r\nabla_r+2\nabla_r\nabla_l+\nabla_l\nabla_l)\rho_0(r)\right]\rho_0(r)-2\left[\nabla_r\rho_0(r)\right]\left[\nabla_r\rho_0(r)\right]\\
&-2\left[\nabla_l\rho_0(r)\right]\left[\nabla_l\rho_0(r)\right]-4\left[\nabla_r\nabla_l\rho_0(r)\right]\rho_0(r)\\
=&2\left[\Delta\rho_0(r)\right]\rho_0(r)-2\left[\nabla_r\rho_0(r)\right]\left[\nabla_r\rho_0(r)\right]-2\left[\nabla_l\rho_0(r)\right]\left[\nabla_l\rho_0(r)\right]-4\left[\nabla_r\nabla_l\rho_0(r)\right]\rho_0(r)
\end{aligned} \tag{B.29}$$

Since $\nabla_r\rho_0$ and $\nabla_l\rho_0$ can be written as a combination of $\mathbf{j}$ and $\nabla\rho$, the only term which is non-zero in symmetric nuclear matter is the one proportional to $[\nabla_r\nabla_l\rho_0(r)]\,\rho_0(r)$. And it is easily seen that both of the terms $\rho_0(r_3,r_1)\rho(r_4,r_2)$ and $\rho_0(r_4,r_1)\rho_0(r_3,r_2)$ will produce the same outcome when

$$\left[\delta(r_1-r_2)\mathbf{k}_{34}^2+\mathbf{k}_{12}^{*2}\delta(r_1-r_2)\right] \tag{B.30}$$

is applied, and it leads to the factor $\frac{1}{2}+\frac{1}{4}=\frac{3}{4}$, thus

$$\begin{aligned}
E_{t_1}^{01} &= \frac{t_1}{8}\int \mathrm{d}^3r(1-x_1)(-\frac{1}{2i})\frac{1}{2i}\frac{3}{4}\,(-4)\,[\nabla_r\nabla_l\rho_0(r)]\,\rho_0(r)\\
&= \frac{t_1}{8}\frac{3}{4}\int \mathrm{d}^3r(1-x_1)\tau_0(r)\rho_0(r)\\
&= \frac{t_1}{8}\frac{3}{4}\int \mathrm{d}^3r(1-x_1)\frac{3}{5}\left(\frac{3\pi^2}{2}\right)^{2/3}\rho_0^{5/3}(r)\rho_0(r)\\
&= \frac{9t_1}{160}\int \mathrm{d}^3r(1-x_1)\frac{3}{5}\left(\frac{3\pi^2}{2}\right)^{2/3}\rho_0^{5/3}(r)\rho_0(r).
\end{aligned} \tag{B.31}$$

The contribution to the EOS is

$$\frac{E}{A}^{(0,1)} = \frac{\mathcal{E}}{\rho_0} = \frac{9}{160}t_1(1-x_1)\left(\frac{3\pi^2}{2}\right)^{2/3}\rho_0^{5/3}(r). \tag{B.32}$$

The contributions of the last two channels are derived correspondingly.

$$\frac{E}{A}^{(0,1)} = \frac{\mathcal{E}}{\rho_0} = \frac{9}{160}t_1(1+x_1)\left(\frac{3\pi^2}{2}\right)^{2/3}\rho_0^{5/3}(r) \tag{B.33}$$

$$\frac{E}{A}^{(1,1)} = \frac{\mathcal{E}}{\rho_0} = 0. \tag{B.34}$$

B.3 The t_2 term of the Skyrme interaction

In the $S=0,T=0$ channel, we have the property $\hat{P}_\tau=\hat{P}_\sigma$ and we get

$$\begin{aligned}
\hat{P}_{S=0}\hat{P}_{T=0}(1+x_2\hat{P}_\sigma) &= \frac{1}{4}(1-2\hat{P}_\sigma+\hat{P}_\sigma\hat{P}_\sigma)(1+x_2\hat{P}_\sigma)\\
&= \frac{1}{2}(1-x_2)(1-\hat{P}_\sigma),
\end{aligned} \tag{B.35}$$

so the expectation value becomes

$$\begin{aligned}
E^{00}_{t_2} =& \frac{1}{2} t_2 \sum_{q\sigma} \int \mathrm{d}^3 r_1 \mathrm{d}^3 r_2 \mathrm{d}^3 r_3 \mathrm{d}^3 r_4 \; \delta(r_1 - r_3)\delta(r_2 - r_4) \times \\
& \mathbf{k}^*_{12} \cdot \delta(r_1 - r_2)\mathbf{k}_{34} \frac{1}{2}(1 - x_2)(1 - \hat{P}_\sigma) \times \\
& [\rho(r_3\sigma_3 q_3 r_1 \sigma_1 q_1)\rho(r_4\sigma_4 q_4 r_2 \sigma_2 q_2) - \rho(r_4\sigma_4 q_4 r_1 \sigma_1 q_1)\rho(r_3\sigma_3 q_3 r_2 \sigma_2 q_2)] \\
=& \frac{1}{4} t_2 \sum_{q\sigma} \int \mathrm{d}^3 r_1 \mathrm{d}^3 r_2 \mathrm{d}^3 r_3 \mathrm{d}^3 r_4 \; \delta(r_1 - r_3)\delta(r_2 - r_4) \\
& \mathbf{k}^*_{12} \cdot \delta(r_1 - r_2)\mathbf{k}_{34}(1 - x_2) \times \\
& [\rho(r_3\sigma_1 q_1 r_1 \sigma_1 q_1)\rho(r_4\sigma_2 q_2 r_2 \sigma_2 q_2) - \rho(r_4\sigma_2 q_2 r_1 \sigma_1 q_1)\rho(r_3\sigma_1 q_1 r_2 \sigma_2 q_2) \\
& - \rho(r_3\sigma_2 q_1 r_1 \sigma_1 q_1)\rho(r_4\sigma_1 q_2 r_2 \sigma_2 q_2) + \rho(r_4\sigma_1 q_2 r_1 \sigma_1 q_1)\rho(r_3\sigma_2 q_1 r_2 \sigma_2 q_2)] \qquad \text{(B.36)}
\end{aligned}$$

Once again, we take sums over q and σ, and use the property $s_0 = s_1 = \rho_1$ of symmetric infinite nuclear matter.

$$
\begin{aligned}
E^{00}_{t_2} =& \frac{1}{4} t_2 \int \mathrm{d}^3 r_1 \mathrm{d}^3 r_2 \mathrm{d}^3 r_3 \mathrm{d}^3 r_4 \delta(r_1 - r_3)\delta(r_2 - r_4) \\
& \mathbf{k}^*_{12} \cdot \delta(r_1 - r_2)\mathbf{k}_{34}(1 - x_2)\times \\
& \left[\frac{1}{2}\rho_0(r_3, r_1)\rho_0(r_4, r_2) + \frac{1}{4}\rho_0(r_4, r_1)\rho_0(r_3, r_2)\right] \\
=& \frac{1}{8} t_2 \int \mathrm{d}^3 r_1 \mathrm{d}^3 r_2 \mathrm{d}^3 r_3 \mathrm{d}^3 r_4 \delta(r_1 - r_3)\delta(r_2 - r_4) \\
& \mathbf{k}^*_{12} \cdot \delta(r_1 - r_2) \left(\frac{1}{2i}\right)(1 - x_2)\times \\
& \left([\nabla_3 \rho_0(r_3, r_1)]\, \rho_0(r_4, r_2) + \rho_0(r_3, r_1)\, [-\nabla_4 \rho_0(r_4, r_2)]\right. \\
& \left. + \frac{1}{2}\,[-\nabla_4 \rho_0(r_4, r_1)]\, \rho_0(r_3, r_2) + \frac{1}{2}\rho_0(r_4, r_1)\, [\nabla_3 \rho_0(r_3, r_2)]\right) \\
=& \frac{1}{8} t_2 \int \mathrm{d}^3 r_1 \mathrm{d}^3 r_2 \mathrm{d}^3 r_3 \mathrm{d}^3 r_4 \delta(r_1 - r_3)\delta(r_2 - r_4)\delta(r_1 - r_2) \\
& \left(\frac{1}{2i}\right)\left(-\frac{1}{2i}\right)(1 - x_2)\times \\
& \left([\nabla_1 \nabla_3 \rho_0(r_3, r_1)]\, \rho_0(r_4, r_2) + [\nabla_3 \rho_0(r_3, r_1)]\, [-\nabla_2 \rho_0(r_4, r_2)]\right. \\
& + [\nabla_1 \rho_0(r_3, r_1)]\, [-\nabla_4 \rho_0(r_4, r_2)] + \rho_0(r_3, r_1)\, [\nabla_2 \nabla_4 \rho_0(r_4, r_2)] \\
& + \frac{1}{2}\,[-\nabla_1 \nabla_4 \rho_0(r_4, r_1)]\, \rho_0(r_3, r_2) + \frac{1}{2}\,[-\nabla_4 \rho_0(r_4, r_1)]\, [-\nabla_2 \rho_0(r_3, r_2)] \\
& \left. + \frac{1}{2}\,[\nabla_1 \rho_0(r_4, r_1)]\, [\nabla_3 \rho_0(r_3, r_2)] + \frac{1}{2}\rho_0(r_4, r_1)\, [-\nabla_2 \nabla_3 \rho_0(r_3, r_2)]\right) \\
=& \frac{1}{8} t_2 \int \mathrm{d}^3 r \frac{1}{4}(1 - x_2)\times \\
& \left([\nabla_r \nabla_l \rho_0(r)]\, \rho_0(r) + [\nabla_l \rho_0(r)]\, [-\nabla_r \rho_0(r)]\right. \\
& + [\nabla_r \rho_0(r)]\, [-\nabla_l \rho_0(r)] + \rho_0(r)\, [\nabla_r \nabla_l \rho_0(r)] \\
& + \frac{1}{2}\,[-\nabla_r \nabla_l \rho_0(r)]\, \rho_0(r) + \frac{1}{2}\,[-\nabla_l \rho_0(r)]\, [-\nabla_r \rho_0(r)] \\
& \left. + \frac{1}{2}\,[\nabla_r \rho_0(r)]\, [\nabla_l \rho_0(r)] + \frac{1}{2}\rho_0(r)\, [-\nabla_r \nabla_l \rho_0(r)]\right) \\
=& \frac{1}{8}\frac{1}{4} t_2 \int \mathrm{d}^3 r (1 - x_2)\left([\nabla_r \nabla_l \rho_0(r)]\, \rho_0(r) - [\nabla_l \rho_0(r)]\, [\nabla_r \rho_0(r)]\right) \qquad \text{(B.37)}
\end{aligned}
$$

Since we can write $\nabla_r \rho_0(r)$ and $\nabla_l \rho_0(r)$ with $\mathbf{j}$ and $\Delta\rho_0$, the term proportional

to $[\nabla_l \rho_0(r)]\,[\nabla_r \rho_0(r)]$ equals to zero in symmetric nuclear matter, and we get

$$\begin{aligned} E_{t_2}^{00} =& \frac{1}{32} t_2 \int \mathrm{d}^3 r (1 - x_2)\,[\nabla_r \nabla_l \rho_0(r)]\,\rho_0(r) \\ =& \frac{1}{32} t_2 \int \mathrm{d}^3 r (1 - x_2) \tau_0(r) \rho_0(r) \\ =& \frac{1}{32} t_2 \int \mathrm{d}^3 r (1 - x_2) \frac{3}{5} \left(\frac{3\pi^2}{2}\right)^{2/3} \rho_0^{5/3}(r) \rho_0(r) \\ =& \frac{3}{160} t_2 \int \mathrm{d}^3 r (1 - x_2) \left(\frac{3\pi^2}{2}\right)^{2/3} \rho_0^{5/3}(r) \rho_0(r) \end{aligned} \tag{B.38}$$

and the contribution to the channel (0,0) follows:

$$\frac{E}{A}^{(0,0)} = \frac{\mathcal{E}}{\rho_0} = \frac{3}{160} t_2 (1 - x_2) \left(\frac{3\pi^2}{2}\right)^{2/3} \rho_0^{5/3}. \tag{B.39}$$

Again, the rest of the contributions are calculated in the very same manner. For the t_2 term the property $\hat{P}_\tau = \hat{P}_\sigma$ hold, so

$$\hat{P}_{S=0} \hat{P}_{T=1} = \frac{1}{4}(1 \cdot 1 - \hat{P}_\sigma \hat{P}_\sigma) = 0 \tag{B.40}$$

which means that there is no contribution from t_2 term in (S,T) = (0,1) channel. Similarly, for the channel $S = 1, T = 0$,

$$\hat{P}_{S=1} \hat{P}_{T=0} = 0 \tag{B.41}$$

and thus no contribution on this channel. In the channel (S,T) = (1,1) we have

$$\hat{P}_{S=1} \hat{P}_{T=1} (1 + x_2 \hat{P}_\sigma) = \frac{1}{2}(1 + x_2)(1 + \hat{P}_\sigma), \tag{B.42}$$

which leads to the energy

$$E_{t_2}^{11} = \frac{27}{160} t_2 \int \mathrm{d}^3 r (1 + x_2) \left(\frac{3\pi^2}{2}\right)^{2/3} \rho_0^{5/3}(r) \rho_0(r) \tag{B.43}$$

and the corresponding EOS channel is

$$\frac{E}{A}^{(1,1)} = \frac{\mathcal{E}}{\rho_0} = \frac{27}{160} t_2 (1 + x_2) \left(\frac{3\pi^2}{2}\right)^{2/3} \rho_0^{5/3} \tag{B.44}$$

B.4 The spin-orbit term of the Skyrme interaction

The contribution of SO term is trivial: whenever deriving the functional from spin orbit term, the functional is proportional to $\mathbf{J} \cdot \nabla\rho$. This will lead to zero contribution in symmetric nuclear matter, because $\nabla\rho = 0$. Thus there is no contribution from the SO term in any channel in symmetric nuclear matter.

Appendix C

S,T decomposition for the finite-range pseudopotential

The lowest order of the pseudopotential is written as

$$\begin{aligned} &V_0^0(r_1, r_2, r_3, r_4) \\ &\quad = \left(W_1^0 \hat{1}_\sigma \hat{1}_\tau + B_1^0 \hat{1}_\tau \hat{P}_\sigma - H_1^0 \hat{1}_\sigma \hat{P}_\tau - M_1^0 \hat{P}_\sigma \hat{P}_\tau\right) \hat{\mathcal{O}}_0^0 \delta(\mathbf{r_{13}}) \delta(\mathbf{r_{24}}) g_a(\mathbf{r_{12}}) \end{aligned} \tag{C.1}$$

where $\hat{\mathcal{O}}_0^0 = \hat{1}$ at the lowest order. We can write the action of $\hat{1}_\sigma$, $\hat{1}_\tau$, $\hat{P}_\sigma$ and $\hat{P}_\tau$ in the expectation value as delta functions, so that

$$\hat{1}_\sigma = \delta_{\sigma_1\sigma_3}\delta_{\sigma_2\sigma_4} \tag{C.2}$$

$$\hat{P}_\sigma = \delta_{\sigma_1\sigma_4}\delta_{\sigma_2\sigma_3} \tag{C.3}$$

and similarly for the isospin operators $\hat{1}_\tau$ and $\hat{P}_\tau$.

C.1 The W_1^0 term of the pseudopotential

Let's start the calculations from the channel $S = 0, T = 0$, when we have

$$\hat{1}_\sigma \hat{1}_\tau \hat{P}_{S=0} \hat{P}_{T=0} = \frac{1}{4}\left(\hat{1}_\sigma \hat{1}_\tau - \hat{1}_\sigma \hat{P}_\tau - \hat{P}_\sigma \hat{1}_\tau + \hat{P}_\sigma \hat{P}_\tau\right), \tag{C.4}$$

which leads to the expression of energy

$$
\begin{aligned}
E_{pot}^{00} =& \frac{1}{2}\sum_{q\sigma}\int \mathrm{d}^3r_1\mathrm{d}^3r_2\mathrm{d}^3r_3\mathrm{d}^3r_4\delta(\mathbf{r_{13}})\delta(\mathbf{r_{24}})g_a(\mathbf{r_{12}})W_1^0\hat{1}_\sigma\hat{1}_\tau\hat{P}_{S=0}\hat{P}_{T=0}\times \\
& (\rho(r_3\sigma_3q_3r_1\sigma_1q_1)\rho(r_4\sigma_4q_4r_2\sigma_2q_2)-\rho(r_4\sigma_4q_4r_1\sigma_1q_1)\rho(r_3\sigma_3q_3r_2\sigma_2q_2)) \\
=& \frac{W_1^0}{8}\sum_{q\sigma}\int \mathrm{d}^3r_1\mathrm{d}^3r_2\mathrm{d}^3r_3\mathrm{d}^3r_4\delta\times \\
& (\mathbf{r_{13}})\delta(\mathbf{r_{24}})g_a(\mathbf{r_{12}})\left(\hat{1}_\sigma\hat{1}_\tau-\hat{1}_\sigma\hat{P}_\tau-\hat{P}_\sigma\hat{1}_\tau+\hat{P}_\sigma\hat{P}_\tau\right)\times \\
& (\rho(r_3\sigma_3q_3r_1\sigma_1q_1)\rho(r_4\sigma_4q_4r_2\sigma_2q_2)-\rho(r_4\sigma_4q_4r_1\sigma_1q_1)\rho(r_3\sigma_3q_3r_2\sigma_2q_2)) \\
=& \frac{W_1^0}{8}\sum_{q\sigma}\int \mathrm{d}^3r_1\mathrm{d}^3r_2\mathrm{d}^3r_3\mathrm{d}^3r_4\delta(\mathbf{r_{13}})\delta(\mathbf{r_{24}})g_a(\mathbf{r_{12}})\times \\
& [\rho(r_3\sigma_1q_1r_1\sigma_1q_1)\rho(r_4\sigma_2q_2r_2\sigma_2q_2)-\rho(r_4\sigma_2q_2r_1\sigma_1q_1)\rho(r_3\sigma_1q_1r_2\sigma_2q_2) \\
& -\rho(r_3\sigma_1q_2r_1\sigma_1q_1)\rho(r_4\sigma_2q_1r_2\sigma_2q_2)+\rho(r_4\sigma_2q_1r_1\sigma_1q_1)\rho(r_3\sigma_1q_2r_2\sigma_2q_2) \\
& -\rho(r_3\sigma_2q_1r_1\sigma_1q_1)\rho(r_4\sigma_1q_2r_2\sigma_2q_2)+\rho(r_4\sigma_1q_2r_1\sigma_1q_1)\rho(r_3\sigma_2q_1r_2\sigma_2q_2) \\
& +\rho(r_3\sigma_2q_2r_1\sigma_1q_1)\rho(r_4\sigma_1q_1r_2\sigma_2q_2)-\rho(r_4\sigma_1q_1r_1\sigma_1q_1)\rho(r_3\sigma_2q_2r_2\sigma_2q_2)] \\
=& \frac{W_1^0}{8}\sum_{q\sigma}\int \mathrm{d}^3r_1\mathrm{d}^3r_2g_a(\mathbf{r_{12}})\times \\
& [\rho(r_1\sigma_1q_1r_1\sigma_1q_1)\rho(r_2\sigma_2q_2r_2\sigma_2q_2)-\rho(r_2\sigma_2q_2r_1\sigma_1q_1)\rho(r_1\sigma_1q_1r_2\sigma_2q_2) \\
& -\rho(r_1\sigma_1q_2r_1\sigma_1q_1)\rho(r_2\sigma_2q_1r_2\sigma_2q_2)+\rho(r_2\sigma_2q_1r_1\sigma_1q_1)\rho(r_1\sigma_1q_2r_2\sigma_2q_2) \\
& -\rho(r_1\sigma_2q_1r_1\sigma_1q_1)\rho(r_2\sigma_1q_2r_2\sigma_2q_2)+\rho(r_2\sigma_1q_2r_1\sigma_1q_1)\rho(r_1\sigma_2q_1r_2\sigma_2q_2) \\
& +\rho(r_1\sigma_2q_2r_1\sigma_1q_1)\rho(r_2\sigma_1q_1r_2\sigma_2q_2)-\rho(r_2\sigma_1q_1r_1\sigma_1q_1)\rho(r_1\sigma_2q_2r_2\sigma_2q_2)] \qquad \text{(C.5)}
\end{aligned}
$$

We apply the sums over products of densities and we get

$$
\begin{aligned}
E_{pot}^{00} =& \frac{W_1^0}{8}\int \mathrm{d}^3r_1\mathrm{d}^3r_2g_a(\mathbf{r_{12}})\times\Big[\rho_0(r_1)\rho_0(r_2)-\frac{1}{4}\rho_0(r_2,r_1)\rho_0(r_1,r_2) \\
& -\frac{1}{2}\rho_0(r_1)\rho_0(r_2)+\frac{1}{2}\rho_0(r_2,r_1)\rho_0(r_1,r_2)-\frac{1}{2}\rho_0(r_1)\rho_0(r_2) \\
& +\frac{1}{2}\rho_0(r_2,r_1)\rho_0(r_1,r_2)+\frac{1}{4}\rho_0(r_1)\rho_0(r_2)-\rho_0(r_2,r_1)\rho_(r_1,r_2)\Big] \\
=& \frac{W_1^0}{8}\int \mathrm{d}^3r_1\mathrm{d}^3r_2g_a(\mathbf{r_{12}})\left[\frac{1}{4}\rho_0(r_1)\rho_0(r_2)-\frac{1}{4}\rho_0(r_2,r_1)\rho_0(r_1,r_2)\right] \\
=& \frac{W_1^0}{32}\int \mathrm{d}^3R\left(\rho_0^2\int \mathrm{d}^3rg_a(r)-\int \mathrm{d}^3rg_a(r)\rho_0(r_2,r_1)\rho_0(r_1,r_2)\right) \qquad \text{(C.6)}
\end{aligned}
$$

After applying the integrals we get

$$E_{pot}^{00} = \frac{W_1^0}{32} \int \mathrm{d}^3 R \rho_0^2 (1 - F_0(\xi)), \tag{C.7}$$

where

$$F_0(\xi) = \frac{12}{\xi^3} \left[\frac{1 - e^{-\xi^2}}{\xi^3} - \frac{3 - e^{-\xi^2}}{2\xi} + \frac{\sqrt{\pi}}{2} \mathrm{erf}\xi \right], \tag{C.8}$$

and that leads us to the EOS:

$$\frac{E}{A}^{(0,0)} = \frac{\mathcal{E}}{\rho_0} = \frac{1}{32} W_1^0 \rho_0 (1 - F_0(\xi)). \tag{C.9}$$

For the contribution of the channel $S = 0, T = 1$ we need to know that

$$\hat{1}_\sigma \hat{1}_\tau \hat{P}_{S=0} \hat{P}_{T=1} = \frac{1}{4} \left(\hat{1}_\sigma \hat{1}_\tau + \hat{1}_\sigma \hat{P}_\tau - \hat{P}_\sigma \hat{1}_\tau - \hat{P}_\sigma \hat{P}_\tau \right) \tag{C.10}$$

and we can immediately see, that the calculation is very similar to the one of (S,T) = (0,0) but with two different signs. Indeed, all the rest contributions are calculated in the same manner and we end up in the results

$$\frac{E}{A}^{(0,1)} = \frac{\mathcal{E}}{\rho_0} = \frac{3}{32} W_1^0 \rho_0 (1 + F_0(\xi)) \tag{C.11}$$

$$\frac{E}{A}^{(1,0)} = \frac{\mathcal{E}}{\rho_0} = \frac{3}{32} W_1^0 \rho_0 (1 + F_0(\xi)) \tag{C.12}$$

$$\frac{E}{A}^{(1,1)} = \frac{\mathcal{E}}{\rho_0} = \frac{9}{32} W_1^0 \rho_0 (1 - F_0(\xi)). \tag{C.13}$$

C.2 The B_1^0 term of the pseudopotential

In the $S = 0, T = 0$ channel we get that

$$\hat{1}_\tau \hat{P}_\sigma \hat{P}_{S=0} \hat{P}_{T=0} = \frac{1}{4} \left(-\hat{1}_\sigma \hat{1}_\tau + \hat{1}_\sigma \hat{P}_\tau + \hat{P}_\sigma \hat{1}_\tau - \hat{P}_\sigma \hat{P}_\tau \right), \tag{C.14}$$

which leads to the contribution

$$\frac{E}{A}^{(0,0)} = \frac{\mathcal{E}}{\rho_0} = -\frac{1}{32} B_1^0 \rho_0 (1 - F_0(\xi)) \tag{C.15}$$

Again, the rest of the contributions are calculated in the very same manner, and we get the contributions

$$\frac{E}{A}^{(0,1)} = -\frac{3}{32}B_1^0\rho_0(1+F_0(\xi)) \tag{C.16}$$

$$\frac{E}{A}^{(1,0)} = \frac{3}{32}B_1^0\rho_0(1+F_0(\xi)) \tag{C.17}$$

$$\frac{E}{A}^{(1,1)} = \frac{9}{32}B_1^0\rho_0(1-F_0(\xi)). \tag{C.18}$$

C.3 The $-H_1^0$ term of the pseudopotential

In the $S=0, T=0$ channel of the $-H_1^0$ term, we have

$$\hat{1}_\sigma\hat{P}_\tau\hat{P}_{S=0}\hat{P}_{T=0} = \frac{1}{4}\left(-\hat{1}_\sigma\hat{1}_\tau + \hat{1}_\sigma\hat{P}_\tau + \hat{P}_\sigma\hat{1}_\tau - \hat{P}_\sigma\hat{P}_\tau\right), \tag{C.19}$$

which leads to the contribution

$$\frac{E}{A}^{(0,0)} = \frac{\mathcal{E}}{\rho_0} = \frac{1}{32}H_1^0\rho_0(1-F_0(\xi)). \tag{C.20}$$

The other contributions are

$$\frac{E}{A}^{(0,1)} = -\frac{3}{32}H_1^0\rho_0(1+F_0(\xi)) \tag{C.21}$$

$$\frac{E}{A}^{(1,0)} = \frac{3}{32}H_1^0\rho_0(1+F_0(\xi)) \quad \text{and} \tag{C.22}$$

$$\frac{E}{A}^{(1,1)} = -\frac{9}{32}H_1^0\rho_0(1-F_0(\xi)). \tag{C.23}$$

C.4 The $-M_1^0$ term of the pseudopotential

In the $S=0, T=0$ channel we end up in the expression

$$\hat{P}_\sigma\hat{P}_\tau\hat{P}_{S=0}\hat{P}_{T=0} = \frac{1}{4}\left(\hat{1}_\sigma\hat{1}_\tau - \hat{1}_\sigma\hat{P}_\tau - \hat{P}_\sigma\hat{1}_\tau + \hat{P}_\sigma\hat{P}_\tau\right) \tag{C.24}$$

which gives

$$\frac{E}{A}^{(0,0)} = \frac{\mathcal{E}}{\rho_0} = -\frac{1}{32}M_1^0\rho_0(1-F_0(\xi)). \tag{C.25}$$

The other contributions follow:

$$\frac{E}{A}^{(0,1)} = \frac{3}{32} M_1^0 \rho_0 (1 + F_0(\xi)) \tag{C.26}$$

$$\frac{E}{A}^{(1,0)} = \frac{3}{32} M_1^0 \rho_0 (1 + F_0(\xi)) \quad \text{and} \tag{C.27}$$

$$\frac{E}{A}^{(1,1)} = -\frac{9}{32} M_1^0 \rho_0 (1 - F_0(\xi)). \tag{C.28}$$

C.5 Total decomposition at LO

When we combine the previous results, we get the full S, T decomposition of EOS in INM for the finite-range pseudopotential at LO:

$$(S,T) = (0,0): \qquad \frac{E}{A} = \frac{1}{32}(W_1^0 - B_1^0 + H_1^0 - M_1^0)\rho_0(1 - F_0(\xi)) \tag{C.29}$$

$$(S,T) = (0,1): \qquad \frac{E}{A} = \frac{3}{32}(W_1^0 - B_1^0 - H_1^0 + M_1^0)\rho_0(1 + F_0(\xi)) \tag{C.30}$$

$$(S,T) = (1,0): \qquad \frac{E}{A} = \frac{1}{32}(W_1^0 + B_1^0 + H_1^0 + M_1^0)\rho_0(1 + F_0(\xi)) \tag{C.31}$$

$$(S,T) = (1,1): \qquad \frac{E}{A} = \frac{9}{32}(W_1^0 + B_1^0 - H_1^0 - M_1^0)\rho_0(1 - F_0(\xi)) \tag{C.32}$$

C.6 Decomposition at local N^{p}LO

Since the local version of pseudopotential can be written as

$$\mathcal{V}_{loc}^{(n)}(r_1, r_2; r_3, r_4) = \left(W_1^{(n)} \hat{1}_\sigma \hat{1}_\tau + B_1^{(n)} \hat{1}_\tau \hat{P}_\sigma - H_1^{(n)} \hat{1}_\sigma \hat{P}_\tau - M_1^{(n)} \hat{P}_\sigma \hat{P}_\tau\right) \times \delta(\mathbf{r_{13}})\delta(\mathbf{r_{24}}) \left(\frac{1}{2}\right)^{n/2} \left[\mathbf{k}_{12}^n g_a(\mathbf{r_{12}})\right]. \tag{C.33}$$

When we recall the property

$$\left(\frac{1}{2i^2}\right)^{n/2} \nabla^n g_a(\mathbf{r}) = \left(-\frac{1}{a}\frac{\partial}{\partial a}\right)^p g_a(\mathbf{r}), \tag{C.34}$$

where $p = n/2$, we see that we get the next-leading-order terms directly from LO just by derivating the non-constant part. Thus, for the terms N^{p}LO, we get the

contributions of different S,T channels:

$$(0,0): \quad \frac{E}{A} = \frac{1}{32}(W_1^p - B_1^p + H_1^p - M_1^p)\rho_0 \left(-\frac{1}{a}\frac{\partial}{\partial a}\right)^p (-F_0(k_F a)) \tag{C.35}$$

$$(0,1): \quad \frac{E}{A} = \frac{3}{32}(W_1^p - B_1^p - H_1^p + M_1^p)\rho_0 \left(-\frac{1}{a}\frac{\partial}{\partial a}\right)^p F_0(k_F a) \tag{C.36}$$

$$(1,0): \quad \frac{E}{A} = \frac{1}{32}(W_1^p + B_1^p + H_1^p + M_1^p)\rho_0 \left(-\frac{1}{a}\frac{\partial}{\partial a}\right)^p F_0(k_F a) \tag{C.37}$$

$$(1,1): \quad \frac{E}{A} = \frac{9}{32}(W_1^p + B_1^p - H_1^p - M_1^p)\rho_0 \left(-\frac{1}{a}\frac{\partial}{\partial a}\right)^p (-F_0(k_F a)) \tag{C.38}$$

Appendix D

S,T decomposition for the zero-range 3-body interaction

Next the S,T decomposition for the 3-body interaction presented in Ref [85] is derived starting from the derivation of the expectation value of the interaction. Three-body terms can be written in our notation as

$$\begin{aligned}\mathcal{V}_{\overline{123}} = & u_0\delta(\mathbf{r_1}-\mathbf{r_2})\delta(\mathbf{r_2}-\mathbf{r_3}) \\ & +\frac{u_1}{2}\left(1+y_1\hat{P}^{\sigma}_{12}\right)\left(\mathbf{k}^{\dagger 2}_{12}\delta(\mathbf{r_1}-\mathbf{r_2})\delta(\mathbf{r_2}-\mathbf{r_3})+\delta(\mathbf{r_1}-\mathbf{r_2})\delta(\mathbf{r_2}-\mathbf{r_3})\mathbf{k}^2_{45}\right) \\ & +u_2\left(1+y_{21}\hat{P}^{\sigma}_{12}\right)\mathbf{k}^{\dagger}_{12}\delta(\mathbf{r_1}-\mathbf{r_2})\delta(\mathbf{r_2}-\mathbf{r_3})\mathbf{k}_{45} \\ & +u_2y_{22}\left(\hat{P}^{\sigma}_{13}+\hat{P}^{\sigma}_{23}\right)\mathbf{k}^{\dagger}_{12}\delta(\mathbf{r_1}-\mathbf{r_2})\delta(\mathbf{r_2}-\mathbf{r_3})\mathbf{k}_{45}. \end{aligned} \tag{D.1}$$

The corresponding expectation value is

$$\begin{aligned}E_x^{\overline{123}} = & \frac{1}{6}\sum_{\substack{\sigma_1\sigma_2\sigma_3\\ q_1q_2q_3}}\int \mathrm{d}^3r_1\mathrm{d}^3r_2\mathrm{d}^3r_3\mathrm{d}^3r_4\mathrm{d}^3r_5\mathrm{d}^3r_6\langle 123|v_x|456\rangle\times \\ & [\rho(r_4\sigma_4q_4,r_1\sigma_1q_1)\rho(r_5\sigma_5q_5,r_2\sigma_2q_2)\rho(r_6\sigma_6q_6,r_3\sigma_3q_3) \\ & -\rho(r_4\sigma_4q_4,r_1\sigma_1q_1)\rho(r_6\sigma_6q_6,r_2\sigma_2q_2)\rho(r_5\sigma_5q_5,r_3\sigma_3q_3) \\ & +\rho(r_5\sigma_5q_5,r_1\sigma_1q_1)\rho(r_6\sigma_6q_6,r_2\sigma_2q_2)\rho(r_4\sigma_4q_4,r_3\sigma_3q_3) \\ & -\rho(r_5\sigma_5q_5,r_1\sigma_1q_1)\rho(r_4\sigma_4q_4,r_2\sigma_2q_2)\rho(r_6\sigma_6q_6,r_3\sigma_3q_3) \\ & +\rho(r_6\sigma_6q_6,r_1\sigma_1q_1)\rho(r_4\sigma_4q_4,r_2\sigma_2q_2)\rho(r_5\sigma_5q_5,r_3\sigma_3q_3) \\ & -\rho(r_6\sigma_6q_6,r_1\sigma_1q_1)\rho(r_5\sigma_5q_5,r_2\sigma_2q_2)\rho(r_4\sigma_4q_4,r_3\sigma_3q_3)] \end{aligned} \tag{D.2}$$

where v_x refers to the different terms of the 3-body interaction. For example, the u_0 term of $v_{\overline{123}}$ produces the following energy in infinite homogeneous nuclear matter:

$$\begin{aligned}
E_{u_0} = &\sum_{\substack{\sigma_1\sigma_2\sigma_3\\ q_1q_2q_3}} \frac{1}{6}\int \mathrm{d}^3r_1\mathrm{d}^3r_2\mathrm{d}^3r_3\mathrm{d}^3r_4\mathrm{d}^3r_5\mathrm{d}^3r_6 u_0 \times \\
&\delta(r_1-r_4)\delta(r_2-r_5)\delta(r_3-r_6)\delta(r_4-r_5)\delta(r_5-r_6)\times \\
&\delta_{\sigma_1\sigma_4}\delta_{\sigma_2\sigma_5}\delta_{\sigma_3\sigma_6}\delta_{q_1,q_4}\delta_{q_2,q_5}\delta_{q_3,q_6}\times \\
&[\rho(r_4\sigma_4q_4, r_1\sigma_1q_1)\rho(r_5\sigma_5q_5, r_2\sigma_2q_2)\rho(r_6\sigma_6q_6, r_3\sigma_3q_3) \\
&-\rho(r_4\sigma_4q_4, r_1\sigma_1q_1)\rho(r_6\sigma_6q_6, r_2\sigma_2q_2)\rho(r_5\sigma_5q_5, r_3\sigma_3q_3) \\
&+\rho(r_5\sigma_5q_5, r_1\sigma_1q_1)\rho(r_6\sigma_6q_6, r_2\sigma_2q_2)\rho(r_4\sigma_4q_4, r_3\sigma_3q_3) \\
&-\rho(r_5\sigma_5q_5, r_1\sigma_1q_1)\rho(r_4\sigma_4q_4, r_2\sigma_2q_2)\rho(r_6\sigma_6q_6, r_3\sigma_3q_3) \\
&+\rho(r_6\sigma_6q_6, r_1\sigma_1q_1)\rho(r_4\sigma_4q_4, r_2\sigma_2q_2)\rho(r_5\sigma_5q_5, r_3\sigma_3q_3) \\
&-\rho(r_6\sigma_6q_6, r_1\sigma_1q_1)\rho(r_5\sigma_5q_5, r_2\sigma_2q_2)\rho(r_4\sigma_4q_4, r_3\sigma_3q_3)] \qquad \text{(D.3)}
\end{aligned}$$

$$\begin{aligned}
=&\frac{1}{6}\int \mathrm{d}^3r u_0 \delta(r_1-r_4)\delta(r_2-r_5)\delta(r_3-r_6)\delta(r_4-r_5)\delta(r_5-r_6) \\
&\Big[\rho_0(r_4,r_1)\rho_0(r_5,r_2)\rho_0(r_6,r_3) - \frac{1}{4}\rho_0(r_4,r_1)\rho_0(r_6,r_2)\rho_0(r_5,r_3) \\
&+\frac{1}{16}\rho_0(r_5,r_1)\rho_0(r_6,r_2)\rho_0(r_4,r_3) - \frac{1}{4}\rho_0(r_5,r_1)\rho_0(r_4,r_2)\rho_0(r_6,r_3) \\
&+\frac{1}{16}\rho_0(r_6,r_1)\rho_0(r_4,r_2)\rho_0(r_5,r_3) - \frac{1}{4}\rho_0(r_6,r_1)\rho_0(r_5,r_2)\rho_0(r_4,r_3)\Big] \qquad \text{(D.4)}
\end{aligned}$$

$$=\frac{1}{6}\int \mathrm{d}^3r u_0 \frac{3}{8}\rho_0(r)\rho_0(r)\rho_0(r) \qquad \text{(D.5)}$$

In our notation the other two components of the three-body interaction are

$$\begin{aligned}
\mathcal{V}_{\overline{132}} =&u_0\delta(\mathbf{r_1}-\mathbf{r_2})\delta(\mathbf{r_2}-\mathbf{r_3}) \\
&+\frac{u_1}{2}\left(1+y_1\hat{P}^\sigma_{13}\right)\left(\mathbf{k}^{*2}_{13}\delta(\mathbf{r_1}-\mathbf{r_2})\delta(\mathbf{r_2}-\mathbf{r_3}) + \delta(\mathbf{r_1}-\mathbf{r_2})\delta(\mathbf{r_2}-\mathbf{r_3})\mathbf{k}^2_{46}\right) \\
&+u_2\left(1+y_{21}\hat{P}^\sigma_{13}\right)\mathbf{k}^*_{13}\delta(\mathbf{r_1}-\mathbf{r_2})\delta(\mathbf{r_2}-\mathbf{r_3})\mathbf{k}_{46} \\
&+u_2y_{22}\left(\hat{P}^\sigma_{12}+\hat{P}^\sigma_{23}\right)\mathbf{k}^*_{13}\delta(\mathbf{r_1}-\mathbf{r_2})\delta(\mathbf{r_2}-\mathbf{r_3})\mathbf{k}_{46}. \qquad \text{(D.6)}
\end{aligned}$$

.

$P^{ST}_{a,b}$		(0,0)	(0,1)	(1,0)	(1,1)
u_0	1,2	0	$\frac{1}{32}u_0$	$\frac{1}{32}u_0$	0
$(\rho_0\rho_0)$	1,3	0	$\frac{1}{32}u_0$	$\frac{1}{32}u_0$	0
	2,3	0	$\frac{1}{32}u_0$	$\frac{1}{32}u_0$	0
u_1	1,2	0	$\frac{1}{64}(u_1 - u_1y_1)$	$\frac{1}{64}(u_1 + u_1y_1)$	0
$(\tau_0\rho_0)$	1,3	0	$\frac{1}{64}(u_1 + \frac{1}{2}u_1y_1)$	$\frac{1}{64}(u_1 - \frac{1}{2}u_1y_1)$	0
	2,3	0	$\frac{1}{64}(u_1 + \frac{1}{2}u_1y_1)$	$\frac{1}{64}(u_1 - \frac{1}{2}u_1y_1)$	0
u_2y_{21}	1,2	$\frac{1}{128}(u_2 - u_2y_{21})$	0	0	$\frac{1}{128}(9u_2 + 9u_2y_{21})$
$(\tau_0\rho_0)$	1,3	$\frac{1}{128}(\frac{1}{4}u_2 + \frac{1}{2}u_2y_{21})$	$\frac{1}{128}(\frac{15}{4}u_2 + 3u_2y_{21})$	$\frac{1}{128}(\frac{15}{4}u_2 + 3u_2y_{21})$	$\frac{1}{128}(\frac{9}{4}u_2 + \frac{3}{2}u_2y_{21})$
	2,3	$\frac{1}{128}(\frac{1}{4}u_2 + \frac{1}{2}u_2y_{21})$	$\frac{1}{128}(\frac{15}{4}u_2 + 3u_2y_{21})$	$\frac{1}{128}(\frac{15}{4}u_2 + 3u_2y_{21})$	$\frac{1}{128}(\frac{9}{4}u_2 + \frac{3}{2}u_2y_{21})$
u_2y_{22}	1,2	$\frac{1}{128}u_2y_{22}$	0	0	$\frac{3}{128}u_2y_{22}$
$(\tau_0\rho_0)$	1,3	$-\frac{1}{256}u_2y_{22}$	$-\frac{3}{128}u_2y_{22}$	$\frac{3}{64}u_2y_{22}$	$\frac{3}{256}u_2y_{22}$
	2,3	$-\frac{1}{256}u_2y_{22}$	$-\frac{3}{128}u_2y_{22}$	$\frac{3}{64}u_2y_{22}$	$\frac{3}{256}u_2y_{22}$

Table D.1: S,T-decomposition of 3-body $V_{\overline{123}}$ with respect to different pairs of particles 1, 2 and 3. The constants in the table must be multiplied by $\rho_0\rho_0$ or $\tau_0\rho_0$ (see the leftmost column).

$P^{ST}_{a,b}$		(0,0)	(0,1)	(1,0)	(1,1)
u_0,	1,2	0	$\frac{1}{32}u_0$	$\frac{1}{32}u_0$	0
$(\rho_0\rho_0)$	1,3	0	$\frac{1}{32}u_0$	$\frac{1}{32}u_0$	0
	2,3	0	$\frac{1}{32}u_0$	$\frac{1}{32}u_0$	0
u_1	1,2	0	$\frac{1}{64}(u_1+\frac{1}{2}u_1y_1)$	$\frac{1}{64}(u_1-\frac{1}{2}u_1y_1)$	0
$(\tau_0\rho_0)$	1,3	0	$\frac{1}{64}(u_1-u_1y_1)$	$\frac{1}{64}(u_1+u_1y_1)$	0
	2,3	0	$\frac{1}{64}(u_1+\frac{1}{2}u_1y_1)$	$\frac{1}{64}(u_1-\frac{1}{2}u_1y_1)$	0
u_2y_{21}	1,2	$\frac{1}{128}(\frac{1}{4}u_2+\frac{1}{2}u_2y_{21})$	$\frac{1}{128}(\frac{15}{4}u_2+3u_2y_{21})$	$\frac{1}{128}(\frac{15}{4}u_2+3u_2y_{21})$	$\frac{1}{128}(\frac{9}{4}u_2+\frac{3}{2}u_2y_{21})$
$(\tau_0\rho_0)$	1,3	$\frac{1}{128}(u_2-u_2y_{21})$	0	0	$\frac{1}{128}(9u_2+9u_2y_{21})$
	2,3	$\frac{1}{128}(\frac{1}{4}u_2+\frac{1}{2}u_2y_{21})$	$\frac{1}{128}(\frac{15}{4}u_2+3u_2y_{21})$	$\frac{1}{128}(\frac{15}{4}u_2+3u_2y_{21})$	$\frac{1}{128}(\frac{9}{4}u_2+\frac{3}{2}u_2y_{21})$
u_2y_{22}	1,2	$-\frac{1}{256}u_2y_{22}$	$-\frac{3}{128}u_2y_{22}$	$\frac{3}{64}u_2y_{22}$	$\frac{3}{256}u_2y_{22}$
$(\tau_0\rho_0)$	1,3	$\frac{1}{128}u_2y_{22}$	0	0	$\frac{3}{128}u_2y_{22}$
	2,3	$-\frac{1}{256}u_2y_{22}$	$-\frac{3}{128}u_2y_{22}$	$\frac{3}{64}u_2y_{22}$	$\frac{3}{256}u_2y_{22}$

Table D.2: S,T-decomposition of 3-body $V_{\overline{132}}$ with respect to different pairs of particles 1, 2 and 3. The constants in the table must be multiplied by $\rho_0\rho_0$ or $\tau_0\rho_0$ (see the leftmost column).

The last part of the three-body interaction, namely $V_{\overline{231}}$, is defined as

$$\mathcal{V}_{\overline{231}} = u_0\delta(\mathbf{r_1}-\mathbf{r_2})\delta(\mathbf{r_2}-\mathbf{r_3}) \tag{D.7}$$

$$+\frac{u_1}{2}\left(1+y_1\hat{P}^{\sigma}_{23}\right)\left(\mathbf{k}^{*2}_{23}\delta(\mathbf{r_1}-\mathbf{r_2})\delta(\mathbf{r_2}-\mathbf{r_3})+\delta(\mathbf{r_1}-\mathbf{r_2})\delta(\mathbf{r_2}-\mathbf{r_3})\mathbf{k}^{2}_{45}\right) \tag{D.8}$$

$$+u_2\left(1+y_{21}\hat{P}^{\sigma}_{23}\right)\mathbf{k}^{*}_{13}\delta(\mathbf{r_1}-\mathbf{r_2})\delta(\mathbf{r_2}-\mathbf{r_3})\mathbf{k}_{45} \tag{D.9}$$

$$+u_2y_{22}\left(\hat{P}^{\sigma}_{12}+\hat{P}^{\sigma}_{13}\right)\mathbf{k}^{*}_{23}\delta(\mathbf{r_1}-\mathbf{r_2})\delta(\mathbf{r_2}-\mathbf{r_3})\mathbf{k}_{45}. \tag{D.10}$$

	$P^{ST}_{a,b}$	(0,0)	(0,1)	(1,0)	(1,1)
u_0	1,2	0	$\frac{1}{32}u_0$	$\frac{1}{32}u_0$	0
$(\rho_0\rho_0)$	1,3	0	$\frac{1}{32}u_0$	$\frac{1}{32}u_0$	0
	2,3	0	$\frac{1}{32}u_0$	$\frac{1}{32}u_0$	0
u_1	1,2	0	$\frac{1}{64}(u_1+\frac{1}{2}u_1y_1)$	$\frac{1}{64}(u_1-\frac{1}{2}u_1y_1)$	0
$(\tau_0\rho_0)$	1,3	0	$\frac{1}{64}(u_1+\frac{1}{2}u_1y_1)$	$\frac{1}{64}(u_1-\frac{1}{2}u_1y_1)$	0
	2,3	0	$\frac{1}{64}(u_1-u_1y_1)$	$\frac{1}{64}(u_1+u_1y_1)$	0
u_2y_{21}	1,2	$\frac{1}{128}(\frac{1}{4}u_2+\frac{1}{2}u_2y_{21})$	$\frac{1}{128}(\frac{15}{4}u_2+3u_2y_{21})$	$\frac{1}{128}(\frac{15}{4}u_2+3u_2y_{21})$	$\frac{1}{128}(\frac{9}{4}u_2+\frac{3}{2}u_2y_{21})$
$(\tau_0\rho_0)$	1,3	$\frac{1}{128}(\frac{1}{4}u_2+\frac{1}{2}u_2y_{21})$	$\frac{1}{128}(\frac{15}{4}u_2+3u_2y_{21})$	$\frac{1}{128}(\frac{15}{4}u_2+3u_2y_{21})$	$\frac{1}{128}(\frac{9}{4}u_2+\frac{3}{2}u_2y_{21})$
	2,3	$\frac{1}{128}(u_2-u_2y_{21})$	0	0	$\frac{1}{128}(9u_2+9u_2y_{21})$
u_2y_{22}	1,2	$-\frac{1}{256}u_2y_{22}$	$-\frac{3}{128}u_2y_{22}$	$\frac{3}{64}u_2y_{22}$	$\frac{3}{256}u_2y_{22}$
$(\tau_0\rho_0)$	1,3	$-\frac{1}{256}u_2y_{22}$	$-\frac{3}{128}u_2y_{22}$	$\frac{3}{64}u_2y_{22}$	$\frac{3}{256}u_2y_{22}$
	2,3	$\frac{1}{128}u_2y_{22}$	0	0	$\frac{3}{128}u_2y_{22}$

Table D.3: S,T-decomposition of 3-body $V_{\overline{231}}$ with respect to different pairs of particles 1, 2 and 3. The constants in the table must be multiplied by $\rho_0\rho_0$ or $\tau_0\rho_0$ (see the leftmost column).

Appendix E

S,T decomposition of the zero-range 4-body interaction

E.1 Energy

The zero-range 4-body interaction is defined as

$$\hat{V}_4 = v_0 \left(\delta_{r_1,r_3}\delta_{r_2,r_3}\delta_{r_3,r_4} + \delta_{r_1,r_2}\delta_{r_3,r_2}\delta_{r_2,r_4} + ...\right) \tag{E.1}$$

and altogether there are

$$\binom{6}{3} = \frac{6 \cdot 5 \cdot 4 \cdot 3!}{3!(6-3)!} = 20 \tag{E.2}$$

terms. In addition, there are 24 different terms coming from the constractions (here we denote $x_i = r_i, \sigma_i, q_i$):

$$
\begin{aligned}
&\langle c_1^\dagger c_2^\dagger c_3^\dagger c_4^\dagger c_8 c_7 c_6 c_5 \rangle \\
&\quad = \quad \rho(x_5,x_1)\rho(x_6,x_2)\rho(x_7,x_3)\rho(x_8,x_4) \\
&\qquad +\rho(x_5,x_1)\rho(x_6,x_2)\rho(x_8,x_3)\rho(x_7,x_4) \\
&\qquad +\rho(x_5,x_1)\rho(x_7,x_2)\rho(x_8,x_3)\rho(x_6,x_4) \\
&\qquad +\rho(x_5,x_1)\rho(x_7,x_2)\rho(x_6,x_3)\rho(x_8,x_4) \\
&\qquad +\rho(x_5,x_1)\rho(x_8,x_2)\rho(x_6,x_3)\rho(x_7,x_4) \\
&\qquad +\rho(x_5,x_1)\rho(x_8,x_2)\rho(x_7,x_3)\rho(x_6,x_4) \\
&\\
&\qquad +\rho(x_6,x_1)\rho(x_5,x_2)\rho(x_8,x_3)\rho(x_7,x_4) \\
&\qquad +\rho(x_6,x_1)\rho(x_5,x_2)\rho(x_7,x_3)\rho(x_8,x_4) \\
&\qquad +\rho(x_6,x_1)\rho(x_7,x_2)\rho(x_5,x_3)\rho(x_8,x_4) \\
&\qquad +\rho(x_6,x_1)\rho(x_7,x_2)\rho(x_8,x_3)\rho(x_5,x_4) \\
&\qquad +\rho(x_6,x_1)\rho(x_8,x_2)\rho(x_7,x_3)\rho(x_5,x_4) \\
&\qquad +\rho(x_6,x_1)\rho(x_8,x_2)\rho(x_5,x_3)\rho(x_7,x_4) \\
&\\
&\qquad +\rho(x_7,x_1)\rho(x_5,x_2)\rho(x_6,x_3)\rho(x_8,x_4) \\
&\qquad +\rho(x_7,x_1)\rho(x_5,x_2)\rho(x_8,x_3)\rho(x_6,x_4) \\
&\qquad +\rho(x_7,x_1)\rho(x_6,x_2)\rho(x_8,x_3)\rho(x_5,x_4) \\
&\qquad +\rho(x_7,x_1)\rho(x_6,x_2)\rho(x_5,x_3)\rho(x_8,x_4) \\
&\qquad +\rho(x_7,x_1)\rho(x_8,x_2)\rho(x_5,x_3)\rho(x_6,x_4) \\
&\qquad +\rho(x_7,x_1)\rho(x_8,x_2)\rho(x_6,x_3)\rho(x_5,x_4) \\
&\\
&\qquad +\rho(x_8,x_1)\rho(x_5,x_2)\rho(x_7,x_3)\rho(x_6,x_4) \\
&\qquad +\rho(x_8,x_1)\rho(x_5,x_2)\rho(x_6,x_3)\rho(x_7,x_4) \\
&\qquad +\rho(x_8,x_1)\rho(x_6,x_2)\rho(x_5,x_3)\rho(x_7,x_4) \\
&\qquad +\rho(x_8,x_1)\rho(x_6,x_2)\rho(x_7,x_3)\rho(x_5,x_4) \\
&\qquad +\rho(x_8,x_1)\rho(x_7,x_2)\rho(x_6,x_3)\rho(x_5,x_4) \\
&\qquad +\rho(x_8,x_1)\rho(x_7,x_2)\rho(x_5,x_3)\rho(x_6,x_4) \qquad \text{(E.3)} \\
&\\
&=: \quad \mathrm{D}(x_1,x_2,...,x_8) \qquad \text{(E.4)}
\end{aligned}
$$

In general for the 4-body system, the energy is calculated as

$$E = \frac{1}{4!}\sum_{\sigma q}\int \mathrm{d}^3r_1\mathrm{d}^3r_2...\mathrm{d}^3r_8\ v_0\delta(r_1-r_5)\delta(r_2-r_6)\delta(r_3-r_7)\delta(r_4-r_8)\times \\ \langle x_1x_2x_3x_4|\hat{V}_4|x_5x_6x_7x_8\rangle \times \mathrm{D}(x_1,x_2,...,x_8) \tag{E.5}$$

and now, for the zero-range interaction of Equation (E.1) it is

$$E = \frac{1}{256}\int \mathrm{d}^3r\ v_0\rho_0\rho_0\rho_0\rho_0\rho_0, \tag{E.6}$$

which is calculated by using Wolfram Mathematica.

E.2 S,T decomposition

The expectation value of $\hat{V}_4\hat{1}$ we get directly from the calculation of energy, namely

$$\langle\hat{V}_4\hat{1}\rangle = \langle\hat{V}_4\rangle = E = \frac{1}{256}\int \mathrm{d}^3r\ v_0\rho_0\rho_0\rho_0\rho_0\rho_0. \tag{E.7}$$

Next we need the expectation value of $\hat{V}_4\hat{\mathrm{P}}_\sigma$, that is

$$\begin{aligned}\langle\hat{V}_4\hat{\mathrm{P}}^\sigma_{12}\rangle =& \frac{1}{24}\sum_{q\sigma}\int \mathrm{d}^3r_1\mathrm{d}^3r_2...\mathrm{d}^3r_8\ v_0\delta(r_1-r_5)\delta(r_2-r_6)\delta(r_3-r_7)\times \\ & \delta(r_4-r_8)\delta(r_5-r_7)\delta(r_6-r_7)\delta(r_7-r_8)\times \mathrm{D}(x_1,...,x_8)\times \\ & \delta_{\sigma_1,\sigma_6}\delta_{\sigma_2,\sigma_5}\delta_{\sigma_3,\sigma_7}\delta_{\sigma_4,\sigma_8}\delta_{q_1,q_5}\delta_{q_2,q_6}\delta_{q_3,q_7}\delta_{q_4,q_8} \\ =& 0\end{aligned} \tag{E.8}$$

Since $\hat{P}^x\hat{P}^\sigma\hat{P}^\tau = -1$, and $\hat{P}^x = \hat{1}$ holds for zero-range interactions without any gradients, we get $\hat{P}^\tau = -\hat{P}^\sigma$, and all the rest of components we need for the S,T decomposition are provided directly:

$$\langle\hat{V}_4\hat{\mathrm{P}}^\tau_{12}\rangle = -\langle\hat{V}_4\hat{\mathrm{P}}^\sigma_{12}\rangle = 0 \tag{E.9}$$

$$\langle\hat{V}_4\hat{\mathrm{P}}^\sigma_{12}\hat{\mathrm{P}}^\tau_{12}\rangle = -\langle\hat{V}_4\hat{\mathrm{P}}^\sigma_{12}\hat{\mathrm{P}}^\sigma_{12}\rangle = -\frac{1}{256}\int \mathrm{d}^3r\ v_0\rho_0\rho_0\rho_0\rho_0\rho_0 \tag{E.10}$$

We recall that

$$\hat{P}_{S=0} = \frac{1}{2}\left(\hat{1}-\hat{P}_\sigma\right) \tag{E.11}$$

$$\hat{P}_{S=1} = \frac{1}{2}\left(\hat{1}+\hat{P}_\sigma\right) \tag{E.12}$$

$$\hat{P}_{T=0} = \frac{1}{2}\left(\hat{1}-\hat{P}_\tau\right) \tag{E.13}$$

$$\hat{P}_{T=1} = \frac{1}{2}\left(\hat{1}+\hat{P}_\tau\right) \tag{E.14}$$

Table E.1: ST decomposition of EOS for projections on particles 1 and 2.

S,T	E/A
0,0	0
0,1	$\frac{1}{512}v_0\rho_0^3$
1,0	$\frac{1}{512}v_0\rho_0^3$
1,1	0

Table E.2: The full ST decomposition of EOS in INM.

S,T	E/A
0,0	0
0,1	$\frac{5}{128}v_0\rho_0^3$
1,0	$\frac{5}{128}v_0\rho_0^3$
1,1	0

and since $\hat{P}_\tau = -\hat{P}_\sigma$, we get

$$\hat{P}_{S=0}\hat{P}_{T=0} = \frac{1}{4}\left(\hat{1} - \hat{P}_\sigma^2\right) = 0 \tag{E.15}$$

$$\hat{P}_{S=0}\hat{P}_{T=1} = \frac{1}{2}\left(\hat{1} - \hat{P}_\sigma\right) \tag{E.16}$$

$$\hat{P}_{S=1}\hat{P}_{T=0} = \frac{1}{2}\left(\hat{1} + \hat{P}_\sigma\right) \tag{E.17}$$

$$\hat{P}_{S=1}\hat{P}_{T=1} = \frac{1}{4}\left(\hat{1} - \hat{P}_\sigma^2\right) = 0. \tag{E.18}$$

The equation of state, $E/A = \mathcal{E}/\rho_0$, where $E = \int \mathrm{d}^3 r\, \mathcal{E}$, follows from that and the results are shown in Table E.1. The final S,T decomposition of 4-body interaction (E.1) is easy to get. Since the full interaction is a sum of delta terms, which all give exactly the same contribution, we have to just multiply the contribution with the number of terms (20). In addition, in principle we should also derive the results from projection on the particles $(1,3)$, $(1,4)$, $(2,3)$ and so on, and finally take the average of them, but this is now trivial since the contributions are exactly the same, and we would only multiply by 6 and divide by 6. Thus, the only thing we have to do, is to multiply by 20, and the final results can be found in Table E.2.

Bibliography

[1] G. Coló. Density functional theory (DFT) for atomic nuclei: a simple introduction, 2018.

[2] Henri Becquerel. Sur les radiations émises par phosphorescence. *Comptes Rendus*, 122:420–421, 1896.

[3] Joseph John Thomson. Cathode rays. *Proceedings of the Royal Institution of Great Britain*, XV:419–432, 1897.

[4] E. Rutherford. VIII. Uranium radiation and the electrical conduction produced by it. *The London, Edinburgh, and Dublin Philosophical Magazine and Journal of Science*, 47(284):109–163, 1899.

[5] E. Rutherford. XV. The magnetic and electric deviation of the easily absorbed rays from radium. *The London, Edinburgh, and Dublin Philosophical Magazine and Journal of Science*, 5(26):177–187, 1903.

[6] E. Rutherford. The scattering of α and β particles by matter and the structure of the atom. *Philosophical Magazine*, 6(21), 1911.

[7] E. Rutherford. XIX. Retardation of the α particle from radium in passing through matter. *The London, Edinburgh, and Dublin Philosophical Magazine and Journal of Science*, 12(68):134–146, 1906.

[8] L. Meitner. Über die Zerstreuung der Alphastrahlen. *Physikalische Zeitschrift*, 8:489–491, 1907.

[9] Hans Geiger. On the scattering of α-particles by matter. *Proceedings of the Royal Society A*, 81(546):174–177, 1908.

[10] Hans Geiger and Ernest Marsden. On the diffuse reflection of the α-particles. *Proceedings of the Royal Society A*, 82(557):495, 1909.

[11] A. S. Eddington. The internal constitution of the stars. *The Scientific Monthly*, 11(4):297–303, 1920.

[12] A Einstein. Ist die Trägheit eines Körpers von seinem Energieinhalt abhängig? *Annalen der Physik*, 18(13):639–643, 1905.

[13] James Chadwick. The existence of a neutron. *Proceedings of the Royal Society A*, 136(830):692–708, 1932.

[14] W. Bothe and H. Becker. Künstliche Erregung von Kern-γ-Strahlen. *Zeitschrift für Physik*, 66:289, 1930.

[15] I. Curie. Sur le rayonnement γ nucléaire excité dans le glucinium et dans le lithium par leas rayons α du polonium. *Comptes Rendus*, 193:1412, 1931.

[16] D. Iwanenko. The neutron hypothesis. *Nature*, 129:798, 1932.

[17] Hideki Yukawa. On the Interaction of Elementary Particles I. *Proc. Phys. Math. Soc. Jap.*, 17:48–57, 1935. [Prog. Theor. Phys. Suppl.1,1(1935)].

[18] C. F. von Weizsäcker. Zur Theorie der Kernmassen. *Zeitschrift für Physik*, 96(7-8):431–458, 1935.

[19] E. Gapon and D. Iwanenko. Zur Bestimmung der isotopenzahl. *Die Naturwissenschaften*, 20:792–793, 1932.

[20] Maria Goeppert Mayer. On closed shells in nuclei. II. *Phys. Rev.*, 75:1969–1970, Jun 1949.

[21] Otto Haxel, J. Hans D. Jensen, and Hans E. Suess. On the "magic numbers" in nuclear structure. *Phys. Rev.*, 75:1766–1766, Jun 1949.

[22] G. Gamow. Zur Quantentheorie des Atomkernes. *Zeitschrift für Physik*, 51(3):204–212, Mar 1928.

[23] Enrico Fermi. Tentativo di una Teoria Dei Raggi β. *Il Nuovo Cimento*, 11(1), 1934.

[24] E. Fermi. Versuch einer Theorie der β-Strahlen. I. *Zeitschrift für Physik*, 88(3):161–177, Mar 1934.

[25] E. Rutherford. XV. The magnetic and electric deviation of the easily absorbed rays from radium. *The London, Edinburgh, and Dublin Philosophical Magazine and Journal of Science*, 5(26):177–187, 1903.

[26] Jouni Suhonen. *From Nucleons to Nucleus*. Theoretical and Mathematical Physics. Springer, Berlin, Germany, 2007.

[27] R Machleidt and I Slaus. The nucleon-nucleon interaction. *Journal of Physics G: Nuclear and Particle Physics*, 27(5):R69–R108, Mar 2001.

[28] Robert Roth, Joachim Langhammer, Sven Binder, and Angelo Calci. New horizons in ab initio nuclear structure theory. *Journal of Physics: Conference Series*, 403:012020, Dec 2012.

[29] P. Moller, J.R. Nix, W.D. Myers, and W.J. Swiatecki. Nuclear ground-state masses and deformations. *Atomic Data and Nuclear Data Tables*, 59(2):185 – 381, 1995.

[30] Michael Bender, Paul-Henri Heenen, and Paul-Gerhard Reinhard. Self-consistent mean-field models for nuclear structure. *Rev. Mod. Phys.*, 75:121–180, Jan 2003.

[31] George E. P. Box. Science and statistics. *Journal of the American Statistical Association*, 71(356):791–799, 1976.

[32] The Editors. Editorial: Uncertainty estimates. *Phys. Rev. A*, 83:040001, Apr 2011.

[33] Enhancing the interaction between nuclear experiment and theory through information and statistics (ISNET). *Journal of Physics G: Nuclear and Particle Physics*, 42(3), Feb 2015.

[34] J Dobaczewski, W Nazarewicz, and P-G Reinhard. Error estimates of theoretical models: a guide. *Journal of Physics G: Nuclear and Particle Physics*, 41(7):074001, may 2014.

[35] Peter Ring and Peter Schuck. *The Nuclear Many-Body Problem*. Springer, 2004.

[36] K. Bennaceur and J. Dobaczewski. Coordinate-space solution of the Skyrme-Hartree-Fock-Bogolyubov equations within spherical symmetry. the program HFBRAD (v1.00). *Computer Physics Communications*, 168(2):96 – 122, 2005.

[37] R. Navarro Perez, N. Schunck, R.-D. Lasseri, C. Zhang, and J. Sarich. Axially deformed solution of the Skyrme-Hartree-Fock-Bogolyubov equations using the transformed harmonic oscillator basis (III) HFBTHO (v3.00): A new version of the program. *Computer Physics Communications*, 220:363 – 375, 2017.

[38] N. Schunck, J. Dobaczewski, W. Satula, P. Baczyk, J. Dudek, Y. Gao, M. Konieczka, K. Sato, Y. Shi, X.B. Wang, and T.R. Werner. Solution of the Skyrme-Hartree-Fock-Bogolyubov equations in the Cartesian deformed

harmonic-oscillator basis. (VIII) HFODD (v2.73y): A new version of the program. *Computer Physics Communications*, 216:145 – 174, 2017.

[39] Markus Kortelainen. HFBTEMP. *Unpublished*.

[40] P. Hohenberg and W. Kohn. Inhomogeneous electron gas. *Phys. Rev.*, 136:B864–B871, Nov 1964.

[41] W. Kohn and L. J. Sham. Self-consistent equations including exchange and correlation effects. *Phys. Rev.*, 140:A1133–A1138, Nov 1965.

[42] K. Hebeler, J.D. Holt, J. Menéndez, and A. Schwenk. Nuclear forces and their impact on neutron-rich nuclei and neutron-rich matter. *Annual Review of Nuclear and Particle Science*, 65(1):457–484, Oct 2015.

[43] D.M. Brink and E. Boeker. Effective interactions for Hartree-Fock calculations. *Nuclear Physics A*, 91(1):1 – 26, 1967.

[44] J. Dechargé and D. Gogny. Hartree-Fock-Bogolyubov calculations with the $D1$ effective interaction on spherical nuclei. *Phys. Rev. C*, 21:1568–1593, Apr 1980.

[45] D. Davesne, J. Navarro, J. Meyer, K. Bennaceur, and A. Pastore. Two-body contributions to the effective mass in nuclear effective interactions. *Physical Review C*, 97(4), Apr 2018.

[46] J. Dobaczewski, M. V. Stoitsov, W. Nazarewicz, and P.-G. Reinhard. Particle-number projection and the density functional theory. *Phys. Rev. C*, 76:054315, Nov 2007.

[47] T. Duguet, M. Bender, K. Bennaceur, D. Lacroix, and T. Lesinski. Particle-number restoration within the energy density functional formalism: Nonviability of terms depending on noninteger powers of the density matrices. *Phys. Rev. C*, 79:044320, Apr 2009.

[48] W. Satuła and J. Dobaczewski. Simple regularization scheme for multireference density functional theories. *Phys. Rev. C*, 90:054303, Nov 2014.

[49] T. H. R. Skyrme. CVII. The nuclear surface. *The Philosophical Magazine: A Journal of Theoretical Experimental and Applied Physics*, 1(11):1043–1054, 1956.

[50] M. Beiner, H. Flocard, Nguyen Van Giai, and P. Quentin. Nuclear ground-state properties and self-consistent calculations with the Skyrme interaction: (I). Spherical description. *Nuclear Physics A*, 238(1):29 – 69, 1975.

[51] D. Vautherin and D. M. Brink. Hartree-Fock Calculations with Skyrme's Interaction. I. Spherical Nuclei. *Phys. Rev. C*, 5:626–647, Mar 1972.

[52] E. Chabanat, P. Bonche, P. Haensel, J. Meyer, and R. Schaeffer. A Skyrme parametrization from subnuclear to neutron star densities. *Nuclear Physics A*, 627(4):710 – 746, 1997.

[53] M. Bender, T. Duguet, and D. Lacroix. Particle-number restoration within the energy density functional formalism. *Phys. Rev. C*, 79:044319, Apr 2009.

[54] L M Robledo. Remarks on the use of projected densities in the density-dependent part of Skyrme or Gogny functionals. *Journal of Physics G: Nuclear and Particle Physics*, 37(6):064020, Apr 2010.

[55] M. Kortelainen, T. Lesinski, J. Moré, W. Nazarewicz, J. Sarich, N. Schunck, M. V. Stoitsov, and S. Wild. Nuclear energy density optimization. *Phys. Rev. C*, 82:024313, Aug 2010.

[56] M. Kortelainen, J. McDonnell, W. Nazarewicz, P.-G. Reinhard, J. Sarich, N. Schunck, M. V. Stoitsov, and S. M. Wild. Nuclear energy density optimization: Large deformations. *Phys. Rev. C*, 85:024304, Feb 2012.

[57] M. Kortelainen, J. McDonnell, W. Nazarewicz, E. Olsen, P.-G. Reinhard, J. Sarich, N. Schunck, S. M. Wild, D. Davesne, J. Erler, and A. Pastore. Nuclear energy density optimization: Shell structure. *Phys. Rev. C*, 89:054314, May 2014.

[58] E. Perlińska, S. G. Rohoziński, J. Dobaczewski, and W. Nazarewicz. Local density approximation for proton-neutron pairing correlations: Formalism. *Phys. Rev. C*, 69:014316, Jan 2004.

[59] B. G. Carlsson, J. Dobaczewski, and M. Kortelainen. Local nuclear energy density functional at next-to-next-to-next-to-leading order. *Phys. Rev. C*, 78:044326, Oct 2008.

[60] F. Raimondi, B. G. Carlsson, and J. Dobaczewski. Effective pseudopotential for energy density functionals with higher-order derivatives. *Phys. Rev. C*, 83:054311, May 2011.

[61] J Dobaczewski, K Bennaceur, and F Raimondi. Effective theory for low-energy nuclear energy density functionals. *Journal of Physics G: Nuclear and Particle Physics*, 39(12):125103, Oct 2012.

[62] F Raimondi, K Bennaceur, and J Dobaczewski. Nonlocal energy density functionals for low-energy nuclear structure. *Journal of Physics G: Nuclear and Particle Physics*, 41(5):055112, Mar 2014.

[63] K Bennaceur, A Idini, J Dobaczewski, P Dobaczewski, M Kortelainen, and F Raimondi. Nonlocal energy density functionals for pairing and beyond-mean-field calculations. *Journal of Physics G: Nuclear and Particle Physics*, 44(4):045106, Mar 2017.

[64] Harry J Lipkin. Collective motion in many-particle systems: Part 1. The violation of conservation laws. *Annals of Physics*, 9(2):272 – 291, 1960.

[65] Yukihisa Nogami. Improved superconductivity approximation for the pairing interaction in nuclei. *Phys. Rev.*, 134:B313–B321, Apr 1964.

[66] G. Fricke, C. Bernhardt, K. Heilig, L.A. Schaller, L. Schellenberg, E.B. Shera, and C.W. Dejager. Nuclear ground state charge radii from electromagnetic interactions. *Atomic Data and Nuclear Data Tables*, 60(2):177 – 285, 1995.

[67] W. Satuła, J. Dobaczewski, and W. Nazarewicz. Odd-even staggering of nuclear masses: Pairing or shape effect? *Phys. Rev. Lett.*, 81:3599–3602, Oct 1998.

[68] H. Häkkinen, J. Kolehmainen, M. Koskinen, P. O. Lipas, and M. Manninen. Universal shapes of small fermion clusters. *Phys. Rev. Lett.*, 78:1034–1037, Feb 1997.

[69] G. Baardsen, A. Ekström, G. Hagen, and M. Hjorth-Jensen. Coupled-cluster studies of infinite nuclear matter. *Phys. Rev. C*, 88:054312, Nov 2013.

[70] B. D. Day. Current state of nuclear matter calculations. *Rev. Mod. Phys.*, 50:495–521, Jul 1978.

[71] B.D. Day and John G. Zabolitzky. Coupled-cluster calculation for nuclear matter and comparison with the hole-line expansion. *Nuclear Physics A*, 366(2):221 – 244, 1981.

[72] W.H. Dickhoff and C. Barbieri. Self-consistent Green's function method for nuclei and nuclear matter. *Progress in Particle and Nuclear Physics*, 52(2):377 – 496, 2004.

[73] R. Navarro Pérez, N. Schunck, A. Dyhdalo, R. J. Furnstahl, and S. K. Bogner. Microscopically based energy density functionals for nuclei using the density matrix expansion. II. Full optimization and validation. *Phys. Rev. C*, 97:054304, May 2018.

[74] Gianluca Salvioni. *Model nuclear energy density functionals derived from ab initio calculations*. University of Jyväskylä, 2019.

[75] Ifan Hughes and Thomas Hase. *Measurements and Their Uncertainties : A Practical Guide to Modern Error Analysis.* OUP Oxford, 2010.

[76] Stefan M Wild, Jason Sarich, and Nicolas Schunck. Derivative-free optimization for parameter estimation in computational nuclear physics. *Journal of Physics G: Nuclear and Particle Physics*, 42(3):034031, Feb 2015.

[77] Karim Bennaceur. FINRES_4. *Unpublished*.

[78] T. Lesinski, K. Bennaceur, T. Duguet, and J. Meyer. Isovector splitting of nucleon effective masses, ab initio benchmarks and extended stability criteria for Skyrme energy functionals. *Phys. Rev. C*, 74:044315, Oct 2006.

[79] N. Schunck, J. Dobaczewski, J. McDonnell, J. Moré, W. Nazarewicz, J. Sarich, and M. V. Stoitsov. One-quasiparticle states in the nuclear energy density functional theory. *Phys. Rev. C*, 81:024316, Feb 2010.

[80] V. Hellemans, A. Pastore, T. Duguet, K. Bennaceur, D. Davesne, J. Meyer, M. Bender, and P.-H. Heenen. Spurious finite-size instabilities in nuclear energy density functionals. *Phys. Rev. C*, 88:064323, Dec 2013.

[81] M. Martini, A. De Pace, and K. Bennaceur. Spurious finite-size instabilities with Gogny-type interactions. *The European Physical Journal A*, 55(9), Sep 2019.

[82] W. Nazarewicz. Challenges in nuclear structure theory. *Journal of Physics G: Nuclear and Particle Physics*, 43:044002, 2016.

[83] L. F. Richardson and J. A. Gaunt. VIII. The deferred approach to the limit. *Phil. Trans. R. Soc. Lond. A*, 226:299, Jan 1927.

[84] M. Wang, G. Audi, A.H. Wapstra, F.G. Kondev, M. MacCormick, X. Xu, and B. Pfeiffer. The AME2012 atomic mass evaluation. *Chinese Physics C*, 36(12):1603–2014, Dec 2012.

[85] J. Sadoudi, T. Duguet, J. Meyer, and M. Bender. Skyrme functional from a three-body pseudopotential of second order in gradients: Formalism for central terms. *Phys. Rev. C*, 88:064326, Dec 2013.

ORIGINAL PAPERS

I

UNCERTAINTY PROPAGATION WITHIN THE UNEDF MODELS

by

T. Haverinen and M. Kortelainen

J. Phys. G: Nucl. Part. Phys. 44, 044008 (2017)

https://doi.org/10.1088/1361-6471/aa5e07

Uncertainty propagation within the UNEDF models

T. Haverinen[1,2], **M. Kortelainen**[2,1]

[1] Helsinki Institute of Physics, P.O. Box 64, FI-00014 University of Helsinki, Finland
[2] Department of Physics, P.O. Box 35 (YFL), University of Jyvaskyla, FI-40014 Jyvaskyla, Finland

E-mail: tiia.k.haverinen@student.jyu.fi, markus.kortelainen@jyu.fi

Abstract. The parameters of the nuclear energy density have to be adjusted to experimental data. As a result they carry certain uncertainty which then propagates to calculated values of observables. In the present work we quantify the statistical uncertainties of binding energies, proton quadrupole moments, and proton matter radius for three UNEDF Skyrme energy density functionals by taking advantage of the knowledge of the model parameter uncertainties. We find that the uncertainty of UNEDF models increases rapidly when going towards proton or neutron rich nuclei. We also investigate the impact of each model parameter on the total error budget.

Keywords: Skyrme energy density functional, uncertainty quantification, error propagation

1. Introduction

Among numerous different nuclear many-body models, the nuclear density functional theory (DFT) [1] is the only one, which can describe nuclear properties microscopically throughout the entire nuclear landscape [2]. The cornerstone of the nuclear DFT is the energy density functional (EDF), which incorporates nucleonic interactions and many-body correlations into a functional constructed from one-body densities and currents. The Skyrme EDF, for its part, relies on local nuclear densities and currents, together with a set of coupling constants as model parameters. Due to the lack of suitable *ab-initio* methods to compute these coupling constants, they must be determined through adjustment to experimental data, such as nuclear binding energies and radii.

During the last couple of decades, numerous Skyrme parameterizations have been obtained from various adjustment schemes, see e.g. the list in [3]. The standard Skyrme EDF has proven to be quite successful, but its limitations have also become apparent. For the sake of better accuracy, more reliable predictive power, and for a spectroscopic-quality level, one has to move beyond the the standard Skyrme EDF [4,5]. Nevertheless, by studying the performance and predictive power of the present EDFs,

valuable information can be obtained which can be used and applied in the work towards forthcoming novel EDFs [6].

As with every model parameters optimization procedure, one of the main challenges is to find the best set of input observables, in order to constrain the parameter space of the model. The predictive power of the EDF highly depends on the input data. Therefore, a comprehensive analysis of the impact of input observables on the parameter space and on the model predictions provides valuable information. Naturally, the nuclear bulk properties are crucial for general constraining and the data especially relating to odd-mass nuclei is important for spectroscopical properties [7]. Binding energies, surface thickness, charge radii, single particle energies and energies of giant resonances are essential properties of nuclei, and used in various EDF optimization schemes.

All model predictions contain several sources of uncertainties. Roughly speaking, these can be divided into two main categories, the systematic model uncertainties and the statistical model uncertainties. The systematic model uncertainty stems from sources like the model deficiency and input data bias. The statistical uncertainty results from the model parameter optimization process.

Despite the importance of uncertainty analysis, error estimate is a rather novel topic in low-energy nuclear physics [8]. During the last few years, efforts have been made to improve this situation in the EDF calculations [9–13], as well as in the domain of *ab-initio* calculations [14, 15]. Various statistical tools have been applied from traditional methods to more modern ones (e.g. the Bayesian framework [16–19]). Apart from the fact that uncertainty quantification is an important topic in itself, with the help of statistical analysis, information about shortcomings of theoretical models and optimization procedures is also obtained.

In this work, we present the quantitative results for statistical uncertainty propagation for three existing UNEDF Skyrme EDF models: the UNEDF0 [20], the UNEDF1 [21], and the UNEDF2 [22]. In particular, we quantify contributions from the model parameters to the total error budget of binding energy in isotopic and isotonic chains of nuclei. By analyzing the obtained information we may recognize potential frailties of these models. In the present study, two-neutron separation energies are also considered, as well as proton quadrupole moments and proton matter radii, and the related uncertainties are worked out. In addition to even-even nuclei, uncertainties related to odd-even nuclei are studied.

This paper is organized as follows. In Sec. 2 we briefly review the theoretical framework related to the topic: Namely, the Skyrme energy density functional and the error propagation. In Sec. 3 we present our results and, finally, conclusions and future perspectives are given in Sec. 4.

2. Theoretical framework

2.1. Skyrme energy density functional

The UNEDF models are based on the Skyrme energy density. The ground state of a nucleus is determined in the framework of the Hartree-Fock-Bogoliubov (HFB) theory [1,23]. The three parameterizations considered in this work, UNEDF0, UNEDF1 and UNEDF2, were adjusted on a experimental data consisting of binding energies for deformed and spherical nuclei, odd-even mass differences, and charge radii. In addition, latter parameterizations include data on fission isomer excitation energies and single-particle energies.

The Skyrme EDF has a form of local energy density functional, stemming from Skyrme energy density. It can be written as

$$E = \int \mathrm{d}^3\mathbf{r}\mathcal{H}(\mathbf{r}) \tag{1}$$

$$= \int \mathrm{d}^3\mathbf{r}\left[\mathcal{E}^{\mathrm{kin}}(\mathbf{r}) + \chi_0(\mathbf{r}) + \chi_1(\mathbf{r}) + \widetilde{\chi}(\mathbf{r}) + \mathcal{E}^{\mathrm{Coul}}(\mathbf{r})\right] . \tag{2}$$

where the energy density $\mathcal{H}(\mathbf{r})$ is a time-even, scalar, isoscalar and real function of local densities and their derivatives. In the equation (2), the Skyrme energy density has been split into kinetic term $\mathcal{E}^{\mathrm{kin}}(\mathbf{r})$, isoscalar ($t = 0$) and isovector ($t = 1$) particle-hole Skyrme energy densities $\chi_t(\mathbf{r})$, pairing energy density $\widetilde{\chi}(\mathbf{r})$ and Coulomb term $\mathcal{E}^{\mathrm{Coul}}(\mathbf{r})$. The time-even part of the isoscalar and isovector particle-hole Skyrme energy densities is given by

$$\chi_t(\mathbf{r}) = C_t^{\rho^2}\rho_t^2 + C_t^{\rho\tau}\rho_t\tau_t + C_t^{JJ}\sum_{\mu\nu}\mathbf{J}_{\mu\nu,t}\mathbf{J}_{\mu\nu,t} + C_t^{\rho\Delta\rho}\rho_t\Delta\rho_t + C_t^{\rho\nabla J}\rho_t\nabla\cdot\mathbf{J}_t\,. \tag{3}$$

In the equation (3), τ_t is the isoscalar or isovector kinetic density and $\mathbf{J}_{\mu\nu,t}$ is the spin-current density tensor. Definitions of these densities can be found in reference [1]. With the UNEDF models, only the time-even part of the total energy density was defined and time-odd part of the energy density was set to zero. The energy density is always time-even, also the part called "time-odd" - the time-odd energy density means that this part of the energy density is built by using time-odd densities.

The pairing energy density $\widetilde{\chi}(\mathbf{r})$ used here has the form of

$$\widetilde{\chi}(\mathbf{r}) = \frac{1}{4}\sum_{q=\mathrm{n,p}} V_0^q\Big[1 - \frac{1}{2}\frac{\rho_0(\mathbf{r})}{\rho_c}\Big]\widetilde{\rho}_q^2(\mathbf{r})\,, \tag{4}$$

where V_0^q ($q = \mathrm{n,p}$) are the pairing strength parameters for neutrons and protons, respectively, and ρ_c was set to the equilibrium density $0.16\,\mathrm{fm}^{-3}$. All the coefficients C_t^x and V_0^q are real constants, except the coefficients $C_t^{\rho\rho}$ which depend on the isoscalar density so that

$$C_t^{\rho\rho} = C_{t0}^{\rho\rho} + C_{t\mathrm{D}}^{\rho\rho}\rho_0^\gamma\,. \tag{5}$$

Table 1. The parameters of UNEDF models used in the sensitivity analysis. Here "x" indicates parameter was included in sensitivity analysis. Parameters which were fixed during the whole optimization procedure are denoted as "–", and the rest of the parameters are those which hit the boundary values during optimization. The index $t = 0, 1$ separates the isoscalar and isovector terms.

EDF	ρ_c	$\frac{E^{\rm NM}}{A}$	$K^{\rm NM}$	$a_{\rm sym}^{\rm NM}$	$L_{\rm sym}^{\rm NM}$	$1/M_s^*$	$1/M_v^*$	$C_t^{\rho\Delta\rho}$	$V_0^{\rm n,p}$	$C_t^{\rho\nabla J}$	C_t^{JJ}
UNEDF0	x	x		x	x		–	x	x	x	–
UNEDF1	x			x	x	x	–	x	x	x	–
UNEDF2	x		x	x		x	–	x	x	x	x

Altogether, there are 13 independent constants from Skyrme energy density and two constants from pairing, namely

$$\{C_{t0}^{\rho\rho}, C_{t\rm D}^{\rho\rho}, C_t^{\rho\Delta\rho}, C_t^{\rho\tau}, C_t^{J^2}, C_t^{\rho\nabla J}\}_{t=0,1}\,,\ \gamma, V_0^{\rm n} \text{ and } V_0^{\rm p}\,. \tag{6}$$

Seven of these parameters for $t = 0$ and $t = 1$, $C_{t0}^{\rho\rho}$, $C_{t\rm D}^{\rho\rho}$, $C_t^{\rho\tau}$ and γ, can be written with the help of the infinite nuclear matter parameters [20, 24]. All in all, the model depends on 15 independent parameters, namely

$$\begin{aligned}&\rho_{\rm c}, \frac{E^{\rm NM}}{A}, K^{\rm NM}, a_{\rm sym}^{\rm NM}, L_{\rm sym}^{\rm NM}, M_s^*, M_v^*, C_0^{\rho\Delta\rho},\\ &C_1^{\rho\Delta\rho}, V_0^{\rm n}, V_0^{\rm p}, C_0^{\rho\nabla J}, C_1^{\rho\nabla J}, C_0^{JJ}, \text{ and } C_1^{JJ}\,,\end{aligned} \tag{7}$$

which were optimized in the previous works, in references [20–22]. Here ρ_c is the saturation density, $E^{\rm NM}/A$ represents the total energy per nucleon at equilibrium, $K^{\rm NM}$ is the nuclear matter incompressibility, $a_{\rm sym}^{\rm NM}$ is the symmetry energy coefficient, $L_{\rm sym}^{\rm NM}$ describes the slope of the symmetry energy, M_s^* is the isoscalar effective mass and the last one, M_v^*, is the isovector effective mass.

In the present work, we have compared calculated theoretical binding energies to the experimental ones from [25]. In order to obtain experimental nuclear binding energies, the experimental atomic masses were corrected by taking into account the electron binding energies, approximated as

$$B_{\rm E} \approx -1.433 \times 10^{-5} Z^{2.39}\,{\rm MeV}\,. \tag{8}$$

2.2. Propagation of error

The UNEDF parameterizations were accompanied by sensitivity analysis, providing covariance matrix of the model parameters. This allows to calculate the standard deviation of any observable predicted by the model. In the present work we consider the statistical errors on binding energies and on two-neutron separation energies.

The statistical standard deviation σ of an observed variable y is given by

$$\sigma^2(y) = \sum_{i,j=1}^{n} {\rm Cov}(x_i, x_j) \left[\frac{\partial y}{\partial x_i}\right] \left[\frac{\partial y}{\partial x_j}\right]\,, \tag{9}$$

where $\mathrm{Cov}(x_i, x_j)$ is the covariance matrix element between the model parameters x_i and x_j, and n is the number of model parameters. The covariance matrix $\mathrm{Cov}(x_i, x_j)$ is related to the corresponding correlation matrix $\mathrm{Corr}(x_i, x_j)$ as

$$\mathrm{Cov}(x_i, x_j) = \mathrm{Corr}(x_i, x_j)\sigma_{x_i}\sigma_{x_j} , \tag{10}$$

where σ_{x_i} and σ_{x_j} are the standard deviations of parameters x_i and x_j, respectively. The correlation matrices of the UNEDF models and the standard deviations of the model parameters are given in Appendix A.

The standard deviation in equation (9) contains a sum of terms connected to the model parameters. Due to correlations between model parameters, off-diagonal components has to be also taken into account. By diagonalizing the covariance matrix (or, equivalently, the curvature matrix of $\chi^2(\mathbf{x})$ function) it is possible analyze eigenmodes, as was demonstrated in reference [26]. This method was also used in analysis of DD-PC1 functional uncertainties [12]. With application of an orthogonal transformation, which diagonalizes the covariance matrix, one obtains the square of the standard deviation $\sigma^2(y)$ expressed as a sum over eigenvalues multiplied by corresponding eigenvectors and partial derivatives of y.

Some of the UNEDF model parameters have been excluded from the sensitivity analysis. Table 1 lists those UNEDF parameters which were included in the sensitivity analysis [20–22] (marked with x), those which were fixed during the whole optimization procedure (-) and those which ended up at their boundaries during the optimization (empty space). Sensitivity analysis can not be performed for fixed parameters or those which drifted onto the boundary during the optimization. However, those parameters which were included in sensitivity analysis have a visible contribution to the statistical error of an observable and their contribution to the total error budget can be calculated from equation (9).

2.3. Numerical methods

In the present work we used the code HFBTHO [27, 28] to calculate observables and their statistical errors. The program solves the Hartree-Fock-Bogoliubov equations for Skyrme EDFs in the axially symmetric harmonic oscillator basis. Time-reversal and parity symmetries were assumed. Because particle number is not a good quantum number in HFB theory, we used the Lipkin-Nogami method to restore it approximately. The HFB equations were solved in a basis consisting of 20 oscillator shells and the convergence criteria was set to 10^{-7}. This means that the desired accuracy has been reached when the norm of the HFB matrix difference between two consecutive iterations is less than 10^{-7}. Both of the Coulomb terms, $\mathcal{E}^{Coul}_{dir}$ and $\mathcal{E}^{Coul}_{exchange}$ were used, but the exchange term was calculated by using Slater approximation. A rough position of the energy minimum, with respect of quadrupole deformation, was first located from a constrained HFB calculation. Then, an unconstrained HFB calculation was performed in order to converge to the precise position of the energy minimum.

In order to obtain standard errors one has to calculate the derivatives of an observable $y(\mathbf{x})$ with respect to the model parameters x_i, as in equation (9). In the present work these derivatives were approximated by a finite differences. That is

$$\frac{\partial y}{\partial x_i} \approx \frac{y(x_1, x_2, \ldots, x_i + \Delta x_i, \ldots, x_n) - y(\mathbf{x})}{\Delta x_i}, \tag{11}$$

where value of ith parameter has been shifted by amount of Δx_i from the model base values. The rounded values of UNEDF parameters and corresponding shifts Δx_i have been listed on Table B1. We tested that the computed statistical errors remained essentially the same when shift parameters Δx_i were slightly varied.

Lastly, we recall that standard deviation does not measure the total uncertainty of a model. Another main ingredient, namely the systematic error, is much more challenging to assess. It can be addressed e.g. by studying a dispersion of different predictions given by various Skyrme EDF models [2, 29]. However, due to lack of exact reference model, precise systematic errors are not within one's reach.

3. Results

3.1. Binding energy residuals

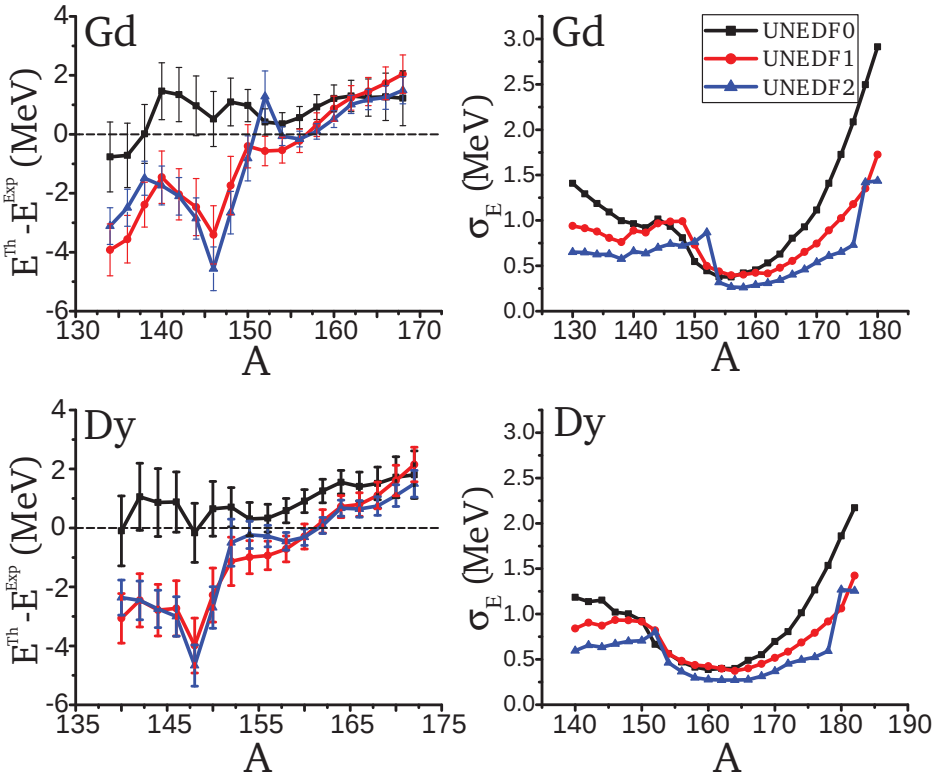

Figure 1. (Color online) Differences between theoretical and experimental binding energies for even-even dysprosium and gadolinium isotopes with error bars representing statistical model error (on the left) and related statistical model error (on the right) as a function of the mass number.

The differences between the theoretical and experimental binding energies for even-even gadolinium and dysprosium isotopes are shown in figure 1. The error bars represent the calculated theoretical standard deviations, and they are also given as a function of the mass number in the graphs on the right. The uncertainties are given for all the calculated binding energies, including also those nuclei for which the experimental binding energy is not currently known. As it can be seen, UNEDF0 gives more consistent results with the measured experimental energies for lighter isotopes, whereas UNEDF1 and UNEDF2 seem to improve their accuracy considerably for heavier isotopes. Most of the theoretical results do not overlap with the experimental values, even when including error bars. Two interesting points can be seen in the graphs on the left: ^{146}Gd and ^{148}Dy. Both of these nuclei have neutron number of $N = 82$, that is, one of the magic numbers. Here, the theoretical predictions for the binding energies given by UNEDF1 and UNEDF2 are comparatively farther away from the experimental results. However, there is no visible increase in the standard deviation of the binding energy of these two nuclei. This suggests that the increased residual is due to underlying model deficiency, and not due to the parameter optimization procedure.

The calculated standard deviations of binding energies are found to be around 0.5–3.0 MeV, 0.4–1.7 MeV, and 0.3–1.5 MeV for UNEDF0, UNEDF1 and UNEDF2, respectively. Even though the standard deviations have a magnitude of one thousandth of the total binding energy, the theoretical uncertainties are still far larger compared to experimental precision, which can be of the order of few keV's [30]. However, uncertainties of the UNEDF models have decreased after every model: The obtained standard deviation for UNEDF0 is larger compared to two later parameterizations.

The behavior of uncertainty is relatively smooth and the uncertainty of binding energy grows quickly when going towards neutron rich nuclei. In addition, one can also see that uncertainties grow when going towards the other extreme, namely proton rich nuclei. This is an indication that isovector part of the EDFs is not as well constrained as the isoscalar part.

The residuals of the two-neutron separation energy, $S_{2\mathrm{n}}$, are shown in figure 2. The two-neutron separation energies were calculated for even-even Dy and Gd isotopes. Similarly to the previous figure, theoretical errors are marked as error bars in the graphs on the left hand side panels, and also given as a function of the mass number on the right hand side panels. The theoretical statistical error is calculated similarly, through finite differences of $S_{2\mathrm{n}}$ values to compute the derivatives. For neutron rich nuclei, all three parameterizations give essentially the same result for $S_{2\mathrm{n}}$, within the error bars. Otherwise, the latest UNEDF2 parameterization seems to differ most from the experimental results when compared to previous two parameterizations.

Since S_{2n} is defined as a difference of two binding energies, the partial derivatives are also calculated from energy difference between two nucleus. As a consequence, some of the parameter uncertainties can cancel each other. In particularly, the uncertainty coming from a relatively less constrained isovector part of the EDF is now partly canceled, resulting to more moderate uncertainty in the neutron rich region compared

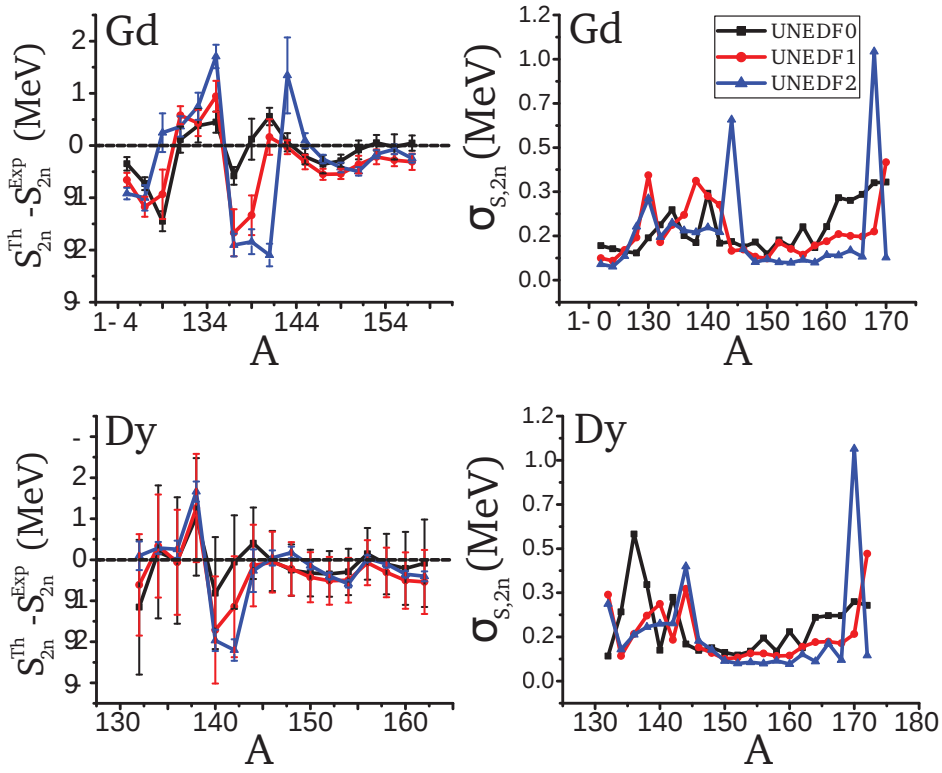

Figure 2. (Color online) Same as figure 1 but for two-neutron separation energy S_{2n}.

to the uncertainty of binding energy. Similar observation was also done at [9].

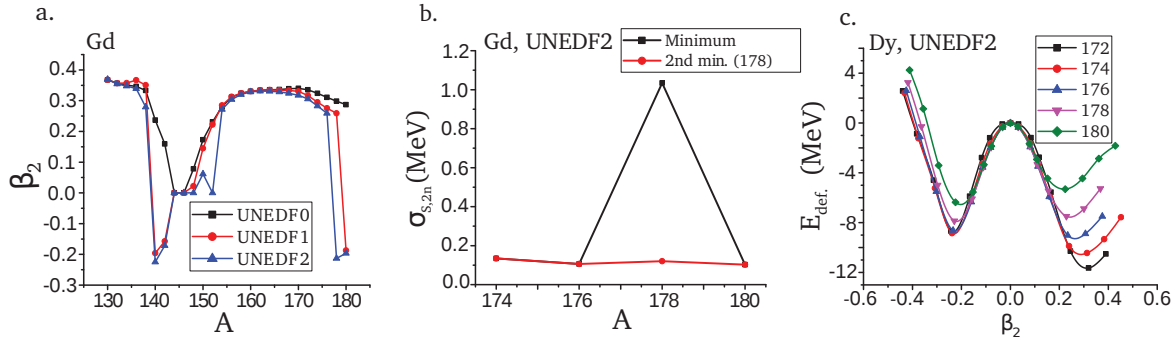

Figure 3. (Color online) Panel a: Deformation parameter β_2 as a function of mass number A. Panel b: Calculated statistical error of $\sigma_{S,2n}$ when using either lowest or secondary energy minimum of ^{178}Gd. Panel c: Deformation energies of five dysprosium isotopes as a function of deformation parameter β_2.

One common feature for all UNEDF models is an existence of a few high peaks in the statistical error of S_{2n}. These peaks are located mainly around the same neutron numbers for Gd and Dy isotopes. For instance, the two highest peaks given by UNEDF2 are located at the nuclei ^{178}Gd and ^{180}Dy. The explanation for all of the high peaks can be found in a sudden change in deformation. Figure 3, in panel a, shows how

deformation parameter β_2 varies with mass number A for Gd. When comparing this to that of $\sigma_{S,2n}$, shown in figure 2, one can notice similarity between uncertainty peaks and large change in the deformation. If there is a significant difference in deformation between two consecutive even-even nuclei, this results to a larger statistical error of two-neutron separation energy.

The relationship between $\sigma_{S,2n}$ and a sudden large change of β_2 can be tested by looking at the secondary local minimum of the deformation energy landscape. For the calculated Gd and Dy nuclei, there usually exists two energy minima, the oblate one and the prolate one, as shown in figure 3, panel c. By picking always the lowest minimum results to large statistical error of S_{2n} when deformation has a large change between two even nucleus. However, if one uses the secondary minimum, in which case the two nuclei appearing in the expression of S_{2n} have similar deformation compared to the each other, one obtains substantially smaller $\sigma_{S,2n}$. In figure 3, panel b, the black line describes the same peak at $A = 178$ given by UNEDF2 as in figure 2, calculated with the lowest energy minima. The second (red) line corresponds to case where second minimum of ^{178}Gd was used, resulting a much smaller $\sigma_{S,2n}$ for ^{178}Gd. Indeed, a large difference in deformation of involved nuclei seems to give large uncertainty on two-neutron separation energy. A possible explanation is considerably different shell structure between these two nuclei due to deformation. The largest impact on the extremely high peaks in $\sigma_{S,2n}$ given by UNEDF2 is connected to the parameter C_1^{JJ}, whereas for UNEDF1 the main contributors are M_s^*, both $C^{\rho\Delta J}$ together with $C_0^{\rho\Delta\rho}$ and V_0^n parameters.

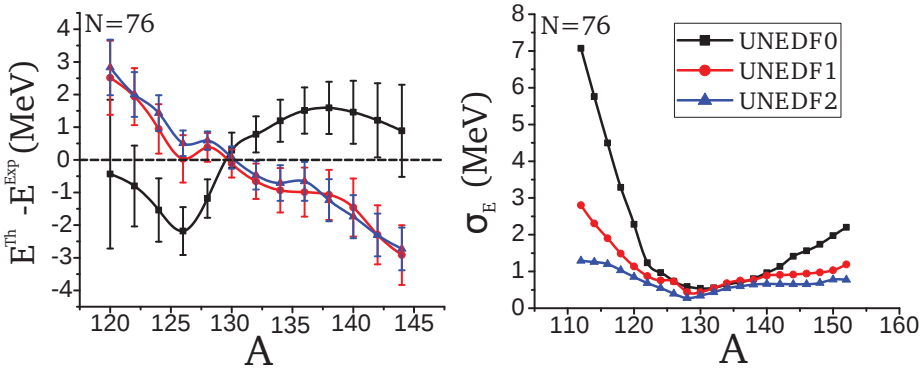

Figure 4. (Color online) Same as figure 1, but for the isotonic chain with the neutron number $N = 76$.

The binding energy residuals between theory and experiment for isotonic chain of $N = 76$ can be found in figure 4. Only even-even nuclei are studied. The UNEDF1 and UNEDF2 parameterizations give rather similar results, but the binding energy behavior of UNEDF0 parameterization is notably different. Compared to the UNEDF0 optimization procedure, in the optimization of UNEDF1 the same set of 12 EDF parameters were optimized but seven additional data points were included in the database and the center of mass correction was neglected [21]. The other important remark is the fact that even though the trend of UNEDF1 and UNEDF2 models is

incorrect – the calculated binding energies for proton rich nuclei are getting further far away from the experimental ones when mass number increases – the uncertainties do not nevertheless become larger.

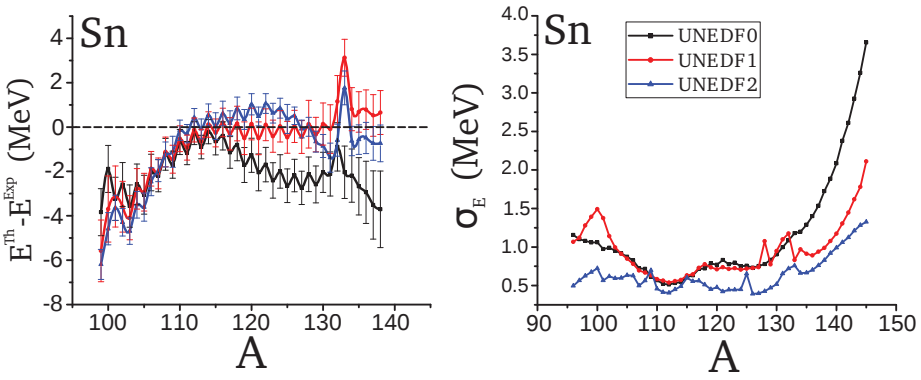

Figure 5. (Color online) Same as figure 1 but for even-even and even-odd Sn isotopes.

We have also considered the statistical error of odd-even nuclei. The binding energy residual for Sn isotopic chain was computed by using all three UNEDF models. The results are shown in figure 5. The odd-even nuclei were calculated by using the quasi-particle blocking procedure with the equal filling approximation [7]. The same blocking configuration, which corresponded the lowest energy with unshifted parameterization, was used for calculation of all partial derivatives. The same set of results for even Sn isotopes, with UNEDF0, was calculated in [9]. The results show that the binding energy residuals of even-even nuclei are relatively greater compared to those of odd nuclei. On this account, the binding energy residuals stagger between the odd and even nuclei. Nevertheless, there are no visible odd-even effects in the standard deviations of binding energy. This can be explained by the lack of time-odd part in the used EDFs.

3.2. Uncertainty of $Q_{2,p}$ and proton matter radius

The standard deviation of proton matter quadrupole moment $Q_{2,p}$ and proton matter root-mean-square (rms) radius $r_{p,rms}$ for all three UNEDF models is shown in figure 6. The scale of σ_{Q2} can be read on the left side and the scale of σ_r on the right side of the figure. As expected, the uncertainty of these two observables behaves similarly and is strongly correlated. High values of uncertainty are located in deformed nuclei next to spherical nuclei, due to soft deformation energy landscape with respect of quadrupole deformation.

Despite the general strong correlation between σ_r and σ_{Q2}, with UNEDF1 and UNEDF2, there are a few points of $Q_{2,p}$ which differ from the major trend. The vanishing uncertainty of $Q_{2,p}$ in ^{152}Gd is explained by the fact that ^{152}Gd is predicted to be spherical by UNEDF2 EDF. This can be seen in figure 3, panel a. The divergent uncertainty of $Q_{2,p}$ in ^{180}Gd (^{178}Gd, ^{180}Gd) in UNEDF1 (UNEDF2) is related to the change of sign in quadrupole moment and deformation parameter β_2 which is shown

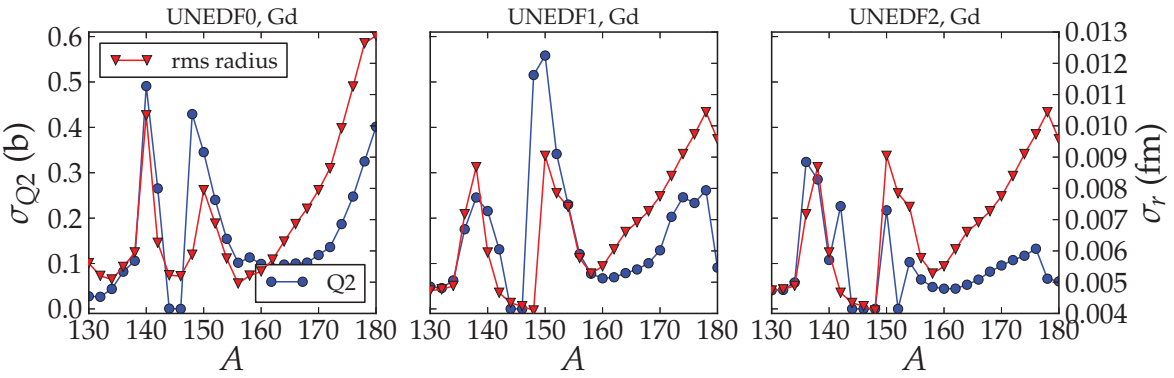

Figure 6. (Color online) The standard deviation of proton quadrupole moment $Q_{2,p}$ and proton rms radius $r_{p,rms}$ for Gd isotopic chain with all three UNEDF models. The scale of σ_{Q2} can be read on the left side and the scale of σ_r on the right side of the figure

also in figure 3, panel a. Most of the nuclei are predicted to be prolate by UNEDF1 and UNEDF2, but above-mentioned nuclei are predicted to be oblate, resulting to rapid changes of the statistical uncertainty of $Q_{2,p}$ for Gd isotopic chain. However, ^{140}Gd and ^{142}Gd isotope are also predicted to be oblate by UNEDF1 and UNEDF2 EDFs, but there is no significant effect in the uncertainties given by UNEDF1. There is no oblate-shaped nuclei among the Gd isotopes calculated with UNEDF0 EDF.

In addition to the large uncertainties next to the spherical nuclei, there is also another visible trend in the uncertainties. Similarly like with the uncertainties of the binding energy, when going towards the neutron rich nuclei, the uncertainties of $Q_{2,p}$ and $r_{p,rms}$ increases systematically. The same behavior is also followed with the uncertainties of the neutron matter radius.

3.3. Contributions of the model parameters

One of the goals of present work is to study contributions of the model parameters to the total error budget of binding energy. The most elementary way to represent the contributions of the model parameters to the total uncertainty is by listing component matrix. Here, every single small color square in the matrix represents the value of one particular cross contribution coming from parameters (x_i, x_j) to the total sum of equation (9). The component matrices for the binding energy uncertainties of ^{154}Gd and ^{180}Gd are shown in figure 7. Some of these components have negative sign, due to a negative partial derivative or a negative covariance matrix element. The total squared standard deviation is always, nevertheless, a positive number. One should also bear in mind that the contribution of a parameter to the standard deviation is visible only if this parameter was included in the sensitivity analysis, as mentioned before.

For ^{154}Gd, which has one of the smallest statistical error of binding energy with all UNEDF parameterizations, the total error budget with UNEDF0 and UNEDF2 EDFs consist of several components. The total error budget with UNEDF1 is simpler, and

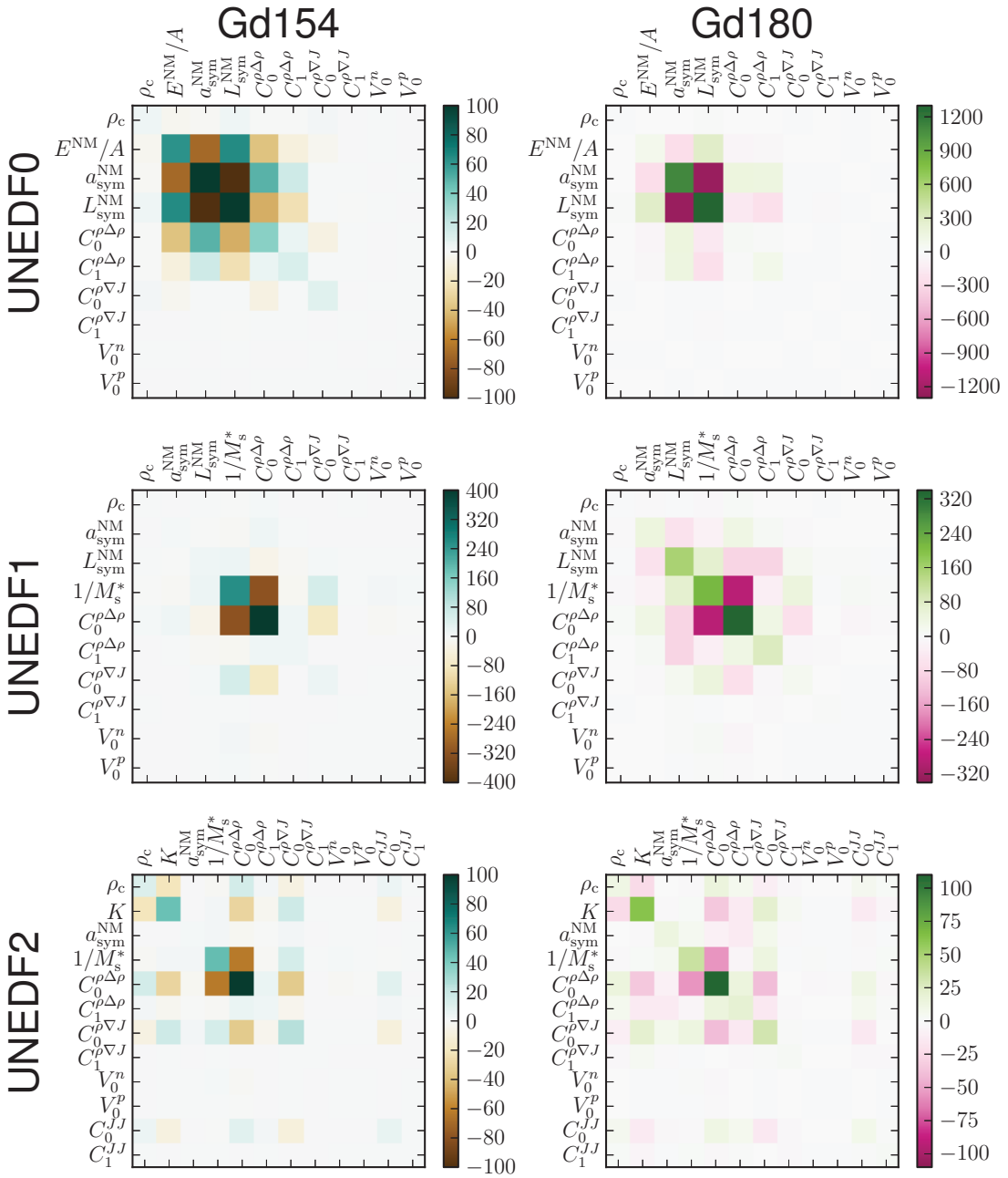

Figure 7. (Color online) Individual contributions of the model parameters (x_i, x_j), in the total sum of equation (9), for the uncertainty of binding energy in ^{154}Gd and ^{180}Gd isotopes and for all three UNEDF models. The contributions are in units of MeV^2.

mainly coming from $1/M_s^*$ and $C_0^{\rho\Delta\rho}$ parameters. On the other hand, the uncertainty budget for the neutron rich nucleus ^{180}Gd splits into several pieces when going from the oldest parameterization to the latest one. The uncertainty of UNEDF0 is affected by a couple of parameters, mainly by $a_{\rm sym}^{\rm NM}$ and $L_{\rm sym}^{\rm NM}$. The most contributing parameters to the uncertainty of UNEDF1 are $1/M_s^*$ and $C_0^{\rho\Delta\rho}$, whereas in the case of UNEDF2

the $C_0^{\rho\Delta\rho}$ parameter have slightly greater contribution. Even though one parameter has slightly greater contribution, the uncertainty of binding energy for neutron rich nuclei is relatively widely spread among the model parameters of UNEDF2.

The component matrix representation shows explicitly how different model parameters contribute to the total error budget pairwise. Unfortunately, this representation requires a lot of space. By considering a summed contribution of one row (or, equivalently, one column) of the component matrix, we can represent the error budget as a stacked histograms for each isotope. We refer this once summed contribution as a *row contribution* of a parameter x_i. Here, components of the total error are calculated by summing over one index in equation (9), resulting the total squared standard deviation being then a sum of all row contributions.

The results for the row contributions are shown in figure 8 for the binding energies of even Dy isotopes and in figure 9 for the binding energies of even $N = 76$ isotones. The error budget for UNEDF0 binding energy is mainly composed of only a few contributing rows. For nuclei close to the valley of stability, two dominant sources of uncertainty are the rows E^{NM}/A and $C_0^{\rho\Delta\rho}$ parameters, whereas in the neutron rich Dy isotopes the rows of $L_{\mathrm{sym}}^{\mathrm{NM}}$ and $a_{\mathrm{sym}}^{\mathrm{NM}}$ dominate. In other words, model parameters related to symmetry energy become more important with neutron rich nuclei. It was found earlier that $L_{\mathrm{sym}}^{\mathrm{NM}}$ has also a strong impact on the statistical error of neutron root-mean-square radii and neutron skin thickness [9, 29]. The most dominant sources of uncertainty are the same for isotopic and isotonic chains.

Contrary to UNEDF0, the error budget of latter two parameterizations is more split among the various different row contributions in neutron rich nuclei. Generally speaking, the rows connected to $a_{\mathrm{sym}}^{\mathrm{NM}}$, both $C_t^{\rho\Delta\rho}$ parameters, $C_0^{\rho\nabla J}$, and $1/M_s^*$ have a significant impact on the total error budget with UNEDF2. It should be noticed that the correlation between $C_0^{\rho\Delta\rho}$ and $1/M_s^*$ is strong: In principle, if one can reduce the uncertainty on $C_0^{\rho\Delta\rho}$, it should also reduce the uncertainty of $1/M_s^*$. The isovector parameters, for their part, are more difficult to constrain, but they impact on the stability of the functional: For instance $C_1^{\rho\Delta\rho}$ is the coupling constant of the gradient term, which has been found to trigger scalar-isovector instabilities [31].

Lastly, we represent the uncertainties of binding energies in the eigenmode formalism in figure 10. The eigenvectors are listed in descending order of eigenvalues. The eigenvectors and eigenvalues are not shown here - it is not a laborious task to diagonalize covariance matrices given in references [20–22]. Basically, a small eigenvalue means that the linear combination of model parameters described by this eigenvector is well constrained. If the eigenvalue is large, the corresponding eigenvector is poorly constrained. The eigenvector representation does not directly tell about the model parameters themselves, but describes how the uncertainty propagates from a certain linear combinations of the model parameters, instead. As we can see, e.g. for neutron rich nuclei, only five eigenvectors of UNEDF0 contribute significantly to the total error budget. The eigenvector having the greatest eigenvalue, and thus being least constrained, has also the biggest contribution to the error budget among the neutron

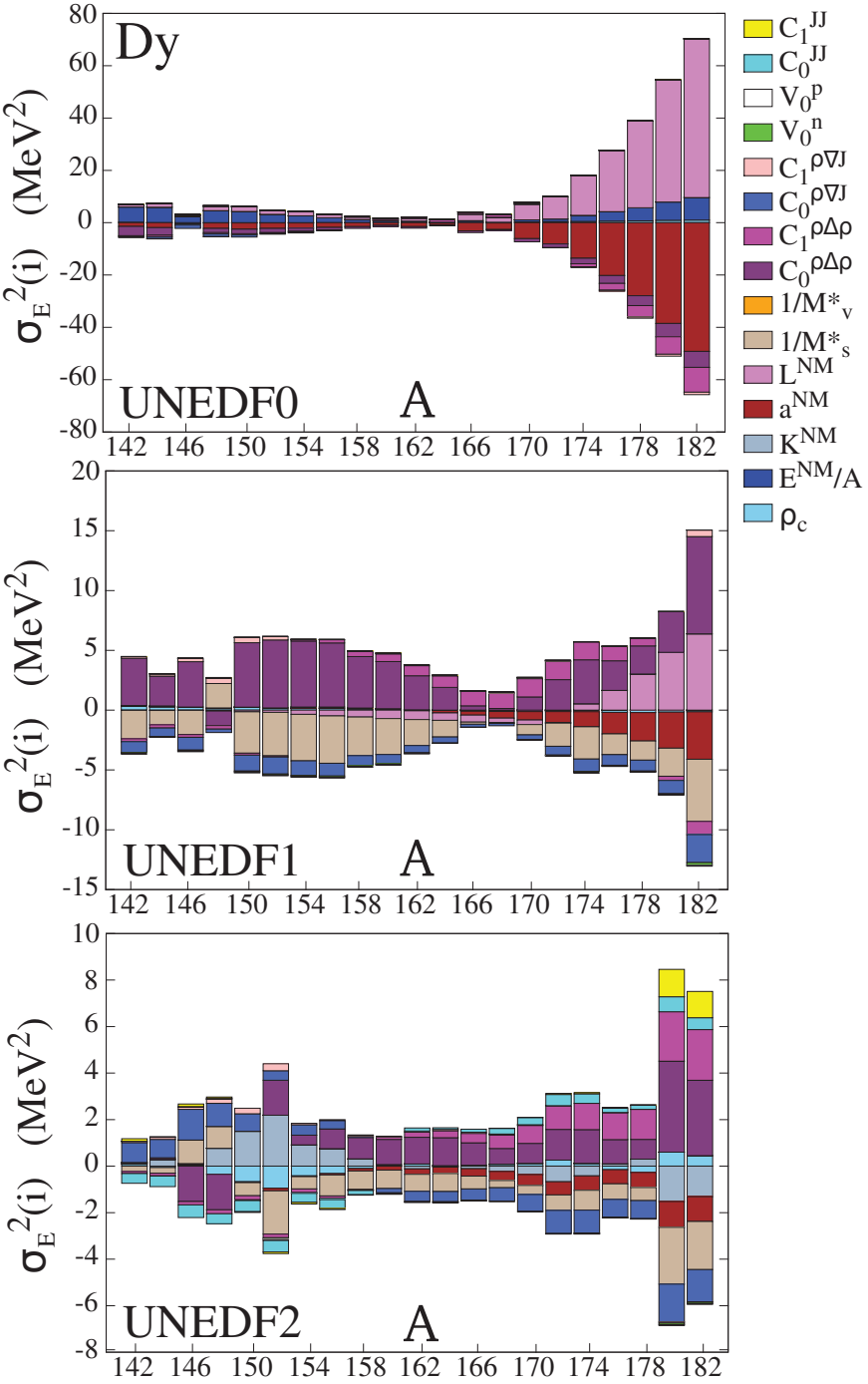

Figure 8. (Color online) Error budget of σ_E^2 for even-even Dy isotopes with UNEDF0, UNEDF1 and UNEDF2 EDFs in the row contribution representation. The contribution of a summed up row is indicated with corresponding model parameter name.

and proton rich nuclei. In the case of UNEDF1, mainly two eigenvectors contribute to the total error budget of a given nucleus, whereas there are 5 significant contributors with UNEDF2 EDF. Interestingly, with UNEDF1, one can see many contributing

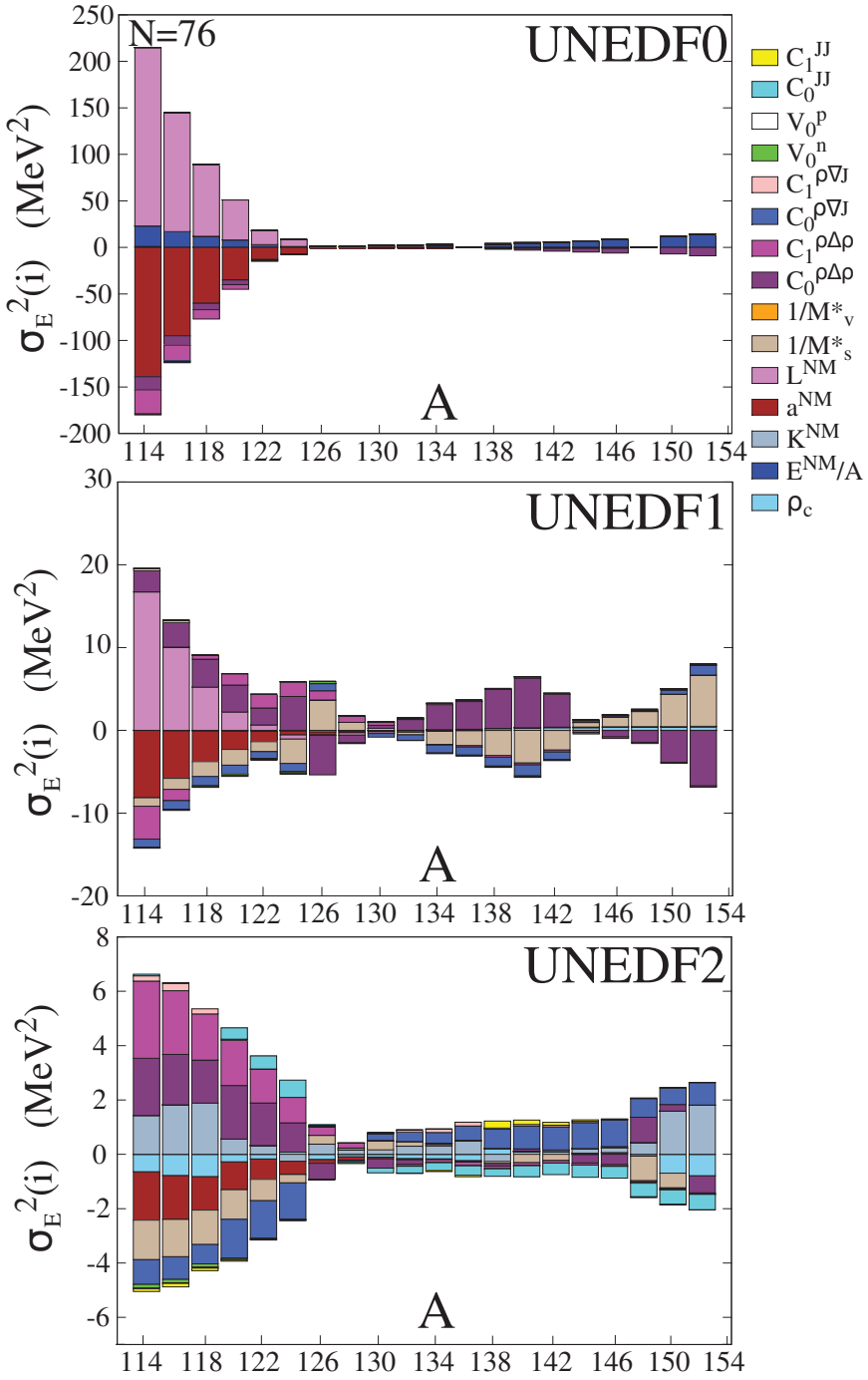

Figure 9. (Color online) Same as figure 8 but for the isotonic chain of $N = 76$.

eigenvectors at deformation transition region around $A = 140 - 152$.

We can also investigate how different model parameters contribute to the uncertainty, in terms of components of one particular eigenvector. For example, with UNEDF0, the first eigenvector has the biggest contribution with neutron rich nuclei. When looking at the individual components of this eigenvector, the main contributing model parameters are $a_{\rm sym}^{\rm NM}$ and $L_{\rm sym}^{\rm NM}$. With the second largest contributing eigenvector,

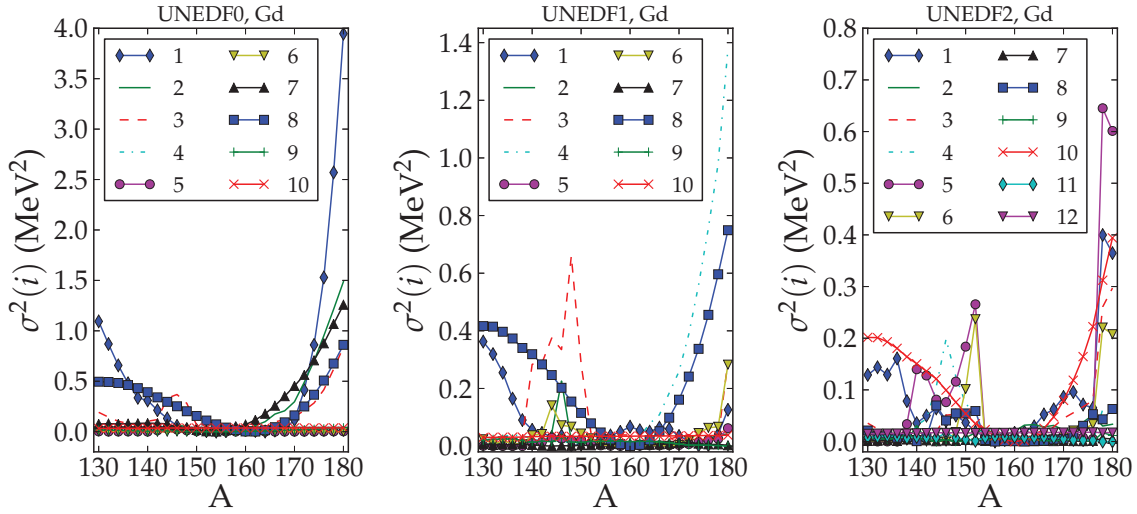

Figure 10. (Color online) The uncertainties of binding energies in the eigenmode formalism. Each curve represents the contribution of one eigenvector. The eigenvectors are different for each UNEDF parameterization, even though symbols and numbering is the same.

the contribution of $a_{\rm sym}^{\rm NM}$ is the largest one and with third most contributing eigenvector, the parameters $C_0^{\rho\Delta\rho}$, $a_{\rm sym}^{\rm NM}$ and $E^{\rm NM}/A$ are the most important ones. With UNEDF1, the uncertainty of binding energy for neutron rich nuclei comes from $a_{\rm sym}^{\rm NM}$, $L_{\rm sym}^{\rm NM}$ and $C_0^{\rho\Delta\rho}$ model parameters when considering the most contributing eigenvector, and from $a_{\rm sym}^{\rm NM}$ and ρ_c when considering eigenvector having the second largest contribution. On the other hand, with UNEDF2, the contributions are more split among various model parameters. Largest contributing components of two most important eigenvectors consist of several parameters (more than five). The uncertainty coming from the third most contributing eigenvector consists almost entirely of $a_{\rm sym}^{\rm NM}$ and ρ_c model parameters.

In the end of this section, we can conclude that three different methods used in this study, namely the component matrix representation, the histogram representation of row contributions, and the eigenmode method, are in support of each other, with each one having their own advantage.

4. Conclusions

In the present work we have calculated statistical errors of the UNEDF models for binding energy, two-neutron separation energy, proton quadrupole moment and proton rms radius by using information about the covariance matrix of the model parameters. The standard deviation has been interpreted as a statistical error. We have also quantified the contributions of each model parameters to the total error budget by using three different methods and checked if there are any visible odd-even effects in the uncertainties of the UNEDF models. We presented our results for the error budget by

using the component matrix representation, the row contribution representation, and finally, by using the eigenmode method. We found out that the standard deviation of binding energy grows quickly when going away from the valley of stability towards proton rich or neutron rich nuclei. Similarly, uncertainties of proton quadrupole moment $Q_{2,p}$ and proton rms radius $r_{rms,p}$ increase rapidly among the neutron rich nuclei as a function of mass number. That is to say, the predictive power of UNEDF models becomes weaker when extrapolating further away from known nuclei to experimentally unknown region. For the Sn isotopic chain, even though there exists odd-even staggering in the residuals of binding energies, no visible odd-even effect was seen in the related errors.

The error budget of the UNEDF parameterizations becomes more evenly split among various model parameters with UNEDF1 and UNEDF2 parameterizations in neutron rich nuclei. This can be seen by using any of the three methods mentioned above. The most dominant contributors to the error budget of neutron rich nuclei with UNEDF0 were $L_{\rm sym}^{\rm NM}$ and $a_{\rm sym}^{\rm NM}$ parameters, that is to say, coefficients related to the symmetry energy. In the case of UNEDF1, $L_{\rm sym}^{\rm NM}$ and $a_{\rm sym}^{\rm NM}$ still have a significant contribution and, in addition, the role of $C_0^{\rho\Delta\rho}$ and $1/M_s^*$ becomes important. With UNEDF2, the role of other model parameters becomes even more prominent.

A comparison of the binding energy standard deviations to the residuals seems to point out that the underlying theoretical model is missing some important physics. One clear indication of this is the increase of the binding energy residuals close to the semi-magic nuclei. However, calculated standard deviation does not usually reflect this kind of behavior. Similar observation was also done in [9]. Also, the systematically incorrect trend of UNEDF1 and UNEDF2 with the binding energy residual in the $N = 76$ isotonic chain does not appear in theoretical uncertainties, as shown in figure 4.

The trend in the UNEDF statistical errors is such that the calculated standard deviation decreases as more data is included in the optimization procedure. From a statistical point of view, the larger uncertainty of the isovector parameters reflects to the increasing uncertainty when going towards the both isospin extremes. Unfortunately, new data may not always help to reduce uncertainties. A sophisticated parameter optimization within Bayesian framework showed that new data points on nuclear binding energies at neutron rich region were not able provide a better constraint for the UNEDF1 model parameters [16]. On the other hand, data on the neutron skin thickness could potentially help to reduce uncertainties related on isovector model parameters [32].

As was concluded for the UNEDF2 parameterization, the limits of standard Skyrme-EDFs have been reached and novel approaches are called for [22]. Information about the shortcomings and uncertainties of present models will provide valuable input for development of novel EDF models. A comprehensive sensitivity analysis of a novel EDF parameterization is essential when addressing its predictive power.

Acknowledgements

T.H. thanks Karim Bennaceur and Nicolas Schunck for great advice and remarks. This work was supported by the Academy of Finland under the Centre of Excellence Programme 2012-2017 (Nuclear and Accelerator Based Physics Programme at JYFL) and under the FIDIPRO programme. T.H. was also supported by a grant (55151927) of the Finnish Cultural Foundation, North Karelia Regional Fund.

Appendix A. Appendix: Correlation matrices

Table A1. Correlation matrix and standard deviations of the UNEDF0 parameter set [20]. The values are rounded. The units are following: ρ_c is in fm^{-3}; E^{NM}/A, a_{sym}^{NM} and L_{sym}^{NM} are in MeV; $C_t^{\rho\Delta\rho}$ and $C_0^{\rho\nabla J}$ are in MeV fm^{-5}, and $V_0^{n,p}$ are in MeV fm^{-3}.

	ρ_c	E^{NM}/A	a_{sym}^{NM}	L_{sym}^{NM}	$C_0^{\rho\Delta\rho}$	$C_1^{\rho\Delta\rho}$	V_0^n	V_0^p	$C_0^{\rho\nabla J}$	$C_1^{\rho\nabla J}$
ρ_c	1.00									
E^{NM}/A	-0.28	1.00								
a_{sym}^{NM}	-0.10	-0.88	1.00							
L_{sym}^{NM}	-0.17	-0.80	0.97	1.00						
$C_0^{\rho\Delta\rho}$	0.09	0.80	-0.81	-0.74	1.00					
$C_1^{\rho\Delta\rho}$	0.20	0.35	-0.47	-0.66	0.23	1.00				
V_0^n	0.02	0.21	-0.23	-0.25	0.23	0.23	1.00			
V_0^p	-0.13	-0.42	0.52	0.56	-0.29	-0.45	-0.14	1.00		
$C_0^{\rho\nabla J}$	0.37	-0.14	0.02	-0.00	0.44	-0.02	0.09	0.16	1.00	
$C_1^{\rho\nabla J}$	-0.06	-0.18	0.27	0.33	-0.38	-0.20	-0.01	0.00	-0.37	1.00
σ	0.001	0.055	3.058	40.037	1.697	56.965	2.105	3.351	3.423	29.460

Table A2. Same as table A1 but for UNEDF1. L_{sym}^{NM} is in units of MeV and $1/M_s^*$ is unitless.

	ρ_c	a_{sym}^{NM}	L_{sym}^{NM}	$1/M_s^*$	$C_0^{\rho\Delta\rho}$	$C_1^{\rho\Delta\rho}$	V_0^n	V_0^p	$C_0^{\rho\nabla J}$	$C_1^{\rho\nabla J}$
ρ_c	1.00									
a_{sym}^{NM}	-0.35	1.00								
L^{NM}	-0.14	0.71	1.00							
$1/M_s^*$	0.32	0.23	0.36	1.00						
$C_0^{\rho\Delta\rho}$	-0.25	-0.25	-0.35	-0.99	1.00					
$C_1^{\rho\Delta\rho}$	-0.06	-0.15	-0.77	-0.22	0.19	1.00				
V_0^n	-0.32	-0.22	-0.36	-0.99	0.98	0.22	1.00			
V_0^p	-0.33	-0.18	-0.29	-0.97	0.97	0.15	0.96	1.00		
$C_0^{\rho\nabla J}$	-0.14	-0.20	-0.32	-0.86	0.91	0.22	0.85	0.84	1.00	
$C_1^{\rho\nabla J}$	0.05	-0.17	-0.13	-0.10	0.07	0.21	0.10	0.07	-0.03	1.00
σ	0.0004	0.604	13.136	0.123	5.361	52.169	18.561	13.049	5.048	23.147

Table A3. Same as table A1 but for UNEDF2. The parameters $C_1^{\rho\nabla J}$ are in units of MeV fm^{-3}.

	ρ_c	K_{sym}^{NM}	a_{sym}^{NM}	$1/M_s^*$	$C_0^{\rho\Delta\rho}$	$C_1^{\rho\Delta\rho}$	V_0^n	V_0^p	$C_0^{\rho\nabla J}$	$C_1^{\rho\nabla J}$	C_0^{JJ}	C_1^{JJ}
ρ_c	1.00											
K_{sym}^{NM}	-0.97	1.00										
a_{sym}^{NM}	-0.07	-0.03	1.00									
$1/M_s^*$	0.08	-0.05	-0.24	1.00								
$C_0^{\rho\Delta\rho}$	-0.43	0.43	0.22	-0.89	1.00							
$C_1^{\rho\Delta\rho}$	-0.42	0.37	0.83	-0.17	0.31	1.00						
V_0^n	-0.06	0.02	0.27	-0.96	0.85	0.17	1.00					
V_0^p	-0.09	0.05	0.21	-0.89	0.80	0.14	0.86	1.00				
$C_0^{\rho\nabla J}$	-0.51	0.50	0.34	-0.40	0.68	0.55	0.36	0.34	1.00			
$C_1^{\rho\nabla J}$	-0.31	0.29	-0.19	-0.00	0.04	0.18	-0.07	-0.02	0.14	1.00		
C_0^{JJ}	0.56	-0.55	-0.26	0.05	-0.35	-0.53	-0.02	-0.02	-0.88	-0.35	1.00	
C_1^{JJ}	0.36	-0.35	0.13	-0.23	0.16	-0.14	0.29	0.25	-0.02	-0.57	0.29	1.00
σ	0.001	10.119	0.321	0.052	2.689	24.322	8.353	6.792	5.841	15.479	16.481	17.798

Appendix B. Appendix: Values of the parameters and used finite differences

Table B1. Rounded values x_i for each UNEDF parameterization and the corresponding used finite differences Δx_i used in the derivatives. The units are the same as in tables A1, A2 and A3.

	UNEDF0		UNEDF1		UNEDF2	
parameter	x_i	Δx_i	x_i	Δx_i	x_i	Δx_i
ρ_c	0.161	0.004	0.159	0.004	0.156	0.004
E^{NM}_{sym}/A	-16.056	0.02				
K^{NM}_{sym}					239.930	2.0
a^{NM}_{sym}	30.543	0.1	28.987	0.2	29.131	0.2
L^{NM}_{sym}	45.080	0.4	40.005	0.4		
$1/M^*_s$			0.992	0.012	1.074	0.012
$C_0^{\rho\Delta\rho}$	-55.261	0.6	-45.135	0.6	-46.831	0.6
$C_1^{\rho\Delta\rho}$	-55.623	2.0	-145.382	2.0	-113.164	2.0
V_0^n	-170.374	2.0	-186.065	2.0	-208.889	2.0
V_0^p	-199.202	2.0	-206.580	2.0	-230.330	2.0
$C_0^{\rho\nabla J}$	-79.531	0.7	-74.026	0.7	-64.308	0.7
$C_1^{\rho\nabla J}$	45.630	1.5	-35.658	1.5	-38.650	1.5
C_0^{JJ}					-54.433	2.0
C_1^{JJ}					-65.903	4.0

References

[1] Bender M, Heenen P-H, and Reinhard P-G. *Rev. Mod. Phys.*, 75:121, 2003.

[2] Erler J, Birge N, Kortelainen M, Nazarewicz W, Olsen E, Perhac A, and Stoitsov M. *Nature*, 486:509, 2012.

[3] Dutra M, Lourenço O, Sá Martins J S, Delfino A, Stone J R, and Stevenson P D. *Phys. Rev. C*, 85:035201, 2012.

[4] Carlsson B G, Dobaczewski J, and Kortelainen M. *Phys. Rev. C*, 78:044326, 2008.

[5] Kortelainen M, Dobaczewski J, Mizuyama K, and Toivanen J. *Phys. Rev. C*, 77:064307, 2008.

[6] Nazarewicz W. *J. Phys. G: Nucl. Part. Phys.*, 43:044002, 2016.

[7] Schunck N, Dobaczewski J, McDonnell J, Moré J, Nazarewicz W, Sarich J, and Stoitsov M V. *Phys. Rev. C*, 81:024316, 2010.

[8] Dobaczewski J, Nazarewicz W, and Reinhard P-G. *J. Phys. G: Nucl. Part. Phys.*, 41:074001, 2014.

[9] Gao Y, Dobaczewski J, Kortelainen M, Toivanen J, and Tarpanov D. *Phys. Rev. C*, 87:034324, 2013.

[10] Schunck N, McDonnell J D, Sarich J, Wild S M, and Higdon D. *J. Phys. G: Nucl. Part. Phys.*, 42:034024, 2015.

[11] Rios A and Roca Maza X. *J. Phys. G: Nucl. Part. Phys.*, 42:034005, 2015.

[12] Nikšić T, Paar N, Reinhard P-G, and Vretenar D. *J. Phys. G: Nucl. Part. Phys.*, 42:034008, 2015.

[13] Kortelainen M. *J. Phys. G: Nucl. Part. Phys.*, 42:034021, 2015.

[14] Ekström A, Carlsson B D, Wendt K A, Forssén C, Hjorth-Jensen M, Machleidt R, and Wild S M. *J. Phys. G: Nucl. Part. Phys.*, 42:034003, 2015.
[15] Lähde T A, Epelbaum E, Krebs H, Lee D, Meißner U-G, and Rupak G. *J. Phys. G: Nucl. Part. Phys.*, 42:034012, 2015.
[16] McDonnell J D, Schunck N, Higdon D, Sarich J, Wild S M, and Nazarewicz W. *Phys. Rev. Lett.*, 114:122501, 2015.
[17] Higdon D, McDonnell J D, Schunck N, Sarich J, and Wild S M. *J. Phys. G: Nucl. Part. Phys.*, 42:034009, 2015.
[18] Graczyk K M and Juszczak C. *J. Phys. G: Nucl. Part. Phys.*, 42:034019, 2015.
[19] Wesolowski S, Klco N, Furnstahl R J, Phillips D R, and Thapaliya A. *J. Phys. G: Nucl. Part. Phys.*, 43:074001, 2016.
[20] Kortelainen M, Lesinski T, Moré J, Nazarewicz W, Sarich J, Schunck N, Stoitsov M V, and Wild S. *Phys. Rev. C*, 82:024313, 2010.
[21] Kortelainen M, McDonnell J, Nazarewicz W, Reinhard P-G, Sarich J, Schunck N, Stoitsov M V, and Wild S M. *Phys. Rev. C*, 85:024304, 2012.
[22] Kortelainen M, McDonnell J, Nazarewicz W, Olsen E, Reinhard P-G, Sarich J, Schunck N, Wild S M, Davesne D, Erler J, and Pastore A. *Phys. Rev. C*, 89:054314, 2014.
[23] Ring P and Schuck P. *The Nuclear Many-Body Problem*. Springer, 2004.
[24] Chabanat E, Bonche P, Haensel P, Meyer J, and Schaeffer R. *Nuclear Physics A*, 627:710, 1997.
[25] Audi G, Wang M, Wapstra A H, Kondev F G, MacCormick M, Xu X, and Pfeiffer B. *Chinese Physics C*, 36:1287, 2012.
[26] Fattoyev F J and Piekarewicz J. *Phys. Rev. C*, 84:064302, 2011.
[27] Stoitsov M V, Dobaczewski J, Nazarewicz W, and Ring P. *Comput. Phys. Commun.*, 167:43, 2005.
[28] Stoitsov M V, Schunck N, Kortelainen M, Michel N, Nam H, Olsen E, Sarich J, and Wild S. *Comp. Phys. Comm.*, 184:1592, 2013.
[29] Kortelainen M, Erler J, Nazarewicz W, Birge N, Gao Y, and Olsen E. *Phys. Rev. C*, 88:031305, 2013.
[30] Kankainen A, Äystö J, and Jokinen A. *J. Phys. G: Nucl. Part. Phys.*, 39:093101, 2012.
[31] Hellemans V, Pastore A, Duguet T, Bennaceur K, Davesne D, Meyer J, Bender M, and Heenen P-H. *Phys. Rev. C*, 88:064323, 2013.
[32] Reinhard P-G and Nazarewicz W. *Phys. Rev. C*, 81:051303, 2010.

II

TOWARDS A NOVEL ENERGY DENSITY FUNCTIONAL FOR BEYOND-MEAN-FIELD CALCULATIONS WITH PAIRING AND DEFORMATION

by

T. Haverinen, M. Kortelainen, J. Dobaczewski and K. Bennaceur

Acta Physica Polonica B, 50 (3), 269-274 (2019)

https://doi.org/10.5506/APhysPolB.50.269

TOWARDS A NOVEL ENERGY DENSITY FUNCTIONAL FOR BEYOND-MEAN-FIELD CALCULATIONS WITH PAIRING AND DEFORMATION*

T. Haverinen[a,b], M. Kortelainen[a,b], J. Dobaczewski[a,c,d]
K. Bennaceur[e]

[a]Helsinki Institute of Physics, P.O. Box 64, 00014 University of Helsinki, Finland
[b]Department of Physics, University of Jyväskylä
P.O. Box 35 (YFL), 40014 University of Jyväskylä, Finland
[c]Department of Physics, University of York
Heslington, York YO10 5DD, United Kingdom
[d]Institute of Theoretical Physics, Faculty of Physics, University of Warsaw
Pasteura 5, 02-093 Warszawa, Poland
[e]IPNL, Université de Lyon, Université Lyon 1, CNRS/IN2P3
69622 Villeurbanne, France

(Received November 16, 2018)

We take an additional step towards the optimization of the novel finite-range pseudopotential at a constrained Hartree–Fock–Bogolyubov level and implement an optimization procedure within an axial code using harmonic oscillator basis. We perform the optimization using three different numbers of the harmonic oscillator shells. We apply the new parameterizations in the O–Kr part of the nuclear chart and isotopic chain of Sn, and we compare the results with experimental values and those given by a parameterization obtained using a spherical code.

DOI:10.5506/APhysPolB.50.269

1. Introduction

Novel approaches are essential when one aims to build an energy density functional (EDF) with spectroscopic quality and high predictive power, possibly applicable for beyond-mean-field calculations.

The two most used families of non-relativistic nuclear EDFs are based on effective Skyrme and Gogny interactions. Despite their ability to reproduce nuclear binding energies fairly well, their shortcomings have also become

* Presented at the Zakopane Conference on Nuclear Physics "Extremes of the Nuclear Landscape", Zakopane, Poland, August 26–September 2, 2018.

apparent. The often used two-body density-dependent term, which is needed to reproduce some nuclear matter properties [1], introduces problems in beyond-mean-field and symmetry-restoration calculations — for example, clear inconsistencies and anomalies can be seen in projected energies [2, 3]. Some strategies have been implemented to handle the problem with singularities, but there is no general solution for these problems unless the total energy is directly derived as an expectation value of a true interaction that is called functional generator [4, 5].

Concerning the predictive power, recent analyses point out to the fact that the uncertainties of state-of-the-art models increase rapidly when going towards both the proton and neutron rich nuclei (see Ref. [6] and references cited therein). In addition, these models miss some important physics, since differences between theoretical calculations and experimental results cannot be explained by statistical errors.

Thus, to achieve significant improvements, novel approaches are called for. One possible direction is an EDF generated by a finite-range pseudopotential [7, 8]. The first EDF parameter adjustment gave promising results [8]. However, propagated errors in deformed nuclei were found to be large, emphasizing the need for input data to constrain deformation properties. Furthermore, if the adjusted parameters are meant to be used for deformed nuclei with a code using a harmonic oscillator (HO) basis, it is interesting to study the dependence of parameters and statistical errors on the dimension of the basis.

2. Methods

We follow the definitions of the finite-range pseudopotential introduced in previous studies [7, 8]. The different orders n of the pseudopotential are written as

$$\mathcal{V}_j^{(n)}(\boldsymbol{r_1},\boldsymbol{r_2};\boldsymbol{r_3},\boldsymbol{r_4}) = \left(W_j^{(n)}\hat{1}_\sigma\hat{1}_\tau + B_j^{(n)}\hat{1}_\tau\hat{P}^\sigma - H_j^{(n)}\hat{1}_\sigma\hat{P}^\tau - M_j^{(n)}\hat{P}^\sigma\hat{P}^\tau\right) \times \hat{O}_j^{(n)}(\boldsymbol{k_{12}},\boldsymbol{k_{34}})\,\delta(\boldsymbol{r_{13}})\delta(\boldsymbol{r_{24}})g_a(\boldsymbol{r_{12}})\,,$$

where $\boldsymbol{k_{ij}} = \frac{1}{2i}(\boldsymbol{\nabla_i} - \boldsymbol{\nabla_j})$ is the relative momentum operator, $\boldsymbol{r}_{ij} = \boldsymbol{r}_i - \boldsymbol{r}_j$ is the relative position, and $\hat{P}^\sigma$ ($\hat{P}^\tau$) is the spin (isospin) exchange operator. We used a Gaussian form for the regulator $g_a(\boldsymbol{r}) = \frac{1}{(a\sqrt{\pi})^3}\mathrm{e}^{-\boldsymbol{r}^2/a^2}$ with $a = 1.15$ fm. There are three operators $\hat{O}_j^{(n)}$ up to next-to-leading order (NLO), namely $\hat{O}_1^0(\boldsymbol{k_{12}},\boldsymbol{k_{34}}) = \hat{1}$, $\hat{O}_1^1(\boldsymbol{k_{12}},\boldsymbol{k_{34}}) = \frac{1}{2}(\boldsymbol{k_{12}^{*2}} + \boldsymbol{k_{34}^2})$ and $\hat{O}_2^1(\boldsymbol{k_{12}},\boldsymbol{k_{34}}) = \boldsymbol{k_{12}^*}\cdot\boldsymbol{k_{34}}$. In addition, the zero-range Skyrme

$$\mathcal{V}_\delta(\boldsymbol{r_1},\boldsymbol{r_2};\boldsymbol{r_3},\boldsymbol{r_4}) = t_0\left(1 + x_0\hat{P}^\sigma\right)\delta(\boldsymbol{r_{13}})\delta(\boldsymbol{r_{24}})\delta(\boldsymbol{r_{12}}) \qquad (1)$$

was used with $x_0 = 1$ and $t_0 = 1000$ MeV fm^3. This term is active in the particle–hole channel only and counteracts the strong attraction from the finite-range term needed to obtain pairing strong enough in the bulk. We considered only the local version of pseudopotential defined by the condition $\hat{O}_i(\boldsymbol{k_{34}} + \boldsymbol{k_{12}}) = \hat{O}_i(\boldsymbol{k_{34}} - \boldsymbol{k^*_{12}})$, and as a consequence, parameters were coupled so that $W_2^1 = -W_1^1$, $B_2^1 = -B_1^1$, $H_2^1 = -H_1^1$ and $M_2^1 = -M_1^1$. In the end, there were 9 parameters to be optimized at local NLO, since one constant defining the zero-range spin–orbit term was also optimized.

We optimized parameters $\boldsymbol{p}$ of the functional by minimizing the penalty function

$$\chi^2(\boldsymbol{p}) = \sum_{i=0}^{N_\mathrm{d}} \frac{(\mathcal{O}_i(\boldsymbol{p}) - \mathcal{O}_i^{\mathrm{exp}})^2}{\Delta\mathcal{O}_i^2}\,, \tag{2}$$

where N_d represents the number of data points, $\mathcal{O}_i(\boldsymbol{p})$ and $\mathcal{O}_i^{\mathrm{exp}}$ correspond to theoretical and experimental values of chosen (pseudo-)observables, respectively, and $\Delta\mathcal{O}_i$ represents the tolerance related to the specific data point. Since the purpose of this study was to quantify the effects of the used model space size and compare the results with a parameterization optimized in a coordinate space, the data set followed the one of Ref. [8]. The only exception was the average neutron pairing gap $\langle\Delta_n\rangle$ in ^{120}Sn. In Ref. [8], the average neutron gap was calculated with $\ell_{\mathrm{max}} = 9$ and $\ell_{\mathrm{max}} = 11$ (see [8] for the definition of ℓ_{max}). In this study, it was calculated only once with the same set-up as the other data points. Otherwise, the data set consisted of binding energies and radii of 8 doubly magic and semi-magic nuclei, namely ^{40}Ca, ^{48}Ca, ^{56}Ni, ^{78}Ni, ^{100}Sn, ^{120}Sn, ^{132}Sn and ^{208}Pb, and altogether six data points of pseudo-observables in the infinite and polarized nuclear matter. Finally, to avoid isovector finite-size instabilities, we used the isovector density $\rho_1(\boldsymbol{r})$ in the center of ^{208}Pb, and we aimed for the value $\rho_1(0) > 0$, in the very same manner as described in Ref. [8].

We used the axial code HFBTEMP [9] together with the optimization algorithm POUNDerS [10] for derivative-free nonlinear least squares problems. The code HFBTEMP expands the solutions of the HFB equations on the axial HO basis and we will use it for fits including deformed nuclei in future. We benchmarked HFBTEMP successfully against HFODD [11], and POUNDerS was already applied earlier in the field of nuclear physics [12]. We optimized the local NLO pseudopotential by using three different numbers of the HO shells, namely 10, 12, and 14, whereby we obtained three parameterizations that we discuss.

3. Results

The convergence of the optimization procedure is shown in Fig. 1. In the upper panel, the values of the objective function χ^2 are represented in a logarithmic scale as a function of the number of the optimization round, whereas in the lower panel, the scale of χ^2 is natural. We observe that the required number of optimization iterations does not significantly depend on the used number of the HO shells. However, the needed computational time for every iteration is, of course, greater when a larger model space is used.

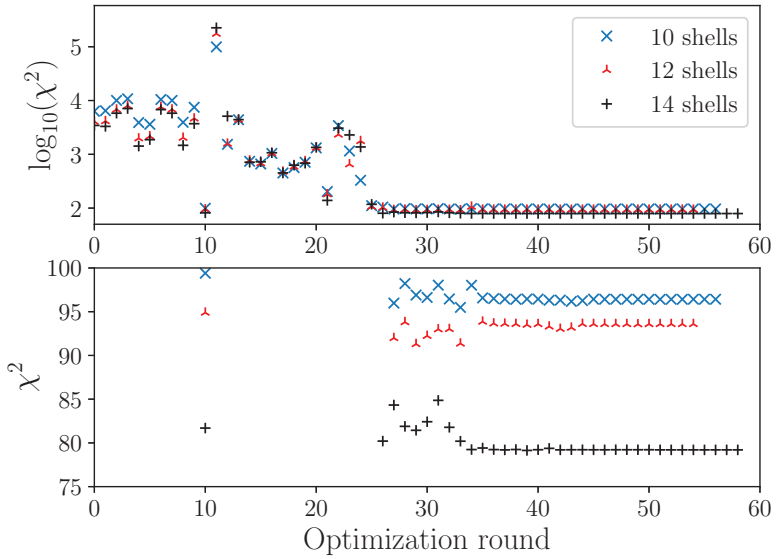

Fig. 1. The objective function χ^2 as a function of the optimization rounds.

Using the same set-up as in the optimization, we tested the three obtained parameterizations by calculating even–even nuclei in the O–Kr part of the nuclear chart. The obtained binding energies are shown in the form of residuals $E_{\mathrm{Th}} - E_{\mathrm{Exp}}$ in Fig. 2. Here, all calculations were done at axially deformed HFB level, that is, for each nucleus, we obtained the energy minimum with respect to deformation. Experimental binding energies were taken from AME2016 atomic mass evaluation [13]. We compare the residuals to the ones given by the parameterization REG2c.161026 of Ref. [8], that was obtained by using the spherical coordinate space code FINRES$_4$ [14]. In this study, the theoretical binding energies given by REG2c.161026 were computed with HFBTEMP and 14 HO shells, assuming axial symmetry.

We observe that the differences between the results obtained with the parameters adjusted for 10, 12, and 14 HO shells are small in this part of the nuclear chart. These results differ more from the ones obtained by REG2c.161026, but still the differences are minor in mid-shell nuclei when comparing to the values of residuals. This can be also seen in Fig. 3, which

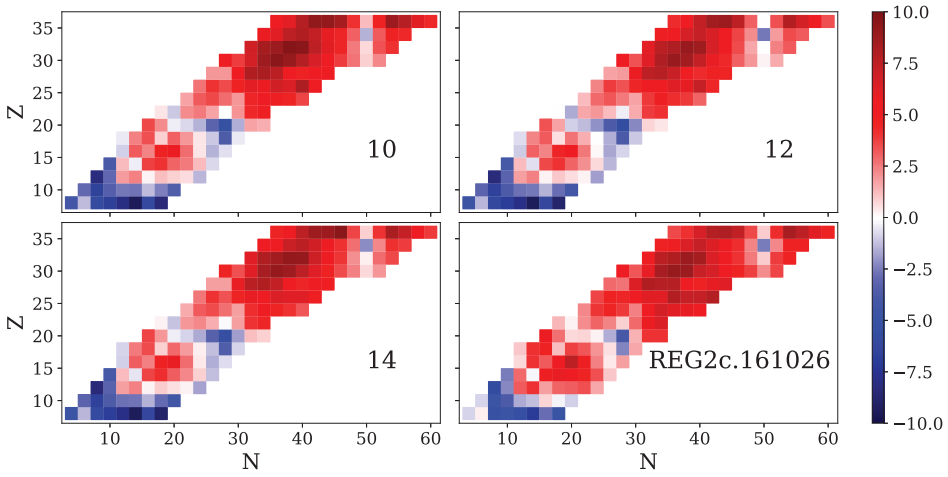

Fig. 2. Binding energy residuals $E_{\mathrm{Th}} - E_{\mathrm{Exp}}$ in units of MeV, calculated with parameter set optimized for 10, 12, and 14 HO shell basis. These are compared to results with REG2c.161026 parameterization [8], calculated here with 14 HO shells.

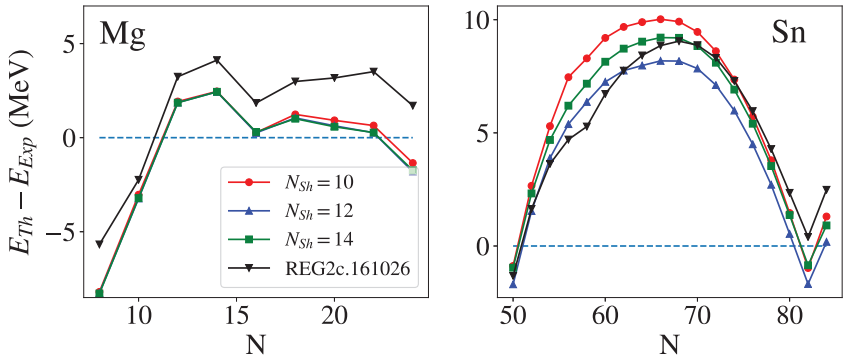

Fig. 3. The same as in Fig. 2, but for the isotopic chains of Mg and Sn and the residual $E_{\mathrm{Th}} - E_{\mathrm{Exp}}$ represented on the ordinate.

represents the binding energy residuals of Mg and Sn nuclei as functions of the neutron number. Figure 3 shows how the binding energy residuals are greater in mid-shell nuclei, as expected, and how the binding energy residuals are not necessarily smaller if a larger model space is used. Our results for REG2c.161026 parameterization give less bound light nuclei since it was optimized with a code using coordinate space representation. This effect fades away in heavier nuclei, since a smaller basis state set can no longer accommodate all relevant aspects of a coordinate-space-based HFB solution.

4. Summary and outlook

We optimized a local finite-range pseudopotential up to next-to-leading order by using 10, 12, and 14 HO shells. We applied the three parameterizations in the O–Kr part of the nuclear chart and Sn isotopic chain. The obtained differences of computed binding energies turn out to be relatively small. This reflects the fact that even though the binding energies do depend on the number of used HO shells, this dependence is fairly well-absorbed in the parameters during the optimization. Nevertheless, importance of the larger model space increases in heavier nuclei. The next step in the optimization of the pseudopotential will be to include data on deformed nuclei in the penalty function, and the work in this direction is in progress.

T.H. was supported by the Finnish Cultural Foundation, North Karelia Regional Fund (grant 55161255). J.D. was supported by the STFC grants Nos. ST/M006433/1 and ST/P003885/1. We acknowledge the CSC-IT Center for Science Ltd., Finland, for the allocation of computational resources.

REFERENCES

[1] D. Davesne *et al.*, *Phys. Rev. C* **97**, 044304 (2018).
[2] J. Dobaczewski *et al.*, *Phys. Rev. C* **76**, 054315 (2007).
[3] M. Bender, T. Duguet, D. Lacroix, *Phys. Rev. C* **79**, 044319 (2009).
[4] F. Raimondi, K. Bennaceur, J. Dobaczewski, *J. Phys. G: Nucl. Part. Phys.* **41**, 055112 (2014).
[5] J. Dobaczewski, *J. Phys. G: Nucl. Part. Phys.* **43**, 04LT01 (2016).
[6] T. Haverinen, M. Kortelainen, *J. Phys. G: Nucl. Part. Phys.* **44**, 044008 (2017).
[7] J. Dobaczewski, K. Bennaceur, F. Raimondi, *J. Phys. G: Nucl. Part. Phys.* **39**, 125103 (2012).
[8] K. Bennaceur *et al.*, *J. Phys. G: Nucl. Part. Phys.* **44**, 045106 (2017).
[9] M. Kortelainen, HFBTEMP code, unpublished.
[10] S.M. Wild, J. Sarich, N. Schunck, *J. Phys. G: Nucl. Part. Phys.* **42**, 034031 (2015).
[11] N. Schunck *et al.*, *Comput. Phys. Commun.* **216**, 145 (2017).
[12] M. Kortelainen *et al.*, *Phys. Rev. C* **85**, 024304 (2012).
[13] M. Wang *et al.*, *Chin. Phys. C* **41**, 030003 (2017).
[14] K. Bennaceur, FINRES_4 code, to be published.

III

REGULARIZED PSEUDOPOTENTIAL FOR MEAN-FIELD CALCULATIONS

by

K. Bennaceur, J. Dobaczewski, T. Haverinen and M. Kortelainen

arxiv:1909.12879

Accepted for publication in Journal of Physics: Conference Series – Proceedings of the 27th International Nuclear Physics Conference (INPC) 2019, Glasgow, UK.

Regularized pseudopotential for mean-field calculations

K Bennaceur[1], J Dobaczewski[2,3,4], T Haverinen[3,5] and M Kortelainen[3,5]

[1] Univ Lyon, Université Claude Bernard Lyon 1, CNRS, IPNL, UMR 5822, 4 rue E. Fermi, F-69622 Villeurbanne Cedex, France
[2] Department of Physics, University of York, Heslington, York YO10 5DD, United Kingdom
[3] Helsinki Institute of Physics, P.O. Box 64, 00014 University of Helsinki, Finland
[4] Institute of Theoretical Physics, Faculty of Physics, University of Warsaw, Pasteura 5, 02-093 Warszawa, Poland
[5] Department of Physics, University of Jyväskylä, P.O. Box 35 (YFL), 40014 University of Jyväskylä, Finland

E-mail: bennaceur@ipnl.in2p3.fr

Abstract. We present preliminary results obtained with a finite-range two-body pseudopotential complemented with zero-range spin-orbit and density-dependent terms. After discussing the penalty function used to adjust parameters, we discuss predictions for binding energies of spherical nuclei calculated at the mean-field level, and we compare them with those obtained using the standard Gogny D1S finite-range effective interaction.

1. Introduction

A new class of pseudopotentials for nuclear structure were introduced several years ago [1, 2, 3]. These pseudopotentials allow for a consistent formulation of the low-energy energy-density-functional (EDF) approach in terms of effective theory. Specifically, this can be done by considering a zero-range effective interaction with derivative terms up to a given order $p = 2n$, hereafter denoted N^{n}LO [4], and replacing the contact Dirac delta function by a regulator,

$$g_a(\mathbf{r}) = \frac{\mathrm{e}^{-\frac{\mathbf{r}^2}{a^2}}}{(a\sqrt{\pi})^3}, \tag{1}$$

where a is the range of the obtained pseudopotential or regularization scale.

In this work we complemented the regularized pseudopotential with the standard zero-range spin-orbit term and two-body zero-range density-dependent effective interaction. Therefore, the obtained EDF is meant to be used at the mean-field (single-reference) level. The density-dependent term represents a convenient way to adjust the nucleon effective mass in infinite nuclear matter to any reasonable value in the interval $0.70 \lesssim m^*/m \lesssim 0.90$ [5]. For this zero-range density dependent term, we use the same form as in the Gogny D1S interaction [6], *i.e.*,

$$\frac{1}{6}\, t_3 \left(1 + x_3\, \hat{P}_\sigma\right) \rho_0^{1/3}(\mathbf{r}_1)\delta(\mathbf{r}_1 - \mathbf{r}_2), \tag{2}$$

where $\hat{P}_\sigma$ is the spin-exchange operator and x_3 is fixed to 1, so for time-even invariant states, this term does not contribute to pairing. Finally, because of the zero-range nature of the spin-orbit term, we omitted its contribution to the pairing channel.

The general EDF derived from this pseudopotential [3], including its particle-hole and particle-particle parts, were limited to the local part. This could constitute a significant restriction to its flexibility. However, such a limitation reduces the number of free parameters to be adjusted and simplifies implementations in the existing codes.

After presenting the ingredients of the penalty function used to adjust the parameters, we present results obtained for binding energy of spherical nuclei along with their comparison with those obtained for the Gogny D1S functional.

2. Adjustments of parameters

The pseudopotentials considered here contain 10 parameters at NLO, 14 at N^{2}LO and 18 at N^{3}LO. We adjusted 15 series of parameters with effective masses of 0.70, 0.75, 0.80, 0.85, and 0.90 at NLO, N^{2}LO, and N^{3}LO. For each series, the range a of the regulator was varied from 0.8 fm to 1.6 fm.

The use of a penalty function containing data for finite nuclei would not be sufficient to efficiently constrain these parameters or even to constrain them at all. Typical reasons for this difficulty are: appearance of finite-size instabilities, phase transitions to unphysical states (for example, those characterized by a very large vector pairing) or numerical problems related to compensations of large coupling constants with opposite signs. To avoid these unwanted situations, the penalty function must contain specially designed constrains that we list here, along with the nuclear data and pseudo-data:

(i) Empirical quantities in infinite nuclear matter: saturation density $\rho_{\rm sat}$, binding energy per nucleon in symmetric matter E/A, compression modulus K_∞, isoscalar effective mass m^*/m symmetry energy coefficient J, and its slope L, see Table 1.

(ii) Decomposition of the potential energy in the different (S,T) channel [7, 8] and binding energy per nucleon in neutron and polarized matter.

(iii) Average pairing gap in infinite nuclear matter for $k_F = 0.4$, 0.8 and 1.2 fm^{-1} with the values obtained with D1S as targets.

(iv) Binding energies of the following 17 spherical (or approximated as spherical) nuclei ^{36}Ca, ^{40}Ca, ^{48}Ca, ^{54}Ca, ^{54}Ni, ^{56}Ni, ^{72}Ni, ^{80}Zr, ^{90}Zr, ^{112}Zr, ^{100}Sn, ^{132}Sn, ^{138}Sn, ^{178}Pb, ^{208}Pb, ^{214}Pb, and ^{216}Th with a tolerance of 1 MeV if the binding energy is known from experiment and 2 MeV if it is extrapolated (values are taken from [9]).

(v) Proton density rms radii (taken from [10]) for ^{40}Ca, ^{48}Ca and ^{208}Pb with a tolerance of 0.02 fm and 0.03 fm for the one of ^{56}Ni (extrapolated from systematics);

(vi) Isovector density at the center of ^{208}Pb and isoscalar density at the center of ^{40}Ca to avoid finite-size scalar-isovector (*i.e.* $S = 0, T = 1$) instabilities. The use of the linear response (as in Ref. [11] for zero-range interactions) would lead to too much time-consuming calculations. Therefore we use these two empirical constraints on these densities which are observed to grow when a scalar-isovector instability tends to develop. Possible instabilities in the vector channels ($S = 1$) are not under control in this series of fits.

(vii) Coupling constants for the vector pairing (given by eq. (36) in [3]) are constrained to be equal to 0 ± 5 MeV fm^3 to avoid transitions to unphysical states with unrealistically large vector pairing.

These adjustments were performed in three steps:

(i) First, we made exploratory adjustments (with fixed values for the effective mass) trying to determine whether the other canonical values for infinite nuclear matter were attainable and,

Table 1. Infinite nuclear matter targeted properties and tolerances used for the final step of the parameters adjustment.

Quantity	E/A [MeV]	$\rho_{\rm sat}$ [fm]$^{-3}$	K_∞ [MeV]	m^*/m	J [MeV]	L [MeV]
Value	-16.0	0.158	230	0.70-0.90	29.0	15.00
Tolerance	0.3	0.003	5	0.001	0.5	0.05

in this case, what would be their optimal values in average. We obtained $\rho_{\rm sat} = 0.158$ fm^{-3}, for the saturation density, $J = 29$ MeV for the symmetry energy coefficient and $L = 15$ MeV for its slope. This value for L is very low compared with what is considered as realistic nowadays [12, 13, 14] but we observed that larger values inevitably lead to finite-size instabilities.

(ii) With effective mass and $\rho_{\rm sat}$, J, and L fixed to these values, and for each value of the effective mass and order of the interaction, we systematically determined the ranges a of the regulator that give the lowest values of the penalty function.

(iii) With these values for the ranges fixed, we readjusted the parameters by relaxing values of $\rho_{\rm sat}$, m^*/m, J, and L and allowing for them narrow tolerances of $\rho_{\rm sat} = 0.158 \pm 0.003$ fm^{-3}, $m^*/m = 0.700 \pm 0.001$, $J = 29.0 \pm 0.5$ MeV, and $L = 15.00 \pm 0.05$ MeV.

The summary of targeted values and tolerances for infinite nuclear matter properties are given in Table 1. The targeted values and tolerances for all other data and pseudo-data will be given and motivated with more details in a forthcoming article [15].

3. Results and discussion

Questions concerning the dependence of the penalty function and observables on the range of the regulator, covariance analysis of the parameters and propagation of statistical errors on calculated quantities will not be discussed in this contribution where we only report results for spherical nuclei. The sets of parameters obtained by minimizing the penalty function will be given in [15].

We have built a set of 214 nuclei with even numbers of protons and neutrons which, according to the predictions obtained with the Gogny D1S interaction [16], can be considered as spherical or almost spherical. In Table 2, we report the obtained average root mean squared deviations $\sqrt{\overline{\Delta E^2}}$ and average deviations $\overline{\Delta E}$. We use the subscript "all" when these quantities are calculated for the full set of 214 even-even nuclei and the subscript "fit" when they are calculated for the 17 nuclei used in the penalty function only.

Since binding energies of nuclei are not the only ingredients used in the penalty function, there is no reason for $\sqrt{\overline{\Delta E^2}}_{\rm fit}$ to decrease when more parameters are used, *i.e.* to decrease with n for interactions at N^{n}LO. Nonetheless, we observe that it decreases with n for all constrained values of the effective mass. Interestingly, $\sqrt{\overline{\Delta E^2}}_{\rm all}$ is also a decreasing function of n for all values of the effective mass but for 0.7. This means that for $m^*/m \geqslant 0.75$, the increase of the number of parameters in the pseudopotential improves its predictive power, at least for the binding energies of spherical nuclei. The average deviation $\overline{\Delta E}_{\rm fit}$ is also a decreasing function of n while, in general, $\overline{\Delta E}_{\rm all}$ has a less regular behaviour, although it does decrease with n for $m^*/m = 0.85$.

To visualize the global behaviour of the results obtained for the binding energies of spherical nuclei, in Fig. 1 we plotted the binding energy residuals obtained for the set of 214 spherical

Table 2. Average root mean squared deviation ($\sqrt{\Delta E^2}$) and average deviation ($\overline{\Delta E}$) for 214 even-even nuclei (with subscript "all") and for the 17 nuclei used in the penalty function (with subscript "fit") for the pseudopotentials at NLO, N^{2}LO and N^{3}LO with effective mass from 0.70 to 0.90.

	m^*/m	0.70	0.75	0.80	0.85	0.90
NLO	$\sqrt{\overline{\Delta E^2}}_{\rm all}$	1.840	1.759	1.801	1.929	2.141
	$\overline{\Delta E}_{\rm all}$	0.382	0.029	-0.301	-0.633	-0.950
	$\sqrt{\overline{\Delta E^2}}_{\rm fit}$	1.899	1.899	1.956	2.052	2.201
	$\overline{\Delta E}_{\rm fit}$	0.112	0.112	0.115	0.121	0.129
N^{2}LO	$\sqrt{\overline{\Delta E^2}}_{\rm all}$	2.028	1.827	1.709	1.594	1.540
	$\overline{\Delta E}_{\rm all}$	0.879	0.670	0.484	0.295	0.116
	$\sqrt{\overline{\Delta E^2}}_{\rm fit}$	1.893	1.741	1.690	1.610	1.602
	$\overline{\Delta E}_{\rm fit}$	0.111	0.102	0.099	0.095	0.094
N^{3}LO	$\sqrt{\overline{\Delta E^2}}_{\rm all}$	1.712	1.577	1.531	1.458	1.490
	$\overline{\Delta E}_{\rm all}$	0.378	0.231	-0.048	-0.105	-0.313
	$\sqrt{\overline{\Delta E^2}}_{\rm fit}$	1.587	1.446	1.690	1.264	1.228
	$\overline{\Delta E}_{\rm fit}$	0.093	0.085	0.080	0.074	0.072

Figure 1. Binding energy residuals obtained with the pseudopotentials with m^*/m constrained to 0.70 at order n = 1, 2 and 3 (black dots) compared with the ones obtained with the D1S Gogny interaction (open square).

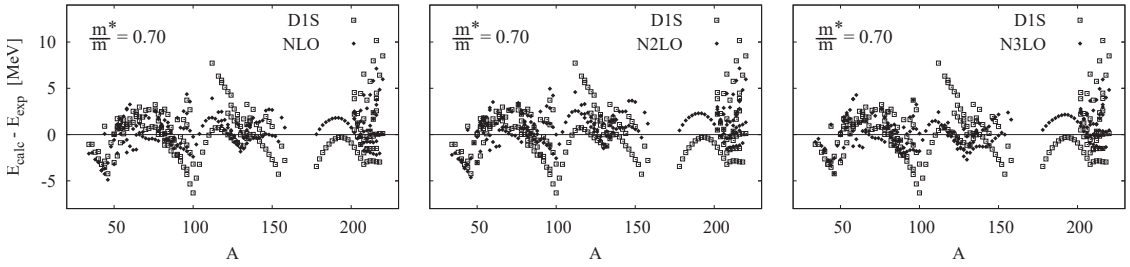

nuclei and for the pseudopotential with $m^*/m = 0.70$ at n = 1, 2, 3. Similarly, in Fig. 2, we plotted those obtained for the pseudopotentials with $m^*/m = 0.85$. We chose these two values because, on the one hand, $m^*/m = 0.70$ is close to the value obtained with D1S and, on the other hand, $m^*/m = 0.85$ is the effective mass that leads to the lowest value for $\sqrt{\overline{\Delta E^2}}_{\rm all}$ (obtained at N^{3}LO). In the same figures, to show the comparison with a commonly used finite-range interaction, we also plotted the residuals obtained for the Gogny D1S EDF. The comparison should be considered with caution, because the Gogny D1S interaction, although often used at the mean-field level only, is supposed to be used in beyond mean-field approaches, such as the 5-dimensional Collective Hamiltonian (known as 5DCH [17]) to provide observables that can be compared with experimental data.

Figure 2. Same as figure 1 for the pseudopotentials with m^*/m constrained to 0.85.

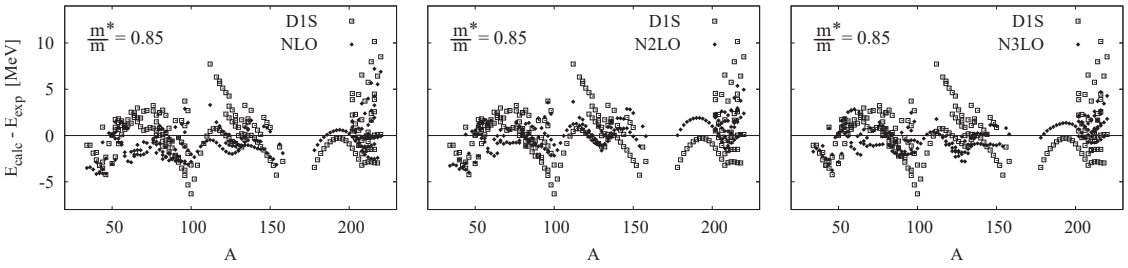

Both figures show that the residuals obtained for the regularized pseudopotentials are more compressed around zero than those obtained for D1S. Fig. 1 explicitly exhibits the information already summarized in Table 2, *i.e.*, for the effective mass of 0.70, adding new parameters in the pseudopotential does not significantly improve the predictive power for the binding energies of spherical nuclei.

Comparing the results shown in Figs. 1 and 2, one can see that the typical arches appearing in the residuals between shell closures are significantly damped. Furthermore, one can see that this damping is more pronounced for higher order pseudopotentials.

4. Conclusion

In this article, we have reported results for binding energies of spherical nuclei obtained for the new class of pseudopotentials introduced several years ago [1, 2, 3]. A more complete study including the discussion of proton radii, single particle energies, and properties of deformed nuclei is in preparation. Although a definitive conclusion can only be drawn after a comparison of a larger body of observables with data, the studied class of pseudopotential looks promising. Possible improvements could still be the inclusion of non-local terms and the use of regularized spin-orbit and tensor terms [2, 3], which will be the subject of future developments. Which part of correlations can be incorporated into the coupling constants of the pseudopotential used at the mean-field (single-reference) level remains an open question.

Acknowledgments

This work was partially supported by the Academy of Finland under the Academy project no. 318043, by the STFC Grants No. ST/M006433/1 and No. ST/P003885/1, and by the Polish National Science Centre under Contract No. 2018/31/B/ST2/02220. We acknowledge the CSC-IT Center for Science Ltd. (Finland) and the IN2P3 Computing Center (CNRS, Lyon-Villeurbanne, France) for the allocation of computational resources.

References

[1] Dobaczewski J, Bennaceur K and Raimondi F 2012 *Journal of Physics G: Nuclear and Particle Physics* **39** 125103

[2] Raimondi F, Bennaceur K and Dobaczewski J 2014 *Journal of Physics G: Nuclear and Particle Physics* **41** 055112

[3] Bennaceur K, Idini A, Dobaczewski J, Dobaczewski P, Kortelainen M and Raimondi F 2017 *Journal of Physics G: Nuclear and Particle Physics* **44** 045106

[4] Carlsson B G, Dobaczewski J and Kortelainen M 2008 *Phys. Rev. C* **78**(4) 044326

[5] Davesne D, Navarro J, Meyer J, Bennaceur K and Pastore A 2018 *Phys. Rev. C* **97**(4) 044304

[6] Berger J, Girod M and Gogny D 1991 *Computer Physics Communications* **63** 365 – 374

[7] Baldo M, Bombaci I and Burgio G F 1997 *Astron. Astrophys.* **328** 274–282

[8] Baldo M 2016 private communication
[9] Wang M, Audi G, Kondev F G, Huang W, Naimi S and Xu X 2017 *Chinese Physics C* **41** 030003
[10] Kortelainen M, Lesinski T, Moré J, Nazarewicz W, Sarich J, Schunck N, Stoitsov M V and Wild S 2010 *Phys. Rev. C* **82**(2) 024313
[11] Hellemans V, Pastore A, Duguet T, Bennaceur K, Davesne D, Meyer J, Bender M and Heenen P H 2013 *Phys. Rev. C* **88**(6) 064323
[12] Li X H, Cai B J, Chen L W, Chen R, Li B A and Xu C 2013 *Physics Letters B* **721** 101 – 106 ISSN 0370-2693
[13] Lattimer J M and Lim Y 2013 *The Astrophysical Journal* **771** 51
[14] Roca-Maza X, Viñas X, Centelles M, Agrawal B K, Colò G, Paar N, Piekarewicz J and Vretenar D 2015 *Phys. Rev. C* **92**(6) 064304
[15] Bennaceur K, Dobaczewski J, Haverinen T, Kortelainen M and Pastore A in preparation
[16] Hilaire S and Girod M 2008 *AIP Conference Proceedings* **1012** 359–361
[17] Libert J, Girod M and Delaroche J P 1999 *Phys. Rev. C* **60**(5) 054301

IV

PROPERTIES OF SPHERICAL AND DEFORMED NUCLEI USING REGULARIZED PSEUDOPOTENTIALS IN NUCLEAR DFT

by

K. Bennaceur, J. Dobaczewski, T. Haverinen and M. Kortelainen

arXiv:2003.10990

Properties of spherical and deformed nuclei using regularized pseudopotentials in nuclear DFT

K Bennaceur[1], J Dobaczewski[2,3,4], T Haverinen[4,5], and M Kortelainen[5,4]

[1]Univ Lyon, Université Claude Bernard Lyon 1, CNRS, IPNL, UMR 5822, 4 rue E. Fermi, F-69622 Villeurbanne Cedex, France

[2]Department of Physics, University of York, Heslington, York YO10 5DD, United Kingdom

[3]Institute of Theoretical Physics, Faculty of Physics, University of Warsaw, Pasteura 5, 02-093 Warszawa, Poland

[4]Helsinki Institute of Physics, P.O. Box 64, 00014 University of Helsinki, Finland

[5]Department of Physics, University of Jyväskylä, P.O. Box 35 (YFL), 40014 University of Jyväskylä, Finland

Abstract. We developed new parameterizations of local regularized finite-range pseudopotentials up to next-to-next-to-next-to-leading order (N^3LO), used as generators of nuclear density functionals. When supplemented with zero-range spin-orbit and density-dependent terms, they provide a correct single-reference description of binding energies and radii of spherical and deformed nuclei. We compared the obtained results to experimental data and discussed benchmarks against the standard well-established Gogny D1S functional.

Submitted to: *J. Phys. G: Nucl. Phys.*

1. Introduction

The nuclear density functional theory (DFT) offers one of the most flexible frameworks to microscopically describe structure of atomic nuclei [1, 2]. A key element in the nuclear DFT is the energy density functional (EDF), which is usually obtained by employing effective forces as its generators. A long-standing goal of nuclear DFT is to construct an EDF with a high precision of describing existing data and a high predictive power.

The Skyrme and Gogny EDFs [1, 3] are the most utilized non-relativistic EDFs in nuclear structure calculations. The Skyrme EDF is based on a zero-range generator, combined with a momentum expansion up to second order, whereas the Gogny EDF is based on the generator constructed with two Gaussian terms. While zero-range potentials are computationally simpler and less demanding, they lack in flexibility of their exchange terms. In addition, in the pairing channel they manifest the well-known problem of nonconvergent pairing energy, which needs to be regularized, see

Refs. [4, 5] and references cited therein. While Skyrme-type EDFs can reproduce various nuclear bulk properties relatively well, their limits have been reached [6], and proposed extensions of zero-range generators [7, 8] did not prove efficient enough [9]. New approaches are, therefore, required.

To improve present EDFs, a possible route is to use EDFs based on regularized finite-range pseudopotentials [10]. Such EDFs stem from a momentum expansion around a finite-range regulator and thus have a form compatible with powerful effective-theory methods [11, 12]. Here, as well as in our earlier studies [13, 14], we chose a Gaussian regulator, which offers numerically simple treatment, particularly when combined with the harmonic oscillator basis. The momentum expansion can be built order-by-order, resulting in an EDF with increasing precision. Due to its finite-range nature, treatment of the pairing channel does not require any particular regularization or renormalization.

The ultimate goal of building EDFs based on regularized finite-range pseudopotentials is to apply them to beyond mean-field multi-reference calculations. However, before that, to evaluate expected performance and detect possible pitfalls, their predictive power should be benchmarked at the single-reference level. The goal of this work is to adjust the single-reference parameters of pseudopotentials up to next-to-next-to-next-to-leading order (N^3LO) and to compare the obtained results to experimental data on the one hand and to those obtained for the Gogny D1S EDF [15] on the other. The D1S EDF offers an excellent reference to compare to, because it contains finite-range terms of a similar nature, although its possible extensions to more than two Gaussians [16], cannot be cast in the form of an effective-theory expansion. Because EDFs adjusted in present work are intended to be used solely at the single-reference level, they include a density-dependent term. This term significantly improves infinite nuclear matter properties, with the drawback that such EDFs become unsuitable for multi-reference calculations, see, e.g., Refs. [17, 18].

This article is organized as follows. In Sec. 2, we briefly recall the formalism of the regularized finite-range pseudopotential and in Sec. 3 we present details of adjusting its parameters. Then, in Secs. 4 and 5, we present results and conclusions of our study, respectively. In Appendices A–D, we give specific details of our approach and in the supplemental material (URL will be inserted by publisher) we collected files with numerical results given in a machine readable format.

2. Pseudopotential

In this study, we use the local regularized pseudopotential with terms at nth order introduced in [13],

$$\mathcal{V}^{(n)}_{\rm loc}(\mathbf{r}_1,\mathbf{r}_2;\mathbf{r}_3,\mathbf{r}_4) = \Big(W_1^{(n)}\hat{1}_\sigma\hat{1}_\tau + B_1^{(n)}\hat{1}_\tau\hat{P}^\sigma - H_1^{(n)}\hat{1}_\sigma\hat{P}^\tau - M_1^{(n)}\hat{P}^\sigma\hat{P}^\tau\Big) \times \delta(\mathbf{r}_{13})\delta(\mathbf{r}_{24})\left(\frac{1}{2}\right)^{n/2}\mathbf{k}_{12}^n g_a(\mathbf{r}_{12})\,, \tag{1}$$

where the Gaussian regulator is defined as

$$g_a(\mathbf{r}) = \frac{1}{(a\sqrt{\pi})^3}\,\mathrm{e}^{-\frac{\mathbf{r}^2}{a^2}}\,, \tag{2}$$

and $\hat{1}_\sigma$ and $\hat{1}_\tau$ are respectively the identity operators in spin and isospin space and $\hat{P}^\sigma$ and $\hat{P}^\tau$ the spin and isospin exchange operators. Standard relative-momentum operators are defined as $\mathbf{k}_{ij} = \frac{1}{2i}\left(\boldsymbol{\nabla}_i - \boldsymbol{\nabla}_j\right)$ and relative positions as $\mathbf{r}_{ij} = \mathbf{r}_i - \mathbf{r}_j$.

Up to the nth order (N^{n}LO), this pseudopotential depends on the following parameters,

- 8 parameters up to the next-to-leading-order (NLO): $W_1^{(0)}$, $B_1^{(0)}$, $H_1^{(0)}$, $M_1^{(0)}$, $W_1^{(2)}$, $B_1^{(2)}$, $H_1^{(2)}$ and $M_1^{(2)}$;
- 4 additional parameters up to N^{2}LO: $W_1^{(4)}$, $B_1^{(4)}$, $H_1^{(4)}$ and $M_1^{(4)}$;
- and 4 additional parameters up to N^{3}LO: $W_1^{(6)}$, $B_1^{(6)}$, $H_1^{(6)}$ and $M_1^{(6)}$.

In the present study, we determined coupling constants of pseudopotentials that are meant to be used at the single-reference level. Therefore, we complemented pseudopotentials (1) with standard zero-range spin-orbit and density-dependent terms,

$$\mathcal{V}_{\mathrm{SO}}(\mathbf{r}_1,\mathbf{r}_2;\mathbf{r}_3,\mathbf{r}_4) = iW_{\mathrm{SO}}\left(\boldsymbol{\sigma}_1+\boldsymbol{\sigma}_2\right)\cdot\left(\mathbf{k}'^{*}_{12}\times\mathbf{k}_{34}\right)\delta(\mathbf{r}_{13})\delta(\mathbf{r}_{24})\delta(\mathbf{r}_{12})\,, \tag{3}$$

$$\mathcal{V}_{\mathrm{DD}}(\mathbf{r}_1,\mathbf{r}_2;\mathbf{r}_3,\mathbf{r}_4) = \frac{1}{6}\,t_3\left(1+\hat{P}_\sigma\right)\rho_0^{1/3}(\mathbf{r}_1)\delta(\mathbf{r}_{13})\delta(\mathbf{r}_{24})\delta(\mathbf{r}_{12})\,, \tag{4}$$

which carry two additional parameters W_{SO} and t_3. The density-dependent term, which has the same form as in the Gogny D1S interaction [15], represents a convenient way to adjust the nucleon effective mass in infinite nuclear matter to any reasonable value in the interval $0.70 \lesssim \frac{m^*}{m} \lesssim 0.90$ [19]. This term contributes neither to the binding of the neutron matter nor to nuclear pairing in time-even systems. To avoid using a zero-range term in the pairing channel, we neglect contribution of the spin-orbit term to pairing.

Expressions giving the contributions to the EDFs of the local regularized pseudopotential (1) can be found in Ref. [14], whereas those of the zero-range spin-orbit (3) and density-dependent term (4) can be found, for example, in Refs. [20, 21].

3. Adjustments of parameters

As explained in Sec. 2, pseudopotentials considered here contain 10 parameters at NLO, 14 at N^{2}LO, and 18 at N^{3}LO. In this study, we adjusted 15 series of parameters with effective masses m^*/m equal to 0.70, 0.75, 0.80, 0.85, and 0.90 at NLO, N^{2}LO, and N^{3}LO. For each series, the range a of the regulator was varied between 0.8 and 1.6 fm.

Our previous experience shows that the use of a penalty function only containing data on finite nuclei is not sufficient to efficiently constrain parameters of pseudopotentials, or even to constrain them at all. Typical reasons for these difficulties are (i) appearance of finite-size instabilities, (ii) phase transitions to unphysical states (for example those with very large vector pairing), or (iii) numerical problems due to compensations of large coupling constants with opposite signs. To avoid these unwanted

situations, the penalty function must contain specially designed empirical constrains. Before performing actual fits, such constrains cannot be easily defined; therefore, to design the final penalty function, we went through the steps summarized below.

- Step 1:
  We made some preliminary fits so as to detect possible pitfalls and devise ways to avoid them. The main resulting observation was that it seems to be very difficult, if possible at all, to adjust parameters leading to a value of the slope of the symmetry energy coefficient L in the range of the commonly accepted values, which is roughly between 40 and 70 MeV [22, 23, 24]. Therefore, for all adjustments performed in this study, we set its value to $L = 15\,\mathrm{MeV}$. This value is rather low, although it is at a similar lower side as those corresponding to various Gogny parameterizations: $L = 18.4\,\mathrm{MeV}$ for D1 [25], $L = 22.4\,\mathrm{MeV}$ for D1S [15], $L = 24.8\,\mathrm{MeV}$ for D1M [26], or $L = 43.2\,\mathrm{MeV}$ for D1M* [27].
- Step 2:
  With the fixed value of $L = 15\,\mathrm{MeV}$, we performed a series of exploratory adjustments with fixed values of other infinite-nuclear-matter properties, that is, for the saturation density of $\rho_{\mathrm{sat}} = 0.16\,\mathrm{fm}^{-3}$, binding energy per nucleon in infinite symmetric matter of $E/A = -16\,\mathrm{MeV}$, compression modulus of $K_\infty = 230\,\mathrm{MeV}$, and symmetry energy coefficient of $J = 32\,\mathrm{MeV}$. These initial values were the same as for the Skyrme interactions of the SLy family [28, 29]. The conclusion drawn from this step was that the favoured values for ρ_{sat} and J were slightly lower than the initial ones. Therefore, we decided to fix ρ_{sat} and J at the results corresponding to pseudopotentials giving the lowest values of the penalty function χ^2, see Fig. 1 and Table 1.
- Step 3:
  In a consistent effective theory, with increasing order of expansion, the dependence of observables on the range a of the regulator should become weaker and weaker. In our previous work [14], where all terms of the pseudopotential were regulated with the same range, such a behaviour was clearly visible. In the present work, the regulated part of the pseudopotential is combined with two zero-range terms. As a result, even at $\mathrm{N^3LO}$, there remains a significant dependence of the penalty functions on a, see Fig. 1. Therefore, in step 3 we picked for further analyses the parameterizations of pseudopotentials that correspond to the minimum values of penalty functions.
  Then, for each of the five values of the effective mass and for each of the three orders of expansion, we optimized the corresponding parameters of the pseudopotential, but this time with the infinite-matter properties not rigidly fixed but allowed to change within small tolerance intervals, see Table 1.

In the supplemental material (URL will be inserted by publisher), the corresponding 15 sets of parameters are listed in a machine readable format. Following the naming convention adopted in Ref. [30], these final sets are named as REGnm.190617, where

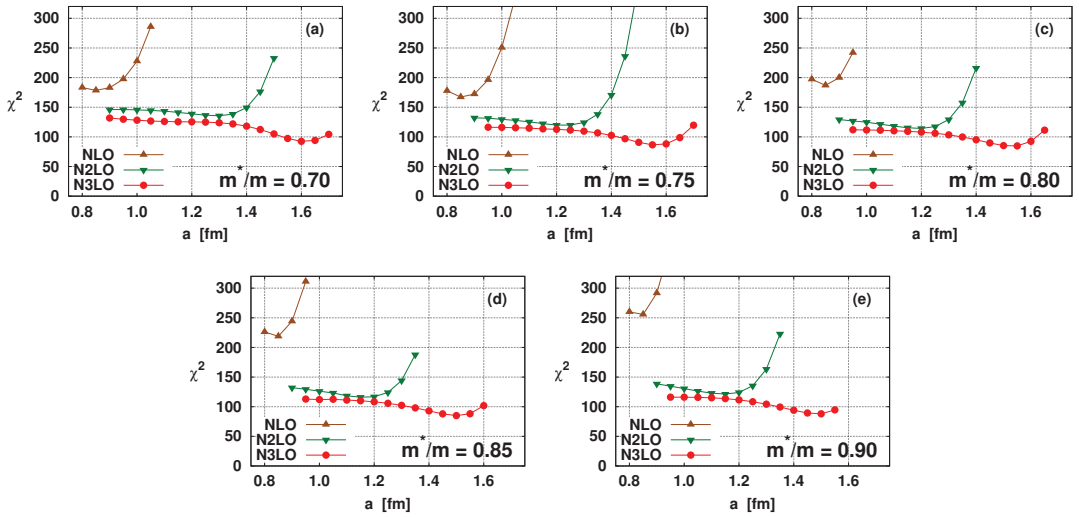

Figure 1. Penalty functions χ^2 obtained in step 2 of the adjustment (see text) as functions of the regulator range a. Panels (a)-(e) correspond to the five values of the effective mass adopted in this study.

Table 1. Target infinite nuclear matter properties and the corresponding tolerance intervals used in step 3 of the adjustment (see text).

Quantity	E/A [MeV]	$\rho_{\rm sat}$ [fm^{-3}]	K_∞ [MeV]	m^*/m	J [MeV]	L [MeV]
Value	-16.0	0.158	230	0.70-0.90	29.0	15.00
Tolerance	0.3	0.003	5	0.001	0.5	0.05

n stands for the order of the pseudopotential ($n = 2$ at NLO, $n = 4$ at N^{2}LO, and $n = 6$ at N^{3}LO), and m = a, b, c, d, or e stands for one of the five adopted values of the effective mass m^*/m 0.70, 0.75, 0.80, 0.85, or 0.90, respectively. For brevity, in the remaining of this paper, we omit the date of the final adjustment, denoted by 190617, which otherwise is an inherent part of the name.

We are now in a position to list all contributions to the penalty function χ^2, which come from the empirical constrains used in step 3 of the adjustment and from those corresponding to the nuclear data and pseudo-data that we used.

(i) Empirical properties of the symmetric infinite nuclear matter. These correspond to: saturation density $\rho_{\rm sat}$, binding energy per nucleon E/A, compression modulus K_∞, isoscalar effective mass m^*/m, symmetry energy coefficient J, and its slope L. The target values and the corresponding tolerance intervals are listed in Table 1.

(ii) Potential energies per nucleon in symmetric infinite nuclear matter. We used values in four spin-isospin channels (S, T) determined in theoretical calculations of

Refs. [31, 32]. Although it is not clear if these constraints have any significant impact on the observables calculated in finite nuclei, we observed that they seem to prevent the aforementioned numerical instabilities due to compensations of large coupling constants with opposite signs. Explicit formulas for the decomposition of the potential energy in the (S,T) channels are given in Appendix A.

(iii) Energy per nucleon in infinite neutron matter. We used values calculated for potentials UV14 plus UVII (see Table III in [33]) at densities below 0.4 fm^{-3} with a tolerance interval of 25 %.

(iv) Energy per nucleon in polarized infinite nuclear matter. Adjustment of parameters often leads to the appearance of a bound state in symmetric polarized matter. To avoid this type of result, we used the constraint of $E/A = 12.52\,\mathrm{MeV}$ at density $0.1\,\mathrm{fm}^{-3}$ (taken from Ref. [34]) with a large tolerance interval of 25 %.

(v) Average pairing gap in infinite nuclear matter. Our goal was to obtain a reasonable profile for the average gap in symmetric infinite nuclear matter and to avoid too frequent collapse of pairing for deformed minima (especially for protons). Therefore, we used as targets the values calculated for the D1S functional at $k_F = 0.4$, 0.8, and $1.2\,\mathrm{fm}^{-1}$ with the tolerance intervals of 0.1 MeV.

(vi) Binding energies of spherical nuclei. We used experimental values of the following 17 spherical (or approximated as spherical) nuclei ^{36}Ca, ^{40}Ca, ^{48}Ca, ^{54}Ca, ^{54}Ni, ^{56}Ni, ^{72}Ni, ^{80}Zr, ^{90}Zr, ^{112}Zr, ^{100}Sn, ^{132}Sn, ^{138}Sn, ^{178}Pb, ^{208}Pb, ^{214}Pb, and ^{216}Th. We attributed tolerance intervals of 1 MeV (2 MeV) if the binding energy was known experimentally (extrapolated) [35]. The motivation for this list was to use open-shell nuclei along with doubly magic ones, so as to better constrain distances between successive shells.

(vii) Proton rms radii. We used values taken from Ref. [36] for ^{40}Ca, ^{48}Ca, ^{208}Pb, and ^{214}Pb with the tolerance intervals of 0.02 fm and that for ^{56}Ni (which is extrapolated from systematics) with the tolerance interval of 0.03 fm.

(viii) Isovector and isoscalar central densities. To avoid finite-size scalar-isovector (*i.e.* $S = 0$, $T = 1$) instabilities, we used isovector density at the center of ^{208}Pb and isoscalar density at the center of ^{40}Ca. A use of the linear response methodology (such as in Ref. [37] for zero-range interactions) would lead to too much time-consuming calculations. As a proxy, we used the two empirical constraints on central densities, which are known to grow uncontrollably when the scalar-isovector instabilities develop. We used the empirical values of $\rho_1(0) < 0\,\mathrm{fm}^{-3}$ in ^{208}Pb and $\rho_0(0) < 0.187\,\mathrm{fm}^{-3}$ in ^{40}Ca with asymmetric tolerance intervals as described in Ref. [14]. For $\rho_0(0)$ in ^{40}Ca, we have used the central density obtained with SLy5 [29] as an upper limit. In the parameter adjustments performed in this study, possible instabilities in the vector channels ($S = 1$) are still not under control.

(ix) Surface energy coefficient. As it was recently shown [38, 39], a constraint on the surface energy coefficient is an efficient way to improve properties of EDFs. For the regularized pseudopotentials considered here, we calculate a simple estimate of the

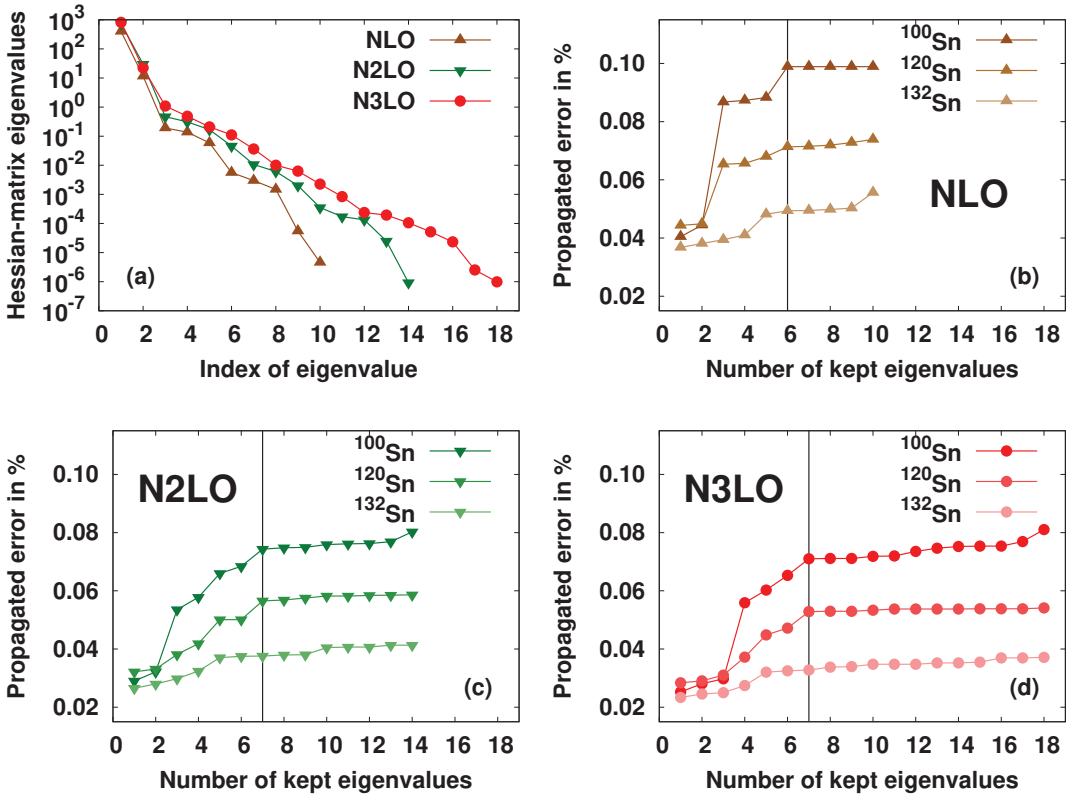

Figure 2. Results of statistical analyses performed for parameterizations corresponding to $m^*/m = 0.85$. Eigenvalues of the Hessian matrices (a) are compared with propagated uncertainties of binding energies of ^{100}Sn, ^{120}Sn, and ^{132}Sn, determined at NLO REG2d (b), N^{2}LO REG4d (c), and N^{3}LO REG2d (d) plotted as functions of the numbers of eigenvalues kept in the Hessian matrices.

surface energy coefficient using a liquid-drop type formula $a_{\rm surf}^{\rm LDM}$ with target value of 18.5 MeV and the tolerance interval of 0.2 MeV. The relevance of this constraint and the motivation for the target value are discussed in Appendix B.

(x) Coupling constants corresponding to vector pairing. Terms of the EDF that correspond to this channel are given in Eq. (36) of Ref. [14]. To avoid transitions to unphysical regions of unrealistically large vector pairing, we constrain them to be equal to 0 ± 5 MeV fm^3.

4. Results and discussion

4.1. Parameters and statistical uncertainties

For the purpose of presenting observables calculated in finite nuclei, we decided to use a criterion of binding energies of spherical nuclei, see Sec. 4.3. It then appears that optimal results are obtained for $m^*/m = 0.85$ at N^{3}LO [40] and $a = 1.50$ fm, that

is, for the pseudopotential named REG6d. Following this guidance, below we also present some results corresponding to the same effective mass of $m^*/m = 0.85$ and lower orders: REG2d (NLO and $a = 0.85\,\mathrm{fm}$) and REG4d ($\mathrm{N^2LO}$ and $a = 1.15\,\mathrm{fm}$). For an extended comparison with the Gogny D1S parameterization [15], which corresponds to $m^*/m = 0.697$, we also show results for $m^*/m = 0.70$, that is, for REG6a ($\mathrm{N^3LO}$ and $a = 1.60\,\mathrm{fm}$). Parameters of the four selected pseudopotentials are tabulated in Appendix C. In the supplemental material (URL will be inserted by publisher) they are collected in a machine readable format.

We performed the standard analysis of statistical uncertainties as presented in Ref. [41]. For REG2d, REG4d and REG6d, eigenvalues of the Hessian matrices corresponding to penalty functions scaled to $\chi^2 = 1$ are shown in Fig, 2(a). The numbers of eigenvalues correspond to the numbers of parameters optimized during the adjustments, and, therefore, vary from 10 (NLO) to 18 ($\mathrm{N^3LO}$).

The magnitude of the eigenvalues of the Hessian matrices reveals how well the penalty functions are constrained in the directions of the corresponding eigenvectors in the parameter space. We observe that for the three pseudopotentials considered here, there is a rapid decrease of magnitude from the first to the third eigenvalue and then a slower and almost regular decrease, where no clear gap can be identified. This suggests that all parameters of the pseudopotentials are important.

For three tin isotopes of different nature: ^{100}Sn (closed-shell, isospin symmetric, unpaired), ^{120}Sn (open-shell, isospin asymmetric, paired) and ^{132}Sn (closed-shell, isospin asymmetric, unpaired), we calculated the propagated statistical uncertainties of the total binding energies as functions of the number of kept eigenvalues of the Hessian matrices, Figs 2(b)-(d) for REG2d–REG6d, respectively. For each of the considered parameterizations, after a given number of kept eigenvalues (denoted in Figs 2(b)-(d) by vertical lines), we observe a saturation of the propagated statistical uncertainties. Therefore, we performed the final determination of the statistical uncertainties by keeping these minimal numbers of eigenvalues, *i.e.* 6 eigenvalues for REG2d (NLO) and 7 for REG4d ($\mathrm{N^2LO}$) and REG6d ($\mathrm{N^3LO}$).

4.2. Infinite nuclear matter

In Table 2, we list quantities characterizing the properties of infinite nuclear matter. We present results for pseudopotentials REG2d, REG4d, REG6d, and REG6a compared to those characterizing the D1S interaction [15]. For the two strongly constrained quantities, m^*/m and L, the target values are almost perfectly met, whereas, for the other ones, we observe some deviations, which, nevertheless, are well within the tolerance intervals allowed in the penalty function.

For pseudopotentials REG6a and REG6d, the isoscalar effective mass in symmetric matter and energies per particle (equations of state) for symmetric, neutron, polarized, and polarized neutron matter are plotted in Fig. 3 along with the same quantities for D1S [15]. The plotted equations of state can be obtained from those calculated in four

Table 2. Infinite nuclear matter properties corresponding to pseudopotentials REG2d, REG4d, REG6d, and REG6a, compared to those of the Gogny D1S interaction [15].

Pseudopotential	E/A [MeV]	$\rho_{\rm sat}$ [fm^{-3}]	K_∞ [MeV]	m^*/m	J [MeV]	L [MeV]
REG2d	-15.86	0.1574	235.4	0.8499	29.24	14.99
REG4d	-15.86	0.1589	225.6	0.8492	29.17	15.00
REG6d	-15.77	0.1584	232.1	0.8496	28.56	15.00
REG6a	-15.74	0.1564	233.6	0.7014	28.23	15.00
D1S	-16.01	0.1633	202.8	0.6970	31.13	22.44

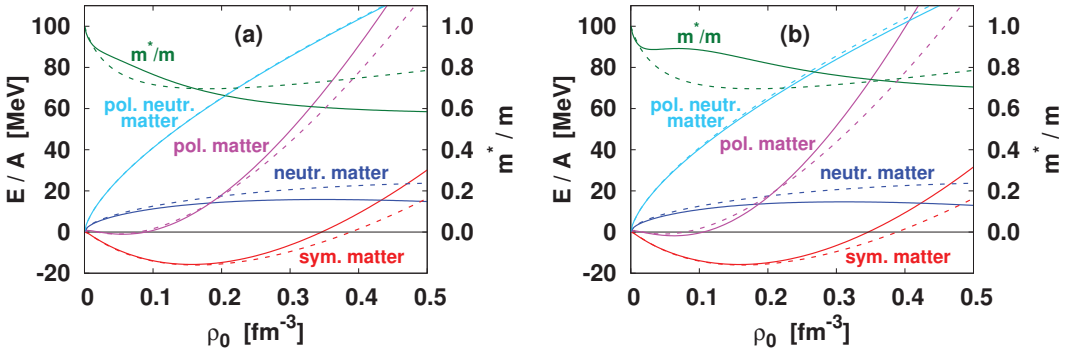

Figure 3. Infinite-nuclear-matter isoscalar effective mass and energies per particle in symmetric, neutron, polarized, and polarized neutron matter as functions of the nuclear density ρ_0. Results calculated for the D1S interaction [15] (dashed lines) are compared with those obtained for the two pseudopotentials at N^{3}LO with $m^*/m = 0.70$ (a) and $m^*/m = 0.85$ (b) (solid lines).

spin-isospin (S, T) channels, see Appendix A. For these two N^{3}LO pseudopotentials, equations of state of symmetric matter are somewhat stiffer than that obtained for D1S. This is because of its slightly larger compression modulus K_∞. We also can see that for polarized symmetric matter, a shallow bound state appears at low density. This feature also affects D1S. The constraint on the equation of state of polarized symmetric matter introduced in the penalty function has probably limited the development of this state, but did not totally avoid its appearance. Further studies are needed to analyze to what extent it could impact observables calculated in time-odd nuclei and how this possible flaw might be corrected.

The two main differences that appear when we compare the properties in infinite nuclear matter of REG6a and REG6d on one hand and those of D1S on the other hand relate to the equation of state of the neutron matter and isoscalar effective

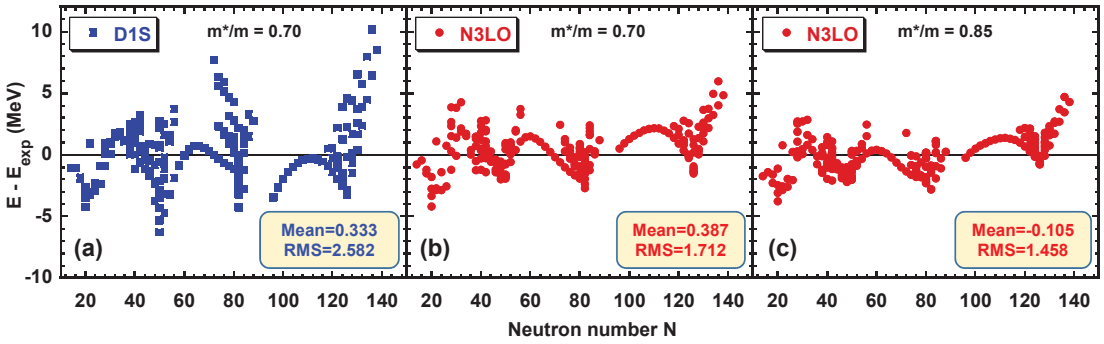

Figure 4. Binding-energy residuals as functions of the neutron number, calculated for a set of spherical nuclei (see text) and plotted for the D1S [15] (a), REG6a (b), and REG6d (c) pseudopotentials.

masses. First, near saturation, the regularized pseudopotentials give equations of state of neutron matter slightly lower than D1S, which can be attributed to its lower symmetry energy. Second, for the N^{3}LO pseudopotentials, dependence of the effective on density is less regular than for D1S. We note, however, that the N^{3}LO effective masses are monotonically decreasing functions of the density, and thus the pseudopotentials obtained in this study do not lead to a surface-peaked effective mass, a feature which was expected to improve the description of the density of states around the Fermi energy [42].

4.3. Binding energies, radii, and pairing gaps of spherical nuclei

In this section, we present results of systematic calculations performed for spherical nuclei and compared with experimental data. For the purpose of such a comparison, we have selected a set of 214 nuclei that were identified as spherical in the systematic calculations performed for the D1S functional in Refs. [43, 44]. In Fig. 4, we present an overview of the binding-energy residuals obtained for the D1S, REG6a, and REG6d functionals. Experimental values were taken from the 2016 atomic mass evaluation [35]. The obtained root-mean-square (RMS) binding-energy residuals are equal to 2.582 MeV for D1S, 1.717 MeV for REG6a, and 1.458 MeV for REG6d. We also see that for REG6d, the trends of binding-energy residuals along isotopic chains in heavy nuclei become much better reproduced. As a reference, we have also determined the analogous RMS value corresponding to the UNEDF0 functional [36, 45], which turns out to be equal to 1.900 MeV.

In Figs. 5 and 6, we show detailed values of binding-energy residuals along the isotopic or isotonic chains of semi-magic nuclei. In most chains one can see a clear improvement of the isospin dependence of masses. In particular, in almost all semi-magic chains, kinks of energy residuals at doubly magic nuclei either decreased or even vanished completely, like at $N = 82$ and 126, see Figs. 6(b) and (c), respectively.

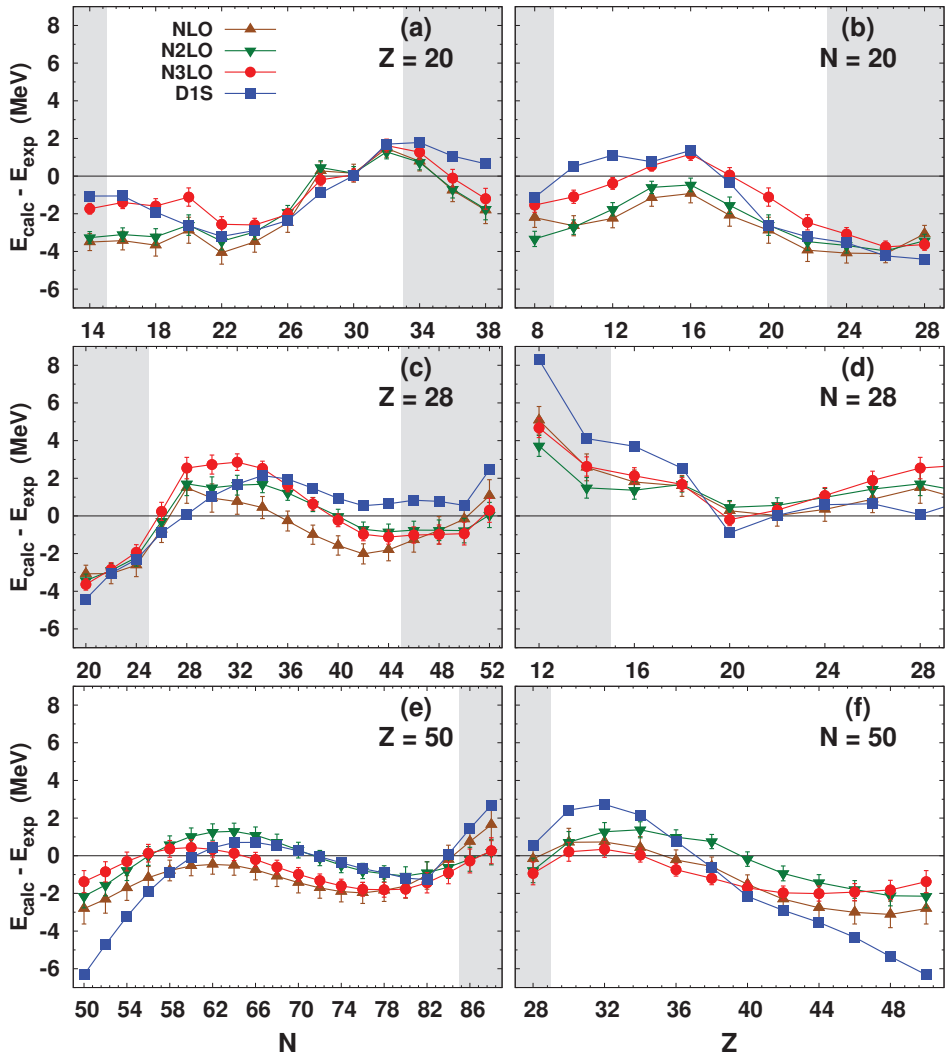

Figure 5. Binding-energy residuals of proton (neutron) semi-magic nuclei with Z (N) equal to 20, 28, or 50, plotted in the left (right) panels as functions of the neutron (proton) number, calculated for the REG2d (up triangles), REG4d (down triangles), REG6d (circles), and D1S [15] (squares) pseudopotentials. Shaded zones correspond to the AME2016 masses extrapolated from systematics [35].

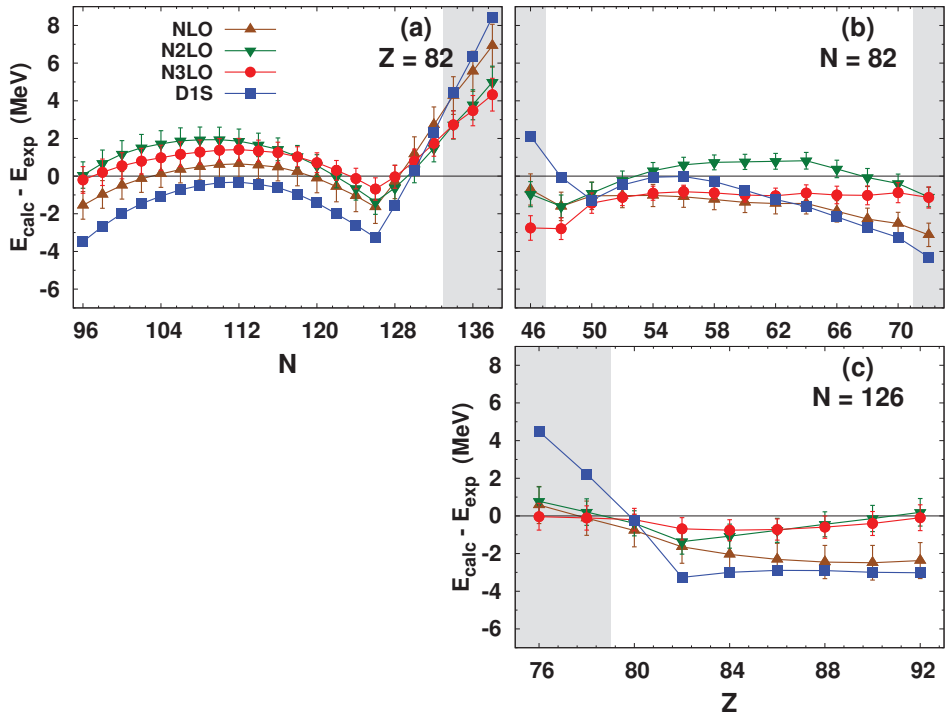

Figure 6. Same as in Fig. 5 but for the semimagic nuclei with $Z = 82$, $N = 82$ and $N = 126$.

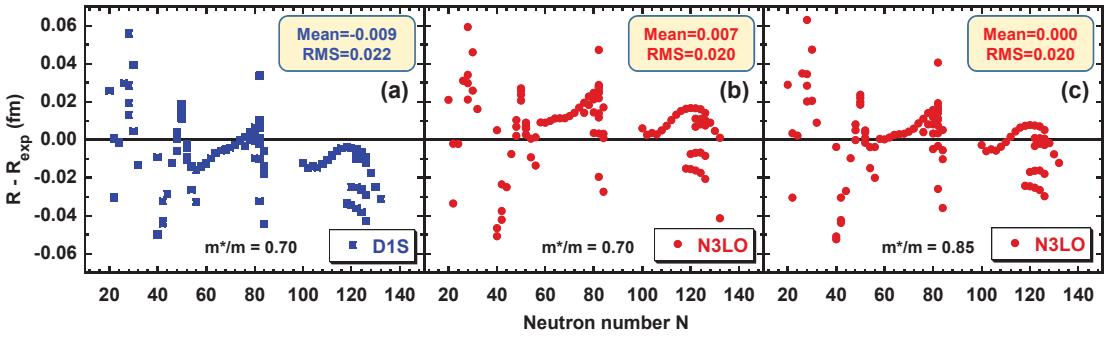

Figure 7. Same as in Fig. 4 but for the charge-radii residuals.

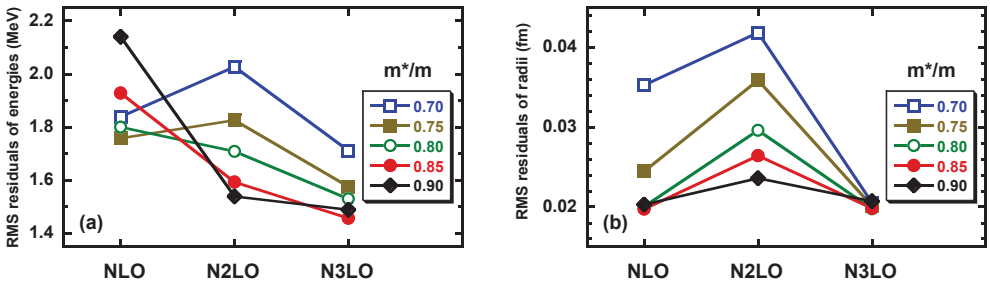

Figure 8. RMS residuals of binding energies (a) and charge radii (b) as functions of the order of pseudopotentials, adjusted in this study for the five values of the isoscalar effective mass m^*/m.

In Fig. 7, for the same set of EDFs and nuclei as those used in Fig. 4, we show the analogous residuals of the charge radii of spherical nuclei. The experimental values were taken from Ref. [46]. Again, the N^{3}LO EDFs provide the smallest deviations from data. We note that the residuals of the order of 0.02 fm are typical for many Skyrme-like EDFs, for example, for the UNEDF family of EDFs [6]. Figures 8(a) and (b) present summary of the RMS residuals of binding energies and charge radii, respectively, which were obtained in this study. We see that a decrease of the penalty functions when going from NLO to N^{2}LO, see Fig. 1, is often accompanied by an increase of the RMS residuals. This indicates that the data for 17 spherical nuclei, which are included in the penalty function, see Sec. 3, do not automatically lead to a better description of all spherical nuclei. Only at N^{3}LO a consistently better description is obtained.

Finally, in Figs. 9 and 10, we show calculated average neutron and proton pairing gaps, respectively. Qualitatively, all three EDFs shown in the figures give very similar results. A thorough comparison with experimental odd-even mass staggering, along with parameter adjustments better focused on the pairing channel, will be the subject of a forthcoming publication.

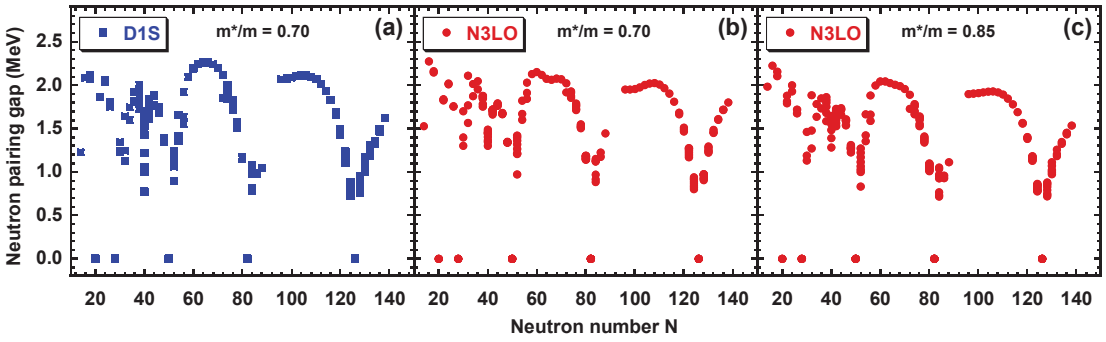

Figure 9. Same as in Fig. 4 but for the average neutron pairing gaps.

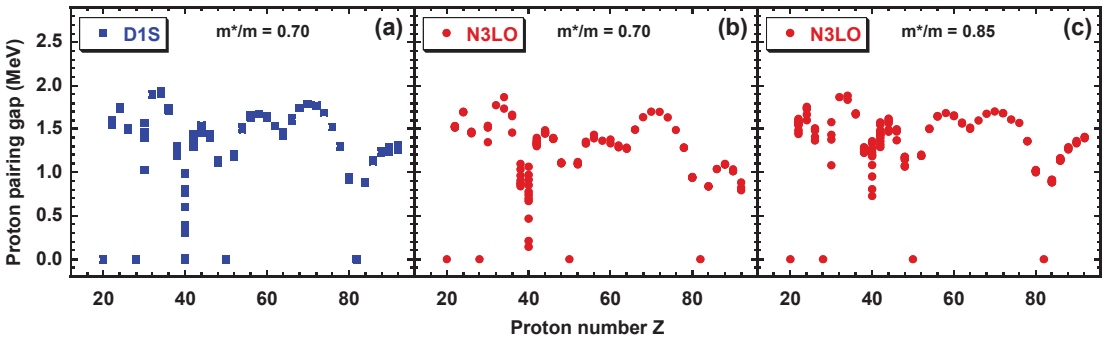

Figure 10. Same as in Fig. 9 but for the average proton pairing gaps.

4.4. Single particle energies

In Figs. 11 and 12, we show comparison of single-particle energies calculated in semi-magic nuclei for the D1S [15], REG6a ($m^*/m = 0.70$), and REG6d ($m^*/m = 0.85$) functionals with the empirical values taken from the compilation published in the supplemental material of Ref. [47], which contains the single-particle energies collected within three data sets. In all panels of Figs. 11 and 12, horizontal lines of the rightmost columns represent average values of the three data sets, whereas shaded boxes represent spreads between the minimum and maximum values. Quantum numbers in parentheses indicate single-particle states with corresponding attributed spectroscopic factors smaller than 0.8 or unknown.

The spin-orbit interaction corresponding to functional REG6a ($m^*/m = 0.70$) is significantly different than that of D1S, which may explain differences between the single-particle energies of states with large orbital angular momenta. Differences between the results obtained for functionals with $m^*/m = 0.70$ and $m^*/m = 0.85$ mostly amount to a global compression. Generally speaking, the calculated single-particle energy spacings are larger than those of the empirical ones, which can be explained by the effective masses being smaller than one.

We note that the comparison between the calculated and empirical single-particle energies is given here only for the purpose of illustration. Indeed, both are subjected to

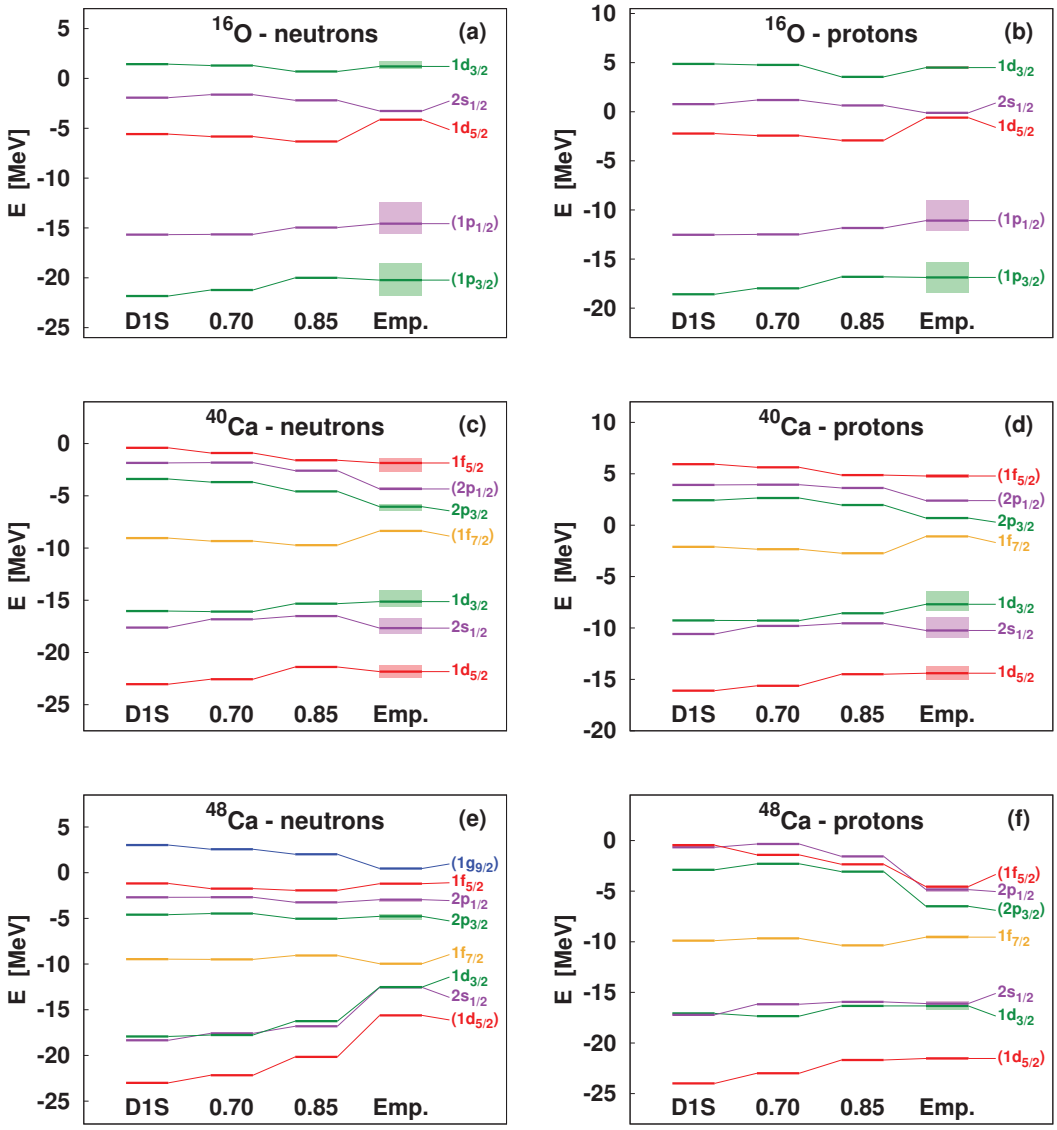

Figure 11. Neutron (left) and proton (right) single-particle energies in ^{16}O (top), ^{40}Ca (middle), and ^{48}Ca (bottom), calculated for the D1S [15], REG6a (N^{3}LO, $m^*/m = 0.70$), and REG6d (N^{3}LO, $m^*/m = 0.85$) functionals. Empirical values were taken from the compilation of Ref. [47].

uncertainties of definition and meaning. The calculated ones, which are here determined as the eigenenergies of the mean-field Hamiltonian, could also be evaluated from calculated odd-even mass differences. Similarly, determination of the empirical ones is always uncertain from the point of view of the fragmentation of the single-particle strengths. For these reasons, we did not include single-particle energies in the definition of our penalty function, see Sec. 3. Nevertheless, positions and ordering of single-particle

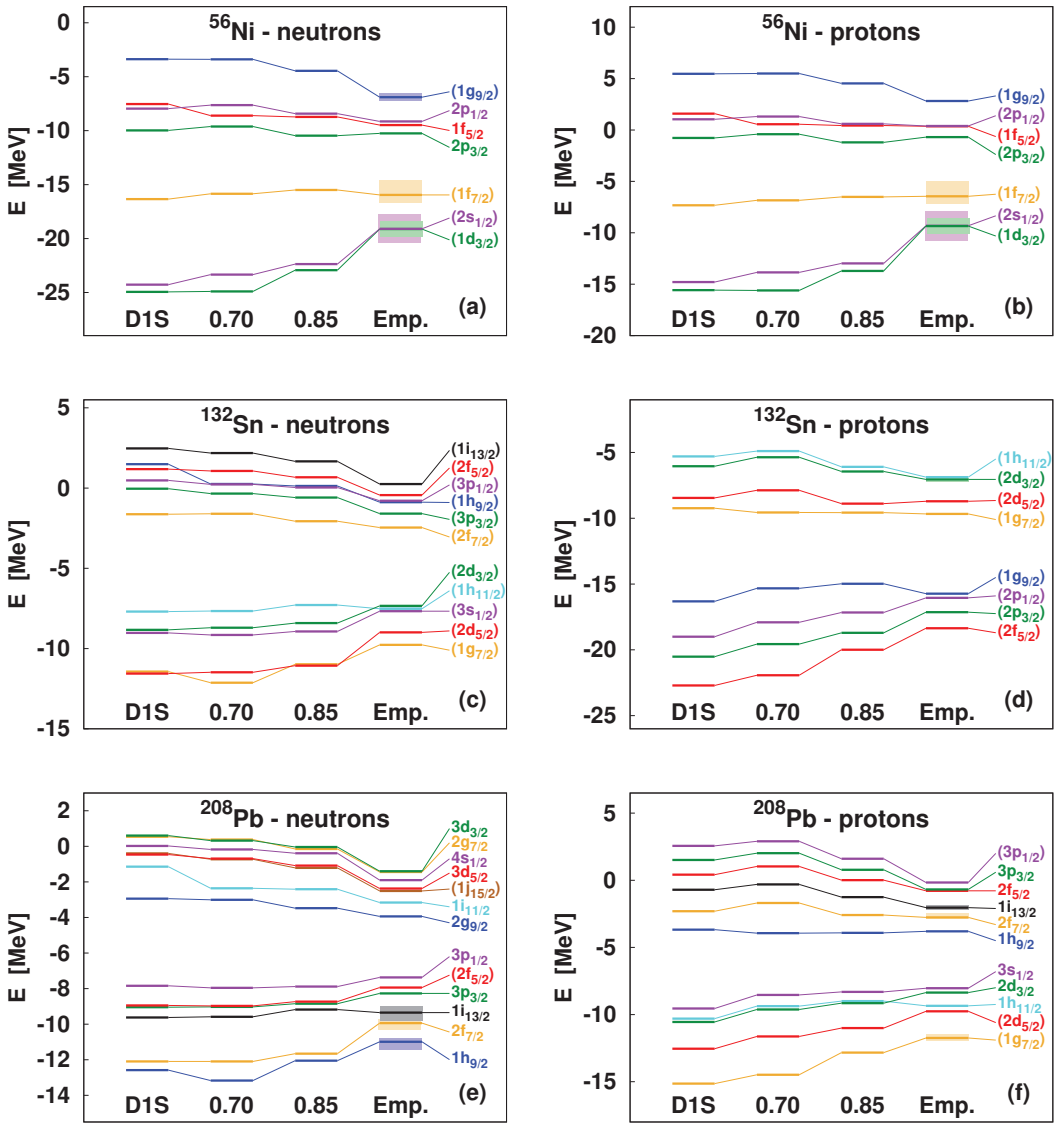

Figure 12. Same as in Fig. 11 but for ^{56}Ni (top), ^{132}Sn (middle), and ^{208}Pb (bottom).

energies are crucial for a correct description of other observables, such as, for example, ground-state deformations or deformation energies. Therefore, we consider comparisons presented in Figs. 11 and 12 to be very useful illustrations of properties of the underlying EDFs.

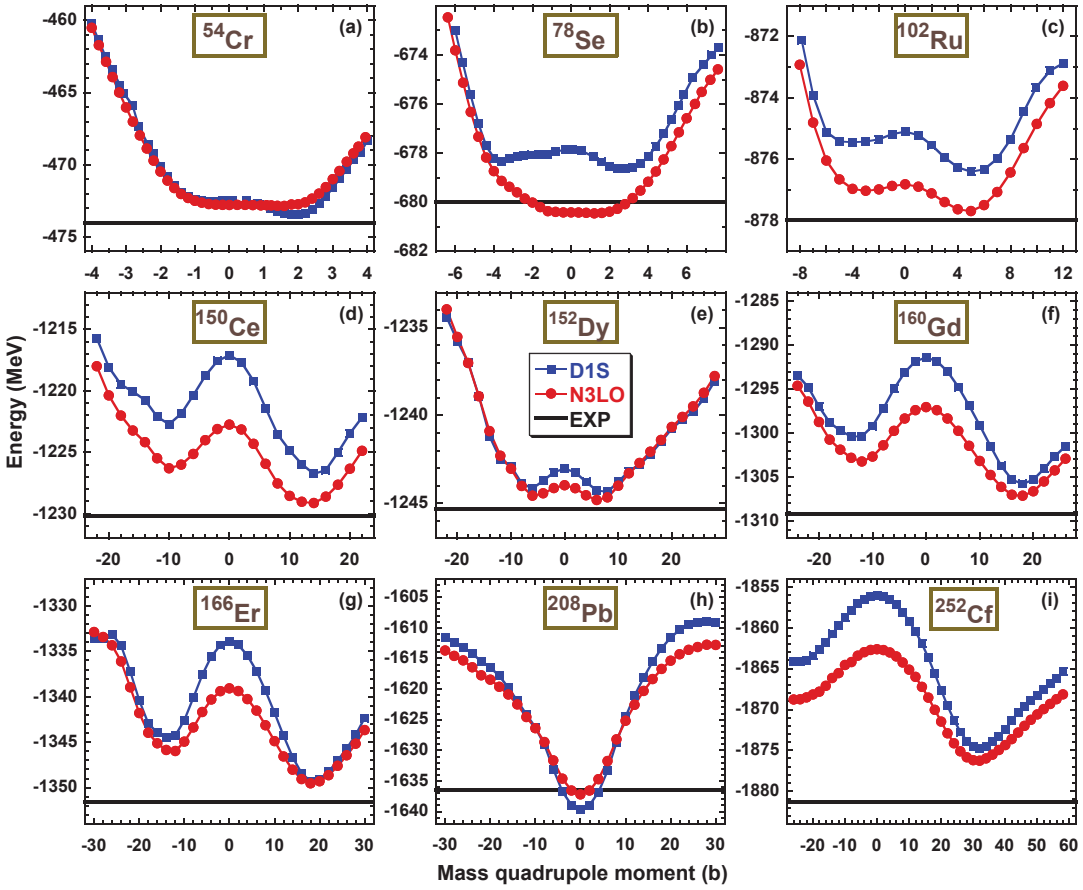

Figure 13. Deformation energies of selected nuclei, calculated for the D1S [15] (squares) and N^{3}LO REG6d (circles) functionals, extrapolated to infinite harmonic-oscillator basis, see Appendix D, plotted in the absolute energy scale, and compared with the experimental binding energies [35] (horizontal lines).

4.5. Deformed nuclei

Using the methodology of extrapolating results calculated for $N_0 = 16$ harmonic-oscillator shells to infinite N_0, presented in Appendix D, for a set of nine nuclei from ^{54}Cr to ^{252}Cf we determined deformation energies, Fig. 13, and binding-energy residuals, Fig. 14. The figures compare results obtained for the D1S [15] and N^{3}LO REG6d functionals.

In general, the pattern of deformations obtained for both functionals is very similar. This is gratifying, because deformed nuclei were not included in the adjustment of either one of the two EDFs. For this admittedly fairly limited sample of nuclei, the pattern of RMS binding-energy residuals is fairly analogous to what we have observed in spherical nuclei, see Sec. 4.3, with REG6d giving values that are about 30% smaller than those for D1S. It is interesting to see that in several instances, the two functionals generate absolute energies of the deformed minima that are more similar to one another than

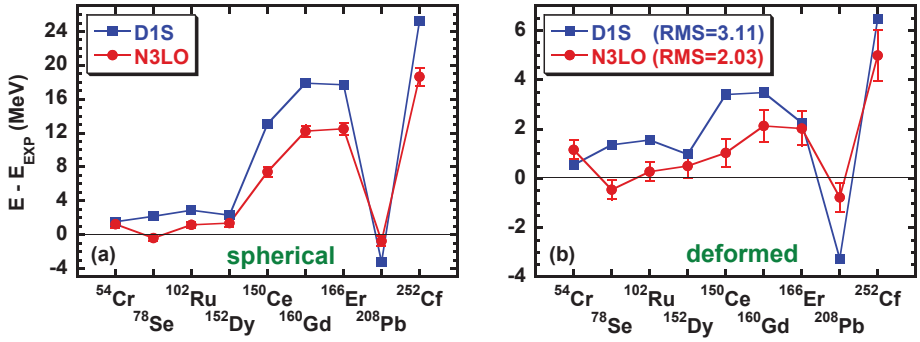

Figure 14. Same as in Fig. 13 but for the binding-energy residuals calculated at spherical shapes (a) and deformed minima (b).

those of the spherical shapes. In the present study we limit ourselves to presenting results only for these very few nuclei, whereas attempts of using deformed nuclei in penalty functions [48] and systematic mass-table calculations [49] are left to forthcoming publications.

5. Conclusions

In this article, we reported on the next step in adjusting parameters of regularized finite-range functional generators to data. We have shown that an order-by-order improvement of agreement with data is possible, and that the sixth order (N^3LO) functional describes data similarly or better than the standard Gogny or Skyrme functionals.

We implemented adjustments of parameters based on minimizing fairly complicated penalty function. Our experience shows that a blind optimization to selected experimental data seldom works. Instead, one has to implement sophisticated constraints, which prevent wandering of parameters towards regions where different kinds of instabilities loom.

We consider the process of developing new functionals and adjusting their parameters a continuous effort to better their precision and predictive power. At the expense of introducing single density-dependent generator, here we were able to raise the values of the effective mass, obtained in our previous study [14], well above those that are achievable with purely two-body density-independent generators [19]. Such a solution is perfectly satisfactory at the single-reference level. However, for multi-reference implementations, the density-dependent term must be replaced by second-order three-body zero-range generators [50], or otherwise entirely new yet unknown approach would be required.

Although a definitive conclusion about usefulness of EDFs obtained in this study can only be drawn after a comparison of observables of more diverse nature, this class of pseudopotentials looks promising, even if it can clearly be further improved. In the future, we plan on continuing novel developments by implementing non-local regularized

pseudopotentials along with their spin-orbit and tensor terms [13]. This may allow us to fine-tune spectroscopic properties of functionals and facilitate precise description of deformed and odd nuclei.

Appendix A. Decomposition of the potential energy in (S,T) channels

The techniques to derive decomposition of the potential energy per particle, $E_{\rm pot}^{(S,T)}/A$, into four spin-isospin (S,T) channels are the same for finite-range and zero-range pseudopotentials. Therefore, we do not repeat here the details of the derivation, which can be found, for example, in Ref. [51].

First, we recall the expression for the auxiliary function $F_0(\xi)$, already introduced in Ref. [30],

$$F_0(\xi) = \frac{12}{\xi^3}\left[\frac{1-\mathrm{e}^{-\xi^2}}{\xi^3} - \frac{3-\mathrm{e}^{-\xi^2}}{2\xi} + \frac{\sqrt{\pi}}{2}\,\mathrm{Erf}\,\xi\right] . \tag{A.1}$$

Then, in the symmetric infinite nuclear matter with Fermi momentum k_F and density $\rho_0 = 2k_F^3/3\pi^2$, contributions of the finite-range local pseudopotential (1) at order zero $(n=0)$ to (S,T) channels can be expressed as:

$$\frac{E_{\rm pot}^{(0,0)}}{A} = \frac{1}{32}\left(W_1^{(0)} - B_1^{(0)} + H_1^{(0)} - M_1^{(0)}\right)\rho_0\left[1 - F_0(k_F a)\right] , \tag{A.2}$$

$$\frac{E_{\rm pot}^{(0,1)}}{A} = \frac{3}{32}\left(W_1^{(0)} - B_1^{(0)} - H_1^{(0)} + M_1^{(0)}\right)\rho_0\left[1 + F_0(k_F a)\right] , \tag{A.3}$$

$$\frac{E_{\rm pot}^{(1,0)}}{A} = \frac{1}{32}\left(W_1^{(0)} + B_1^{(0)} + H_1^{(0)} + M_1^{(0)}\right)\rho_0\left[1 + F_0(k_F a)\right] , \tag{A.4}$$

$$\frac{E_{\rm pot}^{(1,1)}}{A} = \frac{9}{32}\left(W_1^{(0)} + B_1^{(0)} - H_1^{(0)} - M_1^{(0)}\right)\rho_0\left[1 - F_0(k_F a)\right] , \tag{A.5}$$

and those at higher orders n as:

$$\frac{E_{\rm pot}^{(0,0)}}{A} = -\frac{1}{32}\left(W_1^{(n)} - B_1^{(n)} + H_1^{(n)} - M_1^{(n)}\right)\rho_0\left(-\frac{1}{a}\frac{\partial}{\partial a}\right)^{n/2} F_0(k_F a) , \tag{A.6}$$

$$\frac{E_{\rm pot}^{(0,1)}}{A} = \frac{3}{32}\left(W_1^{(n)} - B_1^{(n)} - H_1^{(n)} + M_1^{(n)}\right)\rho_0\left(-\frac{1}{a}\frac{\partial}{\partial a}\right)^{n/2} F_0(k_F a) , \tag{A.7}$$

$$\frac{E_{\rm pot}^{(1,0)}}{A} = \frac{1}{32}\left(W_1^{(n)} + B_1^{(n)} + H_1^{(n)} + M_1^{(n)}\right)\rho_0\left(-\frac{1}{a}\frac{\partial}{\partial a}\right)^{n/2} F_0(k_F a) , \tag{A.8}$$

$$\frac{E_{\rm pot}^{(1,1)}}{A} = -\frac{9}{32}\left(W_1^{(n)} + B_1^{(n)} - H_1^{(n)} - M_1^{(n)}\right)\rho_0\left(-\frac{1}{a}\frac{\partial}{\partial a}\right)^{n/2} F_0(k_F a) . \tag{A.9}$$

Appendix B. Estimate of the surface energy coefficient

In section 3, we introduced a constraint on the estimate of the surface energy coefficient $a_{\rm surf}^{\rm LDM}$, calculated with a liquid-drop-type formula. In the case of local functionals (such as Skyrme functionals), to calculate the surface energy coefficient [38], several approaches

can be considered, such as the Hartree-Fock (HF) calculation [52], approximation of the Extended Thomas Fermi (ETF) type [53] or Modified Thomas Fermi (MTF) type [54], or within a leptodermous protocol, which is based on an analysis of calculations performed for very large fictitious nuclei [55].

Some of these approaches are not usable with the regularized pseudopotentials considered in this article. Indeed, the ETF and MTF methods can only be used for functionals that depend on local densities. In principle, the leptodermous protocol could be used, but it would require a significant expense in CPU time. Moreover, the HF calculations cannot be considered because the Friedel oscillations of the density make the extraction of a stable and precise value of the surface energy coefficient very difficult (see discussion in Ref. [38] and references therein).

Therefore, for the purpose of performing parameter adjustments, we decided to use a very simple estimate of the surface energy coefficient, which is usable with any kind of functional. After determining the self-consistent total binding energy E of a fictitious symmetric, spin-saturated, and unpaired $N = Z = 40$ nucleus without Coulomb interaction, we used a simple liquid-drop formula to calculate the surface energy coefficient,

$$a_{\rm surf}^{\rm LDM} = \frac{E - a_v A}{A^{2/3}}, \tag{B.1}$$

where $A = 80$ and a_v is the volume energy coefficient in symmetric infinite nuclear matter at the saturation point.

Values of $a_{\rm surf}^{\rm LDM}$ obtained in this way do depends on A, but, at least in the case Skyrme functionals, they vary linearly with the surface energy coefficients obtained using full HF calculations. Detailed study of the usability of estimates (B.1) will be the subject of a forthcoming publication [56].

In section 3, we used the value of $a_{\rm surf}^{\rm LDM} = 18.5\,{\rm MeV}$ as the target value of the parameter adjustments. This value is only slightly below the value obtained for the Skyrme functional SLy5s1 (18.6 MeV), which is an improved version of the SLy5 functional with optimized surface properties [38, 39]. This target value we used was only an educated guess, and it may require fine-tuning after a systematic study of the properties of deformed nuclei will have been performed.

Appendix C. Parameters of the pseudopotentials

Parameters of the pseudopotentials used in Sec. 4, REG2d at NLO, REG4d at N^{2}LO, and REG6d at N^{3}LO with $m^*/m \simeq 0.85$, and REG6a at N^{3}LO with $m^*/m \simeq 0.70$ are reported in Table C1 along with their statistical uncertainties. As it turns out, values of parameters rounded to the significant digits, which would be consistent with the statistical uncertainties, give results visibly different than those corresponding to unrounded values. Therefore, in the Table we give all parameters up to the sixth decimal figure. Moreover, the statistical uncertainties of parameters are only given for illustration, whereas the propagated uncertainties of observables have to evaluated

Table C1. Parameters a (in fm), t_3 (in MeV fm^4), $W_{\rm SO}$ (in MeV fm^5), and $W_1^{(n)}$, $B_1^{(n)}$, $H_1^{(n)}$, and $M_1^{(n)}$ (in MeV fm^{3+n}), of pseudopotentials REG2d, REG4d, REG6d, and REG6a with statistical uncertainties.

	REG2d (NLO)	REG4d (N^{2}LO)	REG6d (N^{3}LO)	REG6a (N^{3}LO)
a	0.85	1.15	1.50	1.60
t_3	11516.477663(0.5)	11399.197904(0.1)	11509.501921(0.3)	9521.936183(0.3)
$W_{\rm SO}$	106.098237(2.8)	115.427981(2.2)	116.417478(1.9)	122.713008(1.9)
$W_1^{(0)}$	−2510.198547(3.6)	−689.651657(2.4)	−2253.706132(0.5)	−1478.053786(0.9)
$B_1^{(0)}$	1108.303995(10.0)	−824.881825(6.4)	740.258749(1.9)	87.165128(2.4)
$H_1^{(0)}$	−2138.673166(2.2)	−247.692094(1.1)	−1794.716098(2.2)	−1031.141021(2.3)
$M_1^{(0)}$	746.778833(1.6)	−1270.827895(2.2)	282.583629(1.0)	−362.705492(1.3)
$W_1^{(2)}$	−637.749560(3.7)	−741.229448(2.0)	−3207.567147(2.1)	−2459.995595(2.2)
$B_1^{(2)}$	210.327285(3.1)	434.961848(2.6)	2368.246502(1.2)	1412.933291(1.6)
$H_1^{(2)}$	−892.452162(2.3)	−951.018473(1.0)	−3163.516190(0.8)	−2418.882336(0.8)
$M_1^{(2)}$	379.274480(7.1)	615.750351(2.0)	2319.605187(0.4)	1370.885213(0.6)
$W_1^{(4)}$		442.206742(3.8)	559.364051(1.3)	835.586806(2.1)
$B_1^{(4)}$		−972.382568(2.9)	−1398.820389(0.9)	−1594.561771(1.2)
$H_1^{(4)}$		420.867921(4.9)	351.670752(1.3)	774.195095(1.9)
$M_1^{(4)}$		−953.687931(2.3)	−1197.878374(0.3)	−1535.312092(0.5)
$W_1^{(6)}$			−1603.038264(2.8)	−1700.366589(3.8)
$B_1^{(6)}$			828.626124(2.0)	904.903410(2.8)
$H_1^{(6)}$			−1581.833642(2.0)	−1705.515946(2.4)
$M_1^{(6)}$			802.445641(1.9)	914.640430(2.5)

using the full covariance matrices [41]. Parameters of other pseudopotentials derived in this study along with the covariance matrix corresponding to REG6d are listed in the supplemental material (URL will be inserted by publisher).

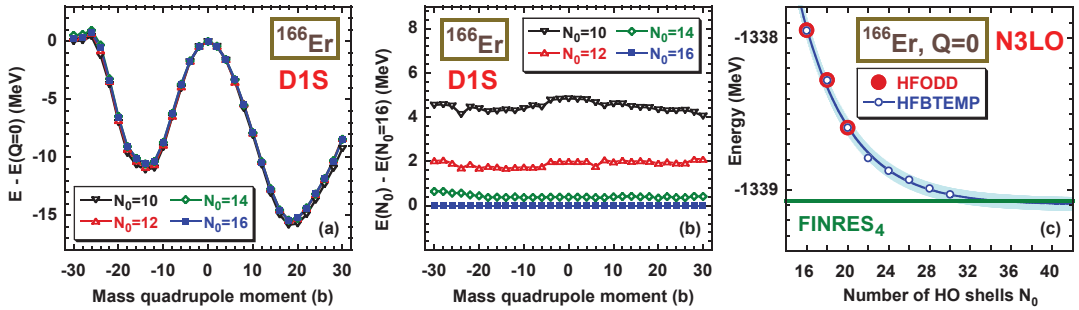

Figure D1. The relative, panels (a) and (b), and absolute, panel (c), binding energies of the spherical point in ^{166}Er, presented in function of the number N_0 of harmonic-oscillator shells used in codes HFODD and HFBTEMP. In panel (c), the horizontal line represents the asymptotic value determined using code FINRES$_4$.

Appendix D. Extrapolation of binding energies of deformed nuclei to infinite harmonic-oscillator basis

In this study, results for spherical nuclei were obtained using code FINRES$_4$ [57], which solves HFB equations for finite-range generators on a mesh of points in spherical space coordinates. Because of the spherical symmetry, it is perfectly possible to perform calculations with a mesh dense enough and a number of partial waves high enough for the results to be stable with respect to any change of the numerical conditions. Results for deformed nuclei were obtained using the 3D code HFODD (v2.92a) [58, 59] or axial-symmetry code HFBTEMP [60]. These two codes solve HFB equations by expanding single-particle wave functions on harmonic-oscillator bases. Since for deformed nuclei the amount of CPU time and memory is much larger than for spherical ones, it is not practically possible to use enough major harmonic-oscillator shells to reach the asymptotic regime, especially for heavy nuclei.

In order to estimate what would be the converged asymptotic value of the total binding energy of a given deformed nucleus, we proceeded in the following way. First, using code FINRES$_4$, we determined the total binding energy $E_{\rm sph}$ of a given nucleus at the spherical point. Second, using codes HFODD or HFBTEMP, for the same nucleus and for a given number of shells N_0, we determined total binding energies $E_{\rm sph}(N_0)$ (constrained to sphericity) and $E_{\rm def}(N_0)$ (constrained to a non-zero deformation). Third, we assumed that with $N_0 \to \infty$, the deformation energy $\Delta E_{\rm def}(N_0) = E_{\rm def}(N_0) - E_{\rm sph}(N_0)$ converges much faster to its asymptotic value than either of the two energies. Fourth, within this assumption, we estimate the asymptotic energies of deformed nuclei as

$$E_{\rm def}(N_0 = \infty) = E_{\rm sph} + \Delta E_{\rm def}(N_0) = E_{\rm def}(N_0) + E_{\rm sph} - E_{\rm sph}(N_0). \quad \text{(D.1)}$$

In Fig. D1, we present typical convergence pattern that supports the main assumption leading to estimate (D.1). Fig. D1(a) shows deformation energies ΔE of ^{166}Er calculated for the numbers of shells between $N_0 = 10$ and 16 using the D1S functional [15]. It is clear that in the scale of the figure, differences between the four

curves are hardly discernible. In a magnified scale, in Fig. D1(b) we show total energies $E_{\rm def}(N_0) - E_{\rm def}(16)$ relative to that obtained for $N_0 = 16$. We see that at $N_0 = 10$ and 12, the relative energies are fairly flat; however, they also exhibit significant changes, including sudden jumps related to individual orbitals entering and leaving the space of harmonic-oscillator wave functions that are included in the basis with changing deformation. Nevertheless, already at $N_0 = 14$, the relative energy becomes very smooth and almost perfectly flat. This behaviour gives strong support to applying estimate (D.1) already at $N_0 = 16$. Such a method was indeed used to present all total binding energies of deformed nuclei discussed in this article.

Finally, in Fig. D1(c), in the absolute energy scale we show total binding energies in ^{166}Er obtained using codes HFODD (up to $N_0 = 20$, large full circles) and HFBTEMP (up to $N_0 = 30$, small empty circles). Calculations were constrained to the spherical point and thus the results are directly comparable with the value of $E_{\rm sph} = -1339.069768$ obtained using the spherical code FINRES$_4$ (horizontal line). These results constitute a very strong benchmark of our implementations of the N^{3}LO pseudopotentials in three very different codes. For $N_0 \leq 20$, differences between the HFODD and HFBTEMP total energies (not visible in the scale of the figure) do not exceed 3 keV. By fitting an exponential curve to the HFBTEMP results (thin line) we obtained the extrapolated asymptotic value of energy $E_{\rm sph}(N_0 = \infty) = -1339.097(34)$, which within the extrapolation error of 34 keV (shown in the figure by the shaded band) perfectly agrees with the FINRES$_4$ value.

This work was partially supported by the STFC Grants No. ST/M006433/1 and No. ST/P003885/1, and by the Polish National Science Centre under Contract No. 2018/31/B/ST2/02220. We acknowledge the CSC-IT Center for Science Ltd. (Finland) and the IN2P3 Computing Center (CNRS, Lyon-Villeurbanne, France) for the allocation of computational resources.

References

[1] Bender M, Heenen P H and Reinhard P G 2003 *Rev. Mod. Phys.* **75**(1) 121–180 URL https://link.aps.org/doi/10.1103/RevModPhys.75.121

[2] Schunck N (ed) 2019 *Energy Density Functional Methods for Atomic Nuclei* 2053-2563 (IOP Publishing) URL http://dx.doi.org/10.1088/2053-2563/aae0ed

[3] Robledo L M, Rodríguez T R and Rodríguez-Guzmán R R 2018 *Journal of Physics G: Nuclear and Particle Physics* **46** 013001 URL https://doi.org/10.1088/1361-6471/aadebd

[4] Bulgac A and Yu Y 2002 *Phys. Rev. Lett.* **88** 042504 (pages 4) URL http://link.aps.org/abstract/PRL/v88/e042504

[5] Borycki P J, Dobaczewski J, Nazarewicz W and Stoitsov M V 2006 *Phys. Rev. C* **73**(4) 044319 URL https://link.aps.org/doi/10.1103/PhysRevC.73.044319

[6] Kortelainen M, McDonnell J, Nazarewicz W, Olsen E, Reinhard P G, Sarich J, Schunck N, Wild S M, Davesne D, Erler J and Pastore A 2014 *Phys. Rev. C* **89**(5) 054314 URL http://link.aps.org/doi/10.1103/PhysRevC.89.054314

[7] Carlsson B G, Dobaczewski J and Kortelainen M 2008 *Phys. Rev. C* **78**(4) 044326 URL http://link.aps.org/doi/10.1103/PhysRevC.78.044326

[8] Davesne D, Pastore A and Navarro J 2013 *Journal of Physics G: Nuclear and Particle Physics* **40** 095104 URL http://stacks.iop.org/0954-3899/40/i=9/a=095104
[9] Szpak B, Dobaczewski J, Carlsson B G, Kortelainen M, Michel N, Prassa V, Toivanen J and Veselý P *et al.*, unpublished
[10] Dobaczewski J, Bennaceur K and Raimondi F 2012 *Journal of Physics G: Nuclear and Particle Physics* **39** 125103 URL http://stacks.iop.org/0954-3899/39/i=12/a=125103
[11] Castellani E 2002 *Stud. Hist. Phil. Mod. Phys.* **33** 251 (*Preprint* arXiv:physics/0101039) URL https://arxiv.org/abs/1909.12879v1
[12] Lepage G 1997 *nucl-th/9706029* URL https://arxiv.org/abs/nucl-th/9706029
[13] Raimondi F, Bennaceur K and Dobaczewski J 2014 *Journal of Physics G: Nuclear and Particle Physics* **41** 055112 URL http://stacks.iop.org/0954-3899/41/i=5/a=055112
[14] Bennaceur K, Idini A, Dobaczewski J, Dobaczewski P, Kortelainen M and Raimondi F 2017 *Journal of Physics G: Nuclear and Particle Physics* **44** 045106 URL http://stacks.iop.org/0954-3899/44/i=4/a=045106
[15] Berger J, Girod M and Gogny D 1991 *Computer Physics Communications* **63** 365 – 374 URL http://www.sciencedirect.com/science/article/pii/001046559190263K
[16] Davesne D, Becker Pand Pastore A and Navarro J 2017 *Acta Phys. Pol. B* **48** 265 URL http://www.actaphys.uj.edu.pl/fulltext?series=Reg&vol=48&page=265
[17] Dobaczewski J, Stoitsov M V, Nazarewicz W and Reinhard P G 2007 *Phys. Rev. C* **76**(5) 054315 URL http://link.aps.org/doi/10.1103/PhysRevC.76.054315
[18] Sheikh J, Dobaczewski J, Ring P, Robledo L and Yannouleas C 2019 *arxiv:1901.06992* URL https://arxiv.org/abs/1901.06992
[19] Davesne D, Navarro J, Meyer J, Bennaceur K and Pastore A 2018 *Phys. Rev. C* **97**(4) 044304 URL https://link.aps.org/doi/10.1103/PhysRevC.97.044304
[20] Engel Y, Brink D, Goeke K, Krieger S and Vautherin D 1975 *Nuclear Physics A* **249** 215 – 238 URL http://www.sciencedirect.com/science/article/pii/0375947475901840
[21] Perlińska E, Rohoziński S G, Dobaczewski J and Nazarewicz W 2004 *Phys. Rev. C* **69**(1) 014316 URL http://link.aps.org/doi/10.1103/PhysRevC.69.014316
[22] Xu C, Li B A and Chen L W 2010 *Phys. Rev. C* **82**(5) 054607 URL https://link.aps.org/doi/10.1103/PhysRevC.82.054607
[23] Viñas X, Centelles M, Roca-Maza X and Warda M 2014 *The European Physical Journal A* **50** 27 URL https://doi-org.libproxy.york.ac.uk/10.1140/epja/i2014-14027-8
[24] Danielewicz P and Lee J 2014 *Nuclear Physics A* **922** 1 – 70 URL http://www.sciencedirect.com/science/article/pii/S0375947413007872
[25] Dechargé J and Gogny D 1980 *Phys. Rev. C* **21**(4) 1568–1593 URL https://link.aps.org/doi/10.1103/PhysRevC.21.1568
[26] Goriely S, Hilaire S, Girod M and Péru S 2016 *The European Physical Journal A* **52** 202 URL https://doi-org.libproxy.york.ac.uk/10.1140/epja/i2016-16202-3
[27] Gonzalez-Boquera C, Centelles M, Viñas X and Robledo L 2018 *Physics Letters B* **779** 195 – 200 URL http://www.sciencedirect.com/science/article/pii/S0370269318301047
[28] Chabanat E, Bonche P, Haensel P, Meyer J and Schaeffer R 1997 *Nuclear Physics A* **627** 710 – 746 URL http://www.sciencedirect.com/science/article/pii/S0375947497005964
[29] Chabanat E, Bonche P, Haensel P, Meyer J and Schaeffer R 1998 *Nuclear Physics A* **635** 231 – 256 URL http://www.sciencedirect.com/science/article/pii/S0375947498001808
[30] Bennaceur K, Dobaczewski J and Raimondi F 2014 *EPJ Web of Conferences* **66** 02031 URL http://dx.doi.org/10.1051/epjconf/20146602031
[31] Baldo M, Bombaci I and Burgio G F 1997 *Astron. Astrophys.* **328** 274–282 URL http://aa.springer.de/bibs/7328001/2300274/small.htm
[32] Baldo M 2016 private communication
[33] Wiringa R B, Fiks V and Fabrocini A 1988 *Phys. Rev. C* **38**(2) 1010–1037 URL https://link.aps.org/doi/10.1103/PhysRevC.38.1010

[34] Bordbar G H and Bigdeli M 2007 *Phys. Rev. C* **76**(3) 035803 URL https://link.aps.org/doi/10.1103/PhysRevC.76.035803
[35] Wang M, Audi G, Kondev F, Huang W, Naimi S and Xu X 2017 *Chinese Physics C* **41** 030003 URL http://stacks.iop.org/1674-1137/41/i=3/a=030003
[36] Kortelainen M, Lesinski T, Moré J, Nazarewicz W, Sarich J, Schunck N, Stoitsov M V and Wild S 2010 *Phys. Rev. C* **82**(2) 024313 URL https://link.aps.org/doi/10.1103/PhysRevC.82.024313
[37] Hellemans V, Pastore A, Duguet T, Bennaceur K, Davesne D, Meyer J, Bender M and Heenen P H 2013 *Phys. Rev. C* **88**(6) 064323 URL http://link.aps.org/doi/10.1103/PhysRevC.88.064323
[38] Jodon R, Bender M, Bennaceur K and Meyer J 2016 *Phys. Rev. C* **94**(2) 024335 URL https://link.aps.org/doi/10.1103/PhysRevC.94.024335
[39] Ryssens W, Bender M, Bennaceur K, Heenen P H and Meyer J 2019 *Phys. Rev. C* **99**(4) 044315 URL https://link.aps.org/doi/10.1103/PhysRevC.99.044315
[40] Bennaceur K, Dobaczewski J, Haverinen T and Kortelainen M 2019 Regularized pseudopotential for mean-field calculations (*Preprint* arXiv:1909.12879) URL https://arxiv.org/abs/1909.12879v1
[41] Dobaczewski J, Nazarewicz W and Reinhard P G 2014 *Journal of Physics G: Nuclear and Particle Physics* **41** 074001 URL http://stacks.iop.org/0954-3899/41/i=7/a=074001
[42] Ma Z and Wambach J 1983 *Nuclear Physics A* **402** 275 – 300 URL http://www.sciencedirect.com/science/article/pii/0375947483904992
[43] Delaroche J P, Girod M, Libert J, Goutte H, Hilaire S, Péru S, Pillet N and Bertsch G F 2010 *Phys. Rev. C* **81**(1) 014303 URL https://link.aps.org/doi/10.1103/PhysRevC.81.014303
[44] Delaroche J P, Girod M, Libert J, Goutte H, Hilaire S, Péru S, Pillet N and Bertsch G F Structure of even-even nuclei using a mapped collective Hamiltonian and the D1S Gogny interaction http://www-phynu.cea.fr/science_en_ligne/carte_potentiels_microscopiques/carte_potentiel_nucleaire_eng.htm
[45] The massexplorer http://massexplorer.frib.msu.edu/
[46] Nadjakov E, Marinova K and Gangrsky Y 1994 *Atomic Data and Nuclear Data Tables* **56** 133 – 157 URL http://www.sciencedirect.com/science/article/pii/S0092640X84710047
[47] Tarpanov D, Dobaczewski J, Toivanen J and Carlsson B G 2014 *Phys. Rev. Lett.* **113**(25) 252501 URL https://link.aps.org/doi/10.1103/PhysRevLett.113.252501
[48] Haverinen T 2020 *et al.*, to be published
[49] Kortelainen M 2020 *et al.*, to be published
[50] Sadoudi J, Duguet T, Meyer J and Bender M 2013 *Phys. Rev. C* **88**(6) 064326 URL http://link.aps.org/doi/10.1103/PhysRevC.88.064326
[51] Lesinski T, Bennaceur K, Duguet T and Meyer J 2006 *Phys. Rev. C* **74**(4) 044315 URL https://link.aps.org/doi/10.1103/PhysRevC.74.044315
[52] Côté J and Pearson J 1978 *Nuclear Physics A* **304** 104 – 126 URL http://www.sciencedirect.com/science/article/pii/0375947478900994
[53] Brack M, Guet C and Håkansson H B 1985 *Physics Reports* **123** 275 – 364 URL http://www.sciencedirect.com/science/article/pii/0370157386900785
[54] Krivine H and Treiner J 1979 *Physics Letters B* **88** 212 – 215 URL http://www.sciencedirect.com/science/article/pii/0370269379904507
[55] Reinhard P G, Bender M, Nazarewicz W and Vertse T 2006 *Phys. Rev. C* **73**(1) 014309 URL https://link.aps.org/doi/10.1103/PhysRevC.73.014309
[56] Da Costa P, Bender M, Bennaceur K, Meyer J and Ryssens W in preparation
[57] Bennaceur K *et al.*, unpublished
[58] Schunck N, Dobaczewski J, Satuła W, Bączyk P, Dudek J, Gao Y, Konieczka M, Sato K, Shi Y, Wang X and Werner T 2017 *Comp. Phys. Commun.* **216** 145 – 174 URL http://www.sciencedirect.com/science/article/pii/S0010465517300942

[59] Dobaczewski J 2020 *et al.*, to be published
[60] Kortelainen M *et al.*, unpublished